Cranfield Institute of Technology
College of Manufacturing

Ph.D. Thesis

Academic Year 1990-1991

C. L. CHAO

Investigations of the Machining of Glasses and Other Normally Brittle Materials in the Ductile Regime

Supervisors: Dr. A. E. Gee & Prof. R. C. Spragg

June 1991

Abstract

Increased demands for precision components made of brittle materials such as glasses and advanced ceramics, are such that conventional (free abrasive) grinding and polishing techniques can no longer meet the requirements of today's precision manufacturing engineering. Both fast production rates and high quality surfaces of complex shapes are required in addition to the spherical or planar surfaces produced which are most readily produced by conventional free abrasive techniques.

The work investigates the feasibility of using ductile-mode single-point diamond turning both as an alternative machining technique in its own right and as a model for certain parameters involved in (rigid-wheel) grinding. Indentation and ruling/scribing were used to study the underlying material properties, mechanical stress fields, the ductile-brittle transition and material removal mechanisms. Several material removal mechanisms were identified and discussed; these were *ploughing*, *cutting*, *delamination* and brittle fracture. The results of indentation and scribing experiments show that, with penetration depth of less than a critical value (the critical cut depth) brittle materials can be machined in a ductile manner and with chips very similar to those obtained from the classical ductile cutting of metal, save that, in this case it is at a much smaller scale. The influence of tool shape has shown to be important in determining the material removal mechanism.

The experiments on single-point diamond turning (facing) machine were carried out on a highly stiff diamond facing machine. During the present project continuous machining of a number of materials to Ra values of nanometres order has been achieved, these include soda-lime glass, fused silica, Zerodur and single crystal silicon. Ductile crack-free machining has been demostrated at spindle speeds up to 4500 rpm. The technical feasibility of ultra-fine single-point machining of optical, electronic and ceramic materials has thus been established.

Investigations were undertaken into methods of measuring the nature and extent of *sub-surface damage* (SSD) using scanning acoustic microscope (SAM), Rutherford back-scattering technique (RBS) and X-ray topography. The results of SSD studies suggested that coarse machining marks could still be detected in the sub-surface region even though the surface has been subsequently machined to a condition of no (optically) visible damage.

Table of Contents

Nomenclature

a	Radius
c	Crack length
d_v	Diagonal length of the Vickers indentation
A	Area
E	Young's modulus
G	Strain energy release rate
H	indentation mean pressure
H_B	Brinell hardness number
H_V	Vickers hardness number
K	Stress intesity factor; conductuivity
P	Hydrostatic pressure
P_L	Normal load
r	Radius
R	Radius
T	Temperature
U	Energy
V	Volume
W	Work
Y	Yield stress

Greek Letters

α	Geometrical angle
δ	Distance (of two approaching solids)
η	Dimensionless factor

κ	Critical shear stress
λ	Wavelength
μ	Coefficient of friction
ν	Poisson's ratio
ω	Angular speed
ψ	Geometrical angle
Ω	Dimensionless factor
φ	Geometrical angle
ψ	Geometrical angle
Ψ	Geometrical angle
ρ	Material density
σ	Stress component
τ	Shear stress component
θ	Geometrical angle

Subscripts

c	Critical
el	Elastic
ep	Elastic-plastic
p	Projection
I	Mode I
M	Mechanical
max	Maximum
min	Minimum
pl	Plastic
res	Residual
S	Surface

Superscripts

el	Elastic
M	Median crack
pl	Plastic
R	Radial crack

Acronyms

AFM	Atomic Force Microscope
CLA	Centre Line Average
LFM	Laser Force Microscope
MFM	Magnetic Force Microscope
RBS	Rutherford Back-Scattering
SAM	Scanning Acoustic Microscope
SEM	Scanning Electron Microscope
SSD	Sub-Surface Damage
STM	Scanning Tunnelling Microscope

List of Figures

Acknowledgements

I am indebted to many people for help, guidance and encouragement in the preparation of this thesis.

First, I would like to express my gratitude to my supervisors Dr A E Gee and Prof R Spragg for their guidance and advice throughout this work and Prof P Hancock, Head of School of Industrial and Manufacturing Science, and to Prof J Crookall, former Head of the College of Manufacturing at Cranfield Institute of Technology.

At Cranfield the work was particularly facilitated by having access to facilities under the stewardship of Cranfield Unit for Precision Engineering (CUPE) and Cranfield Precision Engineering Ltd (CPE). I am most grateful to Prof P McKeown and Mr W Wills-Moren for this and also for helpful discussions regarding the need for the work. For further helpful discussions and assistance, CUPE/CPE staff Messrs. R Read and P Shore are gratefully acknowledged. Particular mention should also be made of the scanning electron microscope facilities of the School of Industrial and Manufacturing Science whose staff, Mrs C Kimpton and Mr C Matthews, are thanked particularly.

This work has been aided considerably by the use of analytical equipment at a number of other establishments. I would like to thank Prof K E Puttick and Mr M Rudman of the Department of Physics at the University of Surrey for arranging the use of surface analysis facilities; in respect of Ion-beam facilities for Rutherford Back-scattering experiments at the same University, Dr C Jeynes of the Department of Electronic and Electrical Engineering is thanked. For the use of a scanning acoustic microscope in the Department for the Science of Materials, University of Oxford, I am grateful to Drs C B Scruby and A D Briggs and to Mr C W Lawrence.

Dr M Moore and Mr R Waggett of the Physics Department, Royal Holloway and Bedford New College, University of London provided X-ray topographical analysis.

Finally I would like to extend to my colleagues, fellow-students and staff, including Mr L Atkins (retd), in Lab. 132, my thanks for their assistance and friendship.

Chapter 1

Introduction

1.1 Opening Remarks

Over the past few decades the accuracy in machining has been advanced at a high pace. Developments in fields such as micro-electronic technology, computer engineering, solid state physics, electro-optical engineering and metrology have both stimulated and assisted the improvement of machining techniques. Increases in the accuracy of machine tools and associated measuring instruments over the past seventy years can be seen in Fig. 1.1 (Taniguchi 1983). The development of machin-

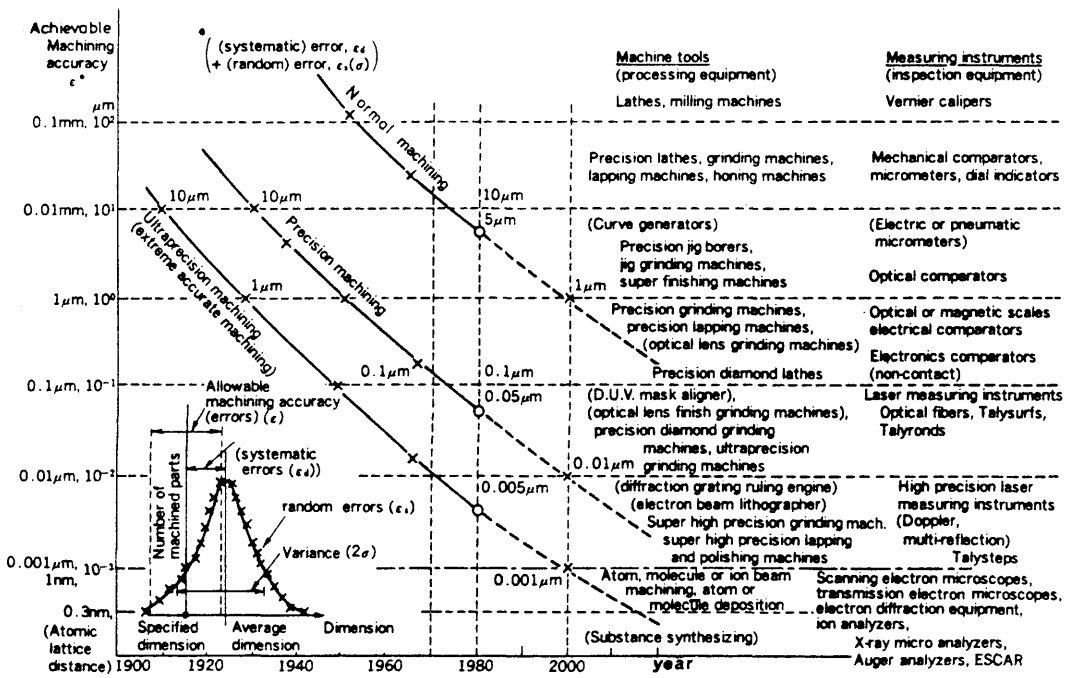

Fig. 1.1 Achievable machining accuracy [after Taniguchi 1983]

ing accuracy has led to the definition of "ultra-precision machining" from dimensional tolerances in the order of 1 μm in 1920s (Taniguchi 1983) to today's nanometres range.

In any work on precision machining, it is appropriate to consider capabilities in the field of position measurement, particularly since it is now possible to measure down to atomic levels and even manipulate the position of individual surface atoms. Just three years after Taniguchi published this figure , G. Binnig and H. Rohrer received half the 1986 Nobel prize for their successful operation of the scanning tunnelling microscope (STM) which, overcame the Abbe barrier and opened up a way to "observe" objects with resolutions of a fraction of a nanometre. The high spatial resolution of the STM image can reveal individual atoms and atom-by-atom variations in the composition of materials. Its success triggered further developments in scanned-probe microscopes such as the atomic force microscope (AFM), laser force microscope (LFM), magnetic-force microscope (MFM), electrostatic-force microscope and scanning thermal microscope which, with differences of detail and designed functions, can all give resolutions in the nanometres range (Wickramasinghe 1989).

This leap in measuring technology opened the way to observations in greater detail whilst, at the same time, stimulating the motivation to improve machining accuracy toward the nanometric capability of scanned probe microscopes. Shortly after the invention of the STM, other IBM workers developed it to spell their logo in atoms. Although 'machining' by moving individual atoms may not yet be a practical manufacturing technique, the requirements for products to be made smaller, faster, lighter, more accurate, reliable and, if possible, cheaper continue to set the goals for manufacturing engineering.

The demand for precision parts which can survive in extreme environments such as encountered in aero-engines and/or maintain a very high dimensional stability is likely to accelerate (McKeown 1987). To satisfy this demand, a new range of materials and new machining techniques are being developed. Among the new machining techniques, diamond turning and grinding are under active consideration to replace conventional techniques such as free abrasive lapping and polishing. The use of diamond tools enables many materials to be machined to nanometre tolerances.

In pursuit of suitable advanced materials, ceramics have received increasing attention from scientists, researchers and engineers for their attributes of high stiffness, dimensional and temperature stability and their ability to resist chemical attack. Modern ceramics encompass a wide variety of materials ranging from single crystal, or dense polycrystalline materials through wholly vitreous substances. The requirement for high performance ceramic materials, particularly those having improved electrical, electronic, piezoelectric, and magnetic and, more recently, pyroelectric and electro-optic/laser properties has increased steadily in recent decades (Davis, 1985).

Although the *brittleness* makes the machining of these materials extremely difficult, the demand for precision parts made of these materials has risen at a very fast rate - simply because of the superior physical, mechanical, optical or electronic properties. Typical examples of components that require precision fabrication of brittle materials are: optical systems, bearings, automobile diesel injectors, gas turbine blades, computer memory components, magnetic heads for computers, microelectronic devices and semiconductor components. Advances in the manufacturing process are critical to the economic production of these parts.

1.2 Ductile-Regime Machining

Glass, ceramic and glass-ceramic materials, as mentioned above, exhibit properties which are needed for today's and future advanced technology applications. However, machinability requirements for their intended applications often directly lead to disadvantages in respect of machining them to required form and/or finish. Hardness and brittleness renders them very difficult to finish-machine using conventional turning or grinding machines without causing substantial brittle fracture.

Finish machining has hitherto required long tedious periods using traditional lapping and polishing processes. Optics manufacturers have long been engaged with the difficulty involved in producing highly accurate glass surfaces. Although the first recorded design-application of optics is fairly accurately dated as being within a year or two of 1280 when it was noted that a French cleric used spectacles in the signing of an ecclesiastical document, little detail is recorded of the means of making them until the sixteenth century. It is known that free-abrasive grinding was employed

using a hard (iron) lap with decreasing grit-size and finally polishing was completed with a soft pitch lap. This process is essentially that upon which lens-making was reliant for seven centuries. The techniques and history are described by Twyman (1952) and by Horne (1978).

From the lapping and polishing process it can be seen that material may be removed from *brittle* materials in a ductile manner if the cutting is carried out at a very small (sub-micrometre) scale. However, lapping and polishing do not meet the demands of today's precision engineering which requires both fast production rate and the machining of surfaces of complex shape. Much effort has been made by researchers to investigate the feasibility of turning/grinding brittle materials and to identify criteria for *ductile mode* machining. The most common and useful ones are critical cut-depth and critical relative cross-feed as they can be easily implemented in the machining process. As will be discussed later in the thesis, for the brittle materials of interest both are generally in the sub-micron range. A super-rigid machine, equipped with advanced control and in-process metrology systems, with minimal internal/external vibration, installed and operated in a constant temperature and humidity environment, is required in order to achieve such accuracy. These requirements were well beyond the capability of conventional turning/grinding machines and the research on machining brittle materials was limited to polishing, indentation and scratching until the introduction of new generation diamond turning/grinding machines.

Early studies of "fixed-load" (as opposed to rigid) scratching of glasses by researchers such as Klemm and Smekal (1941), Taylor (1949, 1950), Marsh (1964), Demichelis (1951), Joos (1957), Ishida and Ogawa (1962) found that glass could be plastically scratched, producing a distinct furrow without visible cracks or the conchoidal chipping characteristic of brittle processes, if the vertical load was low enough. Demichelis (1951), Joos (1957), Busch (1968) and more recently Schinker and Doll (1985, 1987), Puttick et al (1989), Chao & Gee (1989) obtained large scale curly ribbons, up to several centimetres in some cases, in scratching, turning and ruling tests on glasses. These curly ribbons, or in terms of machining terminology - curly "chips", commonly seen in metal cutting, are evidence that glass can be ductilely machined. Research into multi-point diamond grinding carried out by Rice (1979), Bifano (1988) have also yielded promising results.

These results show that plastic flow does occur in ceramic/glass materials and with great care, it can even be ductilely machined. However much needs to be determined in respect of the specific cutting conditions enabling this ductile behaviour to be successfully maintained throughout processes such as turning and grinding.

1.3 Objectives of the Research Programme and Summary of Thesis

Although diamond grinding might appear to offer better machining economics and production rates, it was found in the early stage of this research, that, as a multi-point cutting process, a multiplicity of parameters were involved in grinding (such as cut-depth, cross-feed rate, wheel speed, wheel bonding, diamond grit size, type and shape, concentration and distribution of grit, coolant, working temperature, and material properties of workpiece). To monitor and control these for scientific experimental purposes presupposes machining capabilities which are the purpose of this work.

The single-point process offers fewer variables and the possibility of modelling certain features of the multi-point process. Further, the single point process can be spatially isolated so as to guarantee that a particular point has been machined only once. As a result, the emphasis of this research is mainly on the single point cutting process. Three types of single point "cutting" processes are investigated, namely indentation, ruling/scratching and lathe-facing.

Since different brittle materials can have very different physical properties, it is doubtful that one single set of machining parameters such as cutting depth, rake angle, feed-rate and cutting speed can be used to specify the machining of all brittle materials. The objective of this research is therefore to identify and to optimise machining conditions for machining different brittle materials in ductile mode, and to thereby yield a methodology for the classification of other materials and processes.

Several materials were chosen as typifying glass and glass-ceramic materials; these were soda-lime glass, fused silica, and the Schott glass-ceramic Zerodur. Also, single crystal silicon is employed as a test piece to investigate the problems of cutting brittle anisotropic materials.

In order to identify the machining conditions, a basic understanding of physical material properties is essential. Two fundamental cutting motions are defined by their directional vectors with respect to the surface, namely *digging-in* orthogonally to the surface and *moving* the tool *across* the material-surface; these are closely related to and partly modelled by indentation and ruling/scribing tests.

The following experiments and analysis were undertaken:

Multi-point diamond grinding: This research started with the feasibility of ductile-mode diamond grinding by using a precision diamond grinding machine built and operated by Cranfield Unit for Precision Engineering (CUPE) (McKeown 1986); the work was facilitated by the assistance of Mr. P. Shore. In order to investigate the effects of different cut-depths, a number of step and wedge grinding trials were undertaken on several materials including soda-lime glass and zirconia. However, owing to the complexity of the multiple variables involved in multi-point cutting, following these trials it was decided that single-point modelling and experiments were needed in order to better understand grinding.

Indentation: Vickers indentation tests were performed on soda lime glass, fused silica, Zerodur and single crystal silicon. In each case measurement-data was obtained from some fifteen (for 100, 200, 300 and 500 grams loads) to twenty (for 10, 25 and 50 grams loads) indentations for each load.

Scribing: Using a scribing micro-hardness test-instrument, scribing tests were also used to study material removal mechanisms under conditions of dead-load and slow traverse; these tests were designed to include investigation of sense (directional) effects on the surface of a crystalline material (single crystal silicon).

Ruling : Tests were performed on a grating ruling engine. The ruling test served a similar purpose to that of the scribing tests but at higher traverse velocities ie to investigate, (under dead load cutting conditions), material removal mechanisms and sense effects. However, being designed for ruling gratings over extended periods of time (days), the ruling engine offered more stable "cutting" conditions and a wider range of speeds than the available manually driven scribing tester.

Single-point diamond turning: An experimental rigid single-point diamond facing machine was employed to provide test-data under "real" machining conditions (fixed cut depth, controlled feed rate) equating to those expected on a finish pass. The

ductile-brittle transition with increase of cut depth was studied by using the technique of (wedge) cutting into an inclined surface (so that the cut depth could be arranged to vary from zero to beyond that for brittle fracture). Diamond tools used for this were also studied , monitoring wear of the cutting edge.

Scanning acoustic microscope (SAM): SAM facilities were made available by Oxford University and used in an attempt to find a non-destructive method of measuring sub-surface damage. However, due to the limited availability of the instrument, it was used in the early stage of the study and fine-ground specimens only (and the instrument available was found to have insufficient resolution).

X-ray topography: Lang's method was used in this study; both section and projection x-ray topography were used to investigate the sub-surface damage of single-point diamond turned single crystal silicon specimens at Royal Holloway and Bedford New College, University of London.

Rutherford back-scattering (RBS): The Rutherford back-scattering technique was used (at the University of Surrey) to detect the depth of sub-surface damage by bombarding diamond-turned single crystal silicon specimens with an ion beam and analyzing the energy spectrum of back-scattered ions.

Indentation tests are discussed in chapter 2 and chapter 3 is concerned with ruling and scratching experiments. It should be pointed out that by analogy with cutting, ruling is essentially a minimal-damage process whereas scratching is a less-organised process (brittle, in the case in hand). Plastic deformation and brittle fracture observed in indentation and ruling/scribing tests are compared in chapter 4 where material removal mechanisms of brittle materials and ductile-brittle transition in machining are also discussed.

The results of chapter 2, 3 and 4 allowed the various factors governing ductile mode machining to be studied in rigid turning/facing experiments as detailed in chapter 5. The scanning electron microscope (SEM) and Talystep are employed to examine the machined surface so as to evaluate and to optimise the machining conditions; the results are discussed in chapter 5. The tool tip temperature and wear of diamond are also addressed.

Chapter 6 is devoted to the investigation of sub-surface damage introduced during machining, the results from non-destructive tests such as scanning acoustic microscopy (SAM), X-ray topography and Rutherford back-scattering (RBS); destructive tests like indentation are also discussed.

The influence of material properties, tool shape and machining conditions are addressed in chapter 7.

Chapter 2

Indentation

2.1 Introduction

Indentation techniques have long (ie Brinell test has been used since 1900; see Brinell , 1900) been used as a means of measuring hardness which, on a comparative basis, is a measure of the resistance of a material to local permanent deformation or plastic flow. The indentation test procedure commonly involves pressing a hard indenter into the surface of a material test-specimen at a controlled rate. Usually, a "sharp" indenter such as diamond cone or pyramid (as in Knoop and Vickers hardness tests respectively) or a "blunt" indenter such as a steel sphere (Brinell test) is used as the indenter.

Hardness may be expressed as a number such as the Vickers hardness number (H_v or DPH - Diamond Pyramid Hardness) and the Brinell hardness number (H_B) defined as the ratio of the applied load to the pyramid area (Vickers) or curved area (Brinell) of the residual impression produced by the indenter. Hardness is not an identifiable single fundamental property of a material as values will differ according to test-conditions. Since it follows that there are no absolute standards of hardness, its quoted value is only meaningful when the shape of the indenter, applied load and duration of load are quoted.

Meyer (1908) proposed that hardness should be defined as the ratio of the load to the projected area of the indentation. By doing so, "hardness" could be given profound physical meaning as the mean contact pressure. In the case of the Vickers hardness test, it is easily shown that the relationship between indentation mean pressure, H, and hardness number, Hv, is given by

$$Hv = \frac{2 P_L \sin 68^o}{d_v^2}$$

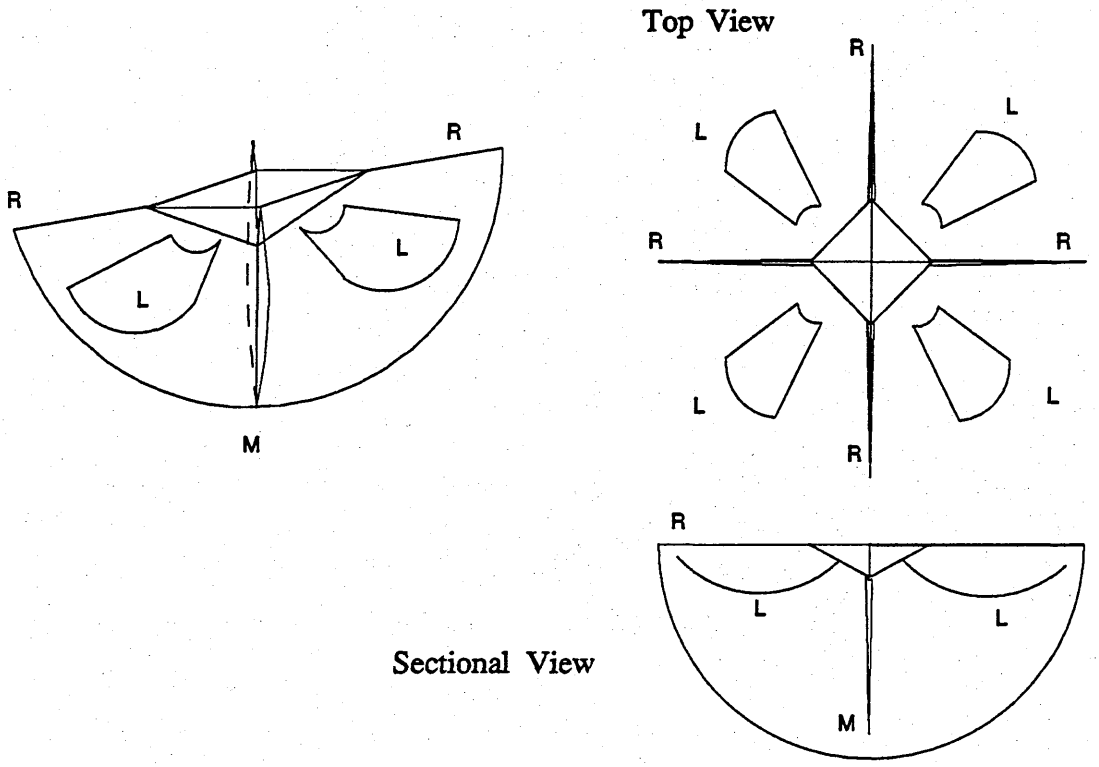

Fig. 2.1 Cracks appear around the indentation: R-radial crack; M-median crack; and L-lateral crack.

$$= 1.8544 \frac{P_L}{d_v^2} = 0.927 H \qquad (2.1)$$

where P_L is the normal load, d_v is the diagonal length of the residue impression.

When measuring the hardness of brittle materials at high loads it is seen that well-defined patterns of micro-cracks namely *cone*, *median*, *radial* and *lateral* cracks (as shown in Fig. 2.1) appear around the indentation. These cracks, especially the radial form, were first regarded as a nuisance, making the measurement of hardness in brittle materials more difficult. However, the similarity between the cracks generated by indentation and by brittle machining were then noticed (Lawn and Fuller 1975). Indeed, apart from *scribing* (or *ruling*) by drawing an indenter across the surface and pushing material aside, both the indenter (in the indentation test) and tool (in machining) are used to *break through* (penetrate) the material surface commonly leading to classical *cutting* action in the ductile metals traditionally used in machining. As a consequence of *penetrating* or *scribing*, a highly localised stress field is introduced around the indenter or tool which, if strong (or large) enough, creates cracks and fractures. In manufacturing processes the presence of cracks in

the resultant product invariably incurs lower performance during use e.g. optical surfaces, bearing, and jet engine components. Use of the information from indentation investigations has led to a new approach to the understanding of abrasive/turning/grinding machining processes employed with brittle materials.

In order to understand what happens in the *break through* (penetration) process as a means of addressing the problem of exceeding the fracture threshold, it is essential to have a clear knowledge of the stress field in the vicinity of the indentation. In search of an understanding of the stress field, much scientific effort, both theoretical and experimental, has been made by researchers and the results show that indentation can offer a lot more than just measures of the hardness of the material.

Palmqvist (1962), Marsh (1964), and Lawn and Fuller (1975), noticing that indentation radial crack length increased with load, suggested that the cracks generated by the indentation could be used as a measure of toughness (by measuring the length of radial crack, see section 2.3.3). Moreover, the way brittle materials respond to indentation eg. changing from plastic 'pile up' or 'densification' (compaction) to brittle chipping off, offers an easy yet powerful method to study the transition from plastic flow to brittle fracture. Consequently, indentation techniques are now extensively used by researchers to study the mechanical properties and to obtain quantitative information on the mechanical response of brittle materials particularly at microscopic levels. As a result, various different equations have been derived to correlate the crack lengths and fracture toughness as will be addressed in following sections.

2.2 Models for Indentation Stress Fields and Deformation Mechanisms

2.2.1 Elastic Contact Model

Although in reality no material is perfectly elastic and/or isotropic, a simplified elastic contact stress field can be useful in initially analyzing the complicated inelastic contact problem. In the elastic contact model, materials are considered to be both (linearly) elastic and isotropic, so that no permanent deformation will occur. Boussinesq (1885) worked out the problem of an elastic half-space subjected to a normal point load P_L (known as "the Boussinesq problem") and suggested that the stress field in such condition could be expressed as (see insert of Fig. 2.2):

$$\sigma_{rr} = \frac{P_L}{\pi R^2}\left[\left(\frac{1-2\nu}{4}\right) sec^2\frac{\varphi}{2} - \frac{3}{2}\cos\varphi\sin^2\varphi\right]$$

$$\sigma_{\theta\theta} = \frac{P_L}{\pi R^2}\left[\left(\frac{1-2\nu}{4}\right)\left(\cos\varphi - \frac{1}{2}sec^2\frac{\varphi}{2}\right)\right]$$

$$\sigma_{zz} = \frac{P_L}{\pi R^2}\left[-\frac{3}{2}\cos^3\varphi\right]$$

$$\sigma_{rz} = \frac{P_L}{\pi R^2}\left[-\frac{3}{2}\cos^2\varphi\sin\varphi\right]$$

$$\sigma_{r\theta} = \sigma_{\theta z} = 0 \qquad (2.2)$$

The principal stresses of the Boussinesq stress field then be derived as (in this the three principal stresses σ_{11}, σ_{22} and σ_{33} are labelled such that $\sigma_{11} \geq \sigma_{22} \geq \sigma_{33}$.)(Lawn and Swain 1975):

$$\sigma_{11} = \sigma_{rr}\sin^2\alpha + \sigma_{zz}\cos^2\alpha - 2\sigma_{rz}\sin\alpha\cos\alpha$$

$$\sigma_{22} = \sigma_{\theta\theta}$$

$$\sigma_{33} = \sigma_{rr}\cos^2\alpha + \sigma_{zz}\sin^2\alpha + 2\sigma_{rz}\sin\alpha\cos\alpha \qquad (2.3)$$

The contours of three principal normal stresses in Boussinesq stress field are illustrated in Fig. 2.2 (Lawn and Swain 1975), for the case of $\nu = 0.25$. As can be seen in Fig. 2.2, the stresses σ_{22} and σ_{33} are everywhere tensile and compressive respectively. The stress σ_{22}, having a "hoop" shape trajectory, is called *hoop stress* and is tensile in a region below the indenter but compressive near the surface (Lawn and Swain 1975, Lawn and Wilshaw 1975).

By using the Boussinesq stress field, Sneddon (1965) proposed the relationship between the load, P_L, and the penetration depth, d, in the case of a frictionless rigid conical indenter normally loaded on a flat elastic body as:

$$P_L = \frac{2Ed^2}{(1-\nu^2)\pi}\tan\theta \qquad (2.4)$$

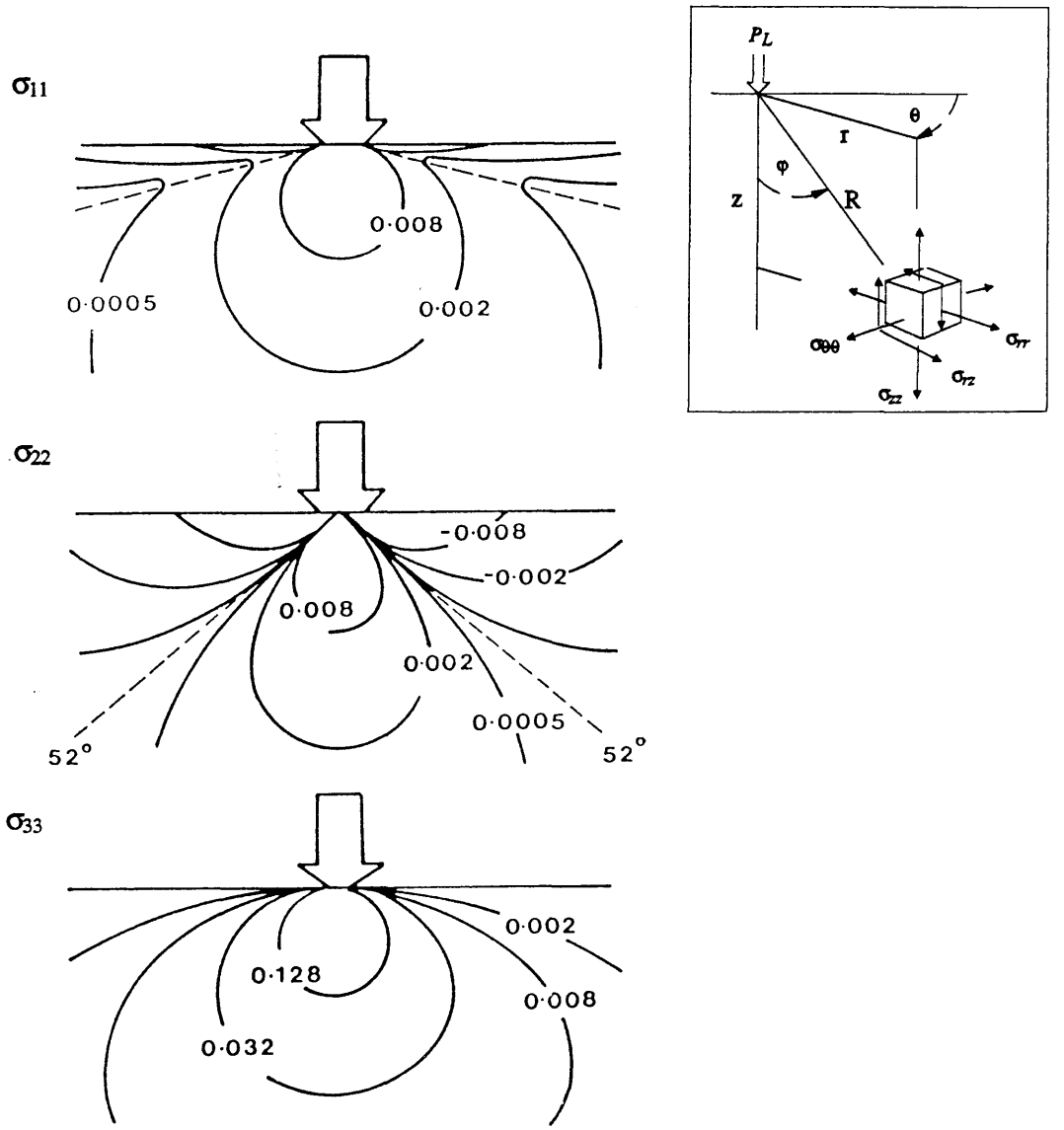

Fig. 2.2 Contours of principal normal stresses in Boussinesq field for the case of $\nu = 0.25$. Unit of stress is P_0, the mean contact pressure. (insert: coordinate system and stresses for axially symmetric point loading P_L)(After Lawn and Swain 1975)

Hertz (1882) took the case of a frictionless spherical indenter loaded on a frictionless elastic half space and proposed that the pressure distribution in the contact area could be written as:

$$p(r) = p_0\left[\,1 - \left(\frac{r}{a}\right)^2\right]^{1/2} \qquad (2.5)$$

where a is the radius of contact circle, p_0 is the maximum pressure and r is the radial distance within the contact circle. By using this assumption, the total load compressing the solids, P_L, is related to the pressure, p_0, by

$$P_L = \int_0^a p(r)\, 2\pi r\, dr$$
$$= \frac{2}{3} p_0 \pi a^2 \qquad (2.6)$$

The radius, a, the mutual approach of distant points in the two solids, δ, and maximum contact pressure, p_0, can be expressed in terms of the total load compressing the solids, P_L, and radius of the spherical indenter, R (Johnson 1985):

$$a = \left(\frac{3 P_L R}{4 E_e} \right)^{1/3}$$
$$\delta = \frac{a^2}{R} = \left(\frac{9 P_L^2}{16 R E_e^2} \right)^{1/3} \qquad (2.7)$$
$$p_0 = \frac{3 P_L}{2\pi a^2} = \left(\frac{6 P_L E_e^2}{\pi^3 R^2} \right)^{1/3}$$

where

$$\frac{1}{E_e} = \frac{1 - \nu_1^2}{E_1} + \frac{1 - \nu_2^2}{E_2}$$

E_1, ν_1 and E_2, ν_2 are the Young's moduli and Poisson's ratios of the indenter and specimen respectively.

The elastic contact model (Boussinesq stress-field and Hertzian stress-field) over-simplifies the stress distribution of the near-field and takes no account of the residual stress and elasto-plastic nature of the material, so it can only serve as an approximation.

2.2.2 Cutting Mechanism and Slip-line Field Model

The slip-line field, originally developed by Hill, Lee and Tupper (1947), is a two-dimensional treatment of a rigid-plastic solid. When a rigid-plastic solid is subjected to uni-axial tension or compression, no deformation occurs (ie it is perfectly rigid) until the yield stress, Y, is reached; it then deforms plastically without work hardening. Since there is no work hardening, it is reasonable to suggest that the hydrostatic pressure does not affect the behaviour, so that the material yields when a critical shear stress, κ, is reached. Generally, this critical shear stress is correlated to yield stress by a using yield criteria. The most widely used yield criteria are Tresca's and von Mises' flow criteria.

Tresca's (1864) criterion is of the form:

$$| \sigma_1 - \sigma_2 | = Constant \qquad (2.8)$$

which means that yielding occurs when the maximum shear stress (the largest one of the three magnitudes $| \sigma_1 - \sigma_2 |$, $| \sigma_2 - \sigma_3 |$, $| \sigma_3 - \sigma_1 |$) in the material reaches a certain value.

Von Mises' (1913) criterion (also proposed by Huber in 1904) is based on yield beginning when the shear strain energy reaches a critical value. The flow criterion may be written as:

$$(\sigma_1 - \sigma_2)^2 + (\sigma_2 - \sigma_3)^2 + (\sigma_3 - \sigma_1)^2 = Constant \qquad (2.9)$$

The constants are usually identified with the tensile yield stress, Y, or the yield shear stress k for a state of pure shear. Comparing the constants obtained in the case of yielding in simple tension ($\sigma_1 = Y, \sigma_2 = \sigma_3 = 0$) and in the case of pure shear ($\sigma_1 = -\sigma_3 = \kappa, \sigma_2 = 0$), it can be derived from the Tresca criterion that

$| \sigma_3 - \sigma_1 | = Y = 2\kappa$

(thereby $\kappa = Y/2$)

while the von Mises criterion gives

$$(\sigma_1 - \sigma_2)^2 + (\sigma_2 - \sigma_3)^2 + (\sigma_3 - \sigma_1)^2 = 2Y^2 = 6k^2$$

(thereby $k = \frac{2}{\sqrt{3}}\left(\frac{Y}{2}\right)$).

The plastic flow occurs when the shear stress in the stress field reaches this critical value k (see Hill 1950, Johnson and Mellor 1983). For a frictionless flat punch P is equal to $2k(1+\pi/2)$. We can correlate P and Y by substituting k with one of the yield criteria.

Generally, the contact pressure can be written as $P = C_t Y$ (Tabor 1951) where C_t is a geometric constraint factor. Hill (1950) and Tabor (1951) proposed that for fully work hardened materials C was very close to 3, thus $\frac{P}{Y} \approx 3$. However, for work hardened materials, elastic deformation is relatively small compared with plastic deformation. As pointed out by Marsh (1964), when this theory was applied to glass it considerably under-predicted the plastic flow stress. The deficiency of this model is related to the large elastic strain of glass. This led Marsh (1964) to conclude that this simple indentation theory was generally inadequate for brittle (highly elastic) materials and to propose the expansion of a spherical cavity model.

2.2.3 Compression Mechanism and Model of Expansion Cavity

Samuels and Mulhearn (1957) and Mulhearn (1959) found that by pressing brass with Vickers, Brinell and cone indenters, the material was often displaced radially outwards from the indentations. The shape of the strain boundaries appeared to be very close to a hemisphere with its' centre located at or slightly below the indentation. Mulhearn (1959) then proposed that indentation by blunt indenters is

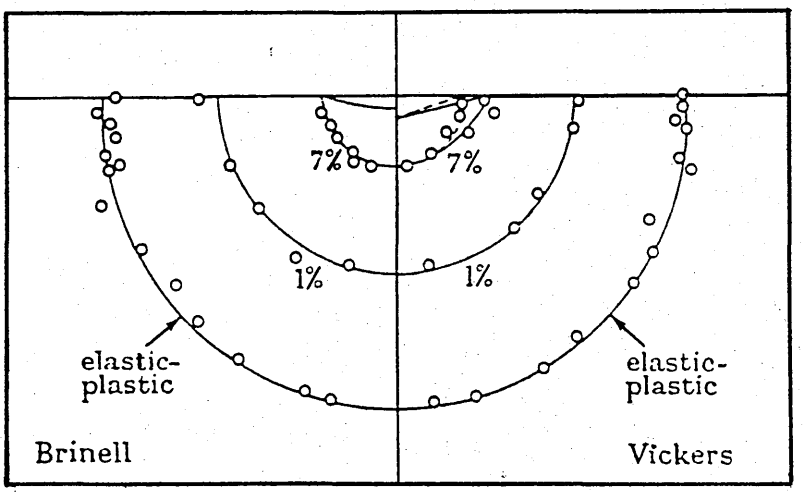

Fig. 2.3 Contours of equal strain around indentations showing the hemispherical symmetry of the strain system. (After Samuels and Mulhearn 1957)

produced by a compression mechanism in which material deformation is similar to that of the radial compression of hemispherical shells centred at the point of the indenter (as shown in Fig. 2.3).

These results obtained by Samuels and Mulhearn led Marsh (1964) to suggest that the indentation-deformation was analogous to the expansion of a spherical cavity into an elastic-plastic solid by an internal hydrostatic pressure P. Generally, Marsh's approach is more suitable for materials of high Y/E ratio (highly elastic) since being less rigid they would be more amenable to radial flow.

The expansion of a spherical cavity in an infinite elastic-plastic solid by an internal pressure P had already been analyzed by Bishop, Hill and Mott (1945) and by Hill (1950) who showed that the internal pressure P was

$$\frac{P}{Y} = \frac{2}{3}\left[\, 1 + \ln \frac{E}{3(1-\nu)Y} \,\right] \qquad (2.10)$$

Marsh (1964) followed Hill's solution but eliminating certain simplifying assumptions to generalise the above equation to

$$\frac{P}{Y} = \frac{2}{3}\left[1 + \frac{3}{3 - \lambda_1} \ln \frac{3}{(\lambda_1 + 3\mu_1 - \lambda_1 \mu_1)} \right]$$

$$= \frac{2}{3} + \frac{2}{3} B \ln Z \qquad (2.11)$$

where

$$\lambda_1 = (1 - 2\nu)\frac{Y}{E} \ ,$$

$$\mu_1 = (1 + \nu)\frac{Y}{E}$$

E is Young's modulus, ν is Poisson's ratio, B and Z are the appropriate functions of λ_1 and μ_1.

Since the constraints around a hemispherical cavity is less than a spherical cavity, Marsh proposed an equation of similar form:

$$\frac{P}{Y} = C_m + K_m B \ln Z \qquad (2.12)$$

where C_m and K_m are constants no longer equal to $\frac{2}{3}$.

One major defect of Marsh's model is that the shape of the indenter has little effect on the indentation stress field. To rectify this, Johnson (1970) took the shape of the indenter into account and replaced the *cavity* of Marsh's model with a semi-cylindrical or hemispherical incompressible hydrostatic *core* of radius, r_{core}, which encased

the surface of the indenter (as shown in Fig. 2.4). The displacement of material is approximately radial from the first point of contact and the displaced material is accommodated by the elastic-plastic expansion of the surrounding material.

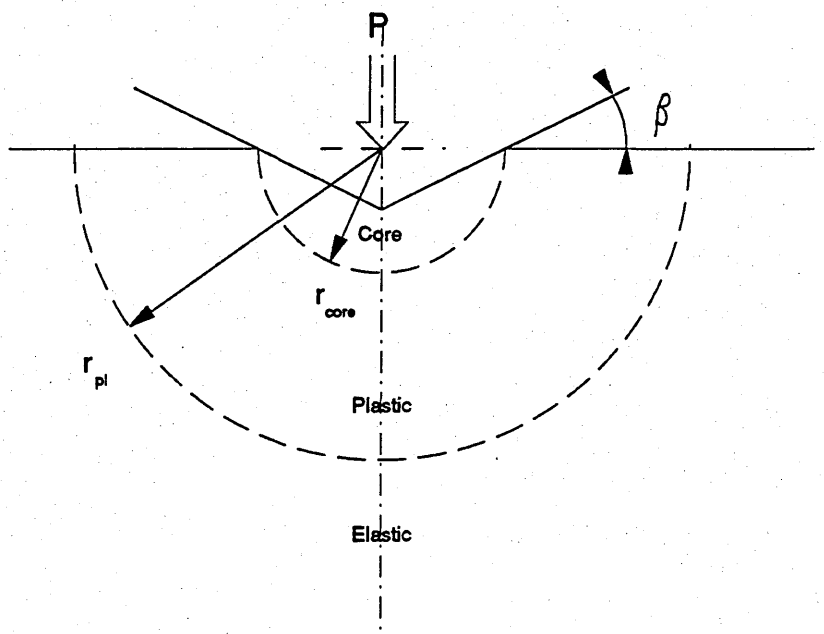

Fig. 2.4 Expansion cavity model of an indentation: a semi-cylindrical or hemispherical plastic 'core' attached to the indenter surrounded by an elastic-plastic region in which the material is displaced radially .(After Johnson 1970)

Johnson (1970) proposed that the hardness of elastic-plastic materials to penetration by a blunt indenter was governed by the single parameter $(\frac{E}{Y})\tan\beta$, where β was the inclination of the face of the indenter to the specimen surface. He showed that for a cone indenter of "inclination angle", β , the final relation of $\left(\frac{P}{Y}\right)$ is given by

$$\frac{P}{Y} = \frac{2}{3} + 2\ln\left(\frac{r_{pl}}{r_{core}}\right)$$

$$= \frac{2}{3} + \frac{2}{3}\ln\left[\frac{\left(\frac{E}{Y}\right)\tan\beta + 4(1-2\nu)}{6(1-\nu)}\right] \qquad (2.13)$$

where r_{pl} is the radius of the plastic zone. If $\nu = 0.5$ this gives

$$\frac{P}{Y} = \frac{2}{3}\left[1 + \ln\left(\frac{E \tan\beta}{3Y} \right) \right]$$

The value of the inclination angle β for a Vickers pyramid is 19.7, obtained by taking the equivalent angle for a cone displacing the same volume of material for the same depth of penetration.

Although Johnson's equation gives reasonable agreement with the experimental data of Marsh (1964), Atkins and Tabor (1965), and Hirst and Howse (1969), there are two deficiencies in his approach. Firstly, there is a step-discontinuity in stresses at the boundary of the hydrostatic core. Secondly, no account is taken of the free surface.

To tackle the first problem, Studman, Moore and Jones (1977) suggested that to replace the hydrostatic "core" with a region in which the stresses are changing from purely hydrostatic at the first contact point to values which enable the von Mises yield criterion to be satisfied at the core boundary. This leads to a modified equation (Studman, Moore and Jones 1977):

$$\frac{P}{Y} = J + 0.5 + \frac{2}{3}\left[1 + \ln\left(\frac{E \tan\beta}{3Y} \right) \right] \qquad (2.14)$$

where J, a geometry constant, takes the value of -0.2 for spherical indenters and is zero for conical and pyramidal indenters.

Chiang, Marshall and Evans (1982) attempted to account for the free surface and remove the restriction in the choice of the core radius (hemispherical cavity model). Based on their indentation experiments on a range of brittle solids over a wide range of indenter geometries, they suggested that the plastic zone exhibited spherical symmetry regardless of indenter geometry and the indentation pressure was in-

denter shape insensitive. Using the uniqueness of the relation between indentation volume ΔV and the plastic zone volume V, the relative indentation dimension β_c is defined as:

$$\beta_c = \frac{r_{pl}}{r_a} = \left(\frac{V}{\Delta V} \right)^{1/3} \qquad (2.15)$$

where r_a is the radius of the hemispherical indentation and r_{pl} is the radius of the hemispherical plastic zone. The β_c values are to be determined from measurements of the indentation and plastic zone dimensions. For pyramidal indentations, with a hemispherical plastic zone Eq. 2.15 becomes

$$\frac{r_{pl}}{r_a} = \left(\frac{2\, r_{pl}}{d_v} \right) \left(\frac{\sqrt{2}\,\pi}{\cot \Psi} \right)^{1/3} \qquad (2.16)$$

where d_v is the indentation diagonal and 2Ψ is the included angle between opposite faces of the pyramid.

The free surface is created by superimposing the Mindlin's (1936) point force field (point forces that do not create either a normal stress or in-plane shear stresses at the surface plane) onto the initial stress field of the expansion of the spherical cavity to eliminate the tangential stress field acting over a plane through the cavity centre. The stresses σ^s created by the surface forces have the general form

$$\frac{\sigma^s_{mm}}{P} = \int_{plastic} dA \, \frac{\sigma_t^{pl}}{P} g_{mm} + \int_{elastic} dA \, \frac{\sigma_t^{el}}{P} g_{mm} \qquad (2.17)$$

where $mm = xx, xz, or\ zz$ (the stress distribution in cartesian coordinates), σ_t is the tangential stress within the initial field, *pl* and *el* indicate the plastic and elastic regions respectively, and g_{mm} are point force function (see Mindlin 1936).

The introduction of these surface forces induces the radial and tangential stresses within the plastic zone and results in a pressure modification. The modified indentation pressure, H, can be related to the cavity pressure P, by superposition (see Lawn and Wilshaw 1975)

$$\frac{H}{P} = 1 - \frac{\sigma_r^s}{P}$$

$$= 1 - m \qquad (2.18)$$

When the specimen is fully unloaded, σ_r^s and m are replaced by σ_r^{rs} and m_r respectively. The variations of m and m_r with β_c are given in Fig. 2.5. The modified ratio of indentation pressure to yield strength thus becomes H/Y and is given by (Chiang, Marshall and Evans 1982):

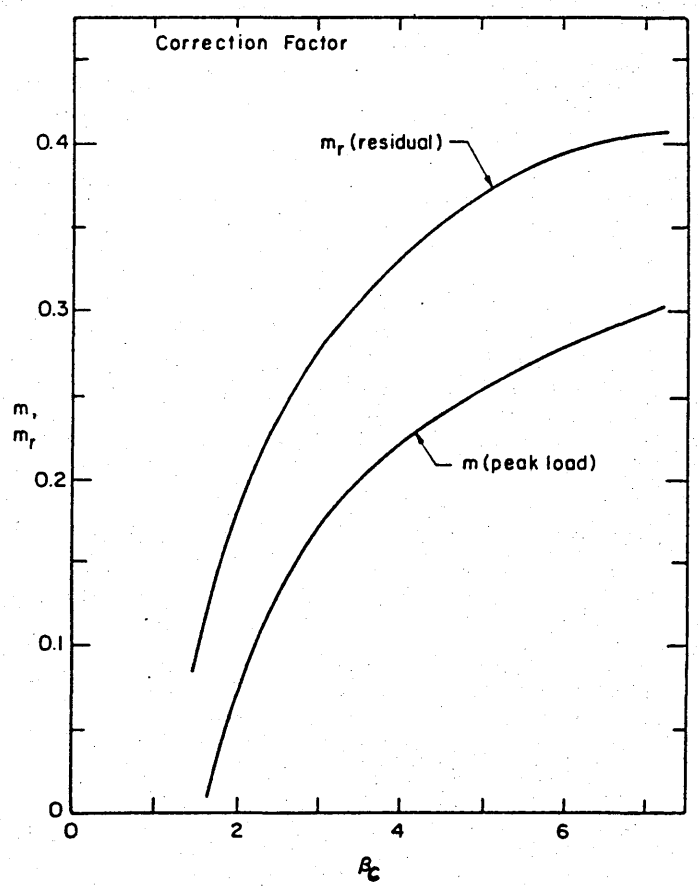

Fig. 2.5 The variation of m and m_r with β_c. (After Chiang, Marshall and Evans 1982)

$$\frac{H}{Y} = \frac{P(1-m)}{Y}$$

$$= \frac{2(1-m)}{3}[1 + \ln(\beta_c)^3]$$

$$= \frac{2(1-m)}{3}\left\{1 + \ln\left[\frac{\left(\frac{E}{Y}\right) + 2(1-2\nu)}{3(1-\nu)}\right]\right\} \qquad (2.19)$$

2.2.4 Other Models

Perrot (1977) proposed that the stress distribution on the indenter and over the indentation interface is a function of the plastic zone size and, in the case of Vickers indenters, the effect of corners should be taken into account. His result indicated that the maximum tensile stress field occurred near the surface, at the indentation corners.

Puttick, Smith and Miller (1977) attempted to simulate the tensile stresses on the surface outside the contact area by suggesting a model of expansion of hole in a plate (plane stress approach). Unlike the other models, they treated the yield stress as a function of strain rate and hydrostatic pressure. Based on this model, the fracture will be initiated at the surface and extend a distance beyond the plastic-elastic boundary governed by the fracture surface energy and the range of the elastic stress field. On penetration into the bulk, the crack tip propagates alone or very close to the contour of the maximum tensile stress. They used this model to predict the fracture of PMMA (polymethyl methacrylate) and the theoretical results showed very good agreement with the crack pattern observed in experiment.

2.3 Indentation Fracture and Crack System

2.3.1 Indentation Cracks

In early work, Brinell (1900) used a blunt (spherical) indenter to make indentations on various materials. The widely-used sharp indenters such as the Vickers pyramid and Knoop indenter were later developed in by Smith and Sandland (1925) and by the US National Bureau of Standards in 1939 (Boyer 1987) respectively. The indentation crack patterns had long been observed but, unfortunately, ignored. It

was only considerably later that Palmqvist (1962, 1963) tried to make use of indentation cracks to measure the material fracture toughness on an empirical basis. He suggested that the average length of the (radial) cracks emanating from the corners of a Vickers' indentation might be use as a measure of relative toughness.

The indentation cracks (fracture patterns) in brittle materials can be categorised into three primary patterns; the *cone* (or *ring*) crack, the *radial* or *median* crack, and the *lateral* crack. The Hertzian cone (ring) crack is generally produced by a spherical (blunt) indenter while the radial crack is commonly seen in indentations of Vickers, conical or Knoop indenters. However, Puttick (1973) and Puttick, Smith and Miller (1977) have observed cracks propagated radially outwards forming the *angel wing* shaped cracks (instead of cone cracks) around the indentation in polymethyl methacrylate (PMMA) by a steel ball. Hagan (1979) and Hagan and Van Der Zwaag (1984) have reported the ring/cone cracks around indentation in fused silica and soda-lime glass by Vickers and conical indenters. Furthermore, Wiederhorn and Lawn (1977) have shown that median and lateral cracks can be induced by overloading a blunt indenter, although the pre-existing Hertzian cone crack tend to inhibit this. It is apparent that indentation fracture is both complex and diverse.

To further the understanding of crack formation, the sequence of crack initiation (how and where the cracks start) and propagation (which path and to what extent the crack grows) for a complete (loading and unloading) indentation cycle, has been extensively studied by Frank and Lawn (1967), Lawn and Fuller (1975), Lawn and Swain (1975), Lawn and Wilshaw (1975a), Swain and Hagan (1976), Lawn and Evans (1977), Evans and Wilshaw (1977), Lawn and Marshall (1978), and Marshall and Lawn (1979) and it is worthwhile looking at these.

Fig. 2.6 (Swain and Hagan 1976) shows schematically the sequence of crack formation and propagation under a blunt (spherical) indenter:

[on the loading half-cycle] (a) the contact of the sphere on the surface is elastic and, as suggested in elastic contact model, a tensile stress field is induced near the shallow skin area. (b) as the normal load increases, so too does the contact area, the strength of tensile and compressive stress field. Upon satisfying the Griffith energy criterion favourably a 'Griffith-flaw' within the tensile stress field runs around the contact area to form a surface ring crack. The ring crack propagates stably downward and, on further increase of load, simultaneously deviates outwards to avoid the

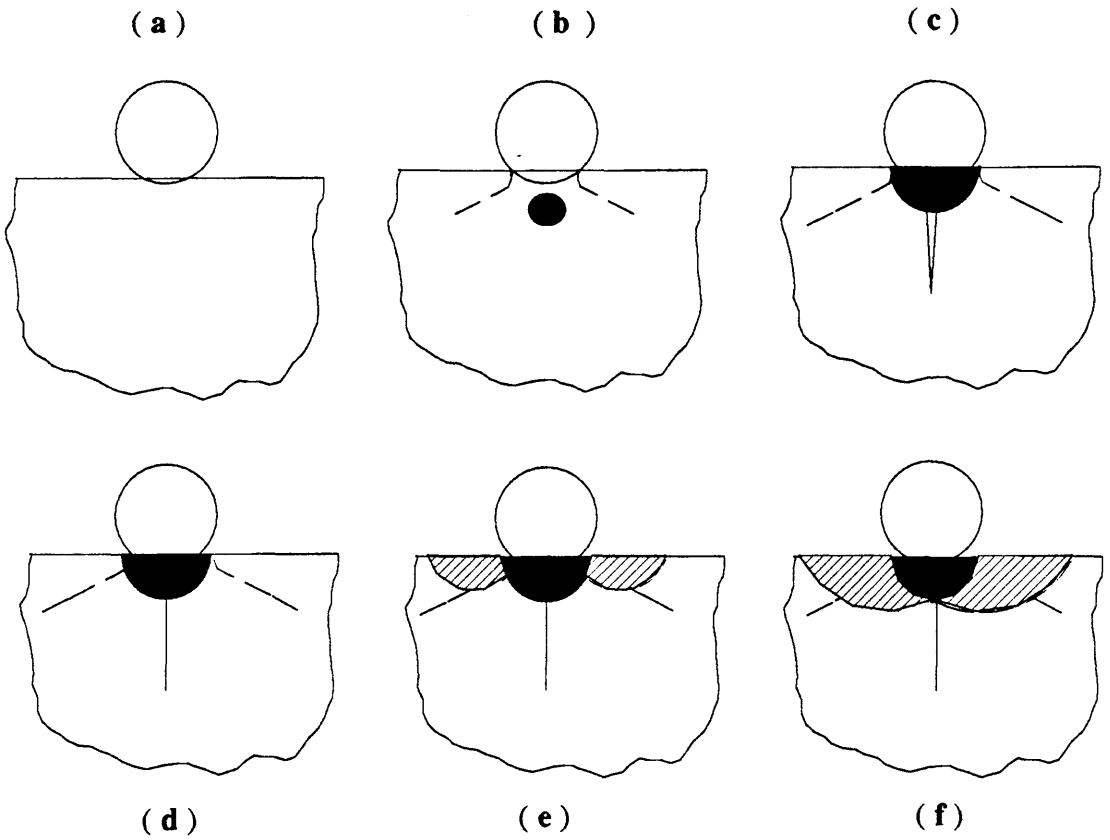

Fig. 2.6 Schematic diagram of crack initiation and propagation during blunt indenter loading (a, b, c) and unloading (d, e, f) half-cycle. (After Swain and Hagan 1976)

compressive field below the indenter; as a result, a Hertzian cone crack is introduced. Based on the Auerbach's (1891) law, this cone crack develops when normal force P reaches a critical value P_c and the critical load P_c is proportional to sphere radius R. (c) as the loading continues, a zone of plastically deformed material develops about the indenter and a median crack forms beneath the plastic zone, and, the cone crack extends deeper.

[on the unloading half-cycle] (d) the median crack begins to close up owing to the compressive stress caused by the elastic deformed zone. (e) The cone crack starts to close up and a system of radial cracks forms about the indentation site. (f) just prior to complete unloading the surface tension component about the deformed zone is sufficiently great to nucleate and propagate a system of lateral cracks.

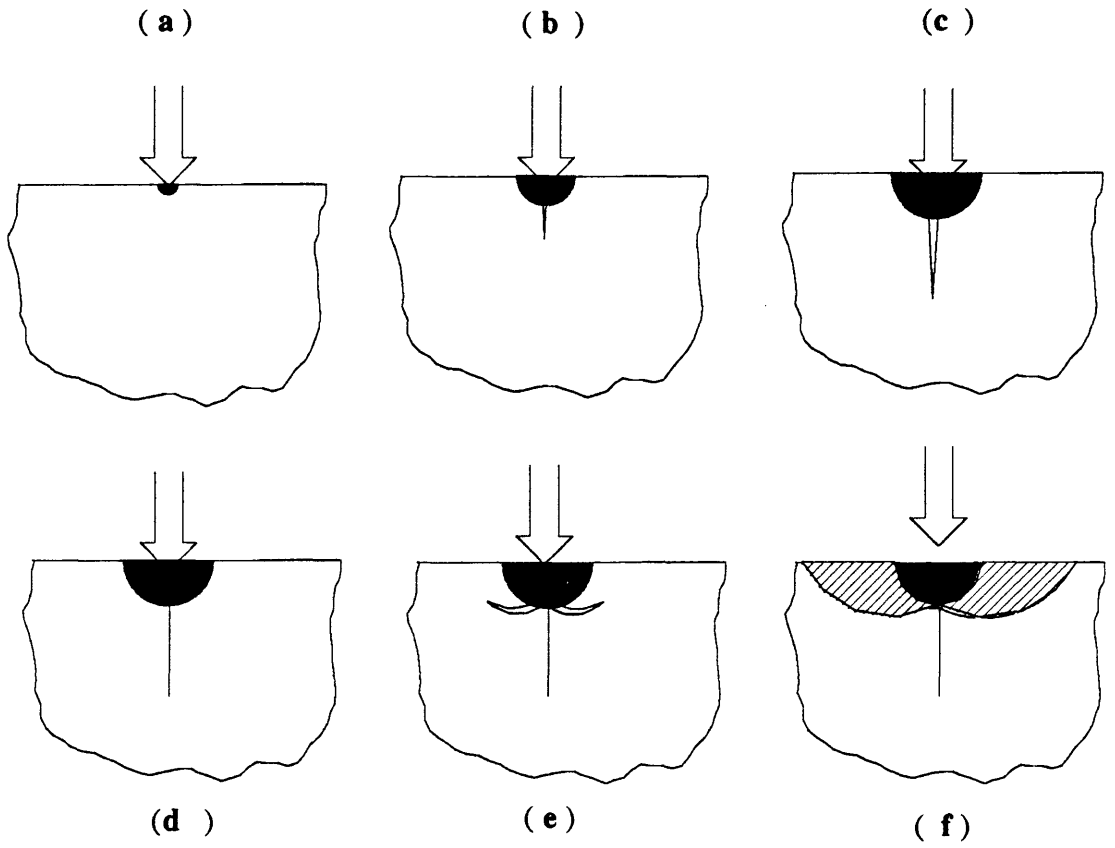

Fig. 2.7 Schematic diagram of crack initiation and propagation during sharp indenter loading (a, b, c) and unloading (d, e, f) half-cycle. (After Lawn and Swain 1975)

For a sharp indenter, the sequence of events which happens during loading and un-loading is shown schematically in Fig. 2.7 (Lawn and Swain 1975) and can be outlined in the following way:

[on the loading half-cycle] (a) on the initial loading, the plastic flow starts right below the contact point of the sharp indenter and introduces a zone of irreversible deformation. (b) at some critical load, the *median vent* (median crack) develops under the indenter where the tensile stresses are greatest. This median vent lies in the plane of the vertical axis and is penny-shaped if it is viewed face-on. The crack is restricted by the compressive stress field (σ_{22}) to expand sideways. (c) upon further penetration, the sub-surface median crack propagates stably. If the load is heavy enough the median crack may break through the confining stress lobes and emerges

at the surface forming the semi-circular median-radial cracks (*half-penny-shaped crack*). In the case of a Vickers pyramid indenter two such cracks normally develop at right angle to each other.

[the unloading half-cycle], at (d) the median vent attempts to close-up on initially unloading but may be prevented from doing so by debris or residual stress field; (e) just prior to removal of the indenter the residual stress field caused by the mismatching at the elastic-plastic boundary gives rise to lateral cracks which originate at the base of the plastic zone and extend side-ways. (f) the lateral cracks continue their extension after complete unloading and may intersect the surface resulting in the formation of chips.

Close observation of the indentation sequences offers a sound foundation for the evaluation of the indentation cracking properties. From this point, it is quite natural for researchers to extend this empirical information to theoretical analysis and attempt to make the fracture processes somehow predictable. In order to build a model of crack initiation and propagation one needs to integrate the knowledge of indentation stress (and residual stress) fields and fracture mechanics. Unfortunately, even for an ideally homogeneous, isotropic solid with the simplified indentation stress field models discussed in section 2.2, it still is a formidable task.

2.3.2 Indentation Fracture

The first model for cracking was suggested by Griffith (1921, 1924) on the basis of the concept of energy balance. Thus, for a static crack system, the total energy, as shown in following equation, is the sum of the work done by the applied force (W_L), the elastic strain energy stored in the medium (U_E) and the free surface energy for creating the new surfaces (U_S).

$$U = U_S + (- W_L + U_E) = U_S + U_M \qquad (2.20)$$

The composite bracket term in the equation $(- W_L + U_E)$ is the mechanical energy (U_M) of the system (see Lawn and Wilshaw 1975b). Griffith proposed that the crack starts to propagate when the energy released from crack growth is sufficient to provide all the energy that is required for crack growth. The equilibrium requirement is given by:

$$\frac{dU}{da_c} = \frac{dU_S}{da_c} + \frac{dU_M}{da_c} = 0$$

or
$$\frac{dU_S}{da_c} = -\frac{dU_M}{da_c} = 0 \qquad (2.21)$$

where a_c is the crack length. The $\left(\frac{dU_M}{da_c}\right)$ is now called (following Irwin 1958) the "elastic strain energy release rate" (G).

Irwin and Kies (1952), and Orowan (1955) modified the Griffith theory by adding a term to account for the plastic energy dissipation in the plastic region around the crack tip. Irwin (1958) later introduced a parameter called the "stress intensity factor" (K) which is defined as :($K = \sigma\sqrt{\pi a_c}$). When stress σ reaches a critical value σ_f (fracture stress) the corresponding value of K is a material parameter called the "critical stress intensity factor"(K_c) or, in the case of (opening) mode I loading, K_{Ic} (see Broek 1986).

The value of G at which specimens appear to fail for (opening) mode I loading is also a material parameter called the "critical strain energy release rate" G_{Ic}. In the case of linear elastic materials is given by Irwin (1958) as:

$$G_{Ic} = \frac{K_{Ic}^2}{E^*} \qquad (2.22)$$

where

$$E^* = E \qquad \text{(for plane stress)}$$
$$= \frac{E}{(1-\nu^2)} \qquad \text{(for plane strain)} \qquad (2.23)$$

Based on the stress field around an elliptical flaw as calculated by Inglis (1913), and the energy balance requirement, Griffith found the crack growth occurs when $\sigma_c = \left(\frac{2E^*\Gamma}{\pi a_c}\right)^{1/2}$ where Γ is the surface energy per unit area. Irwin (1958) modified the original Griffith criterion to :

$$\sigma_c = \left(\frac{E^* G_{Ic}}{\pi a_c}\right)^{1/2} \qquad (2.24)$$

Lawn and Evans (1977) proposed an indentation fracture model for predicting the median crack initiation under a sharp indenter. In their model, the expansion spherical cavity model (see section 2.2.3) and Griffith's equilibrium requirement were used to give the elastic-plastic stress field and crack initiation criterion respectively. Lawn and Evans also made use of observations made by Lawn and Swain (1975) (mentioned in section 2.3.1) and suggested that the maximum tensile stress produced by a sharp indenter was located at the elastic-plastic boundary directly below the contact point. Since the elastic-plastic boundary expands with increasing load, median crack will occur if the maximum tensile stress field meet any suitable flaws. Lawn and Evans then went on to propose the critical flaw dimension C^* and critical indentation load P^* for crack formation (initiation) in brittle material:

$$C^* = \left(\frac{1.76}{c_1^2}\right)\left(\frac{K_c}{H}\right)^2 \qquad (2.25)$$

$$P^* = \left(\frac{54.47\, c_2}{c_3^2\, c_1^4}\right)\left(\frac{K_c}{H}\right)^3 K_c \qquad (2.26)$$

where c_1, c_2 and c_3 are dimensionless constants related to the peak stress at the elastic-plastic boundary beneath the indenter, the indenter geometry, and the spatial extent of the tensile stress field respectively.

Lawn and Evans' model is based on the observation of median crack formation to constitute the threshold of indentation fracture (Lawn and Swain 1975). However, as pointed out by Lankford (1979, 1981), the 2 mm diameter median crack in soda-lime glass shown by Lawn and Swain was produced by a load of 250 N and was therefore not a threshold crack. After indentation (Vickers) experiments conducted on fine polished Al_2O_3, SiC, Si, as-grown Ge, and cleaved NaCl at various loads (from 10 to 2000 g) together with observations of indentation on soda-lime glass reported by Hagan and Swain (1978), Lankford (1981) concluded, that for sufficiently low loads (200 g), radial cracking may occur without median cracking. He then suggested that it was the incorrect assumption of median crack initiation preceding radial cracking which had led Lawn and Evans model to its errors in

quantitatively predicting the threshold load. To rectify Lawn and Evans' model he proposed to use Perrot's (1977) stress field model which substituted the expansion spherical cavity stress field.

From his experimental data, Lankford (1979, 1981) found that the relationship between radial surface trace, ($C' + d_v$) (from the centre of indentation to the tip of radial crack), and load, P, could be, approximately, given by:

$$(C' + a_l) \approx C_1 P^{2/3} \qquad (2.27)$$

with the proportional constant, C_1 , depending upon both material fracture toughness and indenter geometry. Lankford made use of this linear relationship and suggested that the radial-plus-indent flaw could be treated as a composite crack of total dimension $2(C' + a_l)$ in predicting above-threshold crack-growth.

The Perrot (1977) stress field model requires the near-surface stress to be tensile and confined to the plastic zone. As a result, the tangential tensile stresses required to initiate radial cracks,3 occur only within the plastic zone. However, radial cracks are often observed to terminate within the plastic zone (Evans 1979) indicating the presence of a tangential compressive stress. Chiang, Marshall and Evans (1982) suggested that the threshold predicted by Lawn and Evans model could be expressed in terms of a normalized (dimensionless) threshold (Ω)

$$\Omega = \frac{P_c H^3}{K_{Ic}^4} \qquad (2.28)$$

where P_c is the actual threshold load, H is the hardness, and K_{Ic} is the fracture toughness. They used the tensile stress field based on their own stress field model (discussed in previous section 2.2.3) to evaluate Ω .

The results of Chiang, Marshall and Evans' model complied with the observations of Hagan and Swain (1975), and of Lankford, discussed above, that radial cracks initiated first. They (Chiang, Marshall and Evans 1982) concluded that the initiation of radial cracks largely depended on the activation of pre-existence flaws by the indentation surface tensile stress field. If the surface has very low flaw availability

or is subjected to a compressive stress field, radial crack formation will be suppressed. The fracture threshold of median and lateral cracks were limited by the nucleation process which was subjected to considerable uncertainty caused by the unknown severity of the singularity at the nucleation slip (shear) band.

2.3.3 Indentation Technique for Measuring Fracture Toughness

Palmqvist (1962, 1963) was the first to make use of indentation radial cracks for measuring material fracture toughness. Noticing that the Vickers indentation radial crack length increased linearly with load, he suggested that the slope of the plot could be used to evaluate material toughness. Although Palmqvist's proposal was soon challenged by Dawihl and Altmeyer (1964) to be too crude and the character of the surface had a considerable influence on the crack length, no suggestion was made to improve it.

Because of the deficiency of the underlying theoretical bases of indentation stress field and fracture mechanics, progress on this subject was surprisingly slow. It is only with the analysis and development of the indentation stress field and fracture models (see sections 2.2, 2.3.1, and 2.3.2), that the indentation method has become the most widely used technique for measuring mechanical and fracture-mechanics parameters in brittle materials. As a result, the once irritating radial cracks are now a necessary part of the routine.

In order to calculate the stress intensity factor, a detailed analysis of the stress field around the indentation crack is needed. Unfortunately, the indentation stress field, especially the near field stresses, is sufficiently complex that even to establish a reasonable approximation is a considerable task.

A simplified way to calculate the stress intensity factor is to adopt an idealised stress-field and cracking model and to make use of the property of linear superposition. For this purpose the tensile stresses which generate the cracks are to be separated into several components. In the scheme suggested by Marshall and Lawn (1979), the elastic-plastic stress field of a fully loaded indenter may be considered as the superposition of the residual field in the unloaded solid and the field of an ideally elastic contact:

$$\sigma_{ep} = \sigma_{el} + \sigma_{res} \qquad (2.29)$$

where σ_{ep} denotes the elastic-plastic stress tensor at any point, σ_{el} is the purely elastic stress component, and σ_{res} is the residual stress component. This means that a normal indenter load P_L generates median opening force P_{el} (elastic field component) and P_{res} (residual field component).

Assuming penny-like crack geometry, the stress intensity factor due to the residual far field force may be written (Lawn, Evans and Marshall 1980, Sih 1973):

$$K_{res} \approx f(\varphi)\frac{P_{res}}{c^{3/2}} = \chi_{res}\frac{P_{res}}{c^{3/2}} \qquad (2.30)$$

with

$$\chi_{res} = \eta_{res}\left(\frac{E}{H}\right)^{1-m_c}(\cot\Psi)^{2/3} \qquad (2.31)$$

where $f(\varphi)$ is an angular function with value near unity, c is the crack length, η_{res} is a dimensionless term, $m_c \approx 1/2$, and 2Ψ is the included angle of the indenter.

The stress intensity factor for a half-penny crack subject to radial distributed stress is given by (Lawn, Evans and Marshall 1980, Sih 1973):

$$K = f(\varphi)\left(\frac{2}{c}\right)^{1/2}\int \frac{r\sigma(r)\,dr}{(c^2 - r^2)^{1/2}} \qquad (2.32)$$

By assuming the far field elastic stress field can be represented by the point-load Boussinesq model (see section 2.2.1), the elastic stress intensity factor may be taken as:

$$K_{el} = \chi_{el}\frac{P_{el}}{c^{3/2}} \qquad (2.33)$$

with

$$\chi_{el} = \eta_{el}\ln\left(\frac{2c}{r_{pl}}\right) \qquad (2.34)$$

where η_{el} is another dimensionless term, and r_{pl} is the radius of the plastic zone. The toughness can be obtained (Lawn, Evans and Marshall 1980) from

$$K_c = K_{el} + K_{res}$$

$$= \frac{(\chi_{el} + \chi_{res})\, P_L}{c^{\frac{3}{2}}} \qquad \text{(loading half-cycle)} \qquad (2.35a)$$

$$= \frac{\chi_{res} P_L + \chi_{res} P_{Lmax}}{c^{\frac{3}{2}}} \qquad \text{(unloading half-cycle)} \qquad (2.35b)$$

where P_{Lmax} is the peak load. Comparing the equation with experimental data, Lawn et al (1980) suggested the indentation coefficients were:

for median cracks: $\chi_{el}^{M} = 0.032 \pm 0.008$ and $\chi_{res}^{M} = 0.03 \pm 0.003$

for radial cracks: $\chi_{el}^{R} = -0.045 \pm 0.002$ and $\chi_{res}^{R} = 0.049 \pm 0.004$

Since the crack growth is not reversible, the final crack length is the longer one obtained from Eq. (2.35a) and Eq. (2.35b). Thus, the median crack attains its maximum length during the loading half-cycle, whereas the radial crack is expected to continue its growth until unloading is completed.

Although radial cracks can be obtained using Knoop, Vickers or even spherical indenters, the Vickers' indenter is the most commonly used to determine toughness, because the radial cracks can be obtained at four corners consistently.

2.4 Indentation Experiments

2.4.1 Material Selection

Generally, brittle solids can be classified by their micro-structures into three major categories namely, *crystalline*, *vitreous* (glass) or *mixed type* (glass-ceramics). A crystalline material possesses long-range periodicity which means that its atoms are arranged in orderly form over a long distance (compared to the inter-atomic spacing). At the other end of the spatial spectrum, vitreous material (such as glass) exhibits only close range atomic regularity (1 nm).

In order to examine the influence of material properties on machining conditions, it was considered necessary to select at least one material from each major category. The materials selected and their applications, microstructure and physical properties are discussed as follows:

(1) Single crystal silicon (Crystalline solid):

--(a) Application: solid-state devices (e.g. diode, transistor, integrated circuits)

--(b) Structure: silicon has a diamond-cubic structure which belongs to the face centred cubic (fcc) group of the Bravais lattices.

--(c) Physical properties: silicon single crystal is extremely brittle at room temperature and becomes ductile at elevated temperature (above 900 ^oC) where slip occurs in the {111} plane (Gallagher 1952, Geach, Irving and Philips 1957).

The mechanical constants of single crystal silicon at room temperature, its melting point (from Wortman and Evans 1965), and thermal conductivity (from Toulkian 1970) are listed as below :

Density (ρ): 2330 $\frac{kg}{m^3}$

Young's modulus (E) : 131 Gpa

Shear modulus (G) : 79.9 Gpa

Poisson ratio (ν): 0.266

Thermal conductivity : 148 $\frac{W}{m\,K^o}$

Specific heat capacity: 712 $\frac{JKg}{m\,^oK}$ at 25 ^oC

Melting point: 1420 ^oC

(2) Fused silica and Soda-lime glass (Vitreous solids):

--(a) Application: Fused silica (vitreous silica) has an excellent resistance to most chemicals and to radiation damage. It is widely used in optical systems and is an ideal 'glass' for windows in space-vehicles and wind-tunnels. Soda-lime glass accounts for nearly 90% of all the glass produced and is used for containers, and flat (window) glass.

--(b) Structure: Glass can be defined as a substance in which a supercooled state is maintained at a temperature below the melting point (T_f), so that no devitrification (crystallization) occurs, and in which the structure is frozen in the vicinity of the transition point (Izumitani 1986). Technically, it can be classified as a viscous, metastable, supercooled liquid but in practice it behaves in most respects as a solid at room temperature (Thomas 1985). In 1921, Lebedev suggested that glasses are composed of crystallite with dimensions of the order of 0.8-1.5 nm (crystallite model). This was challenged in 1932 by Zachariasen's random-network model which proposed that atoms in glasses form a three dimensional network without periodic order (see Kingery, Bowen and Uhlmann 1975). Glass formers generally have cation-oxygen bond strengths greater than 80 kcal/mol. Oxides with lower strengths do not become part of the network and are called modifiers. Oxides with energies of 80 kcal/mol may or may not become part of the network and are referred to as 'intermediates' (Boyd and Thompson 1985).

--(c) Physical properties: Glass is brittle, amorphous and nearly isotropic. The mechanical and thermal properties of fused silica and soda-lime glass at room temperature are given as below (Boyd and Thompson 1985):

	Fused silica	Soda-lime glass
Density (kg/m^3)	2200	2500
Young's modulus (Gpa)	73	70
Shear modulus (Gpa)	31	28
Poisson ratio	0.17	0.22
Thermal conductivity ($\frac{W}{mK}$)	1.4	1.4
Specific heat ($\frac{J}{kgK}$)	840	750
Softening point (^oC)	1580	705

(3) Schott 'Zerodur' glass-ceramic (mixed type):

--(a) Application: Zerodur is a low-expansion mixture of polycrystalline glass-ceramic which has been used in applications such as telescope mirror blanks (substrate) where minimal thermal expansion and thermal induced distortion are critical.

--(b) Structure: Glass-ceramics are more than 50% crystalline after heat treatment; frequently, the final product is more than 95% crystalline. The micro-structural parameters such as the fractional volume and properties of the crystalline phase(s); the crystal sizes, shapes, and orientations; and the volume, composition, and distribution of the glassy phase decide the properties of a glass-ceramic (Stewart 1985). Generally, glass-ceramics are brittle and contain tiny micro-crystals in their structure which can arrest crack growth. The thermal expansion of a glass-ceramic is normally lower than that of the parent glass which increases its dimensional stability.

--(c) Physical properties: Zerodur is a glass-ceramic material with near zero coefficient of thermal expansion in a wide temperature interval. The mean linear thermal expansion coefficient of Schott's Zerodur over temperature range from 25 ^oC to 100 ^oC is $3\times 10^{-8}/K$ (Morrell 1985). The crystal size is 0.05 μm and content of the crystalline phase is about 70 %. Other mechanical and thermal properties of Schott Zerodur glass-ceramic at room temperature are given as below (Boyd and Thompson 1985):

Density (ρ): 2530 $\frac{kg}{m^3}$

Young's modulus (E) : 91 GPa

Shear modulus (G) : 36.3 Gpa

Poisson ratio (ν): 0.24

Thermal conductivity : 1.64 $\frac{W}{m\,K^o}$

Specific heat capacity: 821 $\frac{J\,Kg}{m\,^oK}$ at 25 ^oC

2.4.2 Indentation of Certain Glasses and Glass-ceramic

Soda-lime glass, fused silica and Zerodur specimens studied were respectively in the form of a $65\times 50\times 1.5\,mm$ microscope slide, a $35\,dia.\times 1.5\,mm$ disc, and a $25\times 25\times 20\,mm$ block each with polished surfaces. Vickers indentation experiments were performed on two types of micro-hardness testers (Leitz Miniload 2 and Matsuzawa Seiki model:MHT-1) with normal loads ranging from 10 g (98.1 mN) to 1000 g (9.81 N). The time of descent (time for the indenter to descend onto the specimen) was approximately 15 seconds and the peak load reached after another 10-15 seconds. The loading time (peak load maintenance-time) was 15 seconds for all the indentation tests in this study.

The resulting indentations were examined by both optical and scanning electron microscopy (SEM). Indentations due to loads of under 50 grams were found to be beyond the resolution of the optical microscope and so the SEM was used. Since none of the selected glasses and glass-ceramics was conductive, a thin layer of gold-palladium (60:40) was coated onto the indented surface for SEM observations.

Being classified as "normal glass" , soda-lime glass is characterized by well-defined, classic sharp indenter patterns. The ability to form well-developed median, lateral, and radial cracks is, as suggested by Swain (1979), related to the formation of shear cracks about the area of contact. These shear cracks start as genuine shear displacements and it is only in the later stages of the deformation that they degenerate into shear cracks (Hagan 1980). Without a material deformation model, like the dislocation model in crystal, it is very difficult to understand the shear plastic flow in soda-lime glass. Peter (1970), Swain (1979), and Hagan (1980) suggested that shear flow-like processes occur only in soda-lime glass or in glasses containing a minimum of network modifiers. Their suggestions were based on the fact that the shearing strength (resistance to shear flow) of glasses depended on the strong covalent Si-O bonding among the silica tetrahedra which can be weakened by the presence of network modifying ions. In other words, it is the network modifiers which provide local weakness (easy-slip path) where the shear flow is initiated.

Although soda-lime glass has been called *normal* glass, abnormalities were observed due to indentations of it such as its slow post-indentation crack propagation and radial cracks not necessarily emanating from the corners. Fig. 2.8 (a) and (b)

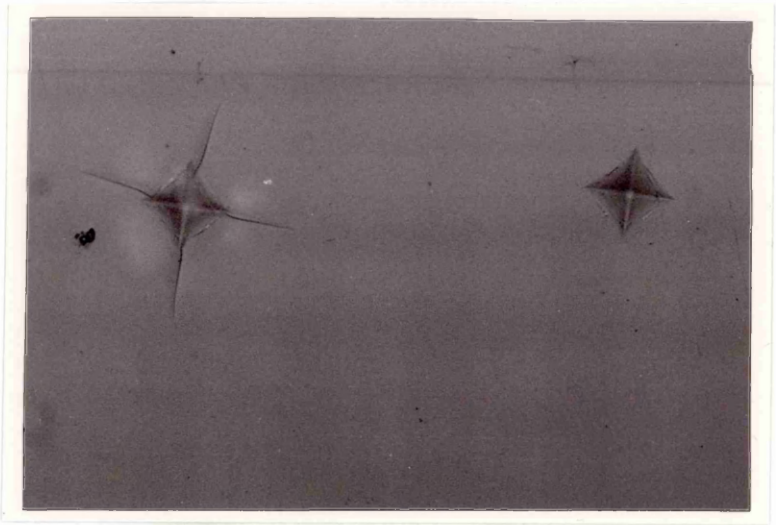

(a)

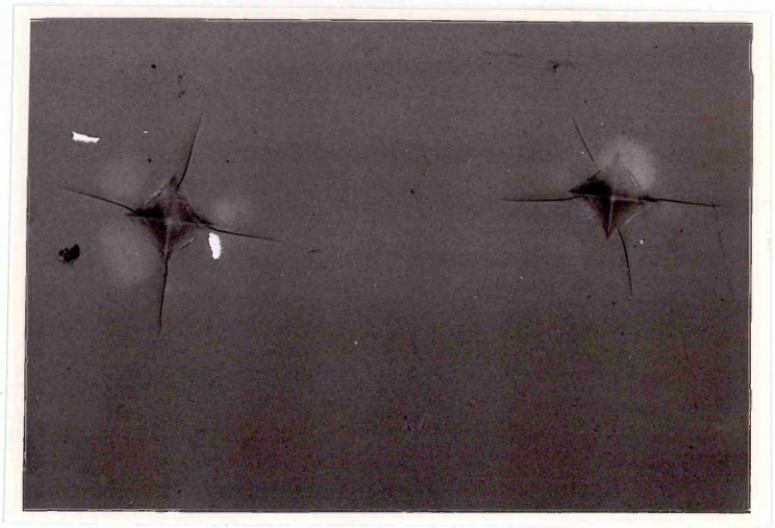

(b)

Fig. 2.8 The optical micrographs of the same indentations (300 g normal load) on soda-lime glass observed (a) 2 minutes and (b) 10 minutes after the right-hand indentation was made. (The left-hand indentation is used here solely as a "landmark" reference.)

show the optical micrographs of the same indentations (300 g normal load) observed (a) 2 minutes and (b) 10 minutes after the right-hand indentation was made (the left-hand indentation is used here solely as a "landmark" reference and this post-indentation crack propagation phenomenon was repeatedly observed on soda-lime glass in this study). No sign of radial and lateral cracks can be seen in Fig. 2.8 (a) but after the indenter had been removed for the longer time (10 minutes), the radial and lateral cracks (causing light to be reflected from beneath the surface) have been initiated and propagated by the residual tensile stresses. This observation shows that in soda-lime glass the radial and lateral cracks may appear "after" the unloading cycle is completed and, at least in low loading (300 g), are not "almost" completed at the time of withdrawal as suggested by Swain (1979). A question remained about the cause of initiation and propagation of the slow post-indentation cracking in soda-lime glass if the suggestion, that network modifiers can make shear flow mechanism favourable, is valid.

Although fused silica glass and Zerodur belong to two different categories of materials, (see section 2.4.1) there are a number of similarities between their indentation crack patterns. The typical Vickers indentation on fused silica glass or Zerodur is a square (residual impression) pattern with radial cracks emanating from the corners and concentric ring cracks surrounded the contact area as shown in Fig.

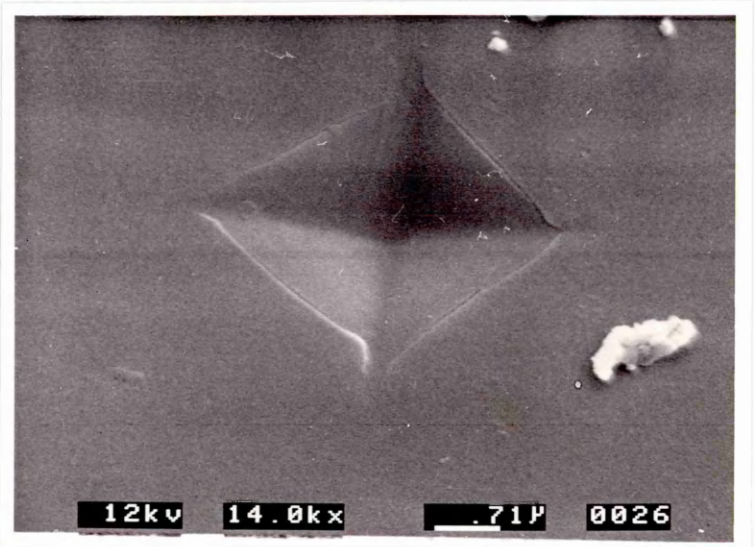

Fig. 2.9 The indentation on polished fused silica surface at normal load of 10 grams shows the "edge cracks" formed at the edge of the contact area. (Mag. 14000, Tilt 30°)

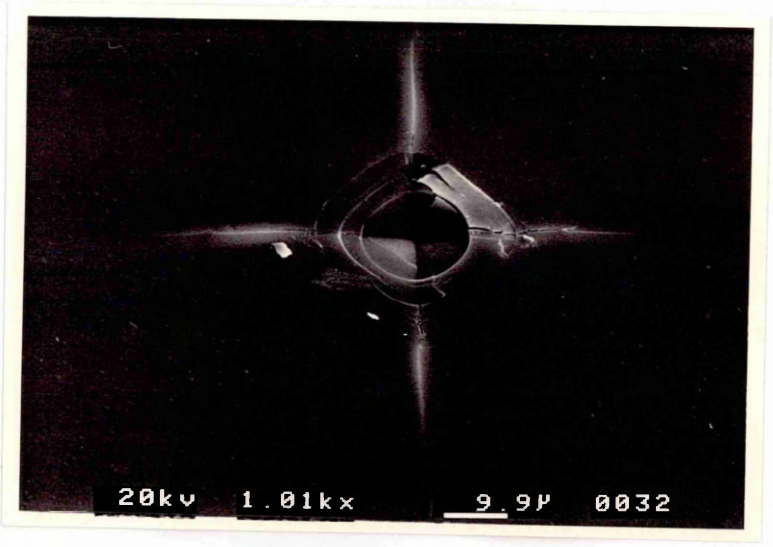

(a)

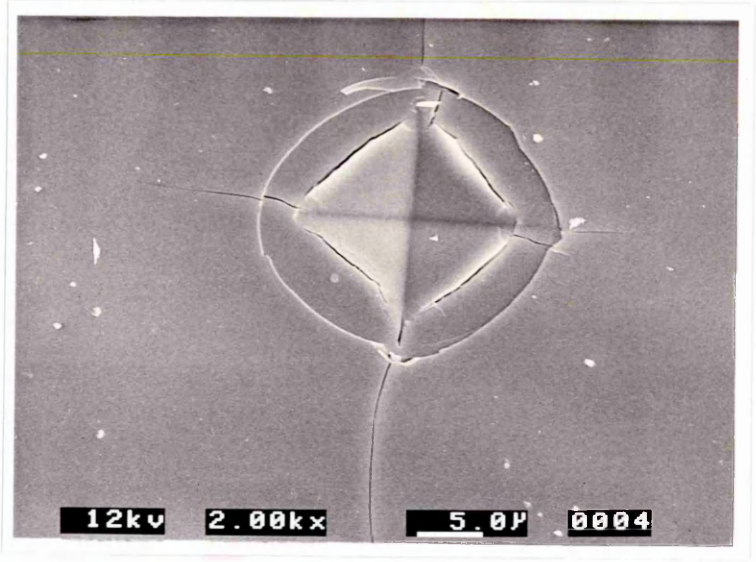

(b)

Fig. 2.10 SEM micrographs of the indentations on (a) fused silica (load: 200 g, mag.: 2000) and (b) Zerodur (load: 500 g, mag.: 1010, tilt: 30°) show that the residual impression are surrounded by ring cracks and have the radial cracks emanating from the corners .

2.10. Hagan (1979) called the glasses, on which this kind of cracks pattern was produced, *anomalous* glasses. This unusual indentation crack pattern appears to be similar to the superimposition of ring/cone cracks (as generated by a spherical indenter) onto radial/median cracks (as generated by a Vickers indenter) but in the case in hand, the ring/cone crack pattern repeated itself periodically instead of the single ring/cone crack found with a sphere.

At loads of 10 grams, as shown in Fig. 2.9, the *edge cracks* (they are too square to be called ring crack) formed just outside the contact area. Since these nearly overlapped with the edges of residual impression, they required the high magnification SEM in order to be observed. As mentioned in the previous section (2.3.2), the fracture threshold models were based on assumptions of fracture starting with either radial or median cracks; the appearance of *edge cracks* might serve as a reminder that these models are, at best, only approximate.

At higher loads (50 grams), a perfect ring crack formed about the edge cracks surrounding the impression. On further loading, this propagated stably downward until it is covered by the contact area where a new ring crack might be initiated.

Radial cracks occurred at loads of 100 g and 50 g on Fused silica and Zerodur respectively. Fig. 2.10 shows that the radial cracks penetrating the surrounding ring cracks and propagating a considerable distance outside the final ring crack. It seemed that the existing ring/cone cracks could only slightly deviate in direction rather than severely restrict the propagation (as suggested by Arora, Marshall and Lawn 1979) of radial cracks.

Lateral cracks might extend to the surface on the unloading half-cycle and intersect with existing cone and radial cracks to cause chipping (as shown in Fig. 2.11).

The differences between the crack-patterns obtained by indentation on soda-lime glass and that on fused silica glass is suggested by Peter (1970), Swain (1979), Hagan (1979) to be due to two different deformation mechanisms. They each showed that generally, the *anomalous* glasses are distinguished by low coefficient of thermal expansion and positive temperature gradient of bulk modulus. These are properties which are highly structure-sensitive, suggestive of a strong dependence on the spatial arrangement of the silica tetrahedra. While soda-lime glass deforms largely by a shear-dominated flow process, *anomalous* glasses such as fused silica deform by a pressure dominated densification process.

(a)

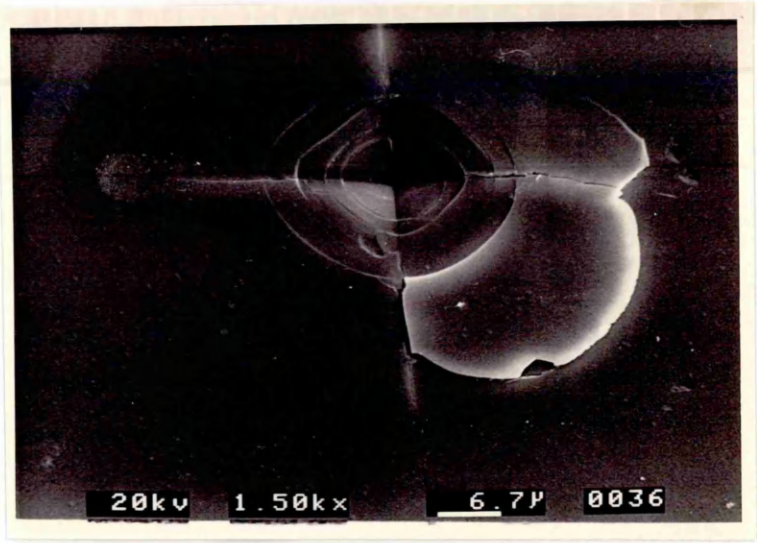

(b)

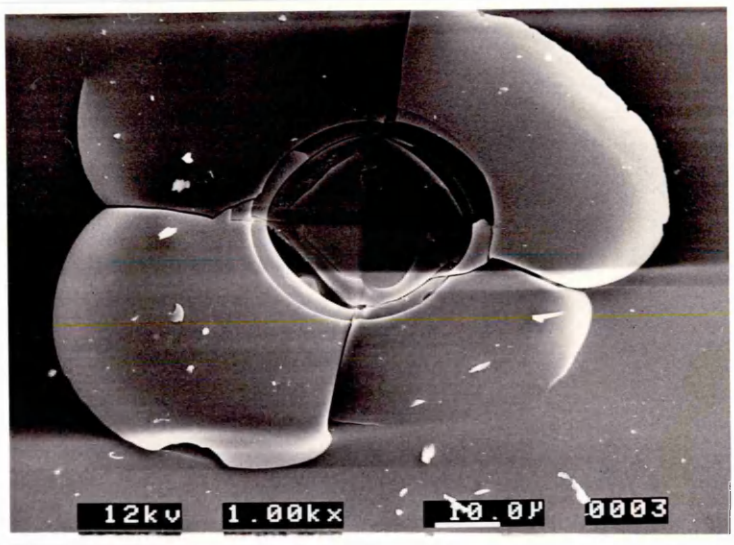

(c)

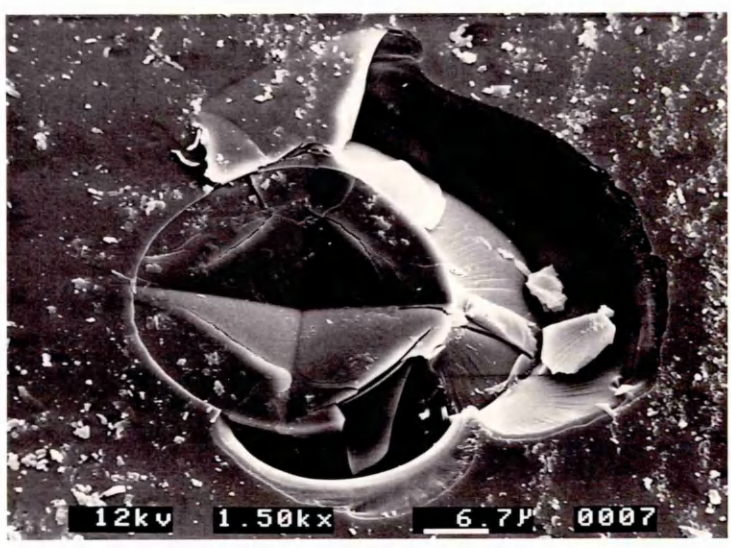

Fig. 2.11 Lateral cracks might extend to the surface on the un-loading half cycle and intersect with exsiting radial cracks to cause chipping . (a) Zerodur, load 300 g, tilt 30°, mag. 1500; (b) fused silica, load 500 g, mag. 1000, (c) fused silica, load 500 g, tilt 30°, mag. 1500, the sub-surface Hertzian crack revealed by the chipping-off.

The radial crack length, c, of the indentation was measured from the SEM micrographs. Fig. 2.12 shows the plot of the ratio $(\frac{P}{c^{3/2}})$ versus loads and it does present reasonable linearity over the tested load range (50 g to 500 g). This means that Eq.(2.35) can be used to obtain fracture toughness with a certain degree of confidence. (see section 2.3.3)

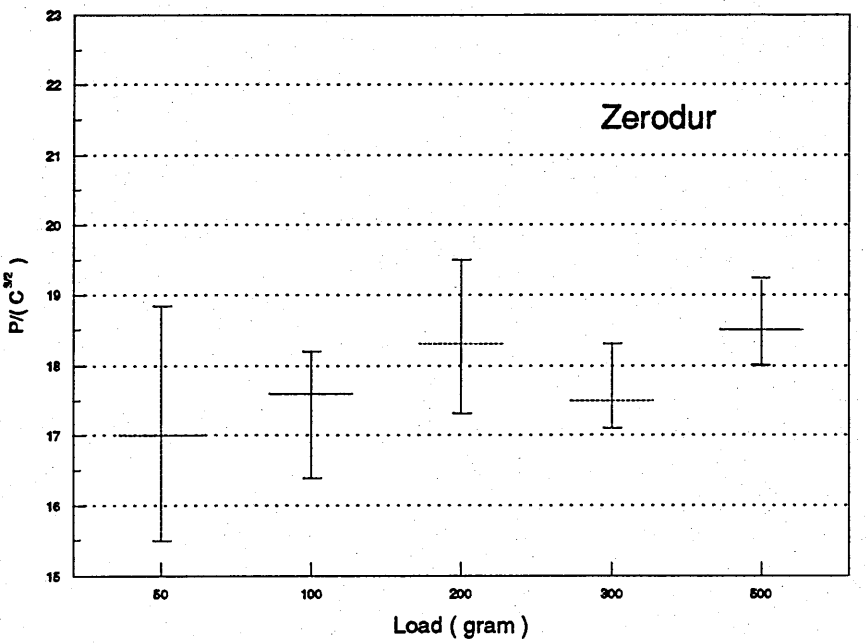

Fig. 2.12 $(\frac{P}{c^{3/2}})$ $(MPa\sqrt{m})$ versus normal loads (gram) [plotted points are means, and ranges (length of the vertical lines)]

2.4.3 Indentation of Silicon Single Crystal

In silicon, being a crystalline material, the structure has decisive effects on its elastic and plastic behaviour. Orowan (1935), Taylor (1935), and Polanyi (1935) each proposed (independently) that dislocation motion could be used to account for plastic deformation in crystals (see Kingery et al 1976). Based on the theory of dislocation, when subjected to shear stress, crystals can be deformed through *edge* and *screw* dislocation-motion. In general, dislocations slip or glide preferentially on planes of high-atomic density (*slip planes*), and in a direction which causes minimum lattice distortion (*slip directions*). A *screw* dislocation may move by *slip* or *glide* in any direction perpendicular to itself, while edge dislocations can glide only in its single slip plane or *climb* in a direction perpendicular to the slip plane (see Reed-Hill 1973).

Since hundreds of thousands of dislocations are needed to cause plastic deformation, it is the ability to nucleate and multiply dislocations (dislocation source) which governs the plasticity of crystals. Frank and Read (1950) proposed that there were *pinning sites* (so named because dislocations are *pinned* or immobilized there) within the crystal where dislocations could not slip pass. However, when subjected to increased shear stress the "immobilized" dislocation could bow out to generate a dislocation loop which encircles the site. This type of dislocation source is called "Frank-Read source" and was later observed in a silicon single crystal by Dash (1957). However, Gilman and Johnston (1957) found no evidence of Frank-Read sources associated with plastic deformation in lithium fluoride (LiF) crystals. In his later experiments, Gilman (1959) applied short stress pulses to lithium fluoride crystals and found that cleavage steps, dislocation loops, glide bands, inclusions (or "dirt" particles), precipitates (as grown), and radiation-induced precipitates could all lead to dislocation nucleation. Gilman then concluded that Frank-Read sources did not play a dominant role in the deformation of LiF crystals, and probably not in other crystals.

Another plastic deformation model for crystalline solids was proposed by Minomura and Drickamer (1962). They suggested that there was a transition pressure under which the crystal structure changed and became metallic (called the "metallic transition pressure"). They give the transition pressure for silicon single crystal as 190 kbar.

The (close-packed) slip directions of silicon single crystal are in the $< 1\,1\,0 >$ plane, running diagonally across the faces of the unit cell. There are four slip planes (close-packed) in the lattice of silicon, called "octahedral planes", with indices $(1\,1\,1)$, $(\bar{1}\,1\,1)$, $(1\,\bar{1}\,1)$, and $(1\,1\,\bar{1})$. Each slip plane contains three slip directions, so the total number of octahedral slip systems is twelve ($6 < 1\,1\,0 >$ directions). Since silicon has a large number of equivalent slip systems well distributed in the lattice, it is almost impossible to strain it without having at least one {111} plane in a favourable position to slip.

The silicon used was in the form of standard epitaxial substrate slices about 600 μm thick, with surfaces oriented some 3 degrees from the $(1\,1\,1)$ direction toward $(1\,1\,0)$. The surfaces were polished and indented by a Vickers indenter with loads ranged from 10 g to 500 g. The indentations were subsequently observed using SEM in order to get the detail images of residual impressions and cracks.

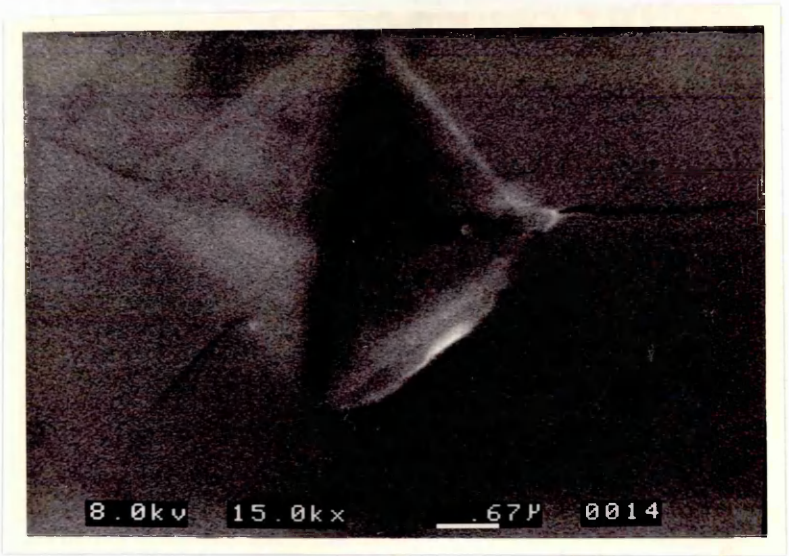

(a)

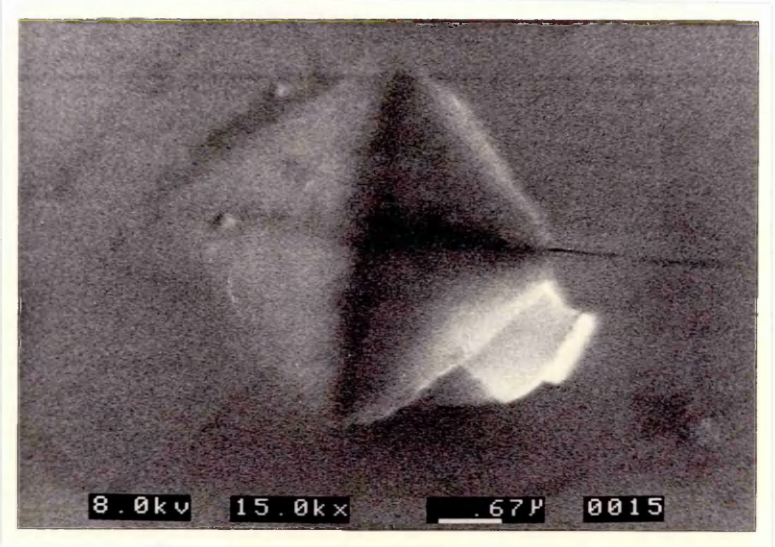

(b)

Fig. 2.13 Indentations on silicon single crystal (1 1 1) surface at load of 10 g. Approximate crack directions (start with right-hand corner then ccw) (a) [1 $\bar{1}$ 0], [$\bar{1}$ 2 $\bar{1}$], [$\bar{1}$ 0 1] (b) [1 $\bar{1}$ 0], [0 1 $\bar{1}$], [$\bar{1}$ 0 1]

(a)

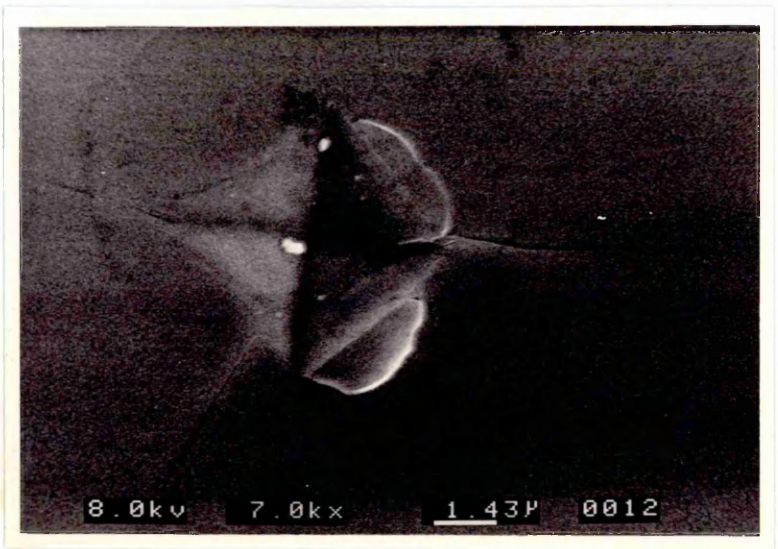

(b)

Fig. 2.14 Indentations on silicon single crystal (1 1 1) surface at load of 25 g. Approximate crack directions (start with right-hand crack then ccw) (a) [$\bar{1}$ 0 1], [1 $\bar{1}$ 0], [0 1 $\bar{1}$](b) [1 $\bar{1}$ 0], [$\bar{1}$ 2 $\bar{1}$], [$\bar{1}$ 0 1]

It was reported by Puttick and Hosseini (1980) that indentations made under loads of 3 grams showed no sign of fracture and cracks were initiated at loads of approximately 4 grams. They observed cracks which appeared to propagate along or close to the $< 1\,1\,2 >$ direction rather than $< 1\,1\,0 >$, with a strong preference for $[\,2\,\bar{1}\,\bar{1}\,]$ and $[\,\bar{1}\,2\,\bar{1}\,]$ followed by $[\,\bar{1}\,\bar{1}\,2\,]$ (rather than the reverse directions). However, micrographs of indentations made under loads of 25 grams in the current study present a quite different picture. Here it has been found (as shown in Fig. 2.13 and Fig. 2.14) that the fracture appeared to propagate along or close to the $< 1\,1\,0 >$ direction rather than $< 1\,1\,2 >$, with preference for $[\,0\,1\,\bar{1}\,]$, $[\,1\,\bar{1}\,0\,]$, and $[\,\bar{1}\,0\,1\,]$ (again, rather than the reverse directions). Although, occasionally, there were some cracks propagating towards $< 1\,1\,2 >$, it was by no means the dominant direction (the ratio of crack-numbers which followed $< 1\,1\,0 >$ to those which followed $< 1\,1\,2 >$ was approximately 9:1). Observations of indentations with different indenter orientations and loads on eight specimens were made and these confirmed the repeatability of the above mentioned results. It is not clear what caused the same indentation tests to yield different results. A possible reason might have been that the ("Vickers") indenter used by Puttick and Hosseini had a rectangular cross-section and a chisel edge instead of the square cross-section used in this study which might introduce a slightly asymmetrical stress field.

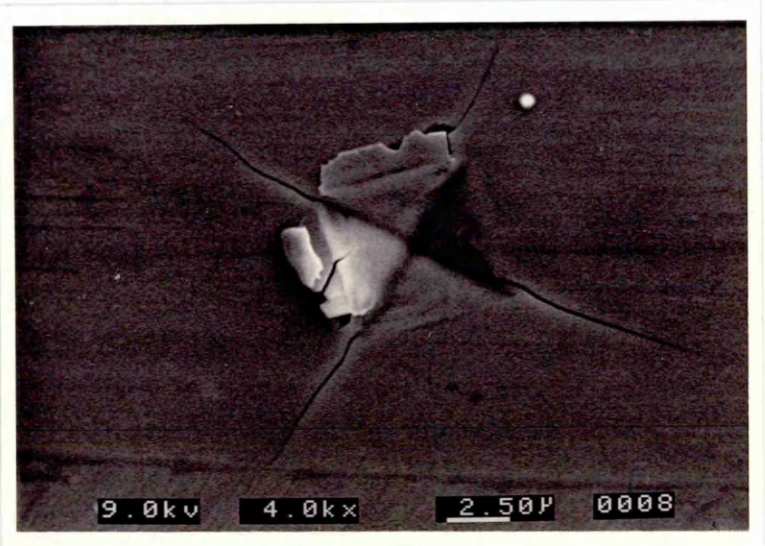

Fig. 2.15 Indentations on silicon single crystal (1 1 1) surface at load of 50 g. Approximate crack directions (start with right-hand crack then ccw) $[\,1\,\bar{2}\,1\,]$, $[\,1\,0\,\bar{1}\,]$, $[\,\bar{1}\,2\,\bar{1}\,]$, $[\,\bar{1}\,0\,1\,]$

At loads of 50 grams and above, corner effects became significant, as shown in Fig. 2.15; cracks appeared to have to compromise between the directions of the crystalline axes and those of the indenter diagonals (in most cases, cracks followed the latter). However, by this stage of increased loading, the radial cracks developed into the "mutually orthogonal" (cross) pattern observed by Lawn, Marshall and Chantikul (1981).

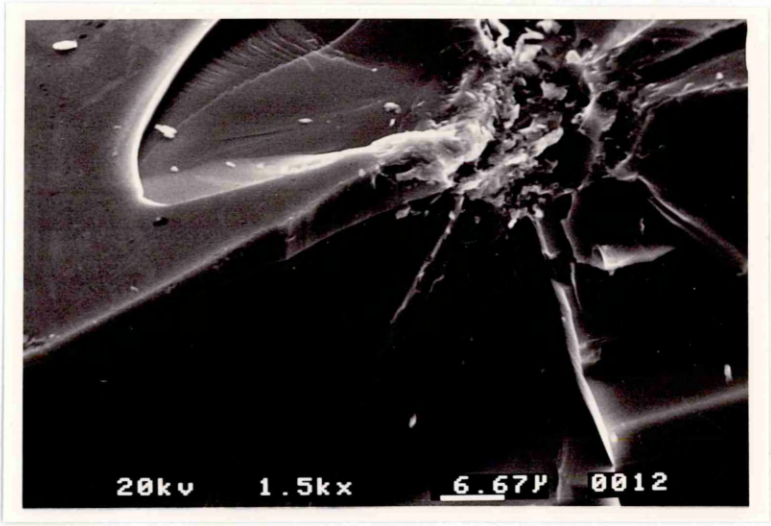

Fig. 2.16 Sectioned indentation on silicon single crystal at load of 100 g reveals the sub-surface damage (median crack, lateral crack).

The specimens used for the study in hand (with well defined radial cracks) were split into two by applying a tensile stress normal to one of the radial crack planes (using three-point bending) to reveal the lateral and median cracks under the surface. The lateral cracks, as shown in Fig. 2.16, emanate from the base of deformation zone and propagate outward nearly parallel to the surface. By emerging toward the surface, the lateral cracks may cause chipping, as can be seen in the background of Fig. 2.16. In general, the median-radial crack-patterns produced at loads of 100 grams and above are of the penny-like configuration as suggested by Lawn, Marshall and Chantikul (1981).

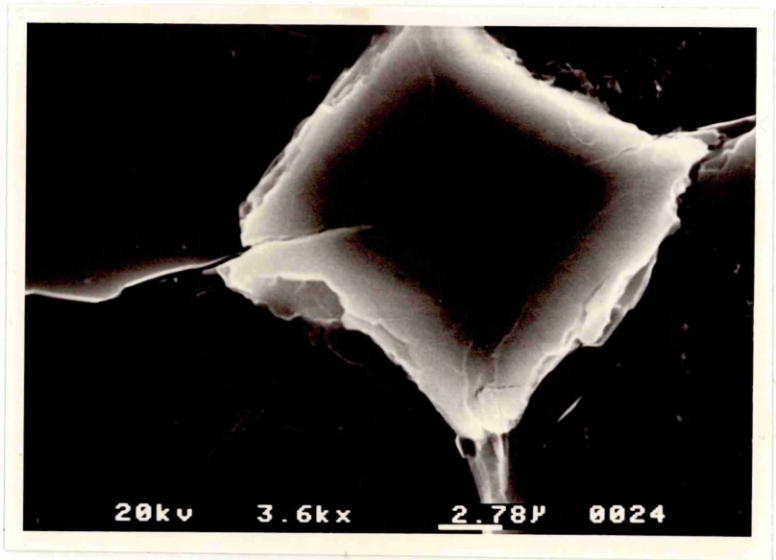

Fig. 2.17 Scanning electronic micrograph of the indentation of single crystal silicon at a load of 100 g shows the detail of the contact zone.

It is worth mentioning that, as the result of close observation of the contact zone (as shown in Fig. 2.17), are (1) the (hydrostatic) compressive stresses around the contact zone are strong enough to "hold" the zone together while severe chipping occurred in the surrounding area; (2) the fact that radial cracks could sometimes propagate into the contact zone was considered to be evidence enough to prove it had experienced tensile stresses.

2.4.4 Size Effect

It has been established that an apparent increase in hardness occurs when the size of the indentation decreases (as shown in Fig. 2.18 (a) and Fig. 2.19). It is also true that, as the load decreases to a critical value, the indentation can be made without fracture. Auerbach (1891) found that the critical normal load P_c applied on a sphere of radius R to generate a ring crack on glass was proportional to R.

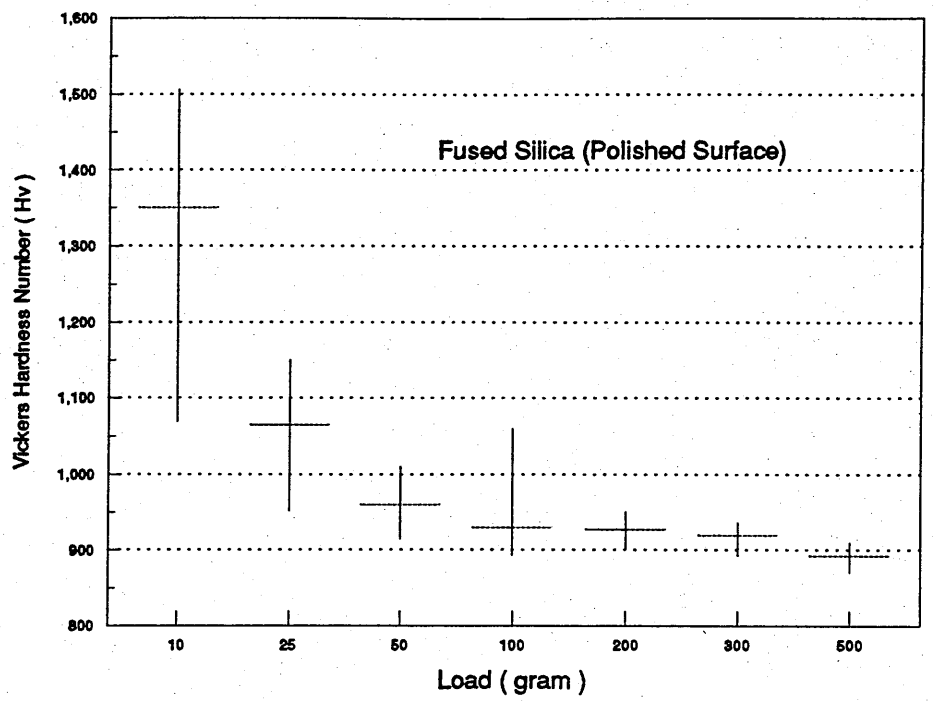

(a)

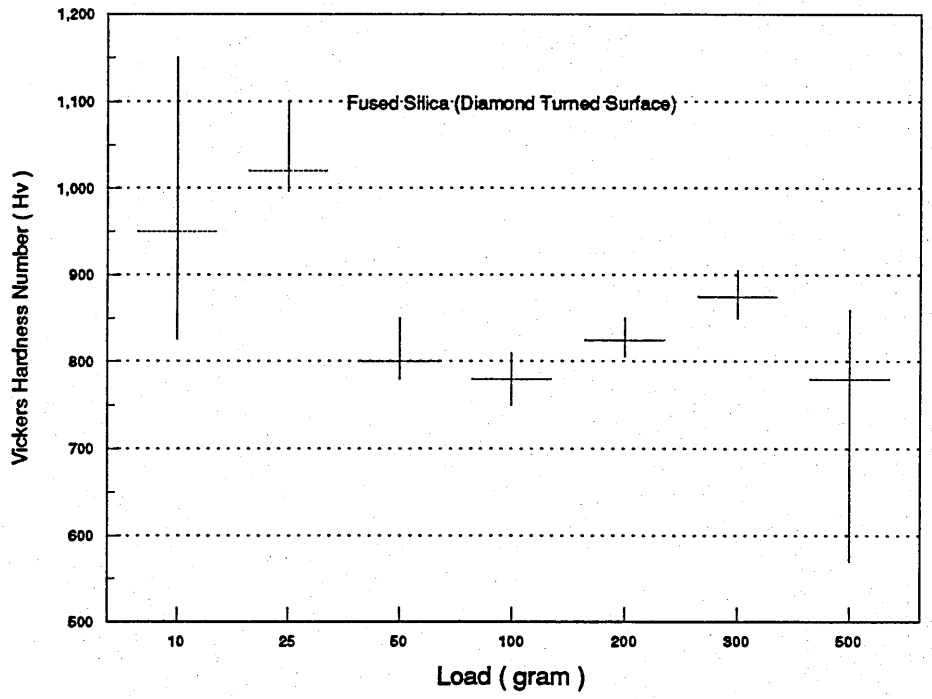

(b)

Fig. 2.18 Vickers hardness number of fused silica versus normal load (gram) (a) polished surface (b) single-point diamond turned surface (depth of cut: 1.2 μm, cross-feed: 0.5 $\mu m/rev$, roof-edge tool). [plotted points are means, and VHN ranges (length of the vertical lines)]

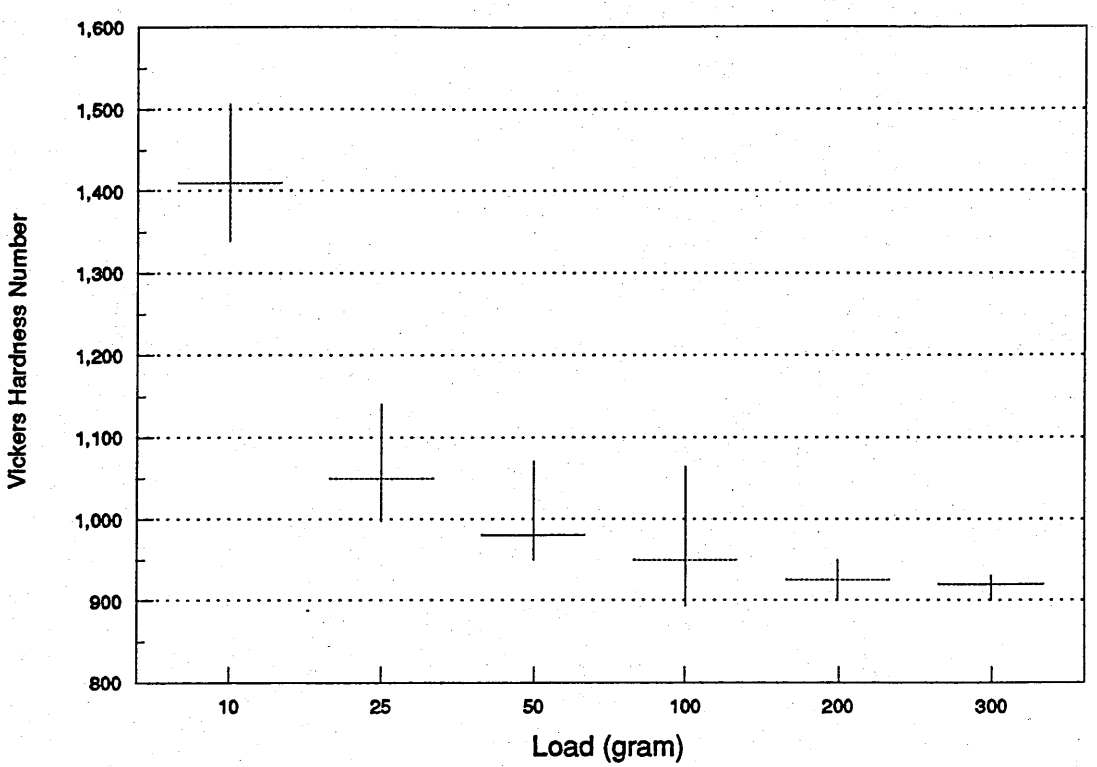

Fig. 2.19 Vickers hardness number of silicon versus load (gram) [plotted points are means, and VHN ranges (length of the vertical lines)]

To explain the increase in hardness, some researchers suggested that the size effect is a consequence of lacking of dislocations, the necessary ingredient for plastic deformation, when the indentation becomes smaller than the spacing of dislocations in the material. However, from the transmission electronic microscopy (TEM) study of indentation on a near (1 1 1) surface of silicon, Puttick, Shahid, and Hosseini (1979) found dense array of dislocations around the indentation made by a diamond indenter under only 2 grams load. This has made lack of dislocation very unlikely.

As to the reason why fracture does not occur at loads lower than a critical value is usually explained by the lower possibility of finding the existing surface flaws when the indentation is very small. But, as will be discussed in the following chapter, a ductile (plastic) groove can be ruled/scribed if the normal load is below a critical value. This again is evidence enough to throw considerable doubt on the theory of flaw statistics, for it is almost impossible to scribe a long groove without running into one or two existing flaws to initiate the cracks.

Roesler (1956) suggested that the scale effect was because fracture could not occur until the supplied energy was sufficient to initiate and propagate the crack. When the size of the indentation increases, so does the strain energy which is needed for crack initiation.

Puttick, Shahid, and Hosseini (1979) proposed that the fracture criterion was the magnitude of the strain energy contained in the field of the tensile stress around the indentation. Thus, there is a minimum size of the stressed volume of material below which a crack can not initiate. The critical linear dimension d_c, as suggested by Puttick (1980), Puttick and Hosseini (1980), and Puttick et al (1989), can be obtained from

$$d_c = \frac{\alpha E R_w}{\sigma_y^2} \qquad (2.36)$$

where E is the Young's modulus, σ_y is the yield stress for plastic flow, R_w is the specific work per unit area required to propagate a crack, and α is a numerical parameter whose magnitude is a function of the type of test.

2.4.5 Indentation of a Machined Surface

Indentation experiments were also performed on single-point diamond turned surfaces. Fig. 2.18 (b) shows the plot of Vickers indentation hardness numbers at various normal loads on fused silica which has been diamond turned with depth of cut 0.3 μm and cross-feed 0.5 $\mu m/rev$. The indentation hardness of machined surface appeared to have reduced, compared to the polished (as received) surface (as shown in Fig. 2.18 (a)).

The SEM micrographs of the polished surface have already been shown in Fig. 2.10 and discussed in section 2.4.2. Radial cracks occurred at loads of 100 grams on polished Fused silica. Fig. 2.20 shows the SEM micrographs of the residual impressions which present no sign of radial cracks even when the normal load is raised to 500 grams. (The small flake-like objects on the surface are chips produced during machining left intact for observation purpose).

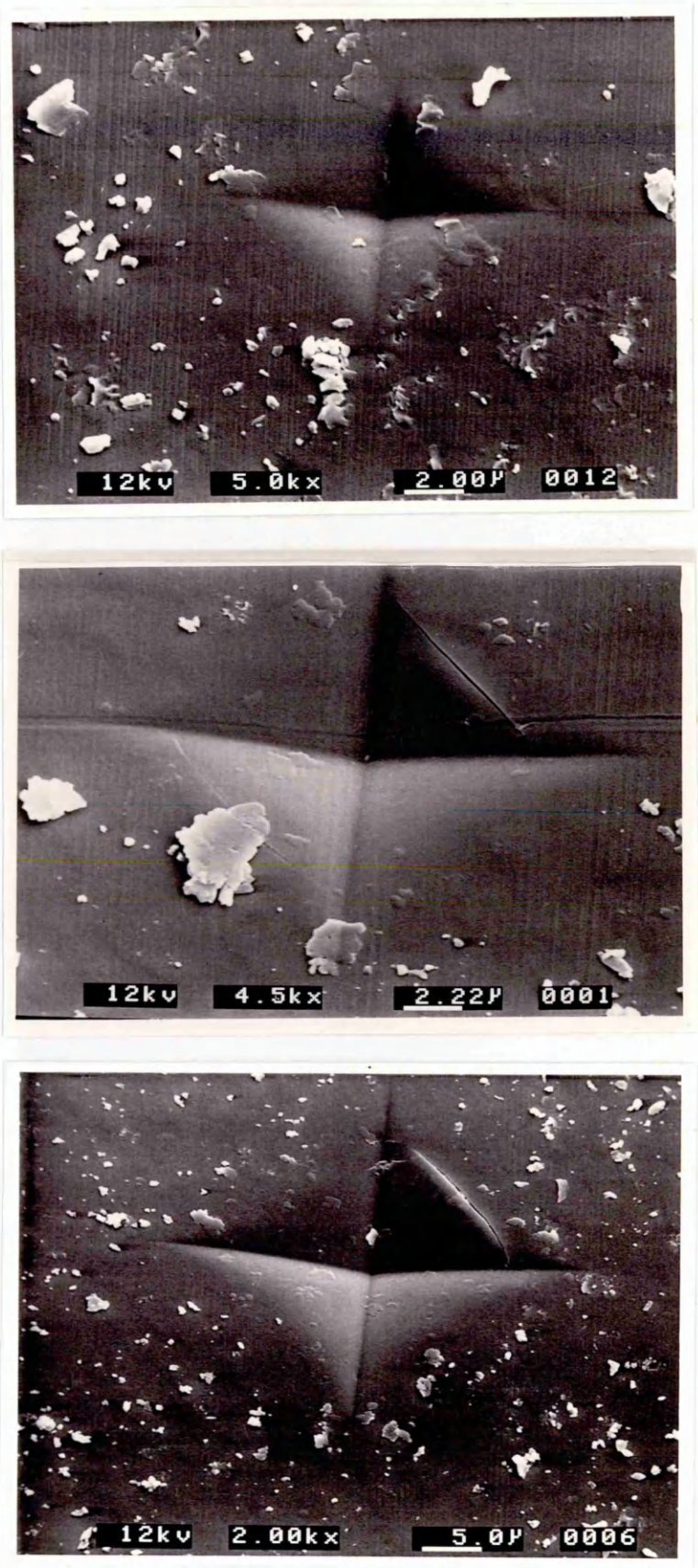

(a)

(b)

(c)

Fig. 2.20 Indentations on single-point diamond turned (machining condition: depth of cut 1.5 μm, cross-feed 0.5 $\mu m/rev$) fused silica surface at loads of (a) 50 g (b) 200 g (c) 500 g.

The diamond turning process has introduced a compressive stress field in the surface layer which suppressed the initiation of radial cracks. The Vickers indenter was arranged in a way that one diagonal was nearly parallel to the grooves (the cutting direction). If there were median cracks underneath the groove, the radial cracks would have followed the existing median cracks and propagated along the groove.

The radial crack failed to appear and the fine machining marks (grooves) been left on the surface means that the surface has been machined in a ductile mode. This also means that even a ductile machined surface may still have some physical property changes introduced in the top layer.

2.5 Summary of the Indentation Tests

Indentation tests on soda lime glass have demonstrated significant post indentation crack propagation which provided the evidence of the importance of residual stress field and the effect of environment.

The SEM micrographs of the indentations (with magnification above 10,000)on fused silica and Zerodur have shown that under 10 grams load "edge" cracks appeared on the edges of the residual impressions (these crack are beyond the resolution of normal optical microscope). At high load (>50 grams) indentations on both materials exhibited a very distinctive crack pattern which has a series of ring cracks surrounding the residual impression, and has radial cracks emanating from the corners of the indentation and penetrating the surrounding ring cracks. Since most of the fracture threshold models (section 2.3.2) are based on the assumption that fracture starts with either radial or median cracks, the appearance of edge crack and the complicated crack pattern might serve as a reminder that these models are only approximate.

The indentation tests on single crystal silicon have shown that the indentation fracture of crystalline material is very complicated. Although the fracture appeared to propagate along or close to the $< 1\,1\,0 >$ direction (with preference for $[\,0\,1\,\bar{1}\,]$, $[\,1\,\bar{1}\,0\,]$, and $[\,\bar{1}\,0\,1\,]$) under low load (10 grams), in general, it followed a path representing a compromise between the demands of the inhomogeneous tensile stress field and those of the crystallographic structure.

In general, single-point diamond turned specimens (fused silica) have lower hardness number than that of the polished. The diamond turned specimen has a layer of compressive residual stress on its surface which was introduced by the tool during machining. The presence of this compressive stress field may inhibit the initiation and propagation of the radial crack.

The micro-hardness measurement results has display a strong size effect (hardness increases when the size of the indentation decreases).

Since the micro-hardness is a function of load, strain rate, loading time, environment (temperature, humidity, and chemical composition), and specimen surface properties; the values of micro-hardness and those microscopic material parameters which are determined by using indentation technique have to be used with precaution.

Chapter 3

Ruling and Scribing: Experiments and Theoretical Analysis

3.1 Introduction

This work is concerned with ascertaining the machinability of materials at fine scales. In Chapter 2, indentation hardness measuring techniques were employed and related to earlier work. However, with respect to machining it is essentially a static process in all but the degree of freedom orthogonal to the surface of interest. It is therefore appropriate to consider extending the mode of operation to include rectilinear lateral motion.

"Scratching" experiments have been performed by a number of researchers from the field of material analysis and reference to this work will be made later in this chapter. However it was considered appropriate to examine analogous processes in the field of fine precision machining. One such machining mode is "ruling", a specialised process used for manufacturing diffraction-gratings and scales. It requires two lateral modes of tool/workpiece motion, one of long (tens of mm) rectilinear travel and one fine (about 1 μm or more) of either rectilinear or angular motion. The diffraction grating is a vital component used for spectroscopic dispersion in major optical instruments and can be readily tested using optical interferometric techniques so the achievements of certain specialised schools in the USA and elsewhere over the last century or more is well-known. The topic area has been reviewed by Stroke (1967) and Palmer et al (1975).

Ruling of gratings however is essentially a process (exclusively) of material **redistribution**; ductile materials such as aluminium or copper are 'grooved' by burnishing and no material chip is removed (unless the tool is misaligned).

Whilst "ruling" would adequately describe a purely plastic process, "scratching" has connotations of being fortuitous. It was considered that neither fully described the analogous mode of material test of glassy materials in the marginal critical depth

region where either process might be encountered; hereafter it will be described as 'scribing' (a more ordered process than scratching but less so than ruling).

All three have been generally constant-load (or "dead-load") processes involving trailing a diamond tool across specimen surface.

Though different from fixed-depth single point diamond turning in the manner by which the tool tip comes to be at a particular depth in the substrate material, as a dynamic process, scribing represents an intermediate process between progress from indentation towards practical machining. However, it is surprising that, compared with static indentation, relatively little work regarding the scribing stress field and fracture is to be found in the literature.

From the viewpoint of the present work, once the tool achieves a particular depth, consideration of the quiescent conditions show that scribing and single point diamond turning are very much alike; the tip of the tool experiences the same force in the direction of the surface-normal in either method. By examining the nature of the tracks (grooves) and cracks left on the specimen surface, the mechanisms of deformation, crack formation, the influence of normal load (and thereby the penetration depth), velocity, and tool shape can be studied.

The micro-hardness testers (Leitz model 'Miniload 2' and Matsuzawa Seiki model: MHT-1) used in indentation experiments in this study are also capable of performing scribing (scratching) experiments with normal loads ranging from 5 g (49 mN) to 100 g (0.981 N).

Ruling experiments were conducted using the Horsfield grating ruling engine (detailed in section 3.3) with loads ranging from 5 g (49 mN) to 250 g (2.45 N). Being designed for ruling optical diffraction grating, a ruling engine must be highly stable in order to rule grooves with high repeatability of shape and spacing. Both ruling and scribing experiments were performed at room temperature (20 ^{o}C) and under "dry" (no coolant or lubricant) conditions.

3.2 Fracture Induced by Sliding Contact

3.2.1 Circular Contact

The stress field created by sliding a hard ball over the surface of a brittle materials has been analyzed by Hamilton and Goodman (1966). They found the position of

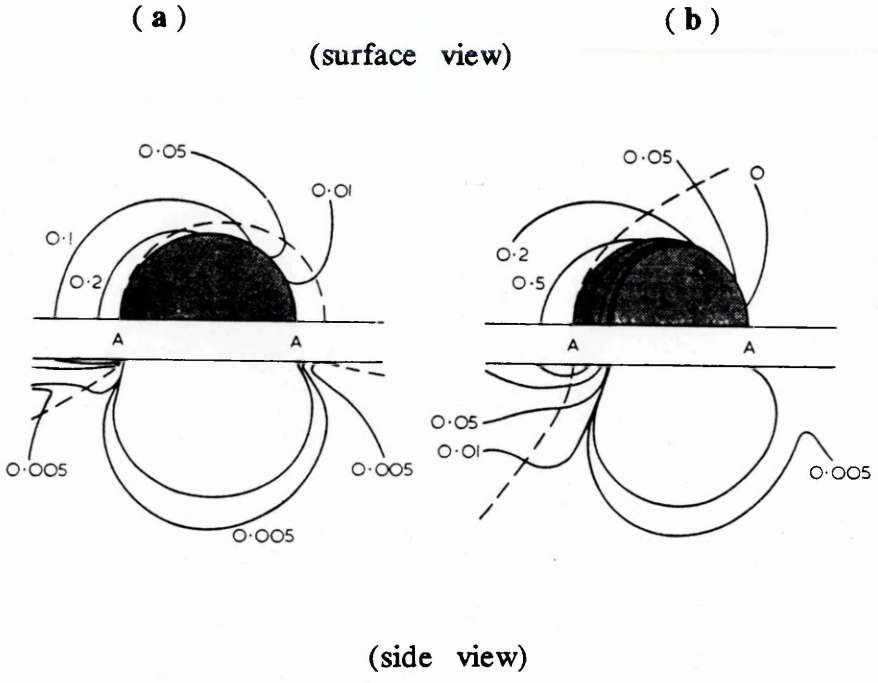

Fig. 3.1 Contours of the principal stress, σ_1 (solid lines), σ_2 (broken lines- surface view), and σ_3 (broken lines- side view) in a semi-infinite elastic medium (surface S-S) in contact with a spherical indenter. Coefficient of friction: (a) $\mu_f = 0.1$ (b) $\mu_f = 0.5$; Unit of stress : P_0 (mean contact pressure); c.z. : compressive zone in which all three principal stresses are negative. (After Lawn 1967)

maximum tensile stress to be in a region centred on the trailing edge of the contact zone and its value to be given by

$$\sigma_{max} = \frac{3P_L}{2\pi a_c^2}\left[\frac{(1-2\nu_2)}{3} + \mu_f \pi \frac{(4+\nu_2)}{8}\right] \tag{3.1}$$

where P_L is the normal load, ν_2 is Poisson's ratio for the indented material, μ_f is the coefficient of friction, and a_c is the radius of the circle of contact, given by

$$a_c^3 = \frac{3}{4}\left(\frac{P_L R}{E_e}\right) \tag{3.2}$$

E_e is defined in Hertz' analysis (see section 2.2.1) as

$$\frac{1}{E_e} = \frac{1-\nu_1^2}{E_1} + \frac{1-\nu_2^2}{E_2} \tag{3.3}$$

where E_1, ν_1 and E_2, ν_2 are Young's modulus and Poisson's ratio for the indenter and tested specimen respectively.

The distribution of the maximum principal stress, σ_1, is shown in Fig. 3.1 (Lawn 1967) for two values of μ_f of (a) 0.1 and (b) 0.5 (Poisson's ratio ν_2 taken to be $\frac{1}{3}$). This is likely to be the stress which initiates fracture.

Preston (1922), Seal (1958), Lawn (1967) and more recently Leu and Scattergood (1988) have investigated the crack patterns induced by sliding a spherical indenter across the surface of brittle material (such as soda lime glass, silicon and germanium) and found that cracks could switch from complete ring (or cone) to open "partial" ring (or cone) form with the increase of the coefficient of interfacial friction.

3.2.2 Pyramidal Contact

Swain (1978) studied the cracks produced by scratching glasses and single crystal and polycrystalline alumina specimens with a Vickers pyramidal indenter (oriented so that one of its diagonals was parallel to the direction of scratching). He sectioned the scratched specimen to reveal the subsurface median and lateral cracks and reported that they both originated from the plastic deformation zone. At higher loads, lateral cracks could extend to the surface causing chipping.

Veldkamp, Hattu and Snijders (1978), and Broese van Groenou and Veldkamp (1978/79) attempted to simulate grinding operations on brittle materials including MnZn, glass, Al_2O_3, NiZn ferrite, and ZnO by conducting scratching experiments with a Vickers indenter. They suggested that three sorts of cracks could clearly be distinguished: median cracks, subsurface cracks and lateral cracks (as shown in Fig. 3.2).

In an attempt to correlate the vertical load, P_L, tangential force F_t, and the generated lateral crack length, C_L, in a scratching test with a sharp indenter, Broese van Groenou and Veldkamp (1978/79) proposed a simplified lateral crack model associated with scratching. They suggested that the tangential (horizontal) force

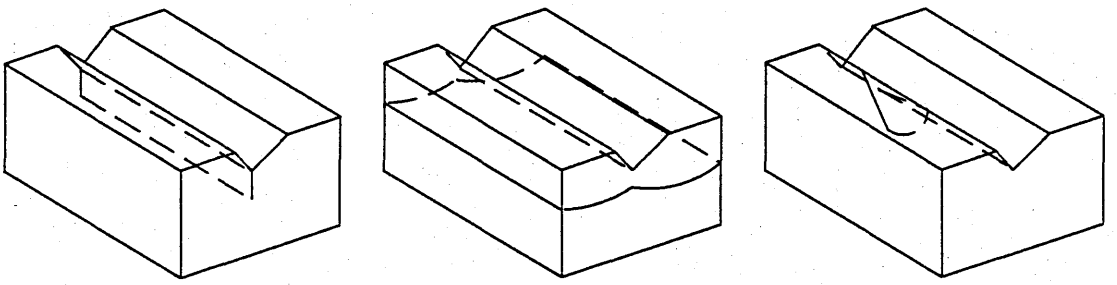

Fig. 3.2 Cracks produced in scribing (a) median crack (b) sub-surface crack (c) lateral crack (After Broese van Groenou and Veldkamp 1978/79)

F_t opened the lateral cracks and was therefore analogous to the "expanding" force in an indentation test.

Using the Irwin (1958) criterion (see section 2.3.2) for crack propagation, $K_{Ic} = \sigma_c \sqrt{\pi a_c}$, and adopting the correlation for load and well-developed half-penny crack length derived by Lawn and Fuller (1975), $P_L = \alpha_v K_c c^{3/2}$, Broese van Groenou and Veldkamp (1978/79) obtained a relation between C_L and F_t as:

$$F_t = \alpha_v K_c C_L \left(C_L + \frac{1}{2}\beta_v W \right)^{1/2} \tag{3.4}$$

where W is the groove width, K_c is the stress intensity factor, and β_v is a constant (with $\beta_v = 12.4$ Broese van Groenou and Veldkamp claimed that the above-mentioned equation could give a good representation of the measured results for the various materials they studied.

3.3 Ruling

3.3.1 Horsfield Grating Ruling Engine

A ruling engine, built by Mr. W.R. Horsfield an independent entrepreneur-inventor, to rule spectroscopic diffraction grating was made available on loan by Optometrics Inc., of Waltham, MA, USA (then, now of Ayer, MA). Unlike other contemporary ruling engines, the finely-indexed carriage carrying the blank (usually a glass plate), is not driven by the usual leadscrew. After much experimentation with non-leadscrew "incher" indexing mechanisms, Horsfield (1965), selected a reciprocating hydraulic pump and ram as the inter-groove actuator. The stroke length and phase was servo-controlled by reference to interferometric position measurement and on this machine Horsfield achieved the notable first of ruling acceptable spectroscopic gratings without resorting to a leadscrew; the machine capacity was 150 mm ruled width × 100 mm groove length.

As the index-pitch was designed to be 1.67 μm (corresponding to 600 grooves/mm) or less, to permit coarser pitch experiments, a DC-motor driven lead screw was

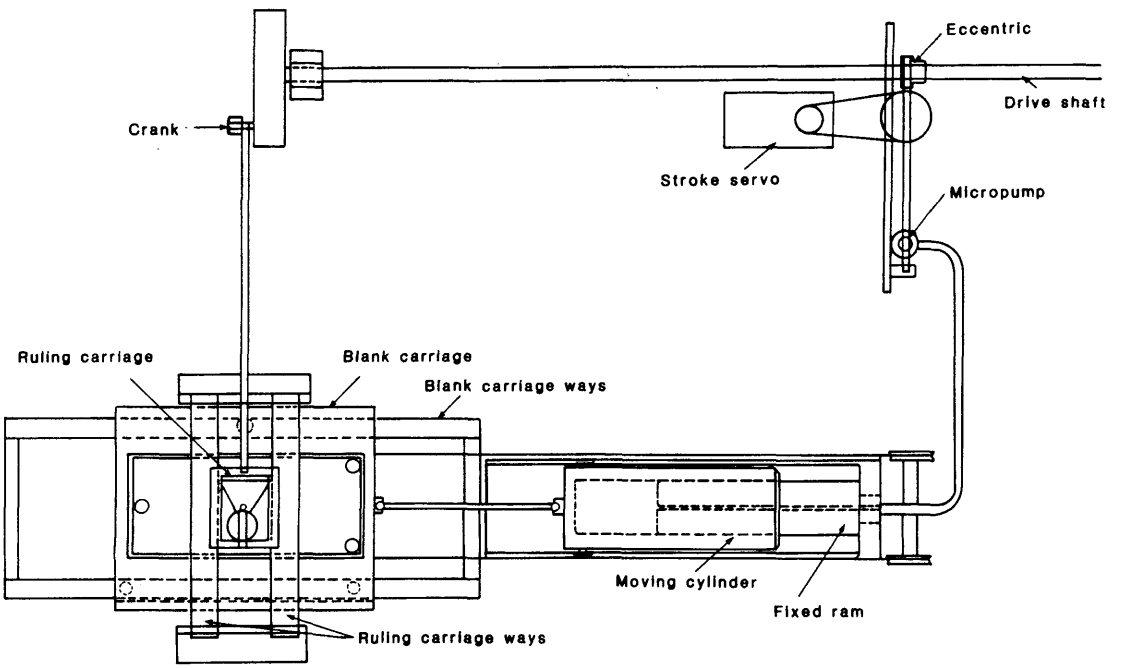

Fig. 3.3 Plan of Horsfield grating ruling engine. (After Horsfield 1965)

added permitting appropriate larger-scale experimentation with higher vertical loads applied.

The general layout of the ruling engine is shown in Fig. 3.3 (Horsfield 1965). The base plate is a standard 900 mm × 900 mm surface plate. The blank carriage support and main guideway, consisting of a normalized iron casting, was lapped to accuracy of 5 μm on two parallel horizontal faces and to 0.025 μm on a vertical face to provide carriage-guidance in "pitch" and "yaw". In Horsfield's (1965) original design this iron casting also served as a container for mercury which supported 95% to 98% of the weight the blank carriage (thereby reducing Coulomb friction by the same factor by substituting viscous friction which, at velocities of a few μm /s, is negligible. Because mercury is highly toxic, the flotation-support was changed to an external raft-structure floating on oil instead of mercury, as tried out and proved effective earlier (Gee 1974). The catamaran-like raft flotation-support consists of four boxes which are framed together by aluminium rods and float on oil in four troughs straddling the machine as shown in Fig. 3.4. The blank carriage is connected to the floating raft-structure through three rods flexibly jointed with stiff coil springs to provide decoupled vertically-constrained support.

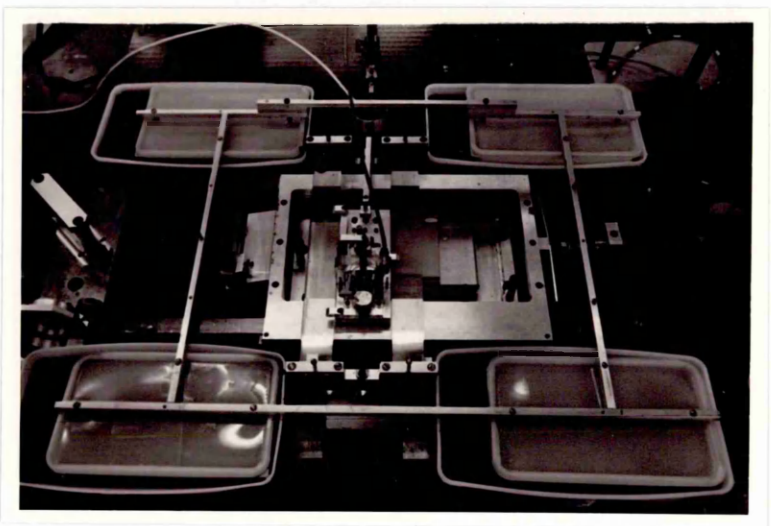

Fig. 3.4 The catamaran-like floatation-support.

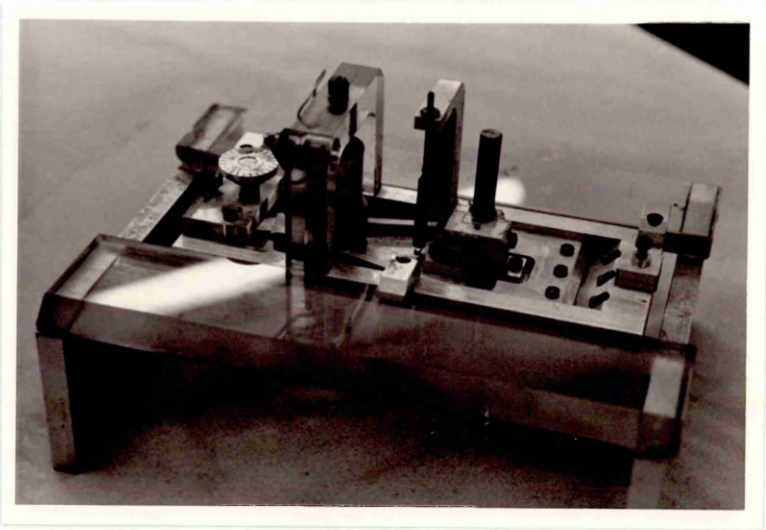

Fig. 3.5 Detail of the diamond tool carriage.

The diamond tool carriage (Fig. 3.5), weighing less than 100 g (Horsfield 1965), reciprocates on a pair of cross ways (Fig. 3.4), consisting of two glass bars 30 mm wide supported by vertical members and bolted to the base-plate forming a bridge structure over the grating carriage. To allow the diamond to travel freely vertically only, the mechanism used by Horsfield is a spring strip hinge and trailing arm, providing the great lateral stiffness needed to ensure straight parallel grooves.

The tool was lifted and lowered by various actuators including pneumatic as described by Horsfield (1965) and electromagnetic (Fig. 3.5) to give more lifting power, permitting a wider range of vertical loads (up to 200 grams vertical load were eventually used in this study whereas the original machine could lift up to 20 grams only).

The Horsfield ruling engine is of the "stop-start" type in which the blank is advanced only between ruling strokes. Since the blank stays still during the ruling strokes, the obtained grooves are straight and the tool experiences no side force.

The diamond tool carriage, pushed and pulled by a rotating crank, travels with near simple harmonic motion. In order to minimise vibrations, ruling speeds were kept

below 100 mm/sec. However, as will be addressed in the following sections, fluctuation of friction force between tool carriage and its guide ways might still induce some vibrations.

Optical scatter and ghost requirements for gratings dictate that periodic errors should be kept down to the order of nanometres and overall errors of run be no more than a few hundreds of nanometres in a ruled width of 150 mm or more. The machine therefore has to be rigid, stable and accurate; thus, for this experiment, the specification of a ruling engine is such as to make it ideal as an instrument for dead-load testing.

3.3.2 Force Measurement

In order to investigate the effect of parameters including tool loading, drive force, cut depth, ruling speed, and tool geometry, strain gauge bridge dynamometers were inserted both into the diamond-carriage drive-linkage and under the carriage table to permit the tangential, lateral and vertical forces transmitted from the tool to the specimen to be measured. The forces were converted into voltage signal by the dynamometers and recorded using a data-logger. The dynamometer was calibrated

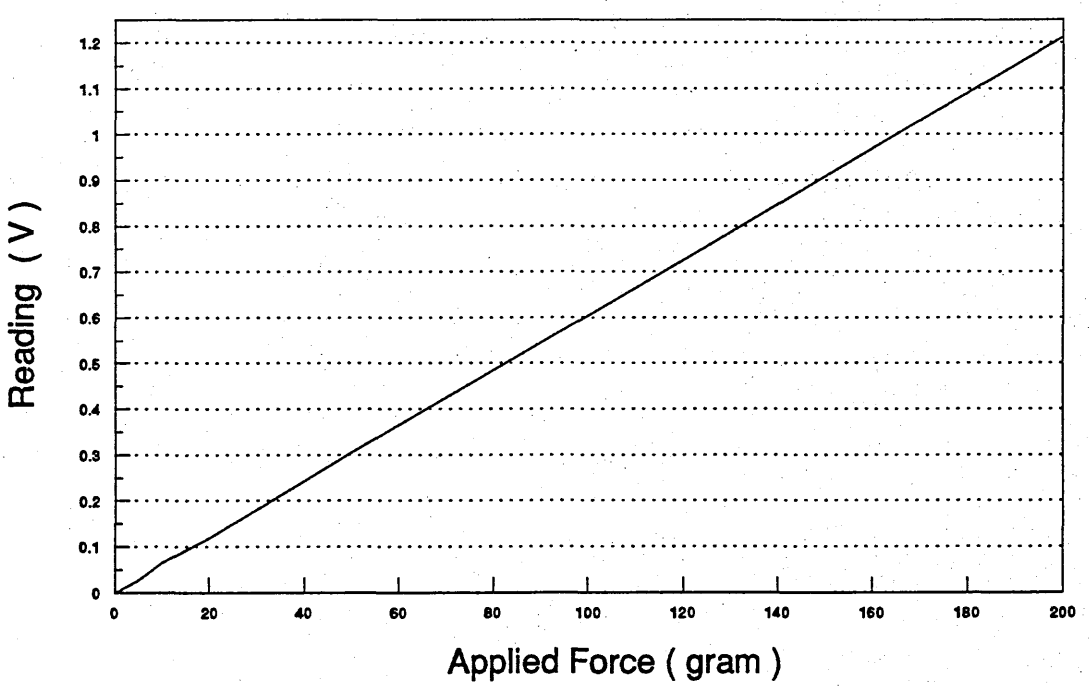

Fig. 3.6 Calibration curve of dynamometer.

using standard weights and the resulting calibration curves (Fig. 3.6) stored into the computer to serve as a conversion table for the logged signal.

Vertical forces were larger than horizontal and so were the principal factor controlling penetration of surface. However, as a dead-load machine, the vertical loads were fixed and the results analyzed in terms of the tangential forces.

3.4 Single-Point Diamond Tools

3.4.1 Physical Properties of Diamond

Diamond is a crystalline form of carbon and, as was shown by W. H. and W. L. Bragg (1913), every carbon atom is surrounded by, and covalently bonded to, its four nearest neighbours which are situated at the corners of a regular tetrahedron (Fig. 3.7). Since the distance between nearest neighbours is only 0.154 nm, the bonds are extremely strong. Due to this strong bonding between carbon atoms and the highly symmetrical arrangement, diamond exhibits some notable and superior properties such as great hardness, high melting point, high thermal conductivity.

Diamonds can be classified as type I and type II according to their absorption in the infrared, visible and ultraviolet regions (Robertson, Fox and Martin 1934; Sutherland, Blackwell and Simeral 1954; Clark, Ditchburn and Dyer 1956). A pure

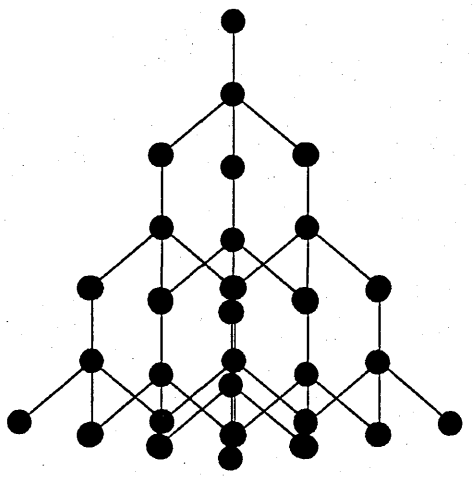

Fig. 3.7 Crystal Structure of diamond.

diamond lattice may be expected to show little absorption in the visible and ultraviolet regions for photon energies appreciably less than the energy corresponding to the fundamental gap between the valence band and conduction band. The difference in the absorption spectra indicates that type II diamonds are relatively free from crystal defects or impurity which produces additional absorption in type I diamonds (Ditchburn, Thomson and Custers 1965).

Most natural diamonds are of type Ia which contains nitrogen, distributed into small aggregates, as an impurity in amounts of the order of 0.1%. Type Ib diamonds contain nitrogen on isolated substitutional lattice sites at concentrations up to 500 ppm and are rare in nature but almost all synthetic diamonds are of this type. Since nitrogen atoms are paramagnetic, their concentration can be determined by electron spin resonance (Berman 1979). Custers (1952, 1955) found that a small proportion of type II diamonds are semi-conductors and proposed to classify the non-conducting type II diamonds as type IIa and the semi-conducting diamonds as type IIb. Both type IIa and IIb are rare in nature and contain a very low concentration of nitrogen (too low to be detected by infrared or ultraviolet absorption measurements).

By using the tetrahedron as a building block, an extremely large molecule can be constructed. Inside this large tetrahedron-based diamond molecule, there are four sets of parallel bonds which correspond to four bonds in the tetrahedron (Fig. 3.7). If, in a perfect diamond model, such a set of parallel bonds is cut through, it will be split into two, with the expenditure of very little energy. This process is call "cleaving" and the planes are called "cleavage planes" which, to be accurate, are the { 1 1 1 } planes. It is critical to recognise these planes of weakness in the design of mechanical systems (such as machine-tools) which use diamond tools. Diamond tools could be easily broken if they are wrongly design-orientated (or abused), although diamond is the hardest material known.

Diamonds are most commonly found in the form of octahedra whose faces are { 1 1 1 } planes or as dodecahedra whose faces are { 1 1 0 } planes (Fig. 3.8). The octahedral planes are extremely resistant to abrasion in all directions. This sometimes leads to request for tools having the working face in this plane, but, one must keep in mind that this is also a cleavage plane. The hardness of diamond varies greatly with direction and to obtain the best result from a diamond mounted as a

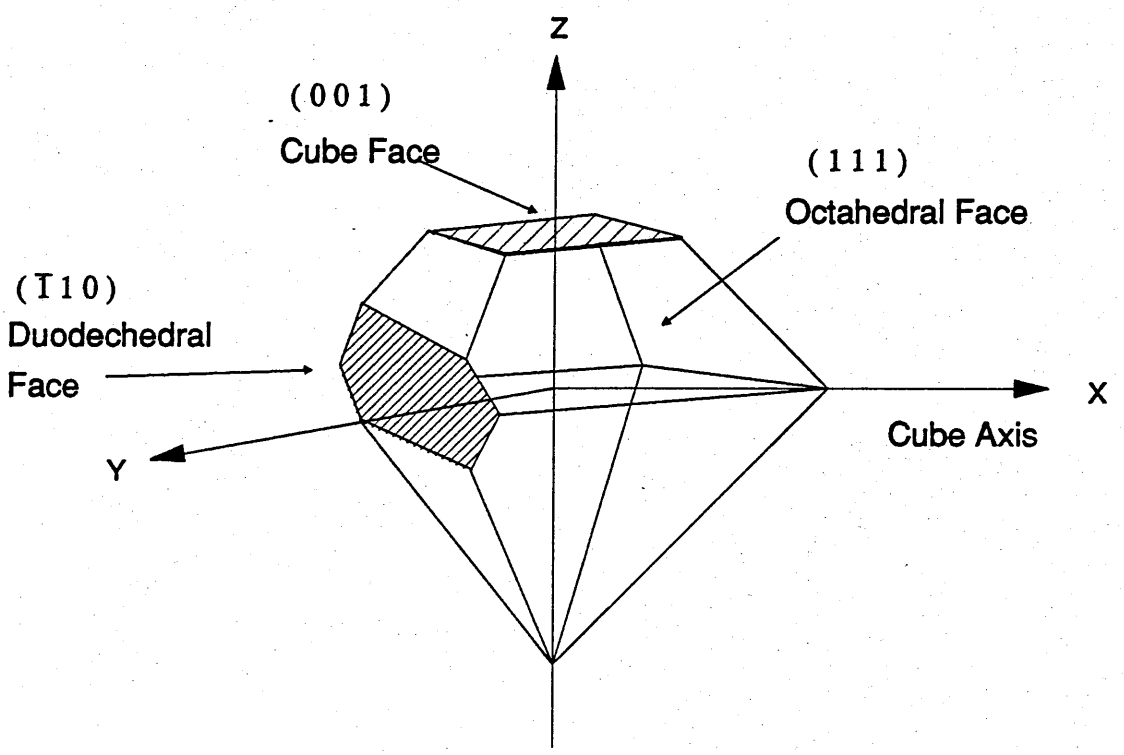

Fig. 3.8 Principal planes of a diamond crystal.

cutting tool, it must be correctly oriented to within about one degree (Wilks and Wilks 1965).

The density of diamond is $(3.51524 \pm 0.00005) \times 10^3 \frac{kg}{m^3}$ at $298\,^oK$ (Mykolajewycz, Kalnajs, and Smakula 1964), and its Young's modulus is 1054 Gpa (McSkimin and Andreatch 1972). The thermal conductivity and specific heat for type Ia diamonds (at $293\,^oK$) are 600-1000 $(\frac{W}{mK})$ and 525 $(\frac{J}{kgK})$ respectively (Berman 1979).

3.4.2 Single-Point Diamond Tools

The single point diamond tools used in this experiment, as shown schematically in Fig. 3.9, can be classified into the following forms:

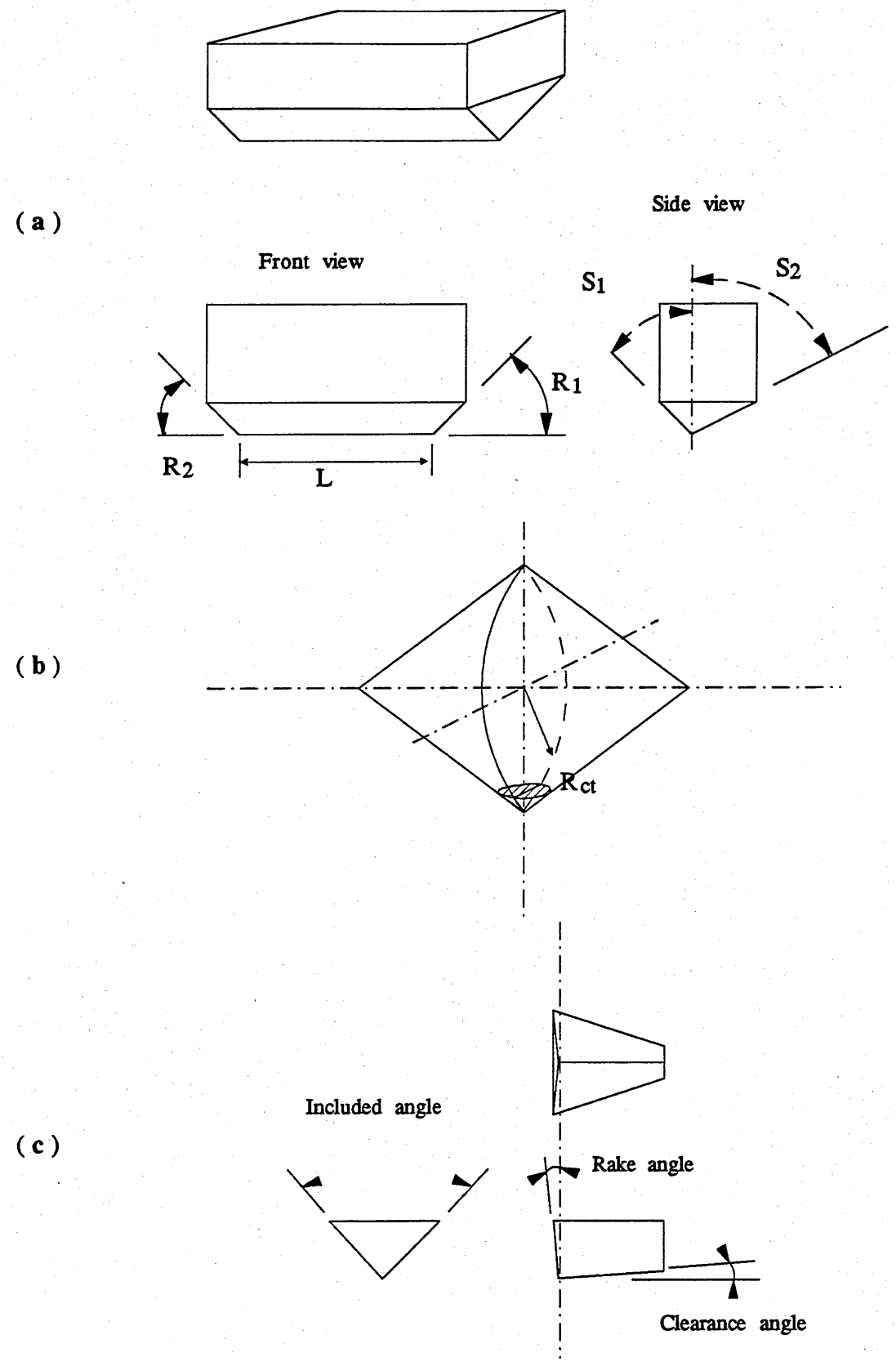

Fig. 3.9 (a) double-ended (roof-edge) type tool (b) double-cone ('canoe'- or 'hatchet'-shaped) type tool (c) scratch diamond tool .

1) The double-ended (roof-edge) type (Fig. 3.9a): each end consists of three planes intersecting at a point and usually with a chisel edge (length, L) connects these two ends. One of the early principal applications for single point diamond tools was in the ruling of diffraction gratings, which was developed considerably over the century between 1875 and 1975. Gratings were required to be 'blazed' with asymmetrical section grooves and for this the diamond tip (edge) is arranged to have a steep side and a shallow side. The angle between the side face and the centre plane is called the 'side-angle'. We use S_1 and S_2 to specify the side angle of steep side and shallow side respectively (thereby $S_1 < S_2$). The included angle, S, between two sides ($S = S_1 + S_2$) ranges from 90 to 120 degrees arc generally. The rake angles (R_1, R_2) range from 45 to 60 degrees.

In the (Horsfield) ruling engine (see section 3.3.1) which was available for this work, the diamond is mounted on a 5 mm diameter steel pin. The projected area produced by roof-edged tool can be described as:

$$A_p = W\,(L + d\tan R_1 + d\tan R_2)$$

where

$$d = \frac{W_1}{\tan S_1} = \frac{W_2}{\tan S_2}$$

is the groove depth, W is the groove width ($W = W_1 + W_2$), W_1 and W_2 are the width of the steep side and shallow side respectively.

2) As its name implies the double-cone ('canoe'- or 'hatchet'- shaped) type (Fig. 3.9b) has a cutting edge shaped like the keel of a canoe which is geometrically the intersection of two coaxial convex conical surfaces (two conical surface intersecting in a circular ridge which has a radius of curvature R_{ct}). Like the double-ended tool, it can have steep and shallow sides [but in this study a tool with equal side angles ($S_1 = S_2$) was used]. The projected area can be expressed as:

$$A_p = \frac{4}{3} W \sqrt{d\,(2R_{ct} - d)}$$

where

$$d = \frac{W}{2\tan(\frac{S}{2})}$$

is the groove depth, W is the groove width and S is the included angle.

3) Pyramid indenter : the standard Vickers Hardness Test diamond indenter with an included angle of 136 degrees arc. The projected area of this can be described as:

$$A_p = W^2$$

where W is the groove width.

4) Scratch diamond tool (Fig. 3.9c) as used in the scribing test: this has 5 degrees arc negative rake angle and 5 degrees clearance angle and the rake face has 120 degrees included angle. The projected area can be described as:

$$A_p = \frac{W^2}{4} \tan 60$$

where W is the groove width.

3.5 The Ruling/Scribing Process

3.5.1 Ruling/Scribing Experiments on Amorphous Glasses and Glass-Ceramics

Beilby (1907, 1921), French (1917), Preston (1921/22), Klemm and Smekal (1941), and Taylor (1949) have observed fine scratch (furrow) marks made by rubbing a hard point against a glass surface and suggested that this was plastic flow.

The diamond tools used in ruling experiments on glasses were either of roof edge from (with side angles $S_1 = 37^o$ and $S_2 = 63^o$, rake angle $\alpha_{rake} = -45^o$) or canoe-shaped (with included angle $S = 90^o$, $R_{ct} = 0.5\ inch$). The roof-edge tool was used both in upright (pin axis perpendicular to the ruling direction) and 5 degrees tilted forward (to simulate a tool with -50 deg. rake angle and 5 deg. clearance angle) manners. Travelling speeds of the diamond tool covered from 1 mm/sec to 95 mm/sec, normal loads ranged from 5 grams to 150 grams, and groove-spacings ranged from 1 μm to 50 μm . Since the diamond tool travels with near simple harmonic motion (see section 3.3), a spectrum (range) of tool speeds can be obtained in one stroke. The speed controller attached to the machine could offer ten speed bands for ruling. This provided a ready means of studying the influence of speed on groove profile.

Fig. 3.10 Scanning electronic micrograph showing the ductile-brittle transition produced by ruling the soda lime glass with a canoe-shaped tool (included angle: 90, R_{ct}: 0.5 inch), 90 grams vertical load, and at 40-90 mm/sec speed range.

At low loads (25 grams), low penetration depth, ductile (fully plastic) grooves formed on soda lime glass at the whole range of speeds studied regardless of the tools used. This low figure (25 grams) was used with the tilted roof-edged tool. The upright roof edge could sustain 60-70 grams with plastic deformation while the canoe-shaped tool could employ 70-80 grams vertical load without damage at all speeds studied. In the cases of loads higher than 150-190 grams (respectively for roof-edged and canoe tools), the grooves produced on soda lime glass were fully brittle for all speeds and tools.

An interesting phenomenon observed with intermediate loads (between fully plastic and fully brittle grooves) was that brittle fracture was normally first encountered at lower speeds (i.e. at start and end of the groove when crank driven). Thereby, very often a brittle to ductile transition appeared at the accelerating end while the ductile to brittle transition could be seen at the decelerating end. As a result, a section of ductile groove was left in the middle. Fig. 3.10 shows one of these ductile-brittle

transition produced by ruling the soda lime glass with a canoe-shaped tool, 90 grams vertical load, and at 40-90 mm/sec speed range.

The ductile-brittle transition in Fig. 3.10 could be divided into three stages, these were:

(1) small lateral cracks appearing at the bottom of the grooves

(2) large post-ruling propagated lateral cracks emerging at the surface which might combine with adjacent lateral cracks and cause post-ruling chipping (the grooves profile could not be so good if chipping occurred before the ruling tool had passed)
(3) severe chipping occurred and left some large holes which could have depth 5-10 times the value of ductile groove depth.

[From Fig. 3.10 the groove depth was measured as 1.2 μm which compares closely with the figure of approximately 1 μm postulated and measured by Puttick et al (1989). Further discussion of the critical cut depth arises in section 4.3].

Usually, this transition phenomenon stretched for several hundred grooves and formed a transition band. The length of the damaged (brittle) part of the groove tended to extend when ruling with lower speed range. Fig. 3.11 shows a typical

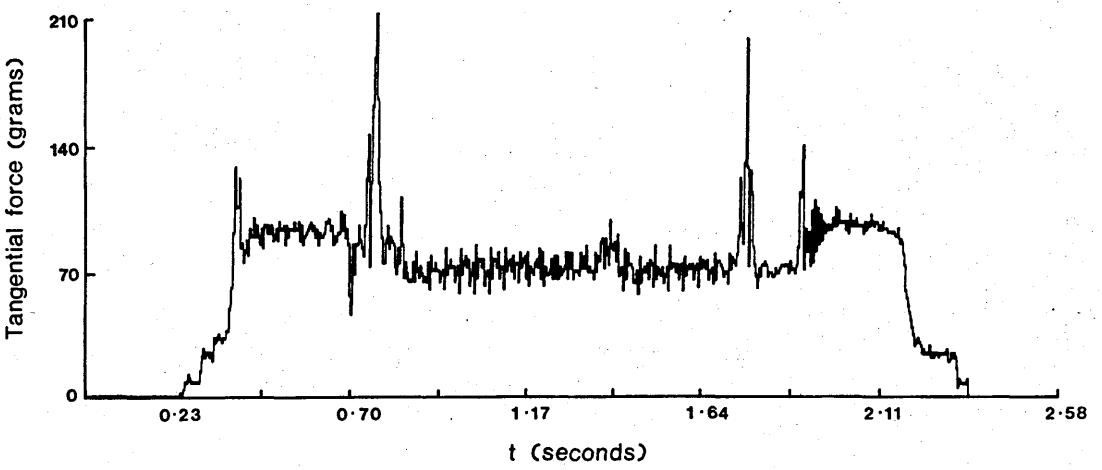

Fig. 3.11 Tangential ruling force versus time trace.

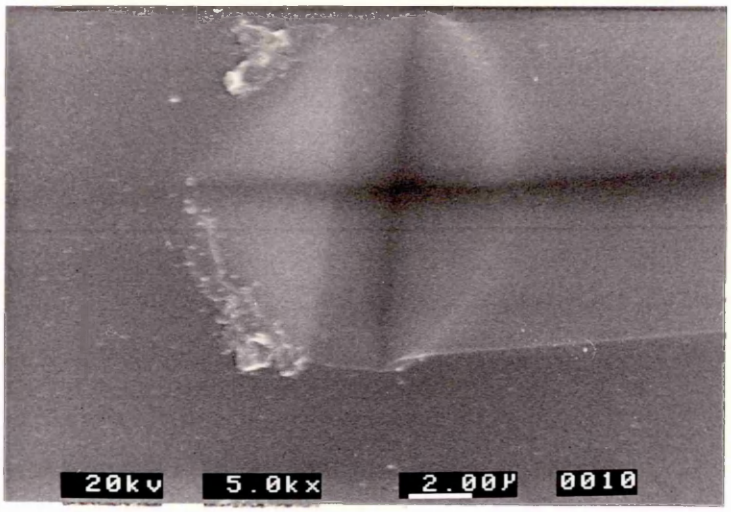

Fig. 3.12 Groove produced by scribing the soda lime glass with a Vickers indenter (notice the residual impression at the end of the groove).

tangential ruling force versus time trace. The large fluctuations at both ends were caused by the large scale chipping (the third stage).

The results of ruling on soda lime glass showed that the ductile brittle transition had a speed dependency on a dead load machine. However, the speeds used in this study were far too slow to generate enough energy to soften the glass, thus, the thermal energy could not be the major reason of the transition (see section 5.5). One possible cause for this speed dependency is that the groove width (and thence the groove depth) is a function of tool speed. Generally, the groove width decreases as the speed increases, probably due to the negative-rake 'keel' effect with tendency of the tool to ride up as the speed increases. (In general, the yield stress is expected to increase with increasing strain rate. This implies that the critical cut depth will decrease with increasing machining speed. Such an argument, however, neglects possible heating caused by friction.)

Fig. 3.12 shows a groove formed by scribing soda lime glass with the leading edge of a Vickers indenter. At the end of the scribing, the indenter was kept still for 5

seconds before it was lifted. During this "keep" time a partial Vickers residual impression was formed and could be seen clearly in the figure. Since part of the clearance faces (faces opposite to the direction of motion) were visible on the residual impression, this indicates that the indenter must has penetrated further down during the five seconds stationary. This indicated that the indenter (tool) needs time to penetrate. For a dead load ruling/scribing experiment, the faster the diamond tool travels, the less time there is for it to penetrate deeper into the material. Also, the shape of the tool may influence the groove depth. Using the canoe shaped diamond tool, the grooves manifested totally brittle fracture for vertical loads above 150-190 grams as compared to 60-100 grams for the tilted roof edge type tool.

Large scale curly swarf (in some cases it could have length as much as several millimetres) were observed after ruling soda-lime glass, as shown in Fig. 3.13, using both roof edge and canoe-shaped type diamond tools. These long curly swarf-chips have also been observed and reported by Demichelis (1951), Joos (1957), Busch (1968) and more recently Schinker and Döll (1985, 1987), Puttick et al (1989), and Chao and Gee (1989). Fig. 3.14 shows a detailed view of one the smaller swarf which

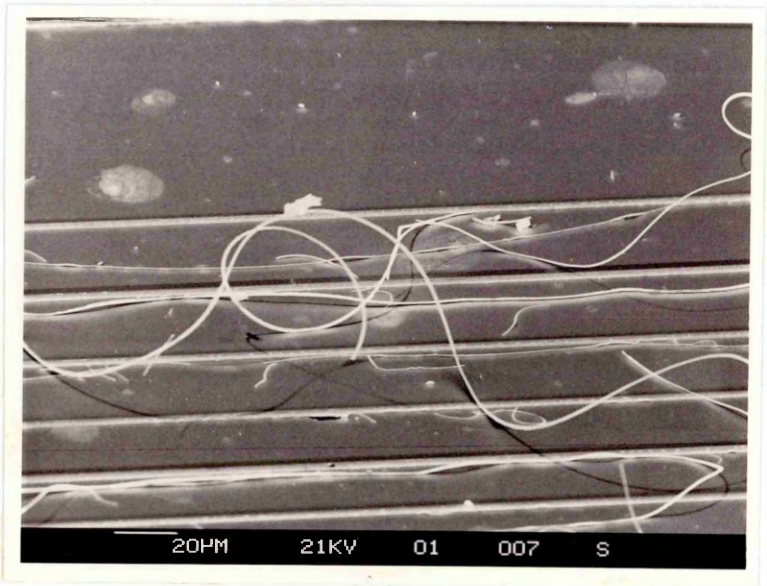

Fig. 3.13 Large scale curly swarf (in some cases it could have length as much as several millimetres) was observed after ruling soda-lime glass.

Fig. 3.14 Detailed view of one the smaller swarf which has both ends still attached to the groove edge and has its middle section arched up to form a "hoop" shape.

has both ends still attached to the groove edge and has its middle section arched up to form a "hoop" shape (similar to the long chips observed by Puttick et al. 1989 in fused silica). A long ribbon could be developed when several of these small hoops link together.

Since a hoop cannot be formed if material is removed ahead of the diamond tool, it must be formed after the passage of the tool. Puttick et al (1989) suggested that the swarf was produced by the compressive residual stress in the machined groove. This removal of material by residual stress they termed "delamination" and will be detailed in the following chapter (see section 4.2).

The grooves shown in Fig. 3.15(a) and Fig. 3.15(b) were produced by scribing on soda lime glass with the Vickers indenter and the scratching tool respectively. Apart from its small (near zero) negative rake angle, the scratching tool was very much like a tilted roof-edge type diamond tool. However, the material removal mechanism obtained with these two tools were quite different. Free from the strong compressive stress field (introduced by large negative rake angle) ahead of the tool,

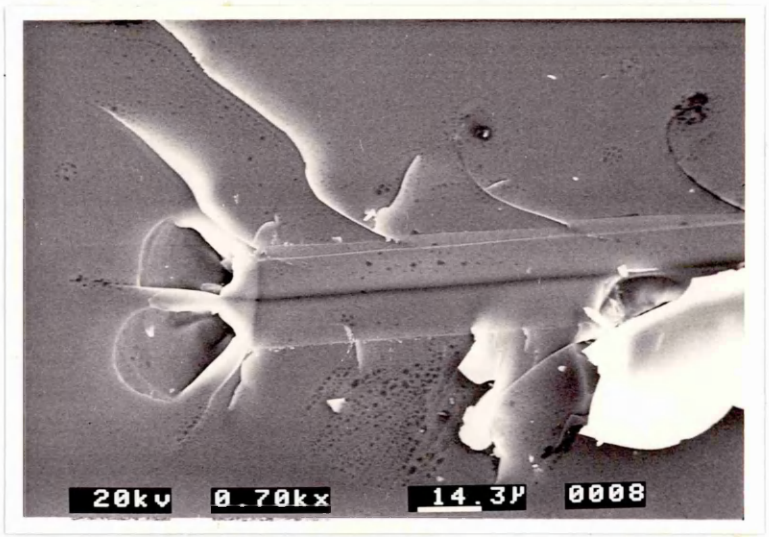

(a)

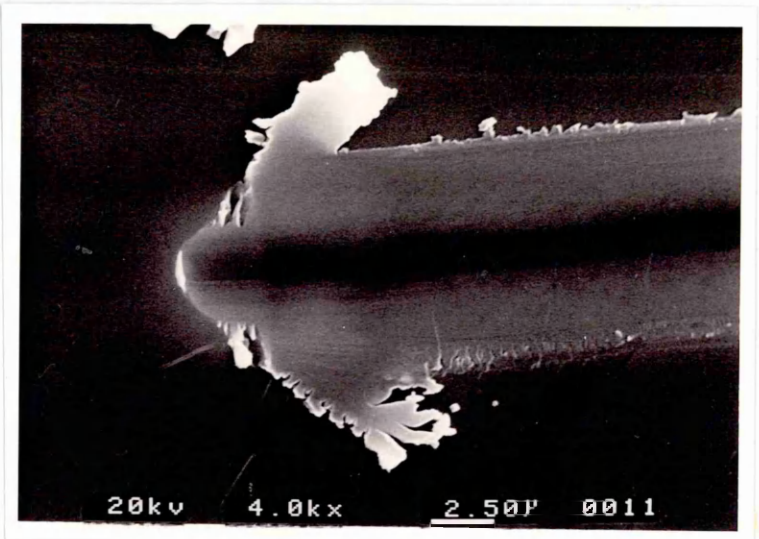

(b)

Fig. 3.15 Grooves produced by scribing on soda lime glass with (a) a Vickers indenter and (b) the scratching tool (with small -near zero negative rake angle).

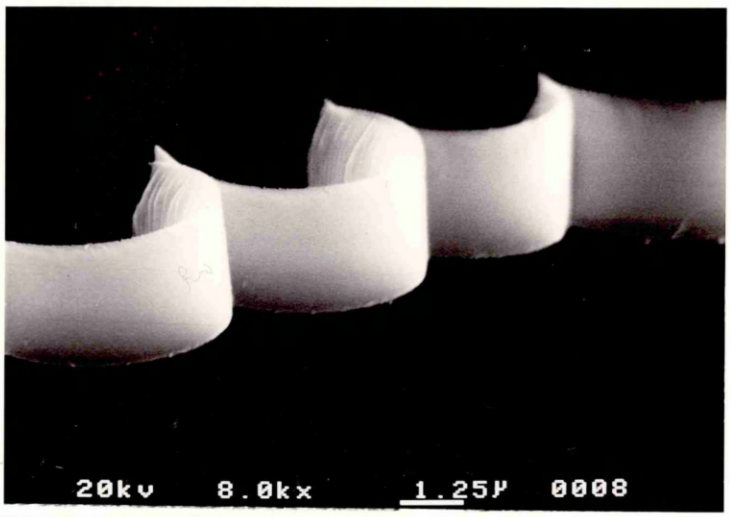

Fig. 3.16 "Arc chips" (or "loose-arc chips").

plastic (shearing) flow appeared to be the preferred material removal mechanism in the case of the scratching tool when the vertical load was below 50 grams. The chips generated by this shear-dominant mechanism, as shown in Fig. 3.16, were curved, continuous and with distinct shearing marks on the back side. This type of continuous-chip, called "arc chips" or "loose-arc chips", is generally produced when cutting ductile materials such as copper, mild steel and aluminium. The appearance of such arc chips and ductile grooves has demonstrated, the likelihood if not certainty, of the feasibility of machining glass in a manner similar to ductile metals.

On the other hand, the Vickers indenter with one diagonal aligned to the scribing direction, could also produce a well-defined, ductile groove on soda lime glass if the vertical loads were under 50 grams. However, no distinctive arc chips or curly swarf (produced by delamination material removal mechanism) were observed.

The long curly ribbons reported by Puttick et al (1989) were obtained using a Vickers indenter, but in their case one of the facets of the pyramid was used as the rake face.

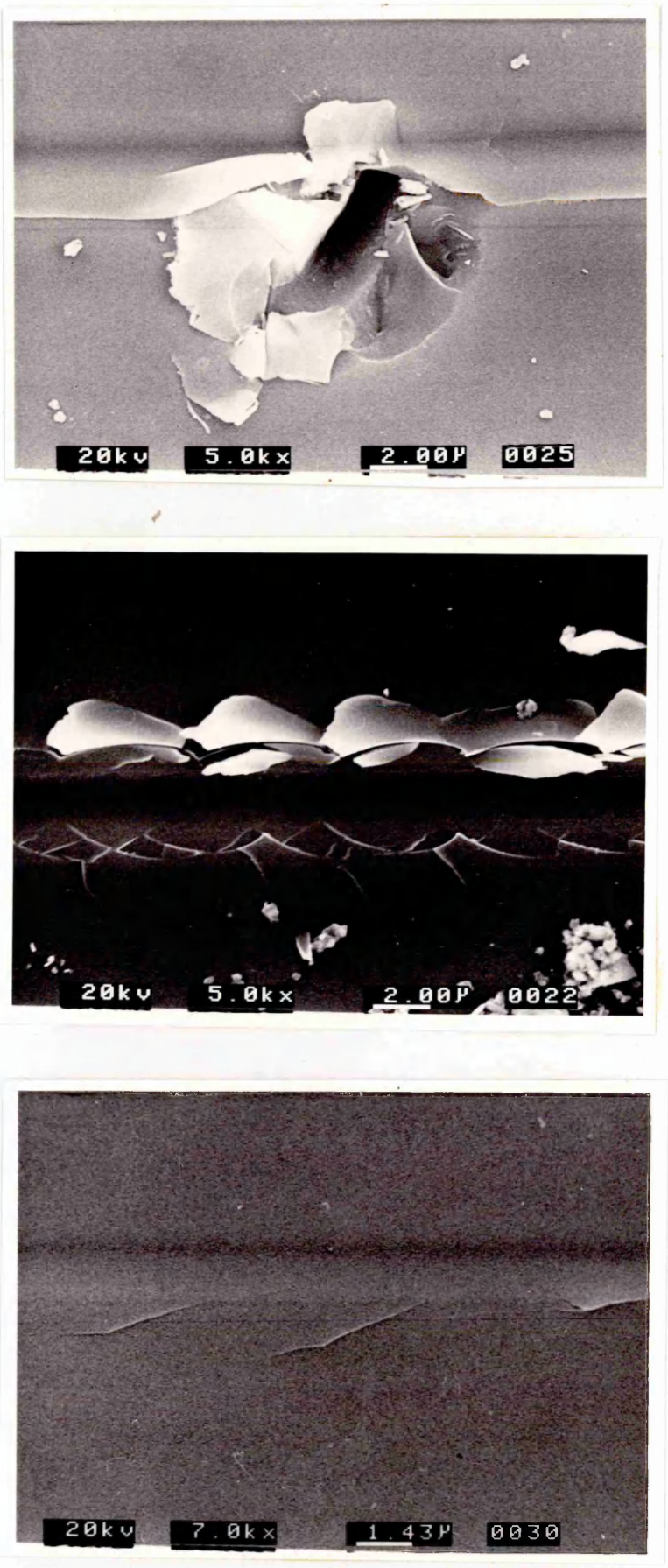

Fig. 3.17 "Some" of the crack patterns produced by scribing fused silica with the scratching tool at a speed of 0.2 mm/sec and 25 grams vertical load.

These various material removal mechanisms mentioned above indicated that the shape of the diamond tool appears to exert a strong influence on the material removal mechanism. The general trend appears to be that the tools with large negative rake angle (roof edge type, canoe-shaped type, Vickers pyramid indenter) tend to generate a compressive stress field in front of the tool which will suppress the shear flow (cutting) mechanism.

As discussed in section 2.4.2, fused silica is classified as "anomalous". The anomalous nature of fused silica is manifest in scribing fracture to an extent that the diversity of crack shapes make it very difficult to categorise. Fig. 3.17 shows "some" of the crack patterns produced by scribing fused silica with the scratching tool at a speed of 0.2 mm/sec and 25 grams vertical load. The scribing crack patterns on 'Zerodur' (a low-expansion polycrystalline glass-ceramics) were as diverse as on fused silica. The scribing (with scratching tool) fracture started when the normal load exceeded 10 grams on Zerodur and 15 grams on fused silica.

3.5.2 Ruling/Scribing experiments on Single Crystal Silicon Near (1 1 1) Surface

Ruling and scribing experiments on silicon single crystal were performed in the same way as on glasses. Like most of the silicon wafers used in the semiconductor industry, the silicon specimens (wafers) used in this experiment were oriented approximately 3 degrees from the (1 1 1) plane towards the (1 1 0) plane, with a reference edge ground parallel to $(\bar{1}\,1\,0)$. Three other {1 1 1} cleavage planes

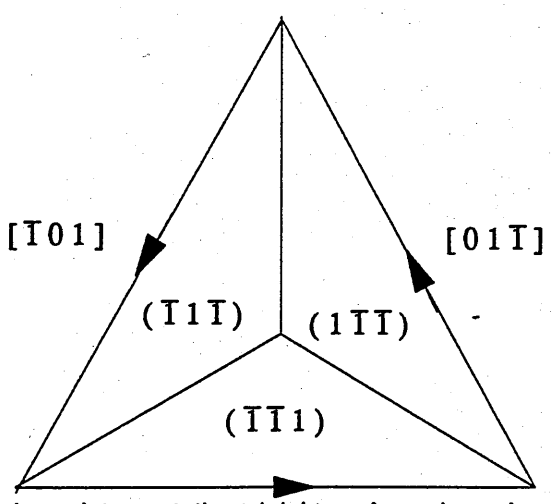

Fig. 3.18 Cleavage planes intersect the (1 1 1) surface planes in < 1 1 0 > directions.

($(1\bar{1}\bar{1})$, $(\bar{1}\bar{1}1)$, and $(\bar{1}1\bar{1})$) intersect the (1 1 1) surface plane in $<1\,1\,0>$ directions to form an inverted tetrahedron (as shown in Fig. 3.18).

Depending on the inherent crystal structure, the ruling and scribing directions have a strong influence on the plastic deformation and fracture characteristics of crystalline silicon. Puttick and Shahid (1977), and Puttick and Hosseini (1980) made scratches on silicon (1 1 1) surface using a Vickers diamond pyramid under constant load and used SEM and X-ray topography to examine the grooves. They found that $[1\,1\,\bar{2}]$ scratches produced cracks on both sides of the groove starting from the edge and growing roughly at 60^o to it (i.e. close to $[\bar{1}\,2\,\bar{1}]$ and $[2\,\bar{1}\,\bar{1}]$) while $[\bar{1}\,\bar{1}\,2]$ scratches nucleated cracks within the groove at a very small angle to its direction, growing outside it at an angle closer to 30^o than 60^o. This direction-dependent behaviour is known as the "sense effect".

Puttick and Hosseini (1980) also reported that scratches in $[\bar{1}\,1\,0]$ and $[1\,\bar{1}\,0]$ did not exhibit any sense effect in $[1\,1\,\bar{2}]$ and $[\bar{1}\,\bar{1}\,2]$, but possessed a marked asymmetry of fracture strongly tending to {1 1 0} cleavage.

The results of ruling with a roof-edge tool and of scribing with a Vickers diamond pyramid on the polished side of the silicon wafer in the $<1\,1\,0>$ and $<1\,1\,2>$ directions generally conformed with the results of Puttick and Hosseini (1980). However, there are a few details about the produced cracks that are worthy of note. These are:

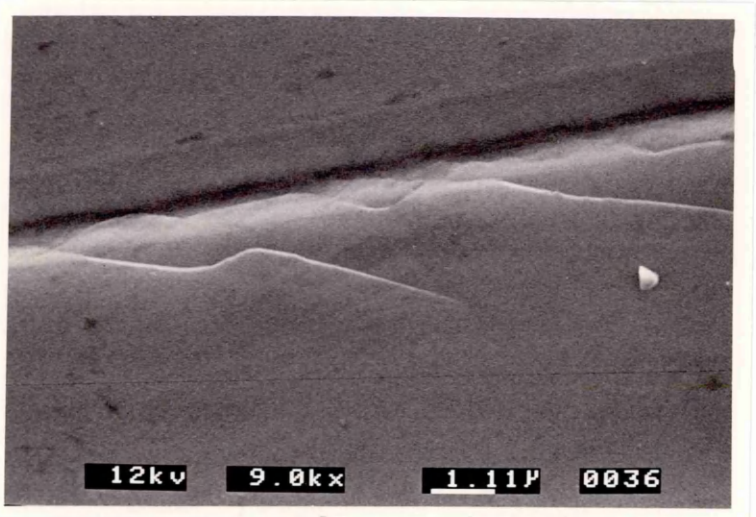

Fig. 3.19 Cracks formed around the groove rulied by a roof-edge diamond tool (S_1:37, S_2: 68, R_1: 45).

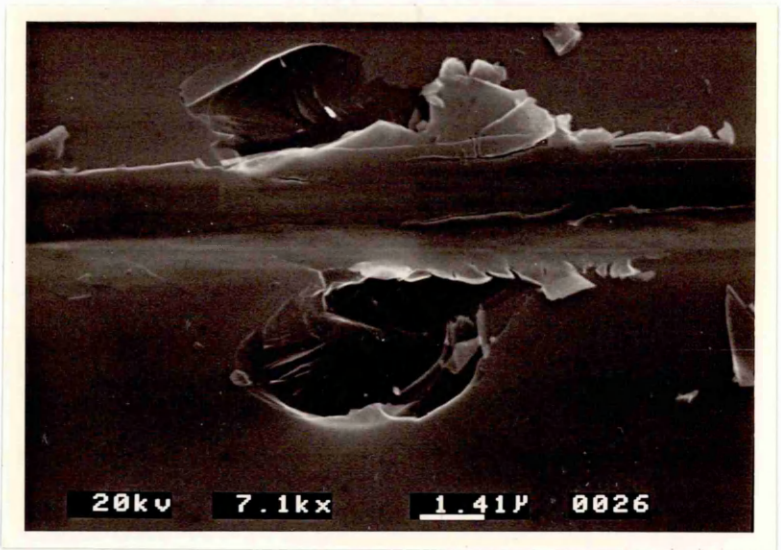

Fig. 3.20 Scanning electron micrograph of a groove ruled by a roof-edge diamond tool (S_1:37, S_2: 68, R_1: 45) with 15 g vertical load and in [$\bar{1}$ 1 0] direction (from left to right as in the figure), showing chip-cavities alone the groove. (mag.: 7100; tilt: 30°)

(1) cracks obtained by scribing with a Vickers diamond pyramid in all the directions tested generally, after an acute exit from the groove (30^o), tended to turn to an angle of 60^o (this conforms with the micrographs shown in the works of Shahid (1977), and Puttick and Hosseini (1980)).

(2) when ruling with a roof-edge diamond tool, the cracks (as shown in Fig. 3.19) often go in and out of the groove several times before finally branching away (also, inside the groove many fine irregular cracks can be seen on the groove face). Moreover, the compressive residual stress introduced by the scribing, manifested itself in that grooves with severe chipping on both sides of the groove and having median cracks at the bottom, as shown in Fig. 3.20, could still have groove faces preserved (see also Fig. 2.17, the effect of compressive residual stress on indentation).

Scribing with a scratching tool (see section 3.4.2), having smaller rake angle than either a Vickers pyramid or a roof-edge ruling tool, produced some crack patterns

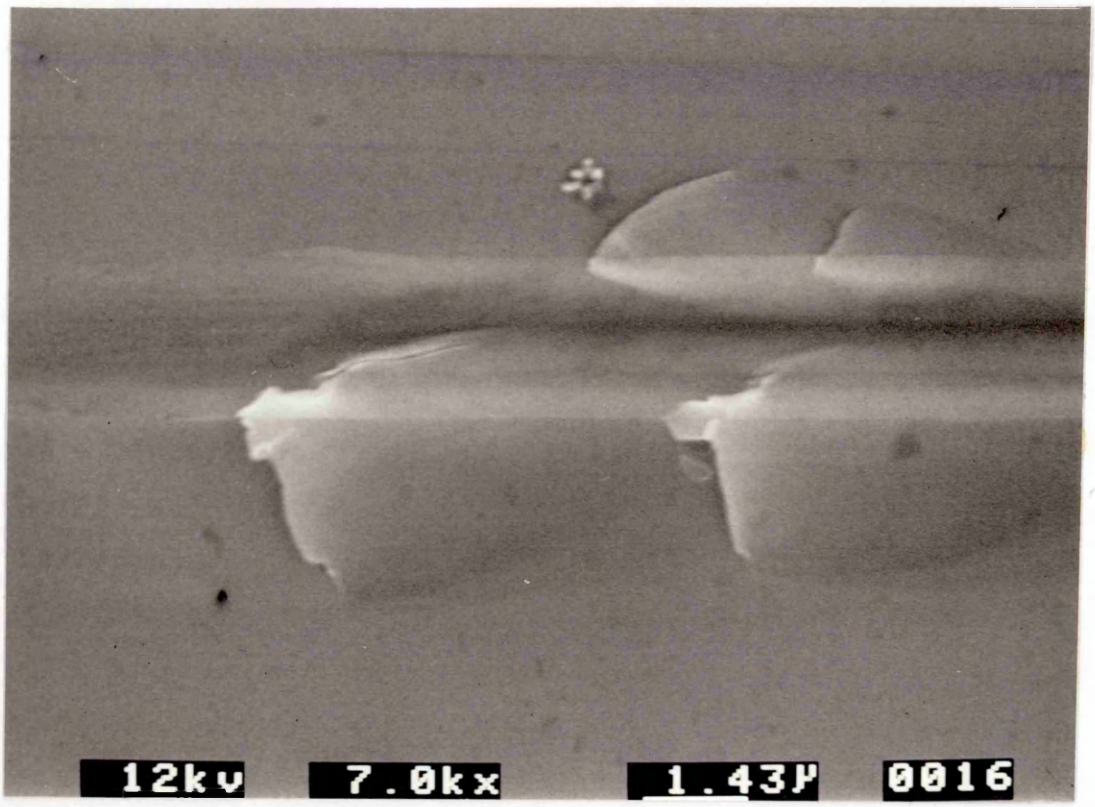

Fig. 3.21 Scanning electron micrograph of a [1 1 $\bar{2}$] (from right to left) scratch (load: 15 g; mag.: 7000).

quite different from the ones obtained by using high negative rake angle tools. At low loads (10 g, 15 g) the cracks appeared to initiate from the valley of the groove, propagate upward and outward, and then intersect the surface to leave a crack (intersection line) in the directions of $< 1\,1\,0 >$ and $< 1\,1\,2 >$. These cracks tend to be lifted from the surface at the emerging end due to the compressive residual stress along the groove after the passage of the tool (as shown in Fig. 3.21). If the residual stress is strong enough, the crack may cause chip-off and a scallop (conchoidal) shaped hole will then be formed. As the load was increased to 25 grams, the crack pattern appeared to change to the "chevron" type crack pattern.

The change of crack patterns with increasing load suggested that there might be a change in material removal mechanism. However, the stress field around the scribing tool and how the stresses interact with crystallographic angle and cleavage planes are still not well understood, and further studies are needed.

Fig. 3.22(a) and (b) show the relationship between normal loads and widths of grooves obtained by scribing in $< 1\,1\,0 >$ and $< 1\,1\,2 >$ directions respectively.

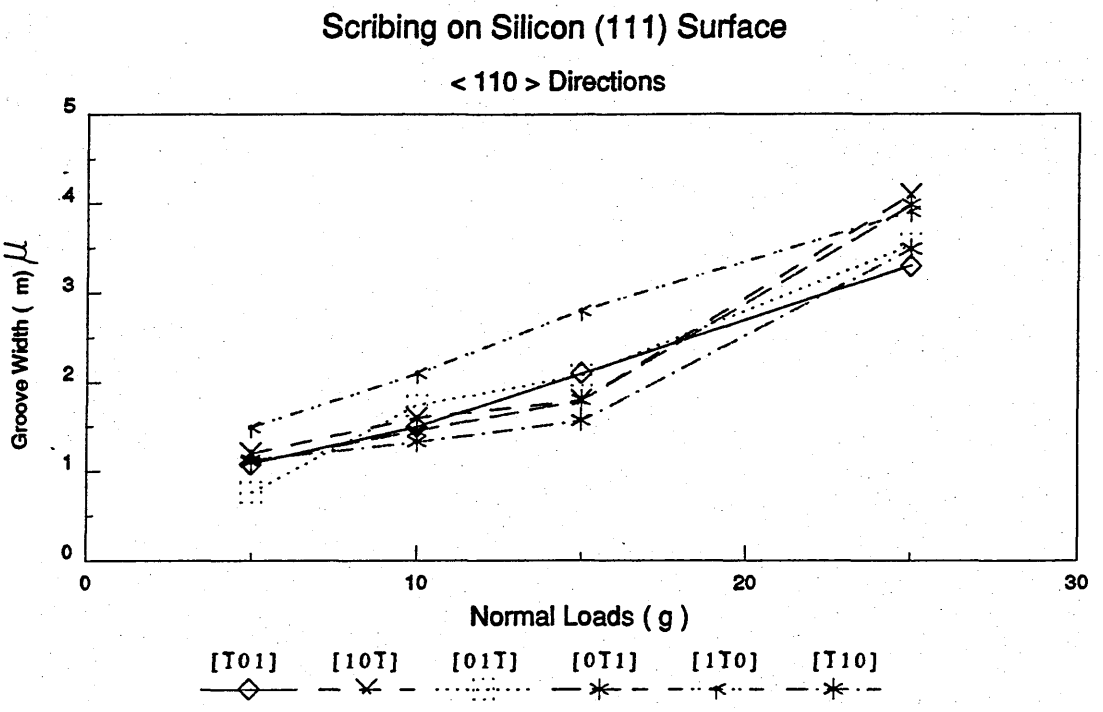

(a)

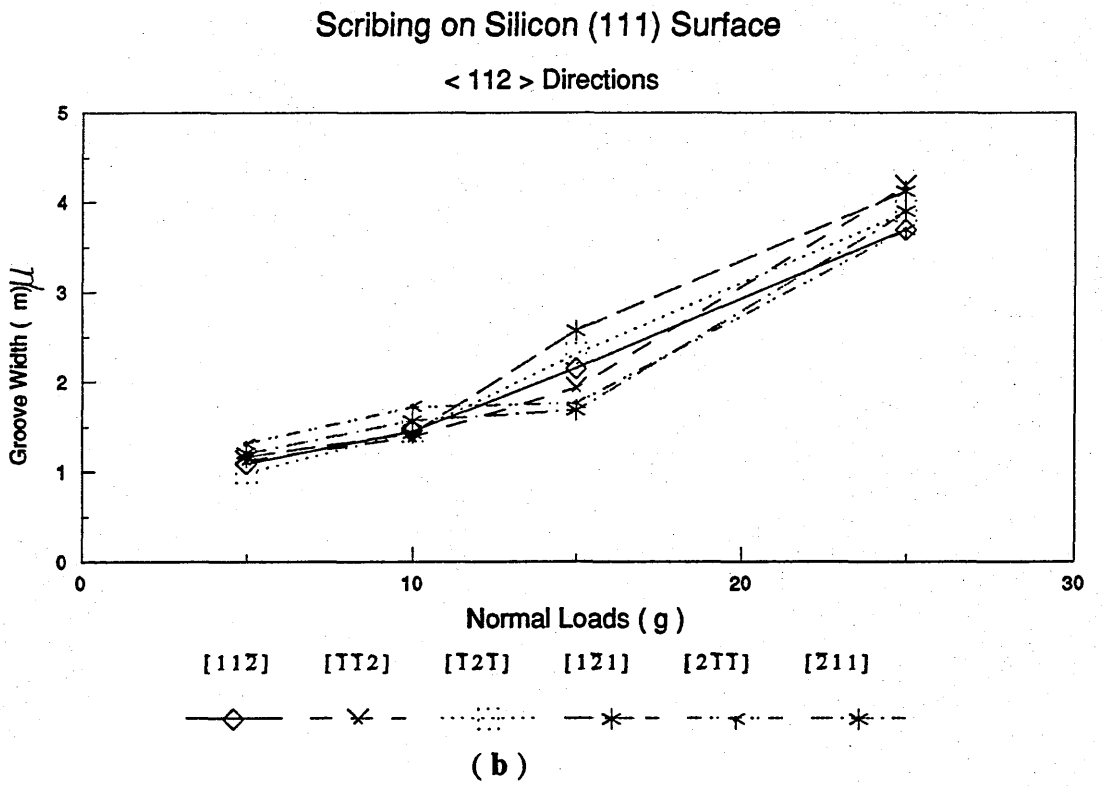

(b)

Fig. 3.22 Relationship between normal loads and widths of grooves obtained by scribing in (a) < 1 1 0 > and (b) < 1 1 2 > directions

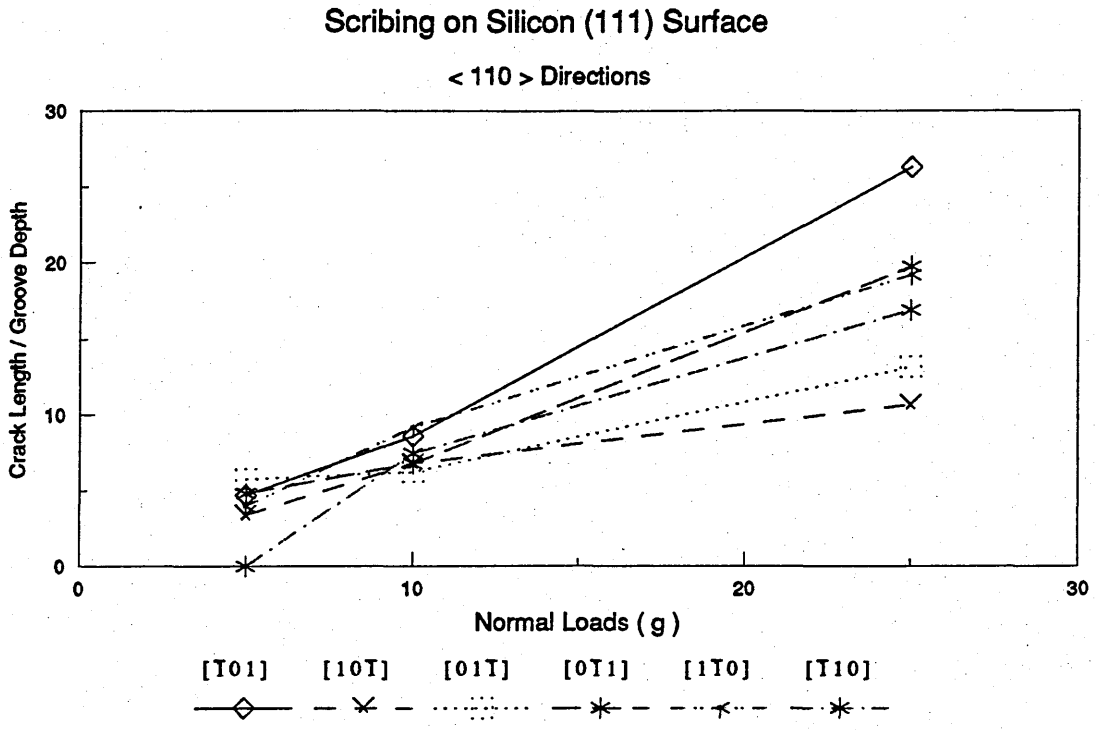

(a)

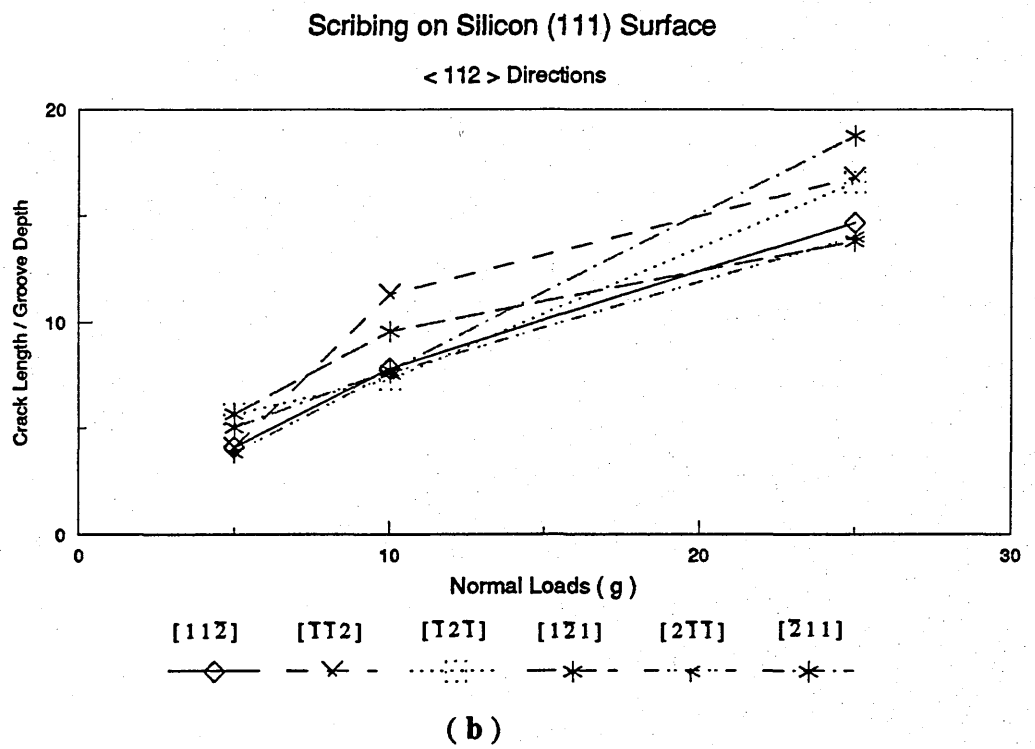

(b)

Fig. 3.23 Ratios of measured maximum crack length (worst case) to groove depth obtained in (a) < 1 1 0 > and (b) < 1 1 2 > scribing.

As can be seen in the plots, the width increased with load reasonably linearly with not much difference between these two direction groups.

In Fig. 3.23(a) and (b) the ratios of measured maximum crack length (worst case) to groove depth obtained in < 1 1 0 > and < 1 1 2 > scribing were plotted against related normal loads. Below 10 grams the ratios in the < 1 1 2 > directions were slightly larger than the ratios in the < 1 1 0 > directions. For the twelve directions scribed with a scratching tool and 5 grams vertical load, only the groove in ($\bar{1}$ 1 0) direction produced no visible crack.

Observations were also made seeking evidence of plastic flow and the possible reasons for its appearance by examining the ductile parts of the grooves. Shown in Fig. 3.24 is one of the "ductile" sections. As can be easily seen, the groove faces are very "lumpy" (with a lot of small lumps sticking out from the groove surface). Since all these small lumps have one end attached to the surface and have the loose end pointing in the opposite direction to that of scribing; this can only have happened after the tool had passed. Fig. 3.25(a) shows one section with "chips" scattered along

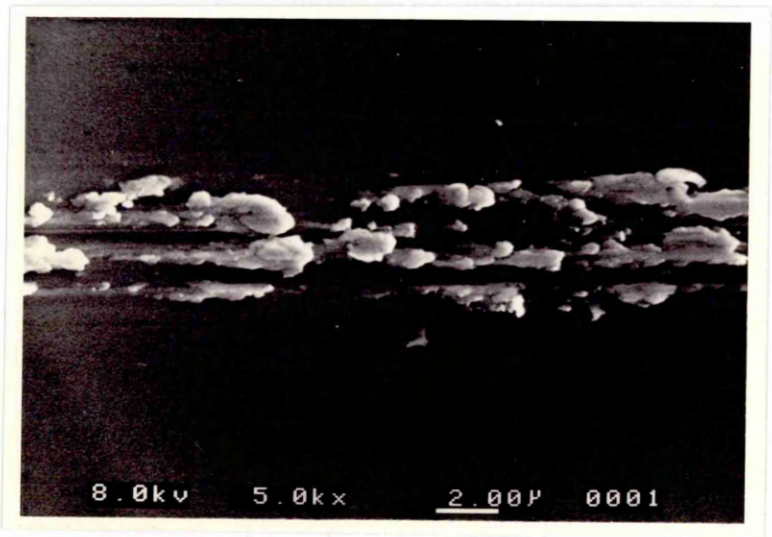

Fig. 3.24 Scanning electron micrograph of a [$\bar{1}$ 1 0] scratch (from right to left) showing the "lumpy" feature of the groove face (load: 25 g, mag.: 5000).

both sides of the groove. Fig. 3.25(b) shows the detail of one of these chips on which the groove image can still be seen.

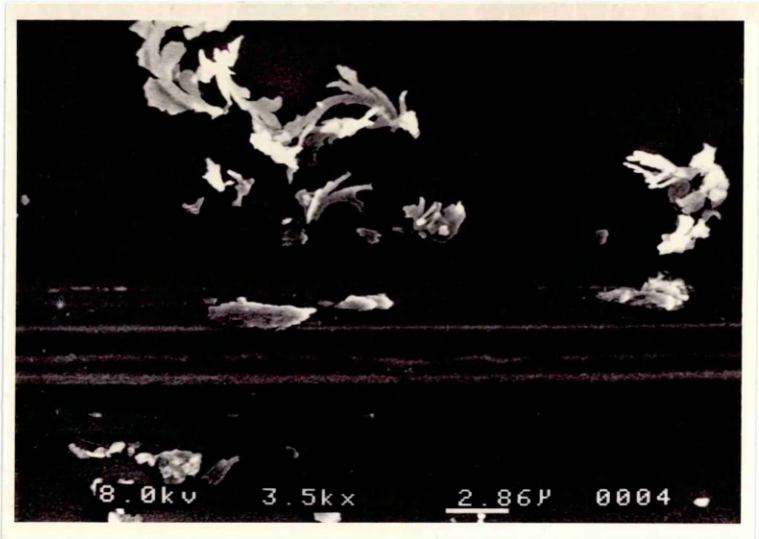

(a)

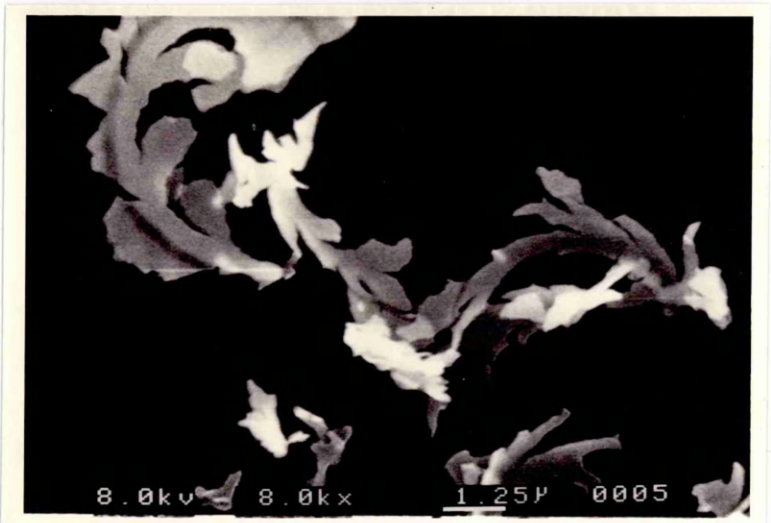

(b)

Fig. 3.25 Scanning electron micrograph of a [$\bar{1}$ 1 0] scratch (from right to left, load 25 g) showing (a) general view of the groove and produced chips (mag. 3500) (b) detail of the chips (mag.: 8000).

Chapter 4

Material Removal Mechanisms in Machining

4.1 Introduction: the Need for Machining of Brittle Materials

When subjected to stress, glasses, ceramic materials and certain important hard crystals like silicon and gallium-arsenide, all fracture before appreciable plastic deformation takes place; this is (classically) said to be evidence of 'brittle' characteristics.

Although such "brittle" effects make the machining of these materials extremely difficult, the demand for precision parts made from them has risen (and continues to rise) at a very fast rate primarily because of other superior physical, mechanical, optical or electronic properties. Advances in manufacturing processes are therefore important to the economic production of these parts.

For some years, it has been possible to diamond-turn certain *traditionally-machinable* metals such as electroless nickel, copper, and aluminium alloy to mirror-like surface finishes, with figure tolerances down to a few tens of nanometres, and with surface roughness of under 10 nm rms. However, optical system designers often prefer to use glass or glass-ceramic materials for their dimensional stability in the case of mirrors; for lenses in the visible spectrum, there are few materials superior to glasses in respect of transmission characteristics. These materials are not so well suited to diamond turning. At normal engineering machine tolerances (several micrometres) diamond-turning was thought to be a "crushing" process (Bryan and Carter 1985) when applied to brittle materials such as glass, producing a surface characterised by conchoidal fractures and a damage-layer up to 50-100 μm deep. However it has been found by optical glass-workers and materials' scientists that glasses and other brittle materials do not always manifest "brittle fracture" when being machined with the finest cuts ($< 1\ \mu m$). This is also apparent in indentation tests at loads of the order of grams and at tip-depths of the order of micrometers (see sections 2.4.2 and 2.4.3). Furthermore, when the indenter is moved laterally at constant (dead) loads, it has been observed that, rather than

brittle chipping, material piled up either side of the groove (Taylor 1949, Marsh 1964, Ishida and Ogawa 1962). Such phenomena have also been found in ruling (Chao and Gee 1989), single point diamond turning (Puttick et al 1989) and grinding (Bifano et al 1988).

Based on such observations, it is apparent that for cut depths below some critical value together with matched machining conditions (tool-shape, cutting speed, cross-feed, coolant), these (macroscopically) brittle materials can be machined in a restricted *ductile-mode* in which material is removed by plastic deformation processes rather than brittle fracture processes.

As to whether this might be a machining process offering potential manufacturing utility is yet to be answered. However, it is possible to affirm that a ductile machining process, analogous to that used on metals and capable of yielding an ultra-fine surface finish on silicate glass, quartz and other brittle materials would present certain major advantages as a manufacturing process. It would open up the possibility for producing aspherical lenses in an economic and deterministic (on profile) manner, thus reducing cost and weight of multi-element optical components and it could also replace the tedious, time consuming and indeterministic free-abrasive grinding and polishing operations traditionally used to produce spherical and plane surfaces in glass.

In order to achieve ductile machining, and thereby to enable all the above mentioned potential prospects, a fundamental understanding of the underlying plastic material "removal" mechanism is vital. However, due to the complexity of the cutting process and the difficulty of accessing the machine-performance which will enable a tool-depth of less than 1 μm to be held, much previous work has been based upon the assumption that previous technology could be extended, relying upon case study, trial-and-error to solve the problems encountered in machining. As a result, many publications in this area have put emphasis on the machined surface and related cutting conditions but only few of them have discussed the related material deformation mechanisms involved in obtaining the finished surface. As pointed out by Shaw (1984), a great many cases must be considered before a sufficient number of examples have been presented to enable all common situations to be covered and this requires not inconsiderable effort and resource.

Several "relatively" simple mechanisms, supported by scanning electron and optical micrographs, will be discussed in this chapter.

4.2 Material Removal Mechanisms

4.2.1 Introduction

Cutting brittle materials by single-point diamond turning, though it is not as complex as multi-point diamond grinding, is by no means a simple process to be described by a single material removal mechanism. Several *relatively* simple mechanisms, supported by scanning electronic and optical micrographs, are discussed in the following sections. Each mechanism has its favourable operating conditions under which it will become the dominant and therefore appropriate mechanism. But, in general, no process can be described by only one of these mechanisms and it is rather frequent to see several mechanisms co-existing on the same specimen.

4.2.2 'Ploughing "(Plastic Flow)

In the *ploughing mode*, material is plastically pushed aside by the tool rake face and a groove (furrow) mark is left behind it. Where there is no or very little evident swarf produced in the *ploughing* process, the "removed" materials may be accommodated either by the surrounding bulk materials via plastic flow or by the densification (compaction) process in the vicinity of the groove. In some materials such as soda-lime glass, a small amount of pile-up material provides evidence for plastic flow. In silicon, a very high dislocation density area is found around indentations and scratched grooves (Puttick, Shahid and Hosseini 1979, Puttick and Hosseini 1980) showing traces of plastic flow.

This material removal mechanism, as learned from scribing and ruling experiments, is normally obtained when the tool penetration depth is very small. Since the cutting depth has to be kept low to maintain the *ploughing* process, this material mechanism is highly inefficient.

4.2.3 "Cutting" Mechanism

The word *cutting* is used here to describe the shearing of materials from the bulk to form a significantly continuous chip generated by sliding away from the bulk along the rake face of the tool. It is the very effective cutting mechanism for ductile materials familiar to those who have used machine-tools.

In ductile metal-cutting, it is well-established that there is a shear plane passing through a point of stress concentration present in the metal being cut. As bulk metal material approaches this shear plane, it undergoes a substantial level of simple shearing as it crosses a thin shear zone (Shaw 1984). The chip then proceeds up the face of the tool and a rough surface develops on the back of the chip as the result of inhomogeneous strain involved in the process. To explain these observations, an ideal cutting process model, called the *card model*, was suggested by Piispanen (1969) which depicted the material cut as a deck of cards inclined to the free surface at an angle corresponding to the shear angle. Although it is an over-simplification not explaining chip curl or predicting shear angle and contact length, it does model the chip-forming process.

Another well known and widely-used model is that of *orthogonal cutting model* which assumes that the material removal process in cutting can be simplified to a two dimensional problem. In the *orthogonal* process, material deforms homogeneously under shear stress and a continuous chip is produced with no built-up edge (Shaw 1984). Since *orthogonal cutting* represents only a two dimensional cutting process, it has eliminated many parameters and eased the theoretical analysis of the complicated three dimensional problem. On the other hand, as a result of these assumptions, the *orthogonal cutting model* can only be used to throw some light on the problem. To tackle the real cutting process, a lot of experiments and careful observations have to be carried out to fill the gap between the theoretical model and observations.

The assumptions on which the *orthogonal model* is based require the cutting edge to be a straight line extending perpendicular to the direction of motion, the width of the tool is greater than that of the workpiece, and the chip does not flow to either side (plane strain) (Shaw 1984). In the case of experiments on metal cutting, to meet

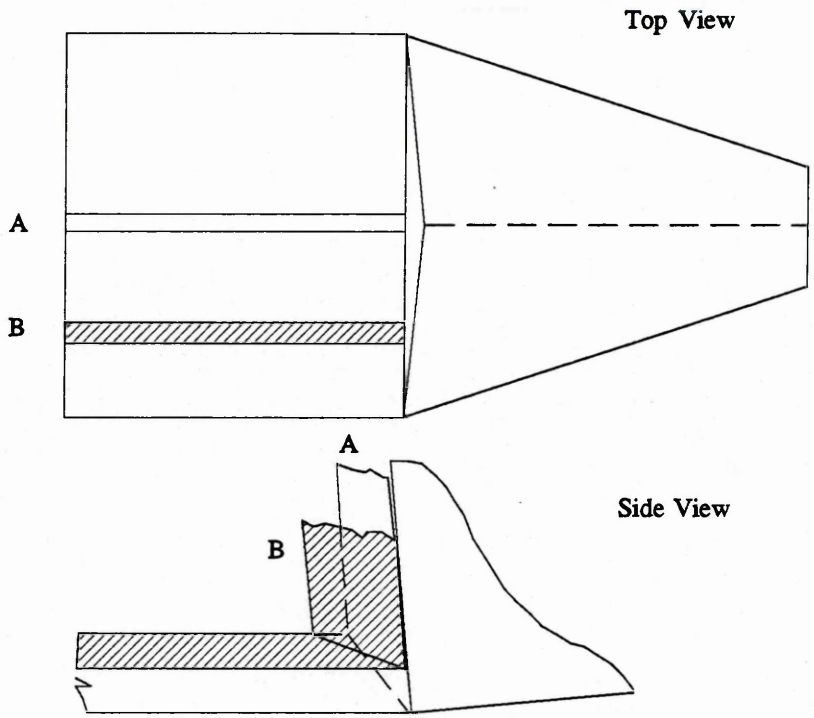

Fig. 4.1 Simplified (two dimensional) cutting model ("*parallel thin plates model*").

these requirements is relatively easy because of the scale of the operation. However, at sub-micrometer cutting depths and complementary small tool dimensions the task assumes high difficulty.

No attempt has been made in this study to design a special tool just to satisfy the assumptions of the *orthogonal cutting model*; instead, a normal diamond tool has been used. But, to adopt the well established theoretical analysis for the orthogonal cutting model, the three dimensional cutting process has been simplified to a two dimensional process cutting multiple parallel thin slices (as if the tool were cutting a deck of thin plates from their edges and is called here as "*parallel thin plates model* ", as shown in Fig. 4.1). This simplified approach, like *orthogonal cutting* itself, serves only as an approximation to the complex cutting case.

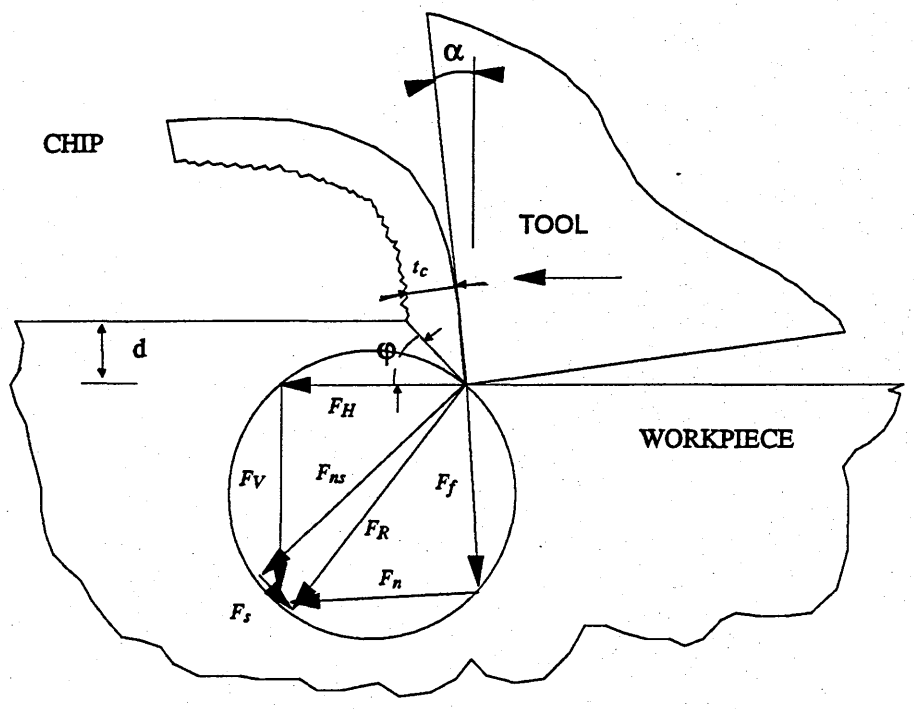

Fig. 4.2 Force diagram for orthogonal cutting.

Based on Piispanen's *card model* (1937) and the *orthogonal cutting model*, Ernst and Merchant (1941), and Merchant (1945) suggested a so-called *shear-angle solution* in which the shear angle φ would take up a value so as to minimise the work done in cutting. Fig. 4.2 shows the force diagram for *orthogonal cutting*; with the aid of Fig. 4.2, the shear angle may be obtained as

$$\tan \varphi = \frac{\gamma \cos \alpha}{1 - \gamma \sin \alpha} \qquad (4.1)$$

where $\gamma = \frac{d}{t_c} =$ cutting ratio

d is the undeformed chip thickness (depth of cut), t_c is the chip thickness, and α is the rake angle.

For a fixed cutting depth, d, and rake angle α, the larger the shear angle φ the longer the chip produced from a unit length of cut. Since under the present cutting mechanism the chip length can not exceed the length of cut, the maximum shear angle is obtained by the bisecting the included angle between the rake face of the tool and the surface to be machined (thus, chip length is equal to the length of cut).

The shear stress, τ, and normal stress, σ on the shear plane can be given as

$$\tau = \frac{F_s}{A_s} = \frac{(F_H \cos\varphi - F_V \sin\varphi)\ \sin\varphi}{b\,d} \qquad (4.2)$$

$$\sigma = \frac{F_{ns}}{A_s} = \frac{(F_H \sin\varphi + F_V \cos\varphi)\ \sin\varphi}{b\,d} \qquad (4.3)$$

where F_s, F_{ns} are the shear and normal force on the shear plane respectively, and b is the width of cut.

Shear (plastic) flow starts when the shear stress τ reaches the critical value. However, this critical shear stress is generally a function of temperature, strain rate and hydrostatic pressure and the detail of this function is not well understood.

Quick-stopping, one of the techniques most commonly employed for study of chip formation in metal cutting, was used in this study to identify this mechanism. As can be seen in Fig. 3.16, those chips shown are curved, continuous and with distinct shearing marks on the back side. This type of continuous-chip, called "arc chips" or "loose-arc chips", is generally produced when cutting ductile materials such as copper, mild steel and aluminium. The chips shown in Fig. 4.3(a) and Fig. 4.3(b), have been produced by cutting soda-lime glass and Zerodur, and resemble the continuous chips obtained in cutting ductile metals at larger scales.

Fig. 4.4 shows clearly that after the curved chip is removed from the end of the groove, distinct shearing marks are left on the shear plane. A simplified model of a typical groove is shown in Fig. 4.5 (a). Using the stop (retreat) point of the tool as a reference point the groove can be divided into the part which tool has moved past and the part ahead of the tool. The former part of the groove has approximately uniform width while the later part, the acting shear plane before the tool stopped, has widths varying from maximum to zero (Fig. 4.4 is one of these shear planes obtained at the end of grooves).

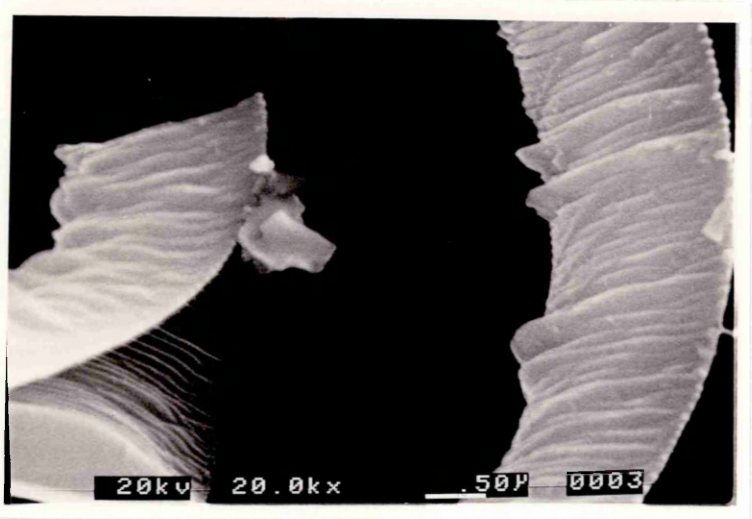

(a)

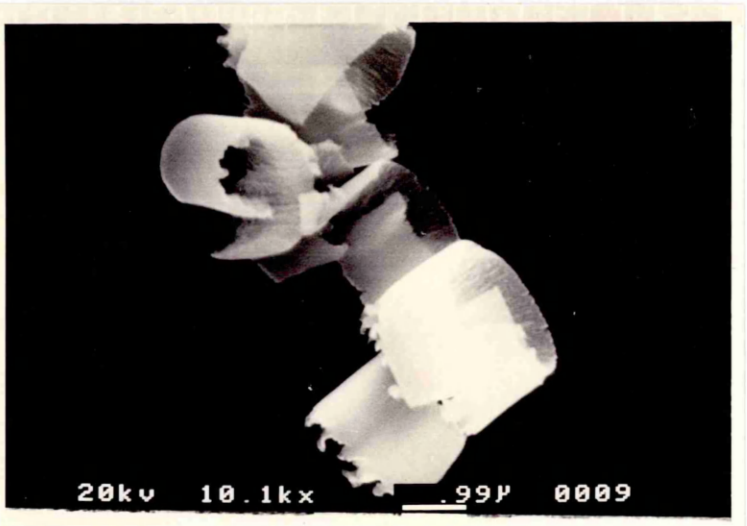

(b)

Fig. 4.3 Scanning electron micrographs of the chips produced by cutting (a) soda-lime glass and (b) Zerodur showing the resemblance to the continuous chips obtained in cutting ductile metals .

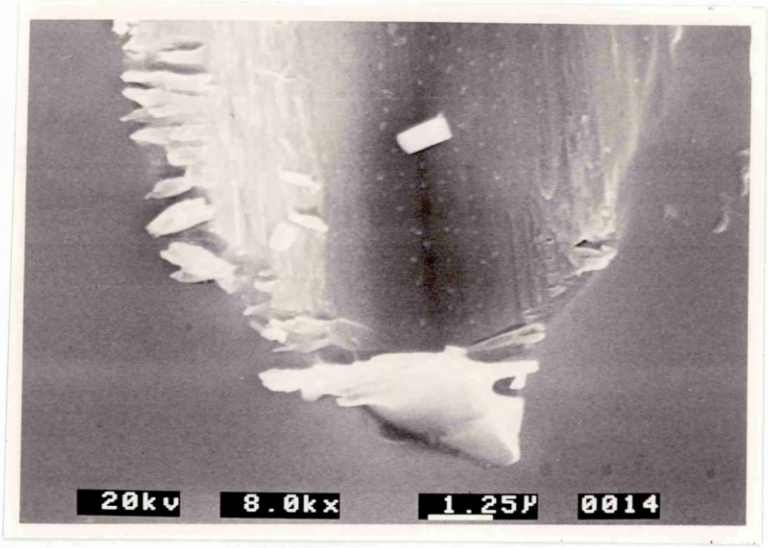

Fig. 4.4 Shearing marks left on the surface of the groove.

Since the shapes of the tools used to cut these grooves are well defined, the ideal correlation between cut-depth, width and tool geometry can be used to estimate, within reasonable agreement, the real groove profile. By examining in detail the shearing marks and measuring the change of width at the end of the groove, the finishing position of the tool and thus the starting point of the shear (slip) plane and the shear angle (φ) can be evaluated.

The scratching diamond tool (see section 3.4.2) was used in this study, having a V-shaped rake face, the obtained groove had a range of cutting depths. By using the "*parallel thin plates model* " outlined earlier in this section, the shear angle can be correlated to the cut depth of each plate (as shown in Fig. 4.5(a)).

The measured shear angles points are plotted against cut depths as shown in Fig. 4.5(b). The shear angle and cut-depth was approximately correlated by applying power curve fitting to these data points to obtain the solid line trace in Fig. 4.5(b) of the form:

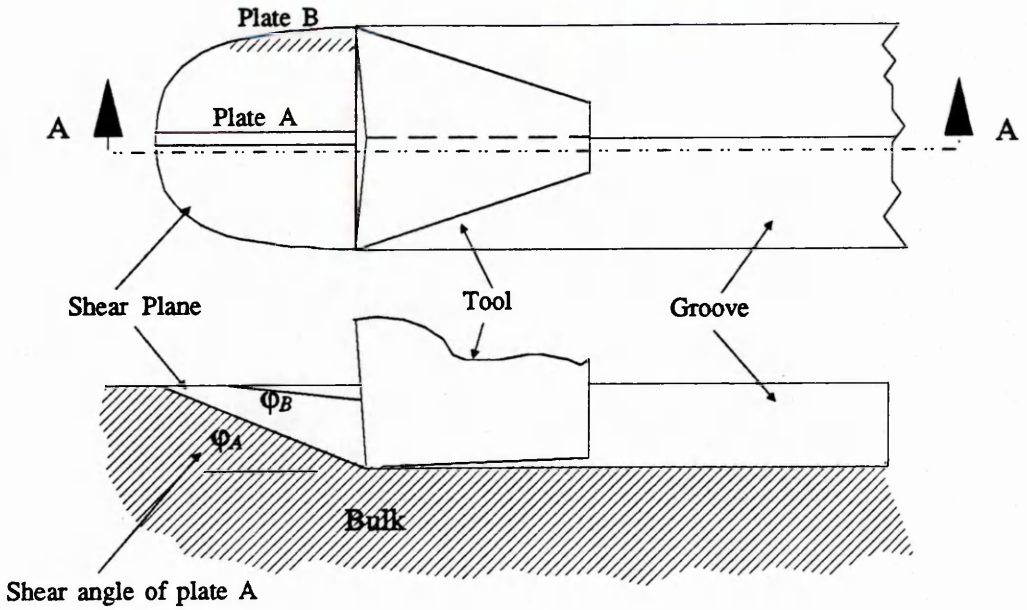

(a)

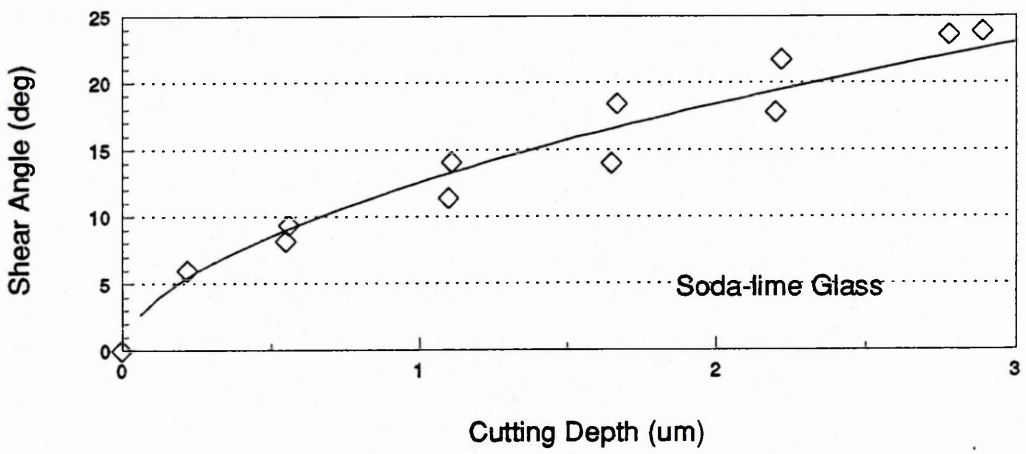

(b)

Fig. 4.5 (a) Showing a simplified model of the groove and shear plane formed by the scratching process (b) Plot of shear angle against the cutting depth (soda-lime glass). The solid line trace was obtained by applying power curve fitting to the data points.

$$\varphi \approx C_1 d^n \qquad (4.4)$$

where $C_1 \approx 12.57$ and $n \approx 0.55$ for soda lime glass.

The shear-angle associated with the centre plate is larger than the corresponding shear angle of the side plate. (The shear angle as well as cutting depth decreased for subsequent plates from centre towards the sides of the groove). If it was the case that the thin plates were independent with no influence (constraining forces) from or to the neighbouring plates, the chip produced from the centre plate would have longer length than the one produced from a side plate. However, in practice, the chip does not consist of separate plates. This means that, in order to keep the chip in one piece, part of the chip (centre) is under compressive stress whilst other parts (edges) are under tensile stress, the magnitude of these stresses depending on the cutting depth. When the cutting depth is small, the tensile stresses are not strong enough to initiate cracks so the chip edges present only small irregularity (as shown in Fig. 4.6(a)). Upon increasing the cutting depth, cracks start to propagate from both edges towards centre of the chip to form the "*centipede*" type chips (as shown in Fig. 4.6(b)). If the tensile stress is strong enough, cracks developed from both edges may meet at the centre to form a partial ring crack (as shown in Fig. 4.6(c)). In some cases, the edge detaches from the main chip body to form a long and thin ribbon (as shown in Fig. 4.7).

In general, for cutting brittle material, the material removal rate of this mechanism is much bigger than the *ploughing* mechanism. It is found in this study the *cutting* mechanism can be obtained when cutting with a near-zero (small positive or small negative) rake angle tool. A large negative rake angle, and resulting large compressive stress ahead of the tool, may suppress this type of material removal mechanism. For given cutting conditions, there is a critical negative rake angle for the tool below which the *cutting* mechanism (therefore chips) dominant will be replaced by a dominating *ploughing* mechanism. Sedricks and Mulheam (1964) have studied this transition of material removal mechanism on a range of ductile metals by scratching the materials with a pyramidal tool, and the critical negative rake angles they obtained were: copper (-45^o), lead (-60^o), nickel (-70^o), and aluminium (-85^o).

(a)

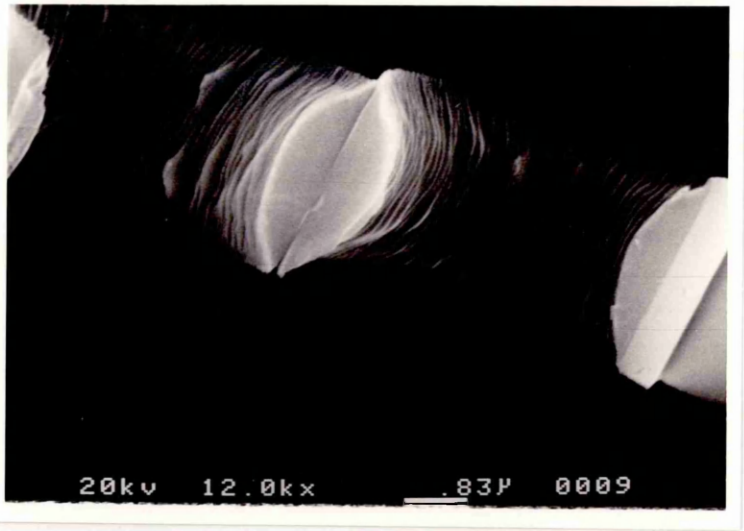

(b)

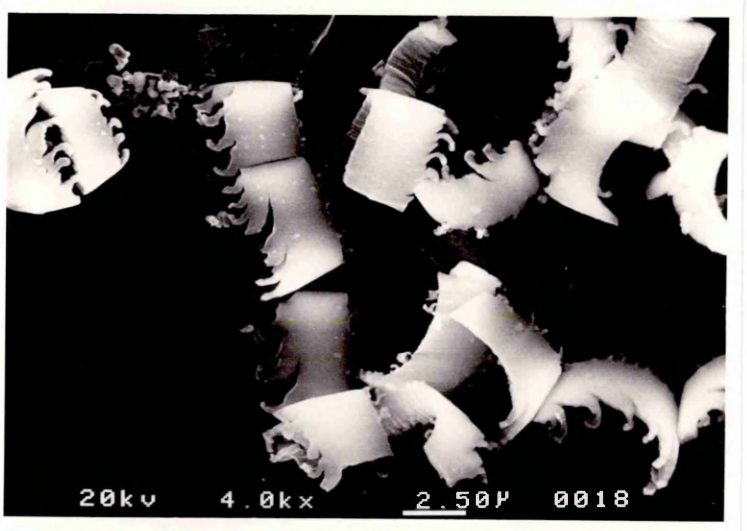

(c)

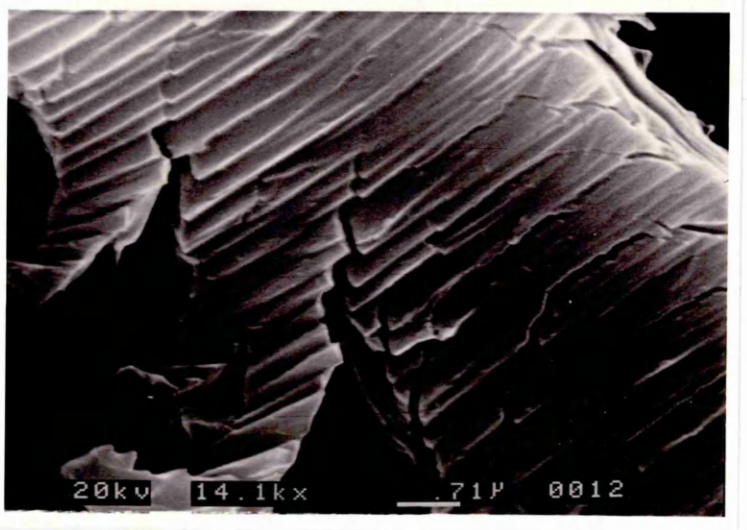

Fig. 4.6 (a) small cutting depth: the tensile stresses are not strong enough to initiate cracks so the chip edges present only small irregularity. (b) increasing the cutting depth, cracks start to propagate from both edges towards centre of the chip to form the "*centipede*" type chips. (c) If the tensile stress is strong enough, cracks developed from both edges may meet at the centre to form a partial ring crack.

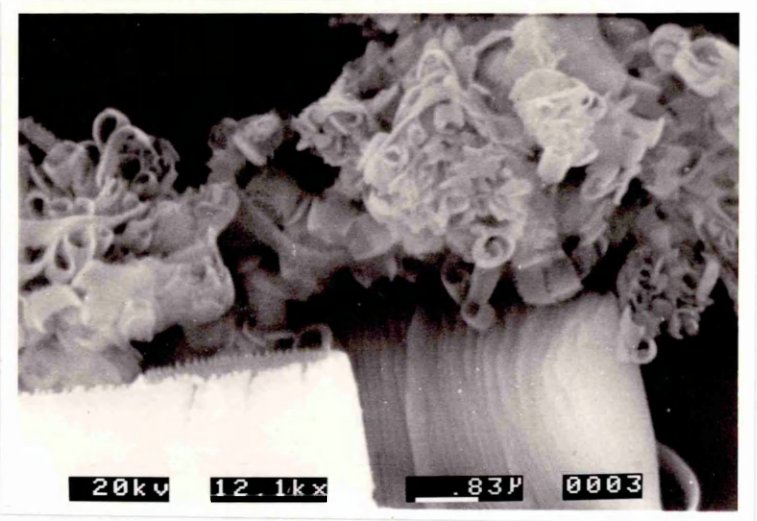

Fig. 4.7 Edge detaches from the main chip body to form a long and thin ribbon.

Another possible reason for the small rake angle being more favourable for the *cutting* mechanism (shearing process) to be dominant, is that large negative angles may make the shear angle impossibly small. If, for example, a Vickers indenter is used as cutting tool with one of its planes facing the cutting direction, the largest shear angle which can be reached is only 11 degrees arc (as a Vickers indenter has a - 68° arc rake angle).

4.2.4 Delamination

Delamination is a process whereby ribbon-like swarf detaches from the workpiece bulk after the passage of the tool, and was proposed by Puttick et al (1989) as a ductile mode material removal mechanism. The *delamination* process is caused by the longitudinal compressive residual stress introduced by the tool immediately following its passage.

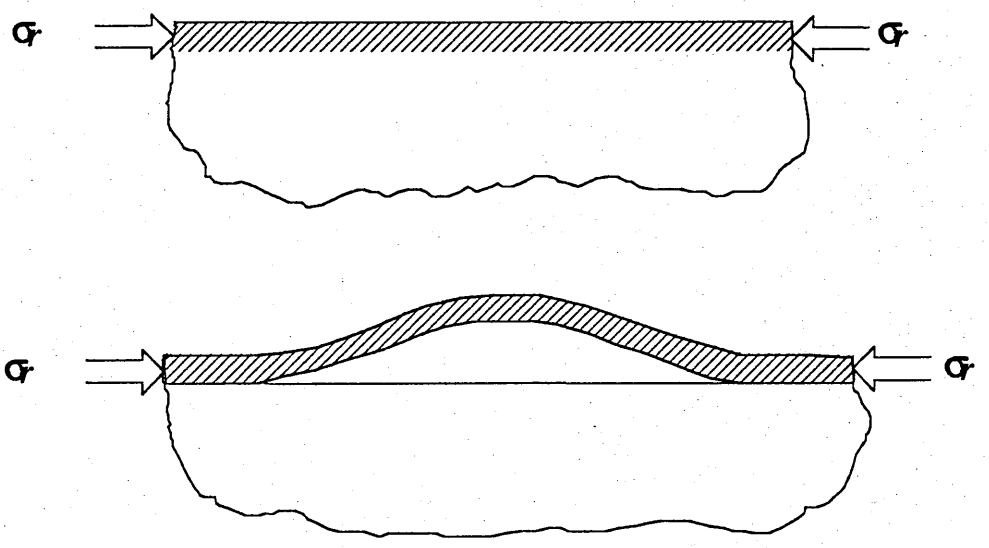

Fig. 4.8 Detachment of the swarf occurred by shearing fracture along a path within the stressed region parallel to the machined surface, followed by the bending or buckling caused by the compressive residual stresses on the end of the free segment. (After Puttick et al 1989)

Puttick et al (1989) observed this mechanism in machining soda-lime glass and fused silica (Spectrosil). They proposed that the detachment of the swarf occurred by shearing fracture along a path within the stressed region parallel to the machined surface, followed by bending or buckling caused by the compressive residual stresses on the end of the free segment (as shown in Fig. 4.8). As a consequence, "*hoops*" of swarf may be formed and extended to form a long ribbon which, in some cases, can be several millimetres long.

Puttick and his coworkers noticed similarities between the *delamination* process and the slitting and buckling of a slender beam by swelling due to moisture absorption. They adopted the solution for the buckling beam given by Mai (1977), as a simple model for solving the criterion of the shear *delamination* problem. By assuming that a thin layer below the machined surface is in a state of uniform residual compressive stress, σ_r, the strain energy Λ, contained in a strained volume

of length a, width w and depth B, due to compression is equal to $\frac{\sigma_r^2 B w a}{2E}$. Thus, the shear *delamination* may be expected to occur when the fracture toughness is shear $R_{II} = -\frac{d\Lambda}{dA} = \frac{\sigma_r^2 B}{2E}$. It follows that the critical value of the depth B_c is

$$B_c \approx \frac{2E R_{II}}{\sigma_r^2} \qquad (4.5)$$

Since the precise magnitude of σ_r is unknown, Puttick et al (1989) suggested that it should be of the same order as the maximum residual stress introduced by successive overlapping indentations. They found that, below the critical depth B_c for chipping, a regime of stable peeling occurs with a lower depth limit

$$B'_c = \frac{2E R_{II}}{\sigma_y^2} \approx \frac{1}{3} B_c . \qquad (4.6)$$

In general, the observed *delamination* process in this study can be categorised into two types, namely *side-delamination* and *centre-delamination*. In case of *side-delamination*, as shown in Fig. 3.14, the material is forced to "pile-up" alongside the groove due to plastic-flow and then to detach itself from the bulk. In the case of *centre-delamination*, a layer of stressed material peels off from the surface after the tool has passed and, as can be seen in Fig. 4.9(a), the pattern of the groove is preserved on the curved swarf. Since different parts of the groove are subject to various degrees of compressive residual stress and the buckling is accompanied by large tensile stresses in the outer layers of the ribbon, the inhomogeneous stress field can cause the detached ribbon to split into several secondary ribbons curved in different directions according to the local stress field (as shown in Fig. 4.9(b)).

From the dimensional control point of view, it is not favourable to remove material by a *central-delamination* mechanism due to its lacking control of the thickness of the detached ribbon and thence of the cutting depth.

(a)

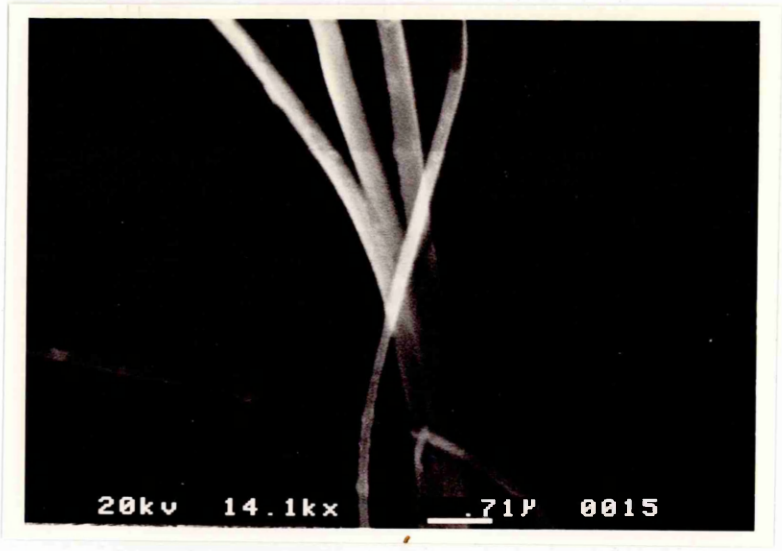

(b)

Fig. 4.9 *Centre-delamination*, (a) a layer of stressed material peels off from the surface after the tool passed (b) the inhomogeneous stress field can cause the detached ribbon to split into several secondary ribbons curved in different directions according to the local stress field.

4.2.5 Elastic Fracture

By increasing the normal load on a tool or indenter, as discussed in section 2.3.1, sub-surface lateral cracking might extend to the surface during unloading, causing part of material to be chipped off. These lateral cracks, as suggested by Hagans and Swain et al (1979), are nucleated by shear deformation and driven by residual stress after the load is removed.

In the case of ruling and scribing, the tensile stress introduced by the friction force between tool and workpiece can cause the sub-surface lateral cracks to propagate along the cutting direction. As a result, it has also been found in ruling and scribing experiments on brittle materials that large chips (debris), over ten times larger than the groove size in some cases, could be produced by brittle fracture (as shown in Fig. 4.10).

It has been suggested by Lawn and Wilshaw (1975a) that this mechanism is responsible for material removal during machining processes such as grit blasting or grinding.

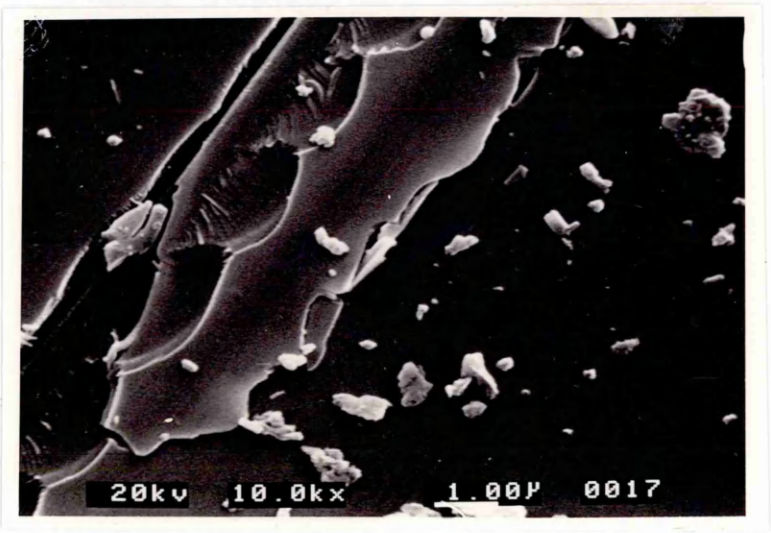

Fig. 4.10 Large chips (debris) produced by brittle fracture.

Owing to the uncertainty of the crack directions and their extent, this material removal mechanism cannot offer the required dimension be accuracy in precision machining, although it can remove materials very effectively. Besides, the surface generated by using this mechanism is normally very rough and large scale sub-surface cracks (lateral and median cracks) may penetrate deep into the material bulk making subsequent machining extremely difficult.

4.3 Ductile-Brittle Transition: Machining Implications

It is true that fracture can happen in machining ductile metals if the cutting depth is very large, it is also the case that normally brittle materials can be deformed in a ductile mode if the scale of deformation is small enough, as experienced in indentation (chapter 2) and ruling/scribing (chapter 3) experiments. These results suggest that the ductile and brittle mode of deformation can happen in the same material and that transition between them can be obtained by changing the scale or the rate of operation. As a result, the traditional way of classifying materials as brittle or ductile by testing the performance of laboratory test-pieces to given standards of geometry and speeds has to be treated with some uncertainty.

Based on the magnitude of the strain induced by the applied load, $\varepsilon_{applied}$, the yield strain, ε_y, the specific work required for cracking, W_r, and the energy rate W_a in the loaded body which may be released for cracking, Atkins and Mai (1985) suggested that the deformation transition regimes could be divided as follows:

(1) when $\varepsilon_{applied} < \varepsilon_y$ and $W_r > W_a$: simple elastic deformation occurs;

(2) when $\varepsilon_{applied} < \varepsilon_y$ and $W_r < W_a$: elastic brittle fracture occurs;

(3) when $\varepsilon_{applied} > \varepsilon_y$ and $W_r > W_a$: simple plastic flow occurs;

(4) when $\varepsilon_{applied} > \varepsilon_y$ and $W_r < W_a$: combined flow and fracture occur.

In regime (3), the deformation takes place in the form of simple plastic flow; this means that it can be used to remove the unwanted materials without initiating a crack. As a result, it is the favoured regime for *ductile mode machining*.

Puttick (1980) classified the fracture transition, depending on the extent of plastic flow in the specimen, into the *lower transition* and the *upper transition*. The *lower* transition is the transition between elastic fracture and elastoplastic flow (when the

yield criterion is just exceeded) while the *upper* transition is the transition between elastoplastic and fully-plastic flow (when the size of the plastic zone which precedes fracture reaches some maximum characteristic dimension). The conditions for these transitions may be stated as:

$$d_{upc} \approx \alpha_{up}\left(\frac{E\,\Gamma}{\sigma_y^2}\right) \quad \text{for the upper transition;}$$

$$d_{loc} \approx \alpha_{low}\left(\frac{E\,\Gamma}{\sigma_y^2}\right) \quad \text{for the lower transition;}$$

where d_{upc} and d_{loc} are the critical dimensions (lengths or size etc.), $\left(\frac{E\,\Gamma}{\sigma_y^2}\right)$ is a material factor, E is Young's modulus, Γ is the fracture surface energy, σ_y is the yield stress, and, α_{up} and α_{low} are factors related to the magnitude of tensile strain energy available to propagate the crack. As pointed out by Puttick (1980), most technologically important transitions are of the *upper* type (e.g. plane strain to plane stress fracture transition), while the lower transition, in which the assumptions of linear elastic fracture mechanics are valid, is widely used in theoretical studies.

The transition can also be produced by hydrostatic pressure or strain rate, as their conditions may make the yield stress higher than the fracture stress so that brittle fracture ensues (see Truss, Duckett and Ward 1981; Atkins and Mai 1985).

Since *ductile mode machining* can produce a smooth polish-like surface with little or undetectable sub-surface damage, it is not surprising that many attempts have been made to identify the "criteria" for *ductile-mode machining*. The most common and useful ones are critical cutting depth and critical cross-feed as they can be easily implemented in the machining process.

Puttick (1980), and Puttick et al (1989) used the brittle-ductile fracture transitions to predict the *critical linear dimension* d_c of the stressed volume of material below which the material will yield rather than crack,

$$d_c = \frac{\alpha E R_w}{\sigma_y^2} \qquad (4.7)$$

where σ_y is the yield stress for plastic flow and R_w is the specific work per unit area required to propagate a crack; α is a numerical parameter whose magnitude is a function of the type of test and it varies from about 0.1 for tensile type test to about the order of 1000 for Hertzian indentation (Puttick 1980). For plastic-elastic indentation, Puttick (1980) has estimated α to be 50. The value of R_w can be determined experimentally by recording loads and deformations simultaneously in a quasi-static crack propagation test proposed by Gurney and Hunt (1967). The yield stress, which is a function of hydrostatic pressure, temperature, and strain rate, can only be approximated by using the indentation technique discussed in section 2.2.3 (Eq. 2.14 or Eq. 2.19).

In the case of linear elastic fracture, the relation between R_w and K_c can be given (see Atkins and Mai 1985) as

$$R_w = \frac{K_c^2}{E^*} \tag{4.8}$$

where

$$E^* = E \qquad \text{(for plane stress)}$$

$$= \frac{E}{1-\nu^2} \qquad \text{(for plane strain).} \tag{4.9}$$

The critical stress intensity for the material can be obtained by using the indentation technique discussed in section 2.3.3 (Eq.2.35) (the values of Young's moduli of tested materials are given in section 2.4.1). This relation can be used to estimate the value of R_w (in the case of lower transition).

It is worth mentioning that the plastic zone at crack tip, r_p, is given by

$$r_p = \frac{K_I^2}{2\pi\sigma_y^2} \tag{4.10}$$

which takes a very similar form as equation (4.7).

Owing to the stress/strain distribution in the plastic zone during machining not yet being fully understood, the value for the test geometry factor α sometime has to resort to empirical data.

Table 4.1 lists the critical cut depth and related parameters needed in equation (4.7) to make the calculation. The values of σ_y were calculated by using equation (2.14) (Studman, Moore and Jones 1977), $P_{fracture}$ were obtained by indentation technique, $d_c(pred.)$ were calculated by using equation (4.7) with α=6.5 which was given by Puttick and Hosseini (1980) for single crystal silicon (111), and $d_c(exp.)$ were determined experimentally and will be addressed in section 5.7.

Table 4.1

	E (GPa)	K_{Ic} ($MPa\sqrt{m}$)	$P_{fracture}$ (GPa)	σ_y (GPa)	$d_c(pred.)$ (μm)	$d_c(exp.)$ (μm)
Si (111) crystal	132	1.84	15.56	10.17	0.18	0.5
Fused silica	73	1.67	12.11	10.4	0.16	0.8
Zerodur	91	1.14	11.18	8.3	0.12	0.8
Soda lime glass	70	0.36	6.54	3.8	0.056	1.2

* Since properties of soda lime glass may vary a lot from batch to batch (or from manufacture to manufacture), the values for soda lime glass given here are to be used with precaution.

The most serious source of error in the use of equation (4.7) to predict d_c quantitatively is in the estimation of σ_y. For highly brittle materials, this may only be derived from values of micro-hardness, a procedure entailing two questionable assumptions:

(1) *The yield stress is proportional to the micro-hardness.* The constant of proportionality in plastic-elastic indentation is a function of the elastic properties of the material, and has been theoretically evaluated by various authors (Marsh 1964,

Johnson 1970, Studman, Moore and Jones 1977, Chiang, Marshall and Evans 1982; see section 2.2.3 for detail). Significant differences exist between the predictions of different equations.

(2) *The micro-hardness values are function of loads* at the low end of the micro-hardness range.

Furthermore, the experimental work of indentation and machining has repeatedly emphasized the importance of the effect of strain rate, temperature and environment on hardness and yield stress. The lack of knowledge of the extent of the effect of these factors yields more uncertainties. As a result, at best, one can not hope to predict d_c to better than an order of magnitude.

Cheng and Finnie (1990) have tried to obtain the critical dimension (and thereby the brittle-ductile transition) by studying the initiation of sub-surface median cracks in glass during indentation and scribing. By adopting the crack initiation model suggested by Hagan (1979b), the crack initiation is caused by dislocations piling up on the shear band formed along the boundary of the plastic zone, and Stroh's (1957) criterion for crack nucleation due to piled-up dislocations, they proposed that the critical size a_c was

$$a_c = A\left(\frac{K_{Ic}}{H}\right)^2 \qquad (4.11)$$

where A is a dimensionless constant with a value of 51 for a 110^o included angle indenter, K_{Ic} is the critical stress intensity factor, and H is the mean pressure.

Marshall and Lawn (1986) suggested a critical threshold condition a_c for the indentation fracture

$$a_c = \mu_c\left(\frac{K_c}{H}\right)^2 \qquad (4.12)$$

where $\mu_c \approx \beta\left(\frac{E}{H}\right)$ and β is a dimensionless constant. This critical size was later adopted by Bifano (see Bifano 1988, Bifano et al 1988) in grinding and by Blake and Scattergood (1989) to predict the brittle-ductile transition during turning.

An aspect left undecided in the above mentioned equations, which is necessary for calculating the critical dimension of brittle-ductile transition, is the dimensionless constants (α, A, β) in the equations. Unfortunately, because of the diversity of cutting conditions due to tool shapes, material properties, and cutting speed (strain rate), these constants have to be derived empirically requiring effort and resource where process utility is in question.

Chapter 5

Single-Point Diamond Turning of Brittle Materials

5.1 Experimental Single-point Diamond Facing Machine

In order to achieve *ductile-mode* capability in machining brittle materials, there are a number of machine requirements which must be met. Essentially these are derived from the criterion to maintain the cut-depth to within the stringent limit of $\approx 1\,\mu m$ as set out in chapter 4 (see section 4.3). As a consequence of these requirements the machine must exhibit high stiffness, precise machine movement (in spindles, slides), minimised internal vibration and isolation from external vibration, temperature stability, and position control based upon nanometric resolution measurement. These parameters should be examined in detail and the total uncertainty of extraneous motion held within the maximum allowance for cut-depth.

High stiffness is required to reduce the deformation of machine when it is subject to substantial cutting force (e.g. in grinding). Precise machine movement and a high resolution control system are necessary for obtaining the (usually) sub-micrometre critical cutting depth for brittle materials. Any vibration, internal or external, will directly affect the dynamic performance of the machine and the surface finish of the workpiece. Temperature variation may change the contours and dimensions of machine components, and cause dimensional instability which will all reflect on the surface roughness and profile (form) accuracy of the workpiece. The temperature variation can be reduced by minimising or eliminating the heat sources, and using heat conducting and convecting mechanisms to dissipate excess heat from the heat sources that cannot be eliminated.

An experimental diamond facing machine with high loop stiffness and negligible tool vibration had been developed during earlier research work of Puttick et al (1989) to investigate single point diamond machining of brittle materials under fixed cut depth machining condition.

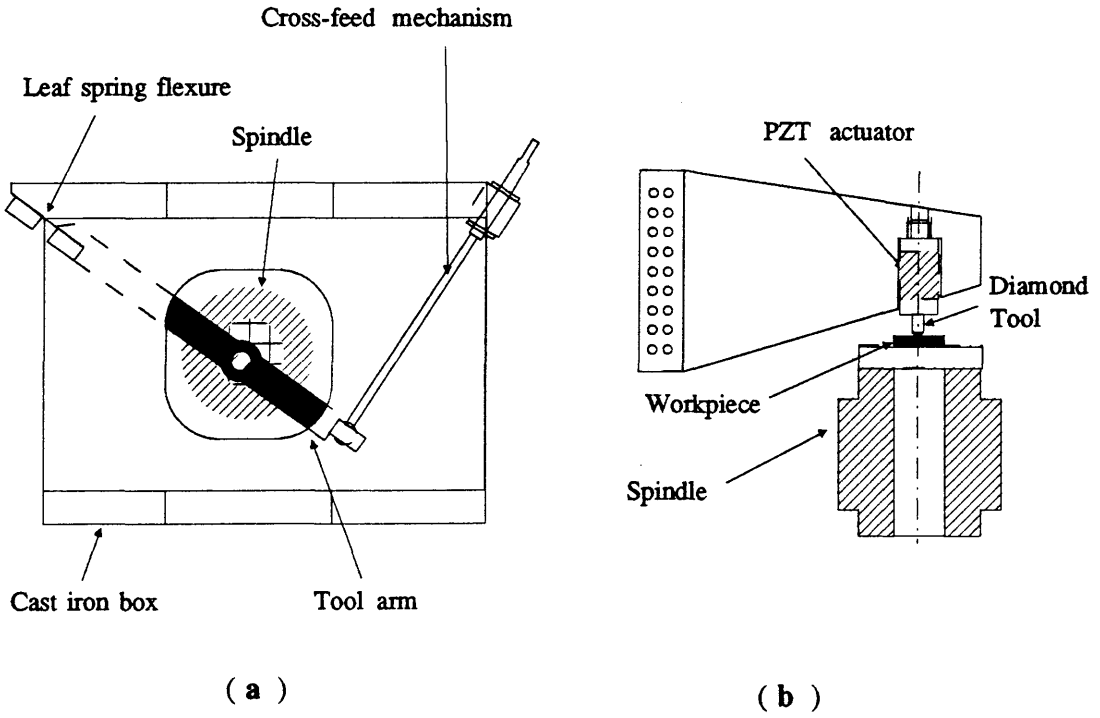

Fig. 5.1 (a) Top view of the central frame of the machine (b) side view of tool arm, tool and PZT actuator.

The machine is essentially a double rotary motion machine where the workpiece rotates on a precision spindle and the tool is fed across the workpiece in a plane at right-angles to the spindle. A similar arrangement has been described by Falter and Dow (1987) .

The central frame of the machine is a thick cast-iron box on which the main spindle bearing and tool arm are mounted, as shown in Fig. 5.1(a) and (b). The spindle is a hydrostatic air bearing (Model 4R "Block-head" made by Professional Instruments Company, Minneapolis, MN, USA), with a radial stiffness of 12 $kg/\mu m$, an axial stiffness of 36 $kg/\mu m$, and with both radial and axial runout less than 50 nm, to give the stiffness and accuracy needed for the intended precision machining. The box is supported by a steel frame which itself is suspended from an outer frame standing on four rubber load bearing joints. The tool arm, joined to a corner of the box by a leaf spring flexure and tapering down radially, provides for the in-feed movement driven by a lead-screw, which itself is driven by a dc motor via a reduction gear box and coupled to the outer end of the arm.

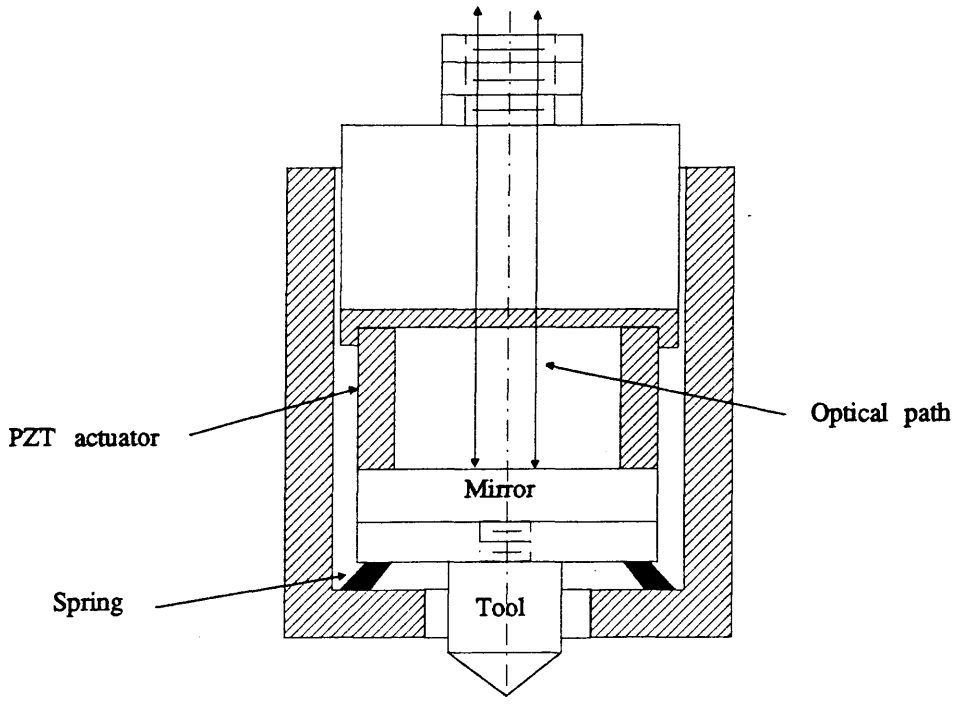

Fig. 5.2 Plan of the tool holder.

The tool holder, with fine piezoelectric in-feed (of about 30 μm) as shown in Fig. 5.2, is mounted on the cast-iron tool arm. The piezoelectric actuator provides fine vertical tool movement and has an integral mirror, as part of optical metrology system, to interferometrically monitor the movement of the tool (detailed in the following section). Fig. 5.3 shows the movement calibration curve of the tool-feed piezoelectric actuator. 20 μm piezoelectric actuator movement results from a drive voltage of 1040 volt dc. The calibration was carried out using a laser interferometer to check against the piezoelectric actuator movement.

The voltage output of the dc-power supply is monitored by a digital voltmeter accurate to milli-volts. In order to examine the stability of the voltage, a two-hour duration stability test was conducted for fifteen selected voltages. The voltage drift in two hours duration was observed to be less than 0.05%. As to the hysteresis, which can be seen clearly in Fig. 5.3, the lost motion can be compensated by using the automatic feedback control system or, in case of manual control, can be adjusted by observing and counting the optical fringe shifting. In both cases, the resolution of tool movement is approximately 10 nm. Also, parallel work in the same laboratory by Duduch and Gee (1990) indicates that, from a control-design viewpoint, particularly in respect of the high-gain (commensurate with stability) required par-

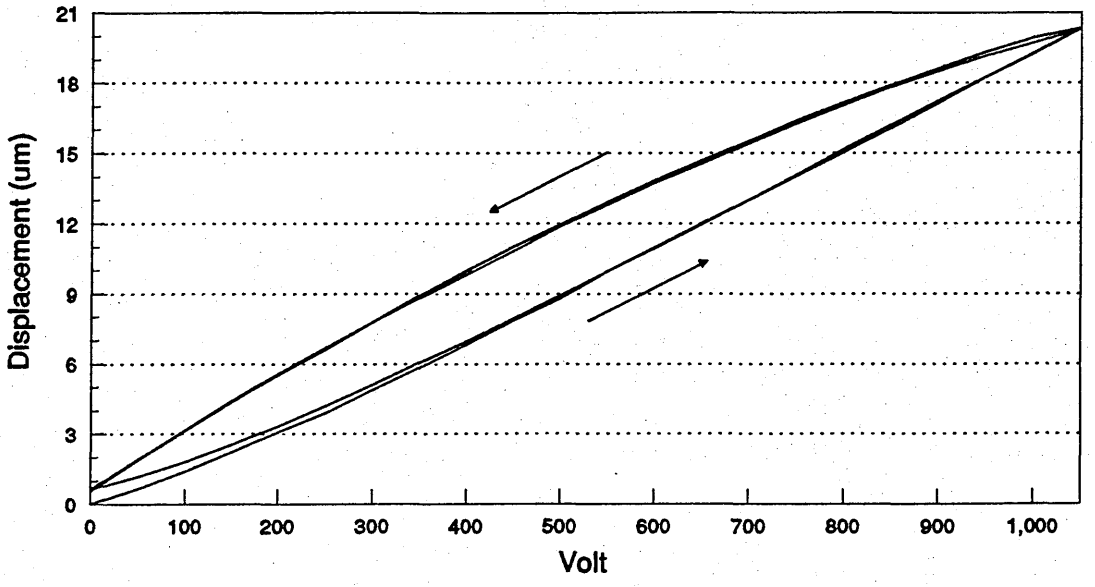

Fig. 5.3 Movement calibration curve of the tool-feed piezoelectric actuator.

ticularly for position feedback control of ultra-precision machining systems, the nature of this form of non-linearity occurring in piezoelectric devices may not be the source of too many problems.

The workpiece, consisting of a plate of thickness between 0.5 mm and 10 mm and diameters from 20 mm to 60 mm, is mounted on an optical flat which is itself clamped onto a vacuum "chuck" (face-plate) stage incorporating tilt adjustment. The whole optical flat and tilting stage assembly is bolted on the air-bearing spindle which rotates around vertical axis.

The machine is located in a laboratory which is equipped with an air-conditioning system which regulates temperature at $20 \pm 0.5\ ^{o}C$ and humidity at $(55 \pm 5)\%$. For an earlier application the building housing the laboratory has a floor and roof consisting of 2 m and 1 m depth of concrete respectively and the walls are 0.3 m thick with external sloped earth-banking to a height of 2 m. Reinforcing steel girders are sandwiched inside all the concrete work thereby making it a massive and rigid box structure which appears to be well-isolated from much external vibration. (Affirmative comment regarding this has been made by one of the major international manufacturers of displacement interferometric measurement systems during a demonstration-visit).

5.2 Metrology

5.2.1 Introduction

As discussed in chapter 4 (section 4.3) the critical fracture threshold depth for most brittle materials is of the order of one micrometer. In any attempt to machine to within this as a maximum cut depth, this must be the total sum of contributions to the cutting depth including the required (set) cutting depth, spindle run-out, thermal expansion (of tool, workpiece, and machine structure) and fluctuation caused by vibrations, both internally and externally-generated. With such a narrow range of tolerance, a small mistake made in the first contact process (plunge-in) or a minute mis-orientation of the specimen could have a drastic consequence (for the cracks induced by a single deep cut might penetrate ten times the cutting depth).

In order to keep the machining depth within the ductile regime and to achieve ultra-fine machining, it appeared to be very necessary to have a measurement system to in-process monitor the cutting process and to ease the setting-up procedure. A Fizeau interferometer, as shown schematically in Fig. 5.4, (model PTI made by Zygo Inc., Middlefield, CT, USA) has been mounted above, and coaxially with, the machine to meet the above requirements and generally extend the performance of such machines (Gee, McCandlish and Puttick 1988).

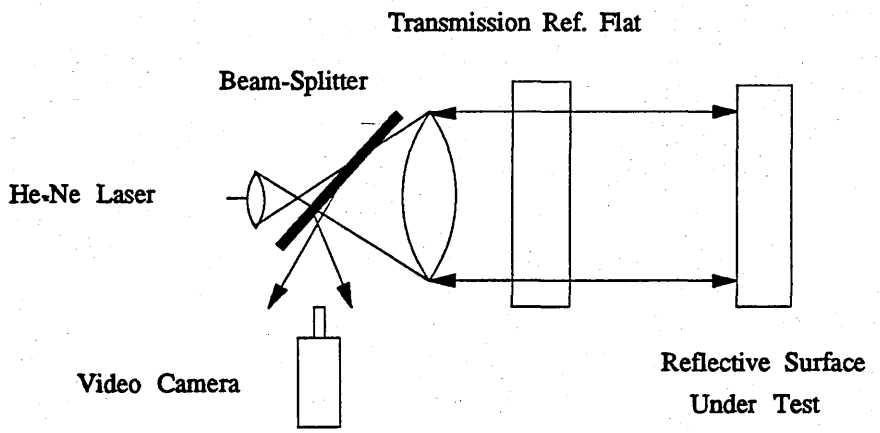

Fig. 5.4 Fizeauinterferometer.

The main function of this optical metrology system is to align the optical axis, spindle axis and workpiece surface-normal. Although this arrangement has proved to be very effective and made levelling the workpiece and in-process interferometric monitoring the tool/workpiece possible, it still takes considerable effort to level the workpiece manually. To ease this difficulty, a tilt-stage was jointly-designed (together with J. Duduch and A. E. Gee Cranfield Inst. of Tech.) to provide the ability to adjust the orientation of the workpiece automatically through controlling piezoelectric actuators. A mathematical model and a control algorithm was also developed to enable the system to be computer-controlled.

5.2.2 Axial Interferometer System

The optical interferometer has long been used as one of the most effective ways to measure surface profile. With the advent of the laser as a long-coherence source the advantages of laser-interferometry are multiple including non-contact, easy set-up and self calibration all making it extremely important in precision engineering.

Gee, McCandlish and Puttick (1988) employed the Fizeau interferometer in the single-point diamond facing machine for in-process monitoring the spindle and workpiece. With this axial mounted interferometer in position, it can monitor the full aperture of a rotating component and provide dynamic information like spindle run-out and tool/workpiece interaction which is critical for in-process control.

The geometric model of the optical metrology system used in this study is shown schematically in Fig. 5.5, where V_o, V_s and V_c are vectors representing optical axis, spindle axis and direction of workpiece surface respectively. Vectors V_{sp} and V_{cp} are the projected components of V_s and V_c on X-Y plane. The angles φ_s, φ and φ_c correspond to the angle between V_o and V_s, V_s and V_c, and, V_o and V_c respectively.

To make the modelling easier, the optical axis vector V_o is made parallel to the Z-axis and of unit magnitude ($V_o = \vec{k}$). The "offset" vector $\vec{r}$ is introduced when the workpiece surface is not perfectly perpendicular to the spindle axis. The direction of vector $\vec{r}$ is always normal to vector V_s and its magnitude is decided by the amount of offset.

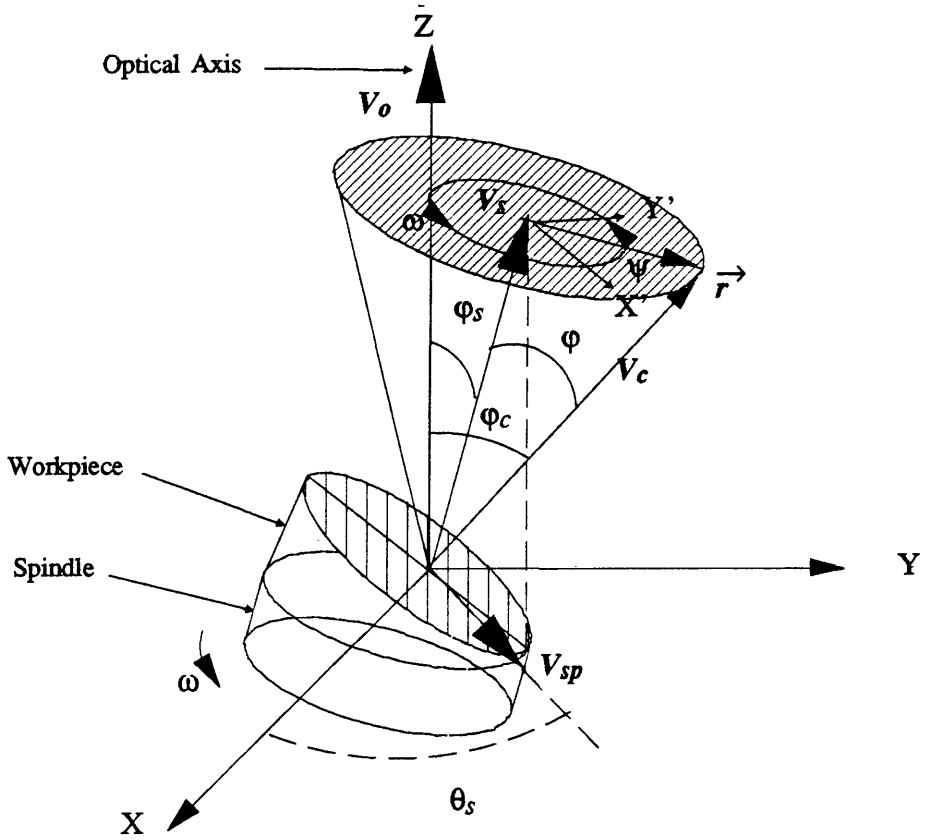

Fig. 5.5 Geometric model of the optical metrology system used in this study.

The resultant of V_s and $\vec{r}$, vector V_c, may be given analytically as follows:

$$V_s = \sin\varphi_s \cos\theta_s \vec{i} + \sin\varphi_s \sin\theta_s \vec{j} + \cos\varphi_s \vec{k} \qquad (5.1)$$

$$\begin{aligned} V_c &= V_s + \vec{r} \\ &= \left[A\cos\psi\cos\varphi_s\cos\theta_s - A\sin\psi\sin\theta_s + \sin\varphi_s\cos\theta_s \right] \vec{i} \\ &+ \left[A\cos\psi\cos\varphi_s\sin\theta_s + A\sin\psi\cos\theta_s + \sin\varphi_s\sin\theta_s \right] \vec{j} \\ &+ \left[\cos\varphi_s - A\cos\psi\sin\varphi_s \right] \vec{k} \end{aligned} \qquad (5.2)$$

where

$$A = \tan\varphi$$

$$\psi = \omega t - \psi_0$$

θ_s is the angle between vector V_{sp} and X axis, ψ is the angle between vector $\vec{r}$ and X' axis, ω is the spindle speed, ψ_0 is the angle between vector $\vec{r}$ and X' axis at t= 0, and t is the elapsed time. As the spindle rotates, vector $\vec{r}$ will rotate around the spindle axis simultaneously. This makes the trajectory of vector V_c prescribe an inverted cone, as shown in Fig. 5.7. The angle between vectors V_c and V_o can be described as:

$$\cos\varphi_c = \frac{V_c \cdot V_o}{|V_c|\,|V_o|}$$

$$= \cos\varphi\cos\varphi_s - \sin\varphi\sin\varphi_s\cos\psi \qquad (5.3)$$

It can be seen in Eq. (5.3) that the number of fringes in the viewed aperture reaches a maximum (ie maximum tilt) when

$$\varphi_c = \varphi_{cmax} = \varphi_s + \varphi$$

and that the minimum number of fringes (ie minimum tilt) occurs when

$$\varphi_c = \varphi_{cmin} = \varphi_s - \varphi .$$

The angles φ_{cmax} and φ_{cmin} may be obtained from the fringe spatial frequency and diameter of the tilting stage. The angular offset caused by the spindle (φ_s) and the offset caused by the workpiece (φ) can be derived as:

$$\varphi_s = \frac{\varphi_{cmax} + \varphi_{cmin}}{2} \qquad (5.7)$$

$$\varphi = \frac{\varphi_{cmax} - \varphi_{cmin}}{2} \qquad (5.8)$$

5.2.3 The Proposed Piezoelectric Actuated Tilt-Stage

A stage which integrates coarse and fine adjustment, and provides for the required adjusting ranges (0.5 mm of coarse adjustment and 10 μm of fine adjustment) is proposed here as a possible option for improving the machining performance.

A basic requirement of inserting a tilt-stage into the 'cutting loop' is to provide the needed functions without overly reducing stiffness. A monolith piezoelectric actuated tilt-stage, as shown schematically in Fig 5.6, was designed to fulfil these conditions.

The stage can be divided functionally into two parts (Fig. 5.6). The upper part of the stage is piezoelectric actuated for fine adjustment while the lower part may be manually driven to give the coarse adjustment required for bringing the system into the adjusting range of piezoelectric stacks when excessive tilting is present.

The lower part, as shown in Fig. 5.6, has three adjusting screws which are located 120^o apart in tapped holes in the bottom plate. The coarse adjustment is obtained by turning these screws downward against the base plate. This will push the double-flexure upward and allow the table to tilt up to 0.4^o to the X-Y (or i-j) plane. Once within the adjustment range of the piezoelectric (PZT) stacks, the surface can be finely adjusted through the three PZT actuators embedded in the supporting blocks (Fig. 5.6).

A geometric model of the tilt-stage is shown in Fig. 5.7. P_1, P_2 and P_3 represent three PZT actuators for tilt control and V_t is the direction vector of the surface defined (or controlled) by P_1, P_2 and P_3. The vector V_{tp} is the projection component of vector V_t onto the X-Y plane, θ_t and φ_t are the angles between (X-axis and V_{tp}) and (Z-axis and V_t). The direction of tilting can be determined by θ_t while the amount of tilting is given by φ_t.

In order to align the optical and spindle axes, and to level the workpiece, two tilt stages are needed. A *workpiece tilt-stage* is used to correct the offset angle of workpiece φ_s so that its surface can be levelled. The *reference-platetilt-stage* is used to minimise the offset angle φ by adjusting the optical reference plate in the Fizeau interferometer system.

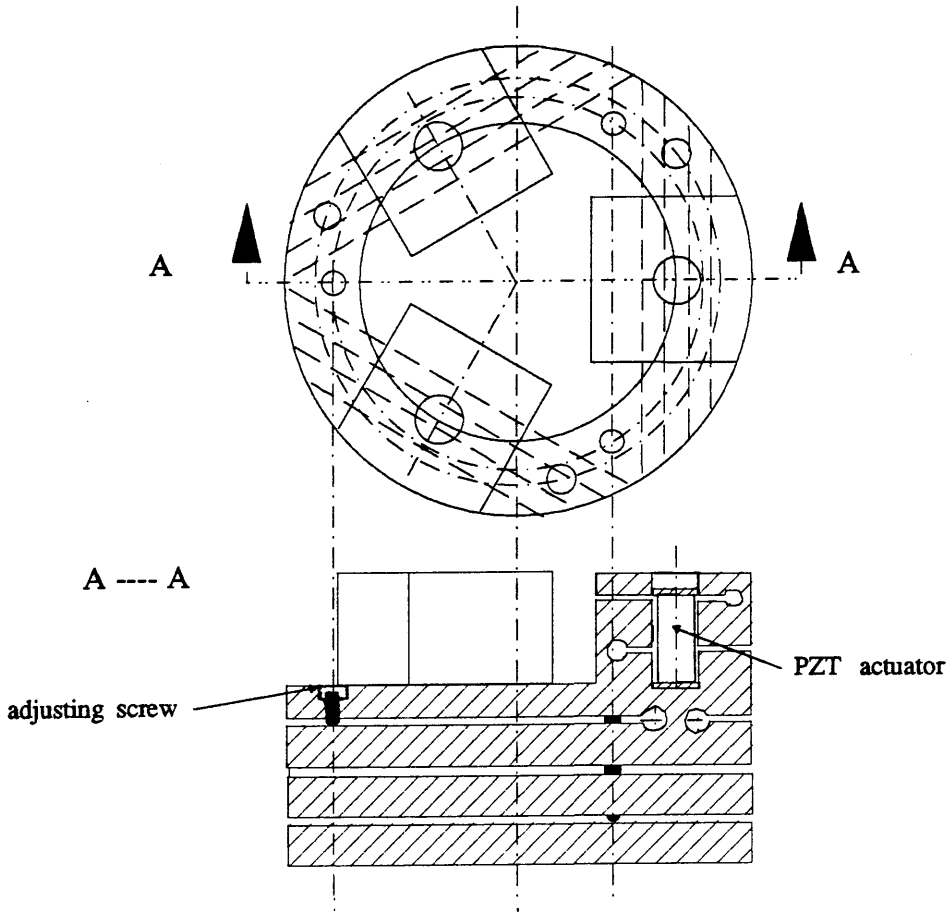

Fig. 5.6 Proposed monolith piezoelectric actuated tilt-stage.

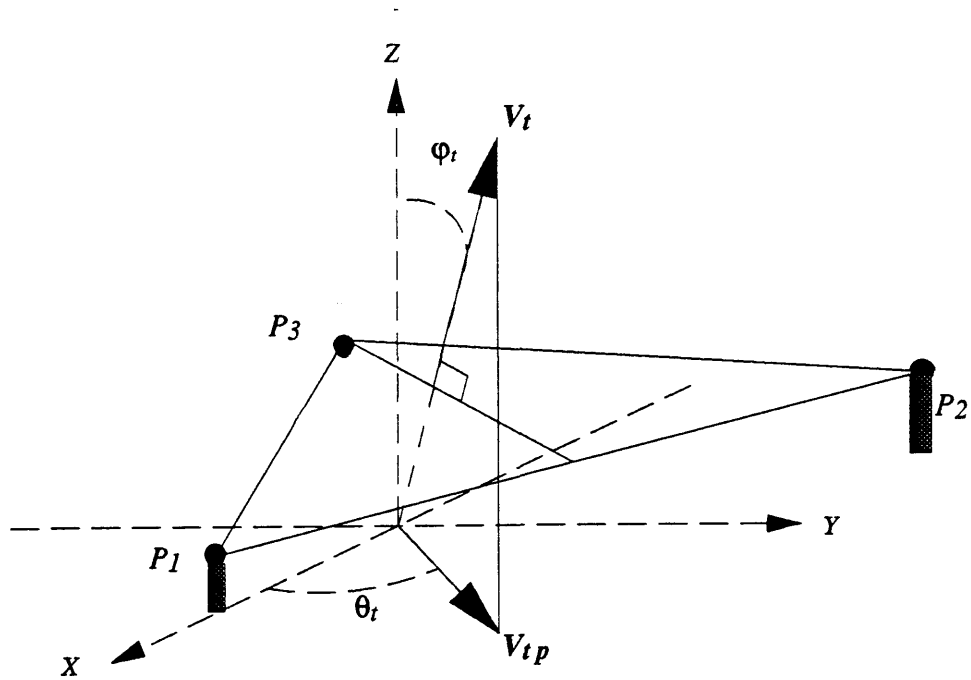

Fig. 5.7 Geometric model of the tilt-stage.

5.2.4 Dynamic Fringe Analysis

The observed interferometric fringe number generated by a tilted circular optical flat is determined by the wavelength, λ, the diameter of the optical flat, R, and the angle between V_o and V_c, φ_c. The vector V_{cp} (the X-Y plane projection of V_c), as shown in Fig. 5.10, is always normal to the fringe-pattern and defined as pointing towards the lower part of the tilted surface and is used here to define the "direction of the fringes". The angle φ_c is a combination of φ_s and φ. It varies as the spindle rotates. As a result, the fringe number as well as fringe orientation will change as the spindle rotates.

Two types of "rotating fringe" dynamics may be observed, namely fully rotating and partially rotating fringe-patterns, as illustrated in Fig. 5.8 (a) and (b) which correspond, respectively, to the cases

(1) $\varphi_s < \varphi$ and

(2) $\varphi_s > \varphi$.

In case (1) ($\varphi_s < \varphi$) the vector V_c as well as vector V_{cp} "rotate" around the optical axis in a full revolution (see Fig. 5.8(a)). The variation of fringe patterns corresponding to the second case is shown in Fig. 9(a). In case (2) ($\varphi_s > \varphi$) the vector V_c "rotates" only on one side of the optical axis as depicted in Fig. 5.8(b). The fringes change their orientation as vector V_{cp} (which defines the direction of fringes) swing back and forth between the maximum and minimum φ_c (as shown in Fig. 5.9(b)).

5.2.5 Possible Control Algorithm for Tilt-Stage

In order to control the piezoelectric (PZT) actuators in the tilt-stage, it is necessary to know (a) which PZT actuators are to be actuated and (b) how much displacement is needed. This information can be obtained from the optical fringe analysis (see section 5.2.4).

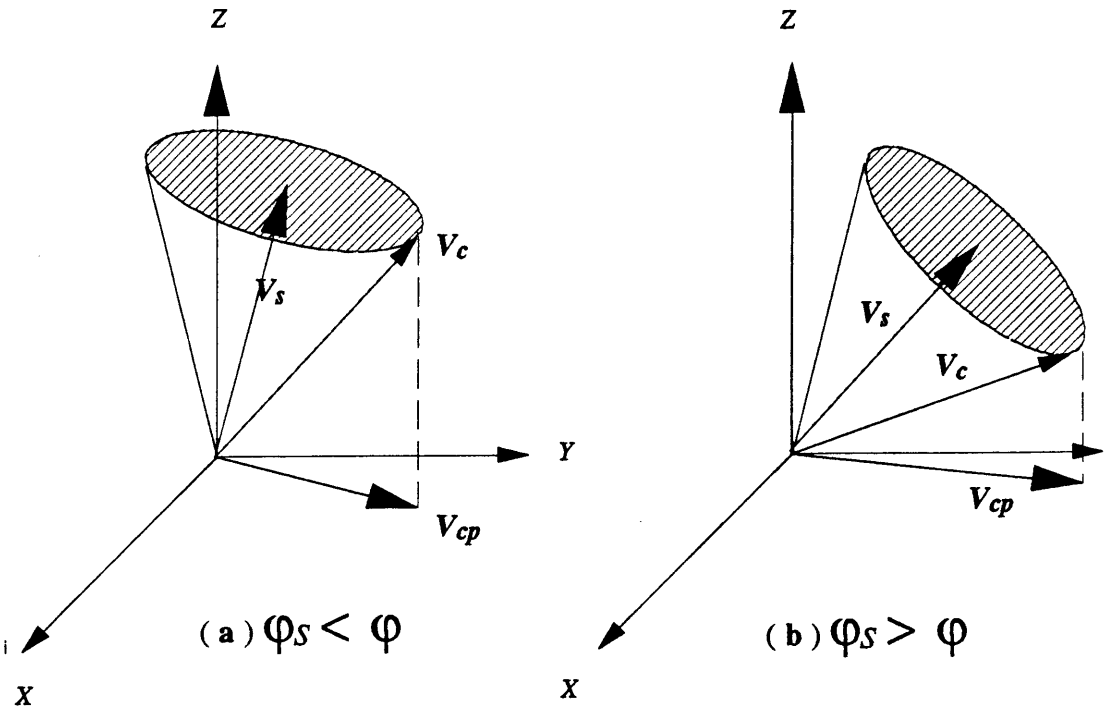

Fig. 5.8 Condition for (a) fully rotating fringe-patterns: $\varphi_S < \varphi$, and (b) partially rotating fringe-patterns: $\varphi_S > \varphi$.

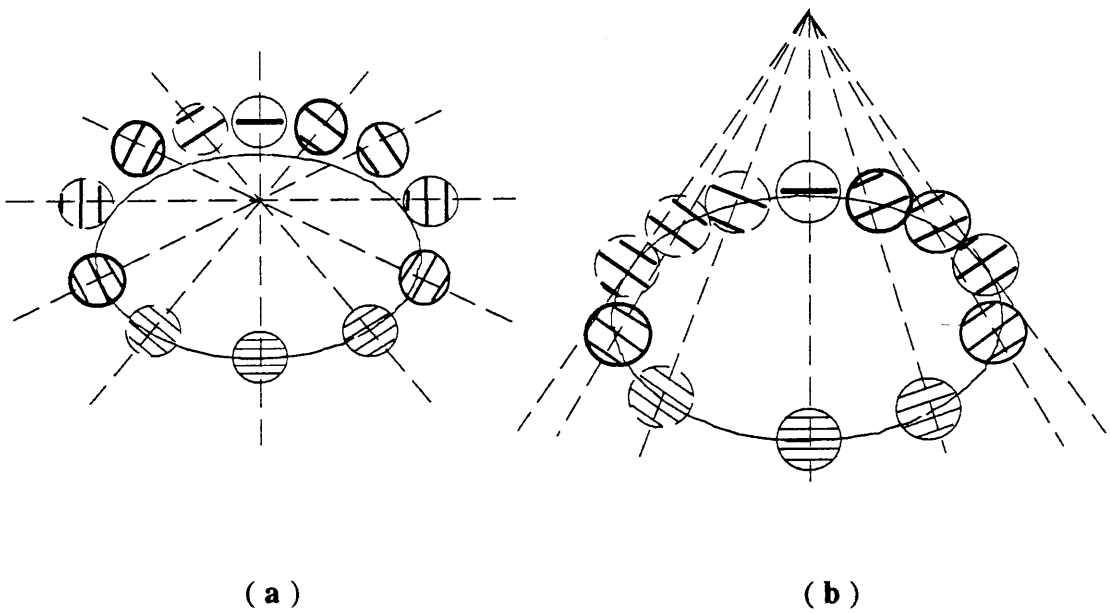

Fig. 5.9 (a) Fully rotating fringe-patterns (b) Partially rotating fringe-patterns.

In the case of tilt, as long as the resulting offset is within the adjusting range of the tilt-stage, only one or two PZT actuators are needed to be adjusted. The vector V_{cp} can be used here to give the answer for the part (1) of the question. As shown in Fig. 5.10, the vector V_{tp} may be used as a pointer; when it is pointing towards any special sector, only the PZT actuators related to the pointed sector are to be activated. If V_{tp} points at P_1, for example, the workpiece is tilted towards P_1. To correct this offset, only the PZT actuator P_1 needs to be activated. The range of these control sectors are detailed as follows:

Sector range	*PZT actuator(s) to be actuated*
$\theta_t = 0^o$	P_1
$0^o < \theta_t < 120^0$	P_1, P_2
$\theta_t = 120^o$	P_2
$120^o < \theta_t < 240^o$	P_2, P_3

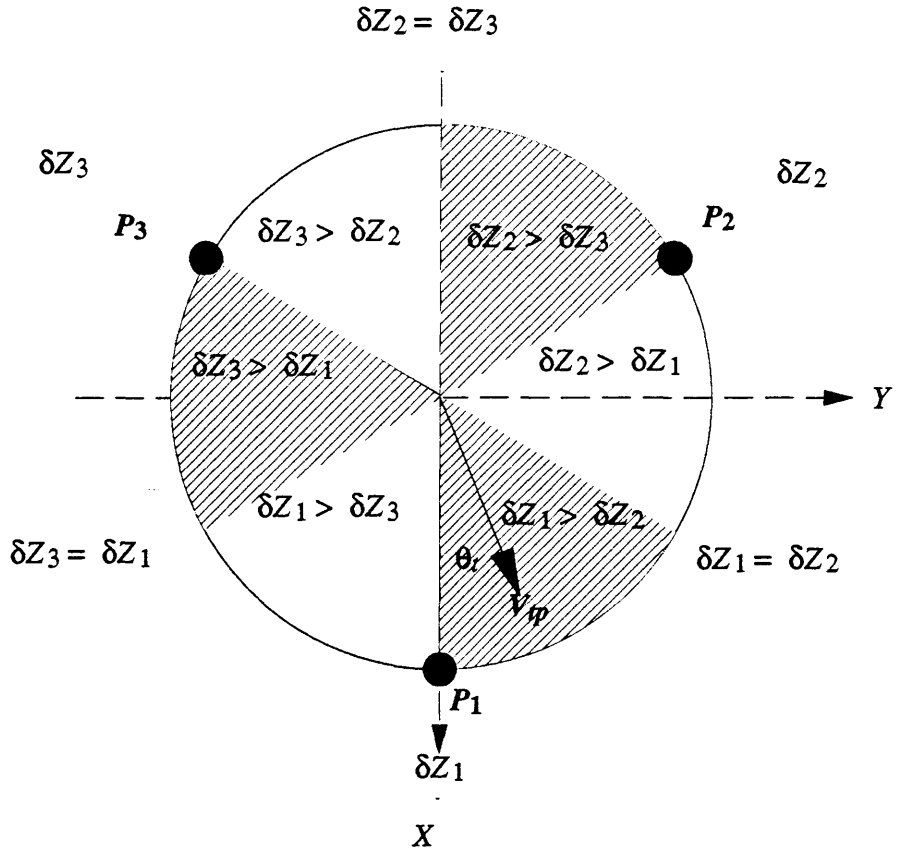

Fig. 5.10 Diagram showing different control sectors and the relative amount of the displacements to be adjusted in each sector.

$\theta_t = 240^o$	P_3
$240^o < \theta_t < 360^o$	P_3, P_1

where $\delta Z_1, \delta Z_2$ and δZ_3 are the displacements of P_1, P_2, and P_3 respectively.

In order to correct the offset angles φ and φ_s, the stages must be controlled to give a tilt angle φ_t which is equal in magnitude but is opposite (in sense) to φ_s (workpiece tilt-stage) or φ (reference-plate tilt-stage).

To simplify the analysis, the offset angle may be treated as if it is caused by the uneven lengths of the PZT stacks (Z_1, Z_2 and Z_3) on the tilt-stage. Once these "notional" lengths are obtained, to compensate the offset it is required to equalise the notional lengths of the PZT stacks. In order to achieve this, it is necessary to correlate the PZT stack lengths with the offset angle and fringe-direction obtained from the optical fringe analysis.

For a given set of PZT stack-lengths, Z_1, Z_2 and Z_3, the tilt-stage surface direction vector may be defined as (shown in Fig. 5.11)

$$\vec{V}_t = \vec{V}_1 \times \vec{V}_2 \qquad (5.9)$$

If the offset angle is equal to φ_t and the fringe direction is θ, the relation between Z_1, Z_2 and Z_3 can be obtained by vector analysis. Using Z_1 as a reference point ($Z_1 = 0$) Z_2 and Z_3, can be given as

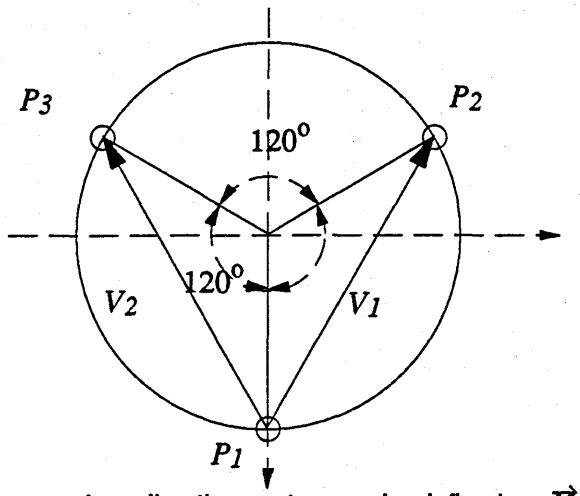

Fig. 5.11 The tilt-stage surface direction vector may be defined as $\vec{V}_t = \vec{V}_1 \times \vec{V}_2$.

$$Z_2 = \left[\frac{B_1}{B_2^{\,2} + B_2 B_3 + 1} \right]^{1/2} \qquad (5.10)$$

$$Z_3 = B_2 Z_2 \qquad (5.11)$$

where

$$B_1 = \frac{[1 - \frac{1}{\cos \varphi_t}]\, 4 C_1^{\,2} C_2^{\,2}}{C_1^{\,2} + C_2^{\,2}}$$

$$B_2 = \frac{1 + C_3}{1 - C_3}$$

$$C_1 = R\,[\cos 60 + 1]$$

$$C_2 = R \sin 60$$

$$C_3 = \frac{C_2 \tan \theta_t}{C_1}$$

As the lengths of Z_1, Z_2 and Z_3 have been obtained, to level the surface it is required to drive the two shorter PZT actuators to the same height as the longest of the three.

5.3 Setting-Up the Machine

5.3.1 Introduction

Before machining, it is necessary to set up the machine to the design-operational conditions. Setting-up procedures include

(1) adjusting the tool arm and spindle so that the tool cross-feed motion is parallel to the spindle surface;

(2) levelling the specimen, with respect to the spindle-axis;

(3) tool-setting (height above specimen, first contact etc).

Of these three, the tool-arm/spindle alignment needs only to be adjusted once and then occasionally checked for alignment while the others are part of the routine which has to be performed for each specimen before machining.

5.3.2 Alignment of Tool Cross-feed Motion with Respect to Spindle Axis

During (facing) machining, the tool arm slowly sweeps across the workpiece using the leaf-spring flexure-hinge as the axis of rotation. The flatness of the machined surface is critically dependent on the parallelism of the plane containing the cross-feed arc and workpiece surface. In order to ensure this, their axes of rotation have to be aligned parallel.

The small interferometer mirror which had been installed inside the tool holder (as described in section 5.1) can now be used in the aligning process as an indicator of the offset between the optical axis, the axis of rotation of the arm, and the actuator-mirror. To bring the tool arm axis and the optical axis into alignment is analogous to aligning the spindle, workpiece and optical axis which has been detailed in previous sections (section 5.2.). In this instance the arm effectively is the 'spindle' and the actuator mirror serves as the 'workpiece' (or a restricted area of the workpiece to be accurate); the theory involved in the adjustment is then the same for both cases.

Once the optical axis has been brought into alignment with the axis of the arm, the spindle can be aligned with the two.

5.3.3 Mounting and Levelling the Specimen

As was the case with much of the earlier recorded work, it has been generally been the case that specimens used were derived from different sources and with various shapes (discs, square plates, cubes etc.) and thicknesses ($300\ \mu m$ to $20\ mm$). Since the specimen was fixed to the spindle via a vacuum chuck, inevitably, some compressive pressure, and thence force, was applied to the specimen. As a result, depending on the thickness of the specimens, distortions were introduced. For thick specimens (or rather specimens of high thickness/diameter eg $> 5\ mm$ in the case in hand), the distortion was negligible (no change of the fringe pattern was ob-

served). However, thin specimens such as silicon wafers could be badly distorted. In order to prevent this, thin specimens were supported on a subsidiary thick optical flat.

As has already been discussed (sections 5.1 and 5.2.1), levelling the workpiece before machining is necessary if an ultra-fine surface finish is to be achieved. A tilting stage has been designed and the control algorithm has been developed to minimize the levelling offset. This levelling system works when the surface-finish of the workpiece is adequate to give an interferometrically-analyzable fringe pattern which is necessary for determining the profile of the surface. However, problems arise when the workpiece surface is "rougher". Without the information given by the optical fringe information, the surface offset cannot be so readily derived or corrected.

Generally, when a workpiece reaches the fine finish machining stage which is the subject of this study, its surface should have been pre-machined to near flat form although the roughness may not necessarily permit near normal reflection. For such a workpiece-surface, the levelling process may be carried out with an optical flat (with polished surface on both sides) placed in contact. The optical fringes obtained from the **bottom** surface of the contacting optical flat can be used for levelling the specimen-surface.

5.3.4 Tool Setting

When the critical cutting-depth is of the sub-micrometre order, knowledge of the relative position of the tool tip and workpiece surface and detecting the first contact are important in controlling the achieved cutting depth. For machining most brittle materials, a "deep" plunge of the tool into the workpiece usually ruins the workpiece-specimen by brittle chipping action.

The tool setting process includes measurement of tool proximity prior to first contact.

An optical proximity sensing technique (Gee, Green and Pain 1988, Gee 1990b) is employed here to further lower the tool. By aiming a laser beam between the tool tip and reflecting workpiece surface, the tool edge and its image will form a virtual *optical slit*, as shown in Fig. 5.12. The incident beam will be diffracted (by single slit Fraunhofer diffraction) by the optical slit of width w (twice the distance between

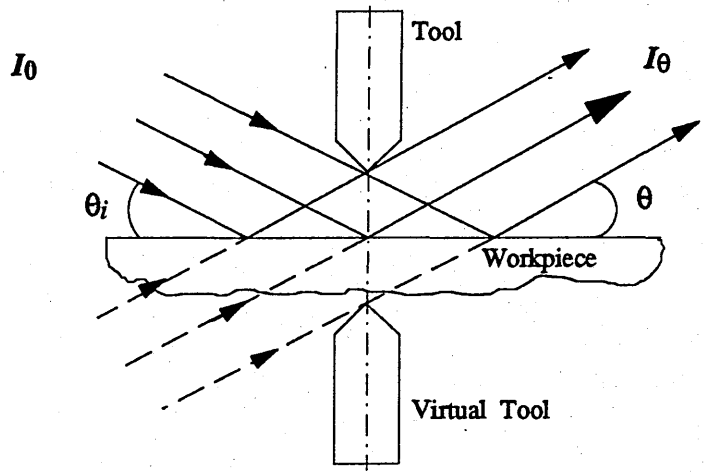

Fig. 5.12 A virtual "optical single slit" formed by the too edge and its image. (After Gee, Green and Pain 1988)

the tool edge and the workpiece surface, b), and the diffraction pattern irradiance distribution in the focal plane, given generally by (see for example Jenkins and White 1981)

$$I_\theta = I_0\left(\frac{\sin\beta}{\beta}\right)^2 = I_0 \, sinc^2\beta \qquad (5.12)$$

where (in case of the incident beam not normal to the slit plane)

$$\beta = \frac{\pi w(\sin\theta - \sin\theta_i)}{\lambda} \qquad (5.13)$$

θ_i is the angle (incident angle) between the incident plane wave and the plane of the slit, λ is the wave length, and I_0 is the incident irradiance and I_θ is the diffraction irradiance for (the diffraction angle) θ. The diffraction irradiance I_θ has minima, equal to zero, when $\sin\beta = 0$ whereupon

$$\beta = \pm\pi, \pm 2\pi, \pm 3\pi...$$

Substituting $\beta = \pi$ into Eq. 5.13 for the first minimum, corresponds to

$$\sin\theta = \sin\theta_i + \frac{\lambda}{w} \qquad (5.14)$$

For a given wavelength, the angular width of the diffraction pattern varies inversely with the slit width, or, the gap between the tool edge and the workpiece surface. Theoretically, the tool-workpiece gap can be reduced to a near-wavelength separation if the incident angle of the laser beam is near zero and the workpiece surface is perfectly smooth. However, in a real machining condition, the incident angle and diffracted beam are limited by the machine structure, the workpiece surface roughness, and the tool-tip included angle. For example, if a symmetrical roof-edged tool with 90 degrees included angle and a He-Ne laser with 633 nm wavelength are used, the smallest tool-workpiece gap which can be achieved is about 1.2 μm.

By using this non-contact measuring technique to estimate the distance between tool edge and workpiece surface, the PZT actuator inside the tool holder can then be activated to lower the tool to the measured distance according to the actuator control calibration curve (see section 5.1).

An accelerometer sensor (type V.P.7., made by Lamerholm Ltd. UK) was attached to the tool holder to detect the vibrations experienced at the tool tip and the signals amplified, filtered, displayed on an oscilloscope and transmitted to a computer via an A/D converter where the data could be logged and analyzed. This arrangement was aimed at detecting the first contact between tool and workpiece and then at monitoring cutting conditions by acoustic emission. The first part was quite straightforward and a large change in signal pattern was detected when the tool made contact with the surface. However, monitoring the cutting condition by analyzing the data (acoustic emission) did not give a satisfactory result. It proved to be possible only to differentiate between signals related to contacting, non-contacting, and large scale brittle fracture. In respect of ductile mode machining and small-scale cracking in the machined area, signals were found to be very similar.

Once first contact had been detected, it gave a reference point for cutting depth so that tool in-feed can be kept below the critical cutting depth value, thereby permitting ductile machining. It is to be expected that this first contact point would be close to the highest point of the surface (determining the maximum cut-depth for the whole surface).

5.4 Ultra-fine (Single-point) Machining Employed

5.4.1 Introduction

To study machined surfaces (roughness, flatness) produced under different machining conditions so that the relation between machining conditions and machined surface can be found is important for all machining processes. In this work, the machined surface was to be examined both at surface and sub-surface level. Surface observations included using:

(1) SEM (Scanning Electronic Microscope) for very detailed information about the machining marks and crack formation (if there is any)

(2) Talystep together with Nanosurf (NPL) surface analysis software to examine the waviness, centre-line average (CLA - denoted Ra) and peak-to-valley height of the surface in nanometre range.

Equally important is the study of the extent of the sub-surface damage introduced by the machining process which will influence the mechanical and electromagnetic properties, including the reliability and performance of the workpiece. Several techniques, both destructive methods such as indentation, scratching and etching tests and non-destructive methods were employed to investigate sub-surface damage, namely SAM (scanning acoustic microscopy) and X-ray topography; these will be detailed in chapter 6.

5.4.2 Machining Results

A number of machined (single-point diamond turned) surfaces which have been examined by using SEM and Nanosurf (or Talystep) are chosen and shown here as the sample surfaces produced in the present study.

Fig. 5.13(a) shows the surface of fused silica (Spectrosil) which has been diamond turned (depth of cut: ≈ 120 *nm*, cross-feed 0.5 μ*m/rev*, spindle speed: 120 rpm) with a canoe-shape tool (included angle: 60^o; see section 3.4.2). The Talystep record of Fig. 5.13(a), shown in Fig. 5.13(b), display a peak-to-valley depth of around 2 nm. Because of such small peak-to-valley value, when the machined surface was examined under SEM it had to be viewed normal to the cutting direction and had a 60^o tilt angle to show the surface feature (fine grooves).

Scanning electron micrographs of slow speed single-point diamond turned (with canoe shaped tool) silicon single crystal (1 1 1) surfaces and their surface roughness traces (recorded by Nanosurf) are shown in Fig. 5.14 and Fig. 5.15(a) respectively. The histogram of peak and valley heights of the surface roughness trace is shown in Fig. 5.15(b) while the centre line average (CLA or denoted as Ra) values for different sampling (trace) lengths are summarised in Table 5.1.

Table 5.1

Sampling Length (μ*m*)	0.25	0.8	2.5	8.00	25.00	80.00
Ra (CLA) (nm)	0.23	0.29	0.36	0.39	0.41	0.5

Fig. 5.16(a) shows the surface of single crystal silicon which was diamond turned with a roof-edge type tool and a high spindle speed (3000 rpm). Fine powder-like "chips" generated during machining can be seen accumulated at the right-hand side of the Fig. 5.16(a). The detail of the machining marks (grooves) is shown in Fig. 5.16(b) where the preset 80 nm/rev cross-feed can be checked by measuring the spacing between the grooves (the small deviation of the spacing was introduced by the speed instability of the cross-feed driving motor).

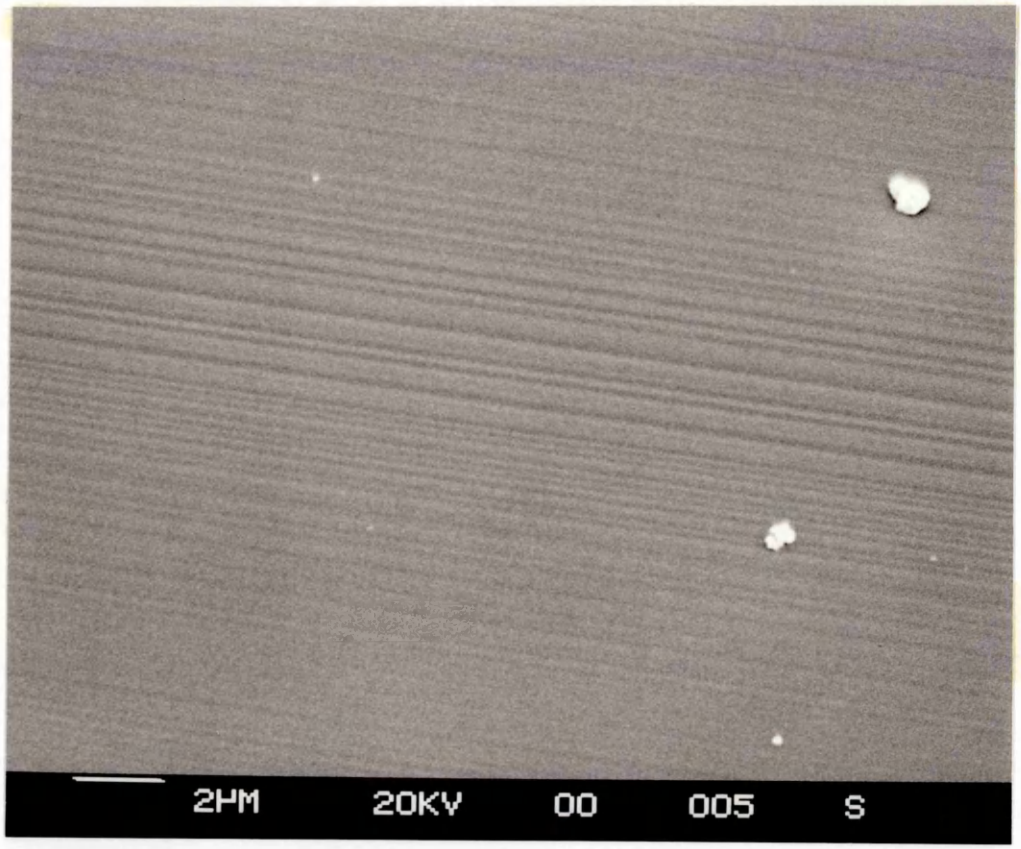

(a)

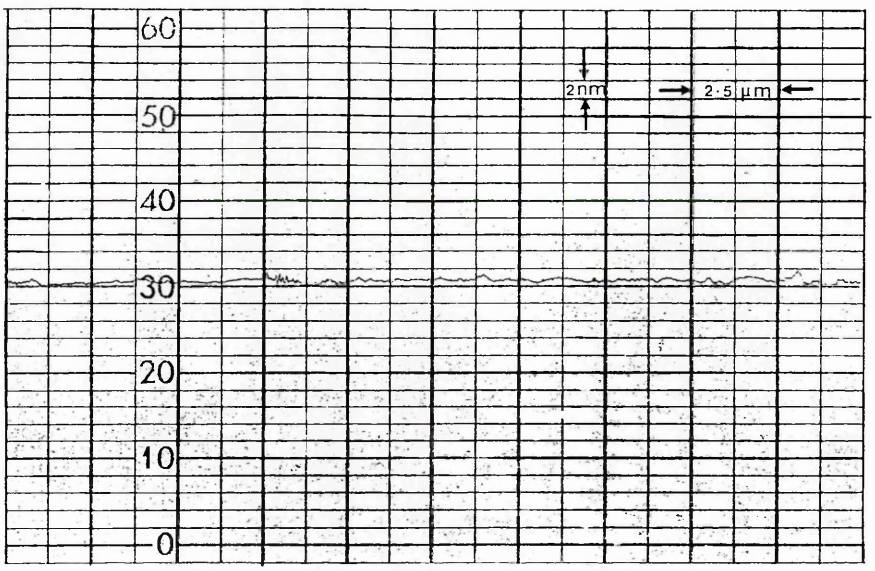

(b)

Fig. 5.13 (a) Scanning electron micrograph showing the surface of fused silica (Spectrosil) which has been diamond turned (depth of cut: ≈ 120 *nm*, cross-feed 0.5 µ*m*/*rev*, spindle speed: 120 rpm) with a canoe-shape tool (included angle: 60°) (b) Talystep record of a) showing a peak-to-valley depth of around 2 nm.

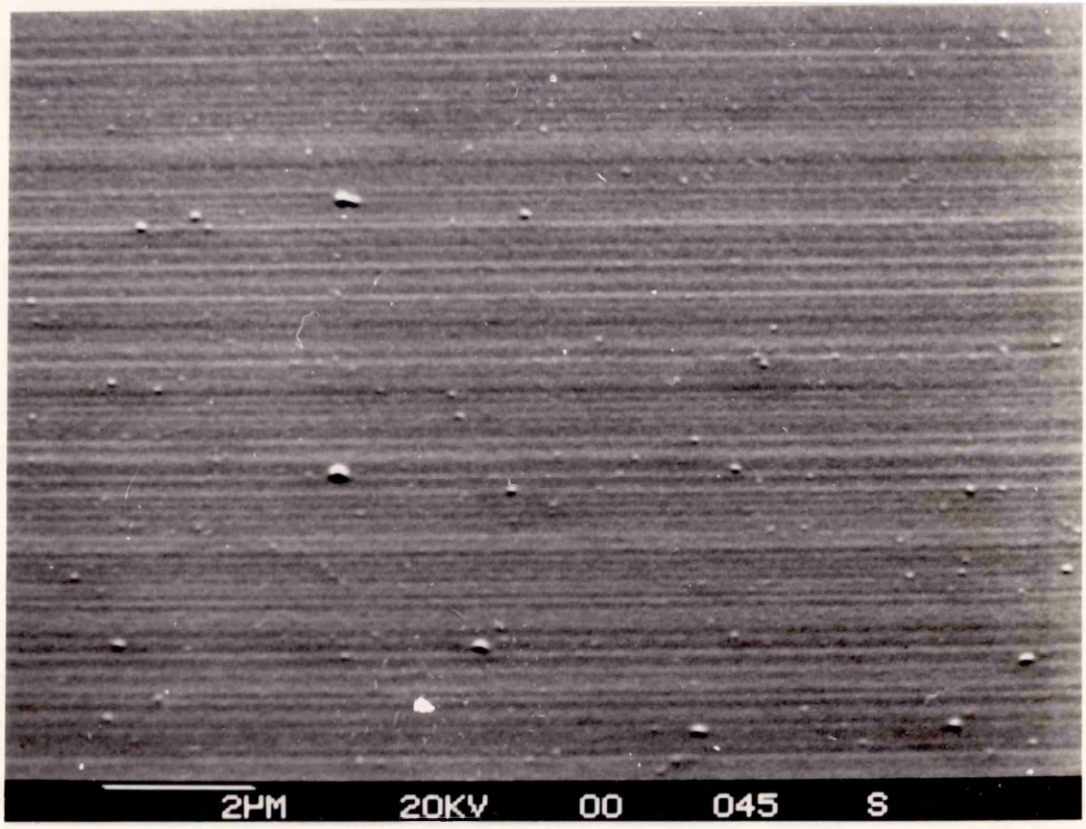

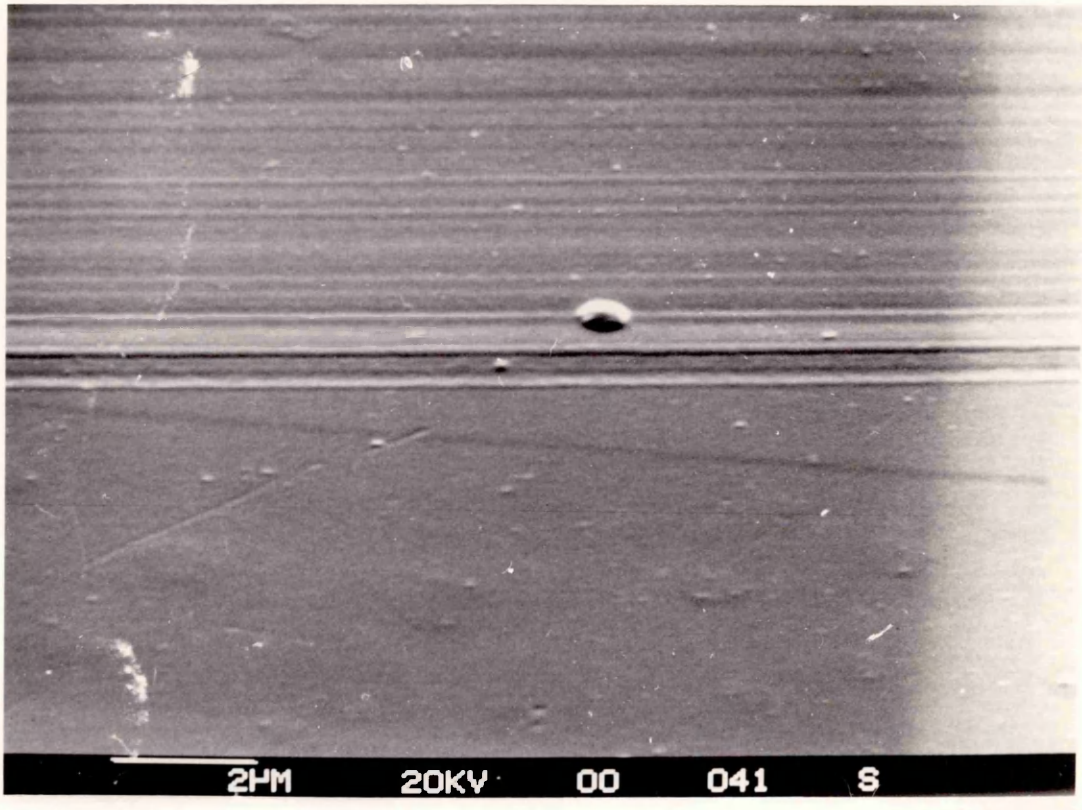

Fig. 5.14 Scanning electron micrographs of slow speed single-point diamond turned (with canoe shaped tool) silicon single crystal (1 1 1) surfaces.

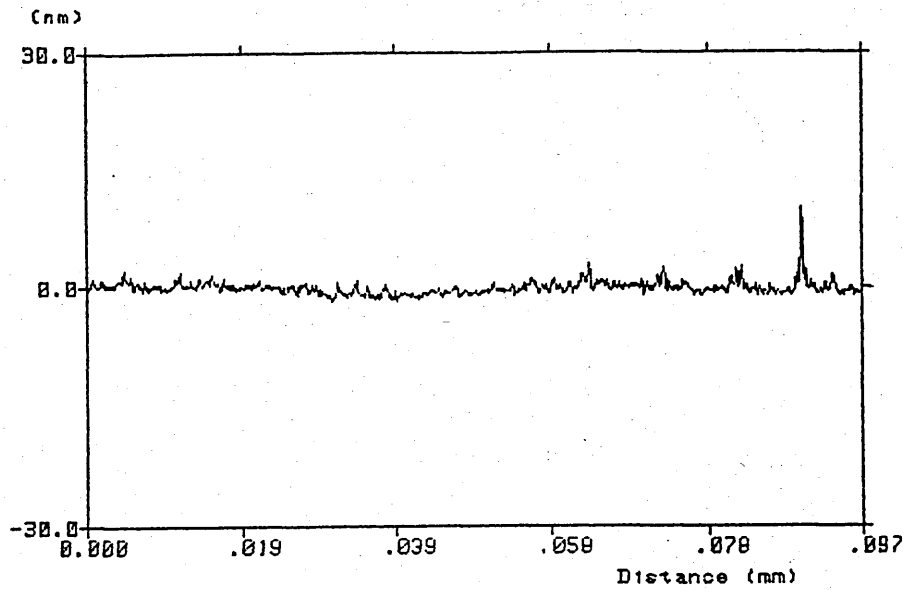

(a)

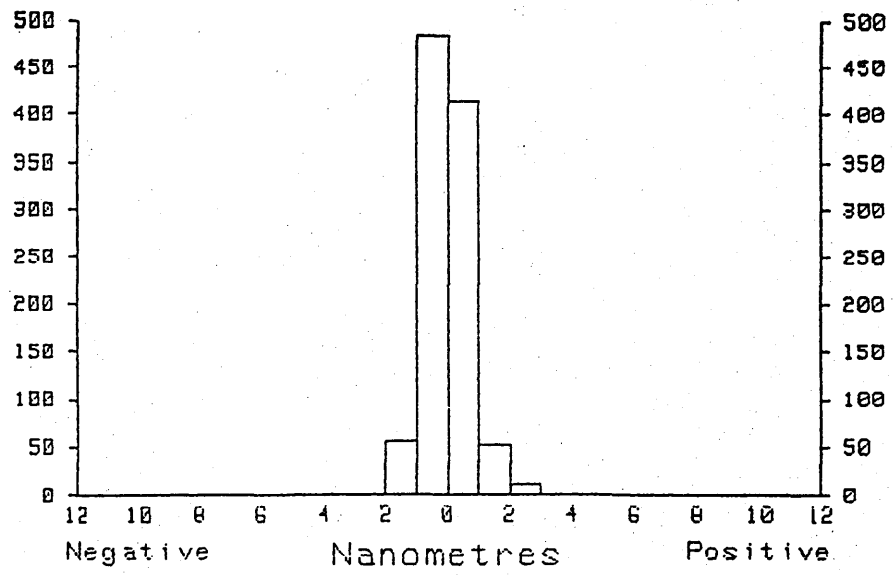

(b)

Fig. 5.15 (a) Surface roughness traces (recorded by Nanosurf) of the surface shown in Fig. 5.14, and (b) the histogram of peak and valley heights of the surface roughness trace.

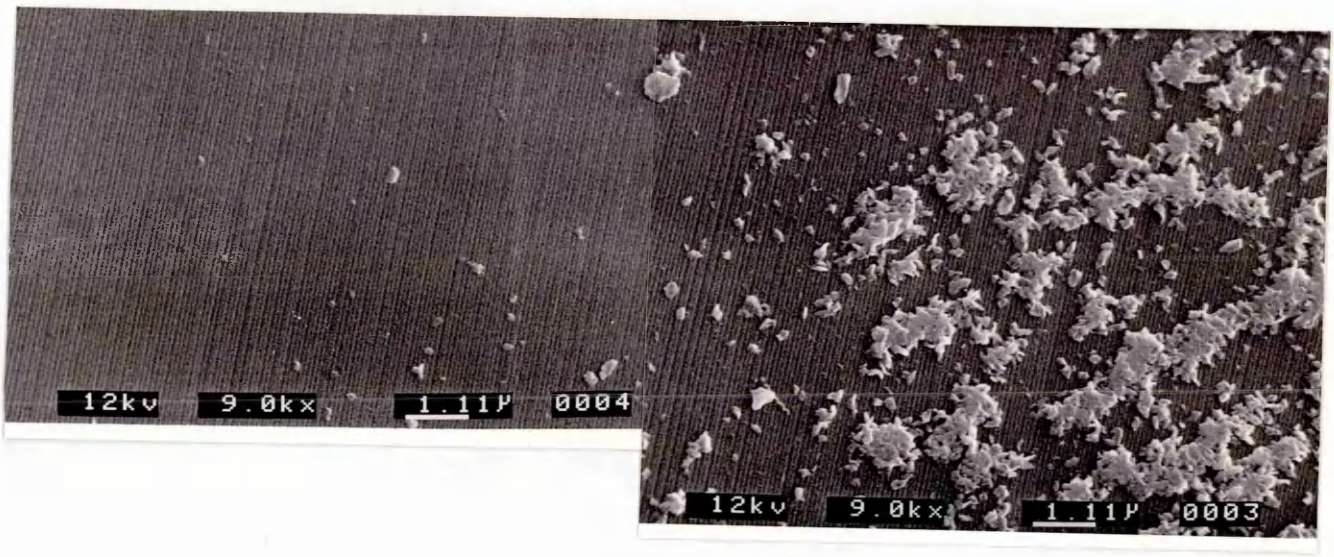

(a)

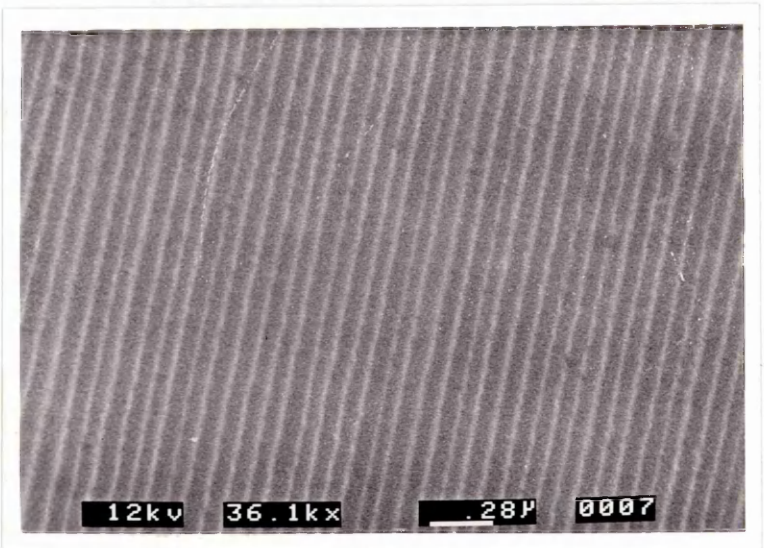

(b)

Fig. 5.16 Scanning electron micrographs showing the surface of single crystal silicon which was diamond turned with a roof-edge type tool and a high spindle speed (3000 rpm) (a) general view (b) detail of the machining marks (grooves).

5.5 Tool-tip Temperature and Wear of Diamond

5.5.1 Tool-Tip Temperature

Measurement of tool tip temperature is complex as it is a function of tool shape, cut-depth, tool, and specimen/workpiece- material (physical properties such as: thermal conductivities, thermal expansion coefficients, Young's modulus, and hardness), cutting speed, ambient temperature and coefficient of convection, cross-feed, coefficient of kinetic friction, material removal mechanism, and, in case of "wet" cutting, the type of coolant (its physical properties such as: heat capacity), and flow rate and coolant intake temperature. During the cutting process the tool is heated by thermal energy generated by friction between tool and workpiece and is cooled by the oncoming (and cooler) part of workpiece and by the air (dry cutting) or coolant (wet cutting) through convection heat transfer, while the workpiece is heated by the source and by conduction from the tool and cooled by air or coolant. As pointed out by Jaeger (1943), the uncertainty of the nature of contact and the very wide range possible in the numerical parameters practically limited mathematical discussion to numerical calculations for a particular model of a specific system, making general discussion difficult.

To investigate the surface temperature of sliding metals, Bowden and Ridler (1936) considered a cylinder sliding over a surface with a velocity v. To simplify this three dimensional heat transfer problem, they lumped the radial temperature-distribution inside the cylinder, thereby making it a one dimensional (axial) problem. This approach has been adopted here to approximate the tool tip temperature.

A few assumptions have been made to further simplify the problem, these are

(1) steady-state conditions;

(2) one-dimensional transfer in the axial direction;

(3) the ambient temperature remains constant, T_∞;

(4) the only heat source is generated by frictional work q_g between tool and workpiece, and a constant fraction, $(1-\alpha_g)\,q_g$, of the generated energy transfers to tool via conduction heat transfer [Thus, if we consider a square slider $(2l \times 2l)$ with normal load P_L, the coefficient of friction μ_f

$$q_g = \mu_f P_L g V$$

$$q_{flux} = \frac{q_g}{l^2}$$

where V is the sliding speed.]

(5) the frictional coefficient, μ_f, remains constant;

(6) the relative speed between tool and workpiece, V, and the contact area, A_k, remain constant during the experiment.

Based on Jaeger's (1943) study of the case of a slider with a square contact of side $2l$, thermal constant K_2 (conductivity), ξ_2 ($= \frac{K_2}{\rho_2 c_{p2}}$ where ρ is the density and c_p is specific heat) and coefficient of convection h from its sides, slides with velocity V on a semi-infinite medium K_1 (conductivity), ξ_1 ($= \frac{K_1}{\rho_1 c_{p1}}$), the value of the fraction, α_g, of heat generated and passing to the medium can be obtained

(1) in case of a long square slider:

(i) for small L ($= \frac{Vl}{2\xi_2}$)

$$\alpha_g = \frac{K_1}{K_1 + 1.338 (l K_2 h)^{1/2}} \qquad (5.15)$$

(ii) for large L, ($L > 5$)

$$\alpha_g = \frac{K_1 V^{1/2}}{K_1 V^{1/2} + 1.504 (\xi_1 K_2 h)^{1/2}} \qquad (5.16)$$

(2) in case of a semi-infinite slider with a square contact of sides $2l$:

(i) for small L ($= \frac{Vl}{2\xi_2}$)

$$\alpha_g = \frac{K_1}{(K_1 + K_2)} \qquad (5.17)$$

(ii) for large L, ($L > 5$)

$$\alpha_g = \frac{K_1 (lV)^{1/2}}{1.125 K_2 \xi_1^{1/2} + K_1 (lV)^{1/2}} \qquad (5.18)$$

Jaeger (1943) suggested that α_g tended to $\frac{1}{2}$ for small value of V, and increased steadily as V increased. Since the real tool cannot be either one of the above mentioned slider shapes, the second case is more suitable for a tool with large included angle.

In the steady state, the heat input rate (via heat conduction), q_{cond}, equals to the heat removal rate (via convection), q_{conv}. Applying the conservation of energy requirement to a differential element of the cylinder, we obtain

$$q_{cond}\,|_{\,z} = q_{cond}\,|_{\,z+dz} + d\,q_{conv}$$

From Fourier's law we know that

$$q_{cond}\,|_{\,z} = -\,K A_k \frac{dT}{dz}$$

The convection heat transfer rate can be expressed as

$$d\,q_{conv} = h\,(d\,A_c)\,(T - T_\infty)$$

where $A_c\,(= P_t\,z)$ is the surface area and P_t is the tool perimeter. Substituting the foregoing rate equation into the energy balance equation we obtain

$$K A_k \frac{d^2 T}{d\,z^2} - h\,P_t\,(T - T_\infty) = 0$$

Its general solution is of the form

$$T - T_\infty = C_1\,e^{m\,z} + C_2\,e^{-\,m\,z}$$

where

$$m^2 = \frac{h\,P_t}{K\,A_k} \qquad (5.19)$$

By using the boundary conditions

(1) $T \to T_\infty$ when $z \to \infty$, and

(2) $q_{cond}\,|_{\,z=0} = (1 - \alpha_g)\,q_g$,

the constants can be obtained as $C_1 = 0$ and $C_2 = \frac{(1-\alpha_g)\, q_g}{(h K P_t A_k)^{1/2}}$.

Thus, the temperature distribution with respect to z may be expressed as

$$T - T_\infty = \frac{(1-\alpha_g)\, q_g}{(h K P_t A_k)^{1/2}}\, e^{-mz} \qquad (5.20)$$

To estimate the coefficient of convection and to determine if the effect of convection is negligible for dry cutting conditions, again, it is necessary to resort to a simplified two-dimensional approach. The problem of a heated cylinder in cross-flow is adopted here to get some ideal of the effect of convection comparing to conduction. We assume that the air flows normal to the axis of the tool with a velocity of the magnitude of the cutting speed, V, and temperature of T_∞. In the case of fly-cutting the cutting speed can be given as: $V = \omega R$ where ω is the angular speed of the fly cutter and R is the radius of rotation. In the case of fixed tool and rotating workpiece facing process, however, the velocity is not a constant. The laminar flow over a disc rotating with an angular speed of ω was analyzed by von Karman (1921), who assumed that the tangential velocity is of the form

$$V = \omega R\, G(\zeta) \qquad (5.21)$$

where

$$\zeta = z\left(\frac{\omega}{\nu_{vis}}\right)^{1/2} \qquad (5.22)$$

z is the vertical distance from the disc, ν_{vis} is the kinematic viscosity of air and $G(\zeta)$ is a function of ζ which equals to 1 when $\zeta = 0$, 0.5171 when $\zeta = 0.9$, and 0 when $\zeta = \infty$ (see Owen and Rogers 1989). The tool tip of interest is only several millimetres long where the tangential velocity drops from ωR (at z = 0) to near zero. To take a very crude approach, we use half the maximum velocity as an average velocity.

An empirical equation was proposed by Churchill and Bernstein (1977):

$$\overline{Nu} = 0.3 + \frac{0.62\,\mathrm{Re}^{1/2} Pr^{1/3}}{\left[1+\left(\frac{0.4}{Pr}\right)^{2/3}\right]^{1/4}}\left[1+\left(\frac{\mathrm{Re}}{28200}\right)^{5/8}\right]^{4/5} \qquad (5.23)$$

where $\overline{Nu} = \frac{h D}{K}$ is the Nusselt number, $\mathrm{Re} = \frac{\rho V D}{\mu_{vis}}$ is the Reynold's number, Pr is the Prandtl number, D is the diameter of the cylinder, μ_{vis} is the viscosity of air. The properties of air are decided by "film" temperature, T_f which is defined as the average of ambient temperature, T_∞, and cylinder surface temperature, T_s, thus $T_f = \frac{T_\infty + T_s}{2}$.

Since the surface temperature is unknown, the ambient temperature may be used as the surface temperature (thereby as film temperature) to make the first estimate of h. This estimate h may then be used to derive the approximate surface temperature which in turn can be used to calculate the film temperature and h. Few such calculation cycles may be needed before reasonable repeatability is reached.

For a square source the maximum temperature change of the workpiece surface, suggested by Jaeger (1943), can be approximated as:

(i) for small L

$$\Delta T_{\max} \approx 1.122 \frac{\alpha_g q_{flux} l}{K_1} \qquad (5.24)$$

(ii) for large L

$$\Delta T_{\max} \approx \frac{2\,\alpha_g q_{flux}}{K_1}\left(\frac{2\,\xi_1 l}{\pi V}\right)^{1/2} \qquad (5.25)$$

In the case of single-point facing soda-lime glass using a (Vickers indenter) diamond tool with cut depth of 0.5 μm, spindle speed of 4000 rpm , workpiece radius of 30 mm, coefficient of friction 0.4 (as determined experimentally in this study), vertical force 0.01 N, α_g (from equation 5.17) equals 1.34×10^{-3}, film temperature $\approx$ 1225 ^oK, kinematic viscosity of air at film temperature 166×10^{-6}, Prandtl number 0.726, Reynolds number 299, Nusselt number 9.2 (equation 5.23), coefficient of

convection 11.6×10^{-3}, m equals to 684.8 (equation 5.19), then, from equation 5.20, it follows that the diamond tip temperature is 2154 ^{o}K. This estimate suggests that temperature rises very significant both for workpiece and tool materials may be generated at high spindle speeds.

5.5.2 Wear of Diamond Tools

As mentioned in chapter 3 (section 3.4.1), diamond tools can be readily abused if not handled properly although diamond is the hardest material known. However, after a certain amount of cutting operations part of a diamond tool (especially around the cutting edge) will be worn away, even if it has been handled with great care. Tolkowsky (1920), and Wilks and Wilks (1959) suggested that diamond wears in such a way that small flakes are chipped off from the area of contact. They suggested that this process of micro-chipping was very sensitive to direction and not thermal activated.

Apart from the above mentioned gradual wear, relatively large scale irregular chipping and cracking may appear in the vicinity of the tool tip. The possible cause of such premature cracking or fracture is a defect or an imperfection in the diamond (King and Wilks 1976, Wilks and Wilks 1979). As pointed out by Wilks (1980) and more recently by Motonishi, Hara and Yoshida (1990), the most obvious defects are inclusions, especially those close to a surface or an edge.

Fig. 5.17(a) and (b) show some of the chipping sites on the cutting edge of one of the diamond tools used in this study. The detailed view of Fig. 5.17(a) is shown in Fig. 5.17(c); the regular layer-pattern on the surface suggested that it might be caused by cleavage fracture. Several cracks can also be seen in Fig. 5.17(b) which are possible chipping sites in the subsequent machining.

Diamond is extremely brittle and does not become plastic until a temperature of 1900 ^{o}K (type IIa diamond) or 2100 ^{o}K (type Ia diamond) is reached (Evans and Wild 1965, Evans 1967). Farris and Chandrasekar (1990) used the infrared radiation at the diamond-sapphire interface to monitor the temperature. They found the average tip temperature increase with increasing sliding velocity and the average diamond indentor temperature during sliding against sapphire with a wheel velocity of 37 m/sec, depth of cut 0.01 mm, and average diamond tip diameter 15 μm , was $1270 \pm 80\ ^{o}C$ ($1543 \pm 80\ ^{o}K$).

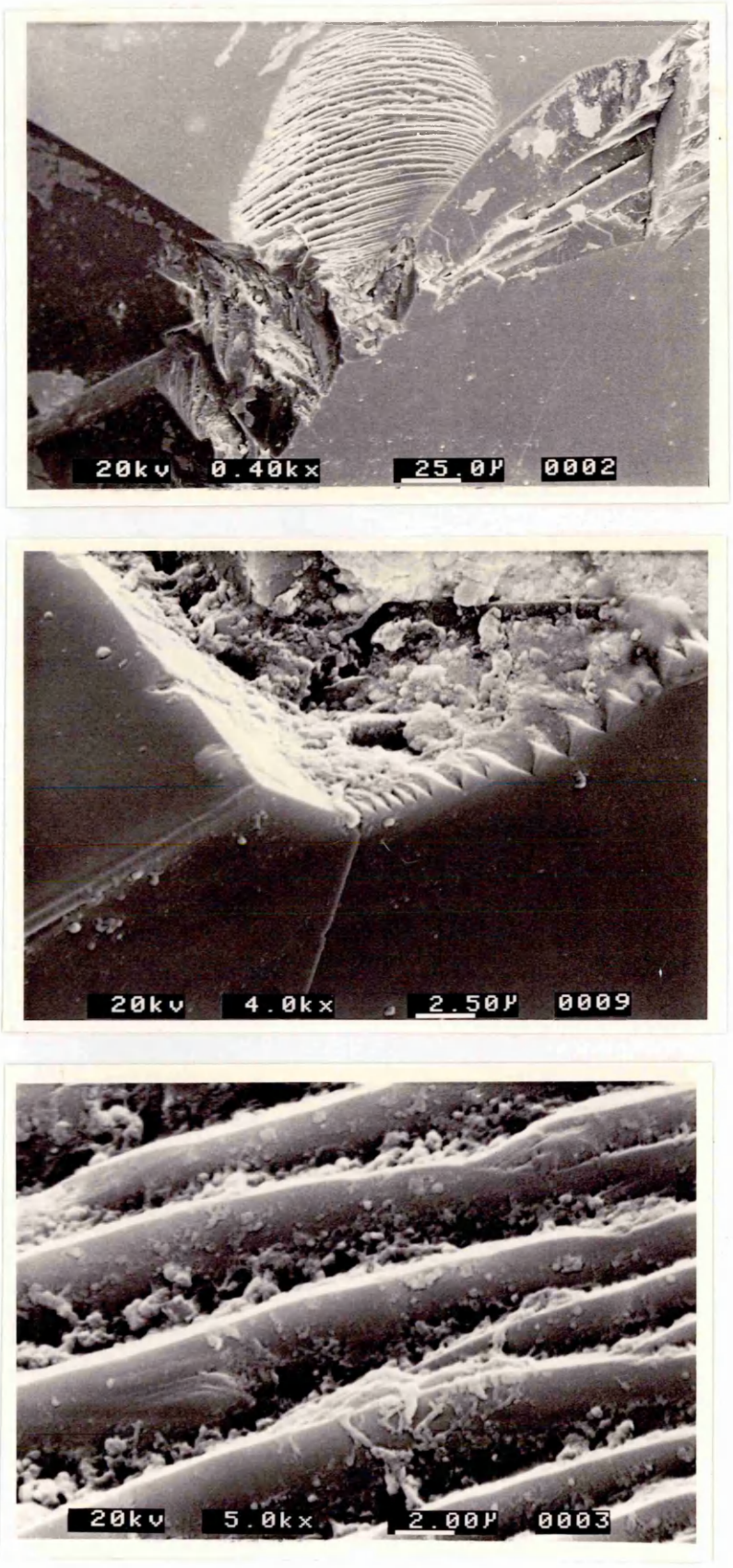

Fig. 5.17 (a) , (b) General view of the chipping sites on the cutting edge of one of the diamond tools used in this study (c) detail view of (a).

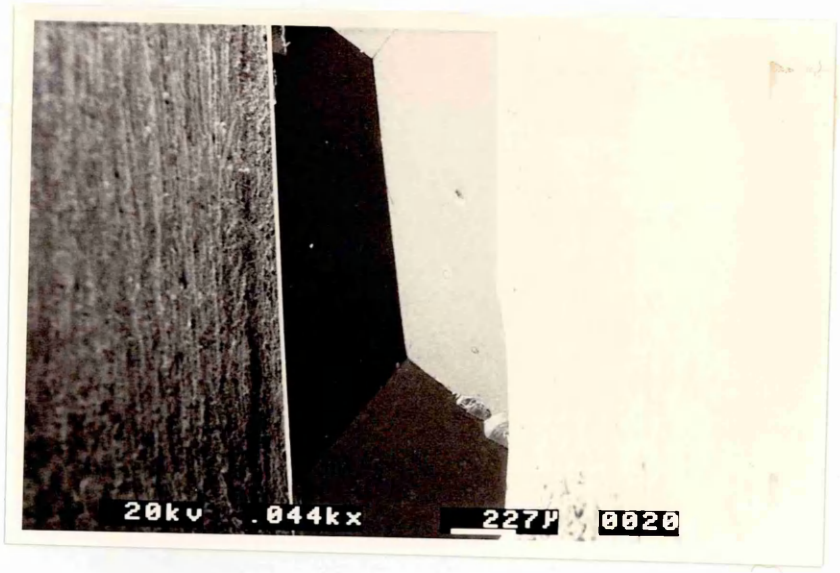

(a)

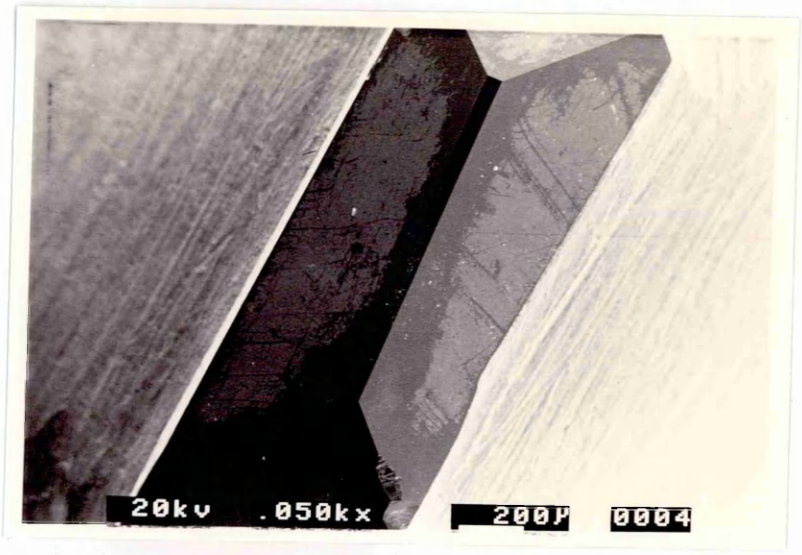

(b)

Fig. 5.18 Roof-edge tool (a) before and (b) after it was used as the tool for high speed diamond turning of silicon.

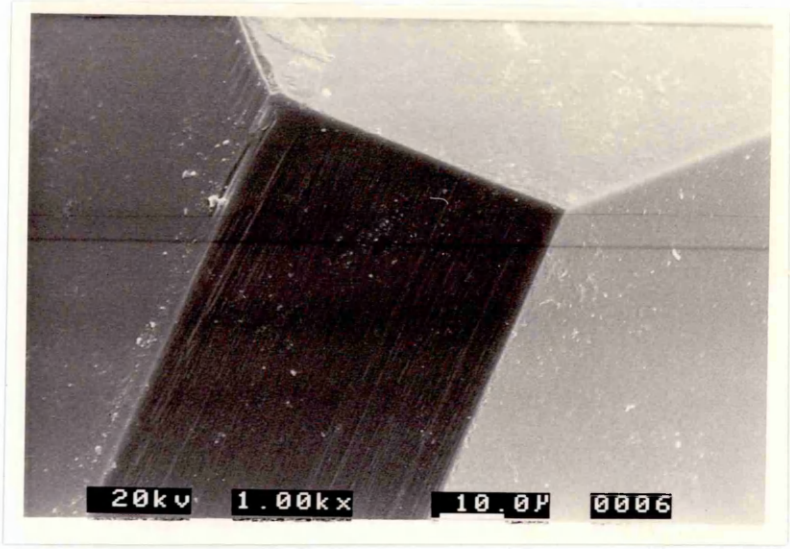

(a)

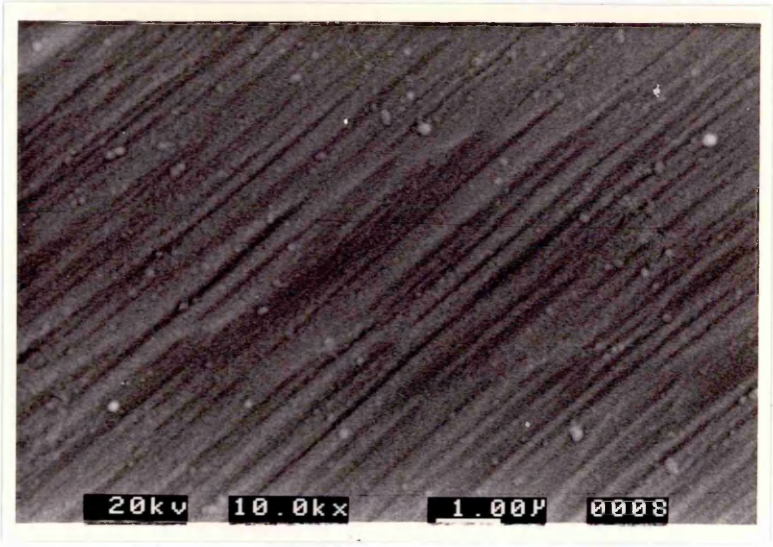

(b)

Fig. 5.19 Detail views of the worn "facet" on the cutting edge of what had been the edge of a roof-edge type diamond tool (a) corner (b) face.

The single diamond grain used by Farris and Chandrasekar (1990) was mounted on the periphery of an aluminium disc and worked like a fly-cutter (discrete contact-lengths). This means that in case of a continuous cutting process, such as single point diamond turning, the contact temperature should be even higher than the value obtained from fly cutting. Since the maximum diamond temperature measured by Farris and Chandrasekar (1990) was around 1620 ^oK, it is very possible that the temperature may reach the transition temperature (2100 ^oK) (type Ia diamond) suggested by Evans and Wild (1965).

Shown in Fig. 5.18(a) and Fig. 5.18(b) are the same tool (a) before and (b) after it was used as the tool for high speed diamond turning of silicon. Fig. 5.19(a) and Fig. 5.19(b) are detail views of the worn "facet" on the cutting edge of what had been the edge of a roof-edge type diamond tool. Although this tool had been used in previous low speed (200 rpm) diamond turning experiments on silicon single crystal, no great wear appeared on the edge (Fig. 5.18(a))until it was engaged in high speed (4000 rpm) machining (Fig. 5.18(b)). Fine grooves on the smooth worn "surface" (cutting "edge") suggest that the wear could not be caused by small scale flaking and chipping.

As a consequence of the cutting edge getting blunt after period of machining, the contact area is increased which, in case of fixed cutting depth, means higher vertical cutting force and tensile friction force. The thermal energy it generates as well as the tensile stress it applies to the workpiece during the cutting process will be higher compared with that on a sharp tool under the same machining conditions. If the tool is badly worn, the "cutting" process will become rather like a sliding process. The effect of this wearing/blunting process is manifest in the change of machining conditions as the contact area becomes larger.

In order to study the ductile-brittle transition, quite often in this study the diamond tools were subject to relatively high cutting forces to get brittle fracture, otherwise avoided in normal machining. Although efforts here have been made to obtain an estimate of the wearing mechanism of diamond tools, it is by no means an attempt to undertake comprehensively the range of problems in diamond wear.

5.6 Critical Cut Depth and the Influences of Pre-machining History and of Surface Roughness

In a series of single point turning experiments on silicon and fused silica for the present study, a ductile-brittle transition band was created by cutting into specimen-wedges (with tilt-angle about 3 to 5 arc second and cut-depth starting from zero). The value critical cut depth could therefore be measured using a stylus instrument (eg Rank-Taylor-Hobson 'Talysurf') at any point on the wedge. Fig. 5.20 shows such a ductile-brittle transition band on a specimen of single crystal silicon obtained by this 'wedge-cut' method.

The critical cut depths of soda lime glass, fused silica, and single crystal silicon (111), as obtained from the above experiments, are 0.9-1.4 μm, 0.5-0.9 μm and 0.5-0.8 μm respectively.

Since the cracks generated by a deep cut can propagate more than ten times the set cutting depth (Kirchner, Gruver and Richard 1979), both surface and sub-surface damage resulting from "coarse" machining may make finish machining (ie diamond turning to a ultra-fine surface finish) extremely difficult. To investigate the feasibility of diamond turning such a damaged specimen to the required fine surface finish, a series of multiple-pass experiments were conducted. The first pass was to

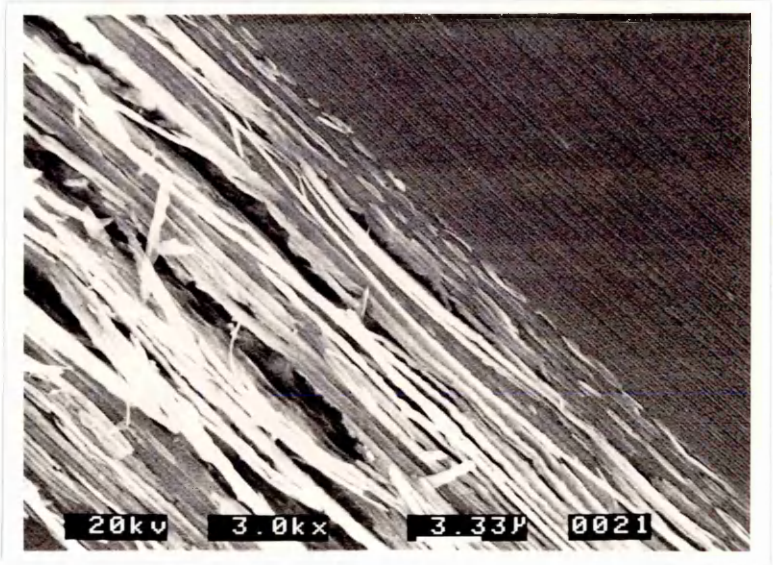

Fig. 5.20 A ductile-brittle transition band on single crystal silicon obtained by the 'wedge-cut' method (canoe shape diamond tool, spindle speed 3000 rpm, cross-feed rate ≈ 80 nm/rev).

introduce a ductile-brittle transition band by cutting into a wedge. The scale of the surface and sub-surface damage layer became larger as the tool went deeper into the wedge (ie qualitatively observed as cut depth increased). Whilst machining, the tool was then moved in and out of the damaged section several times (ie cross-fed back and forth) with the cut-depth increased, by less than the critical depth, at each reversal. The range of cross-feed rates used in these multi-pass experiments (with respect to spindle rotation) was 60-200 nm/rev.

It was found that

(1) when the accumulation of sub-critical amounted to cuts subsequent cutting depth was close to the critical cutting depth: the transition band did not change if the cross-feed direction was from ductile part towards the brittle part, but the brittle region started to expand into the ductile region if the tool was fed the other way

(2) with the subsequent (small-cut) cutting depth set to about half the critical cutting depth, the transition band could be moved into the previously brittle region, when cutting from ductile part toward the brittle; however, the same region was reoccupied by brittle damage when the tool motion was reversed.

(3) with a subsequent cutting depth of about one quarter to one third of the critical value, there was greater damage recovery than re-damage.

(Within the tested range, the influence of cross-feed rate on the results was insignificant).

Based on the results of these experiments, it is clear that, to prevent further propagating of the existing cracks, the cutting depth has to be kept very small (less than one quarter of the critical cutting depth). This makes single point diamond turning likely to be uneconomical for machining a heavily-damaged specimen due to the large number of passes necessary to remove the damaged layer. (Creep-feed diamond grinding may be a possible answer for this kind of work. However, as will be discussed in chapter 6, a very good surface finish does not guarantee that the deeply-penetrating median cracks have been totally removed.)

To investigate the influence of roughness of the workpiece, sawn and etched (to remove the residual stress on the surface) silicon wafers, shown in Fig. 5.21(a) (as received), were used as a test piece. When silicon was machined from polished side the critical cutting depth was around 0.5 to 0.8 μm . However, a fine machined surface was produced on the rough side even when a cutting depth of 5 μm was

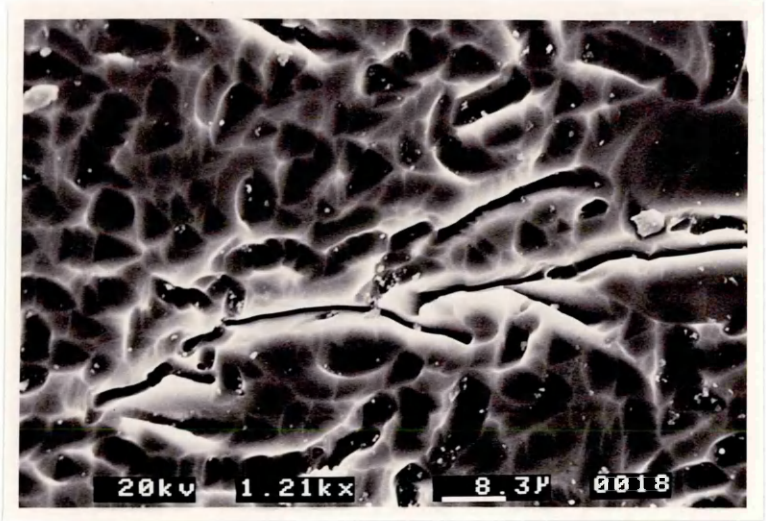

(a)

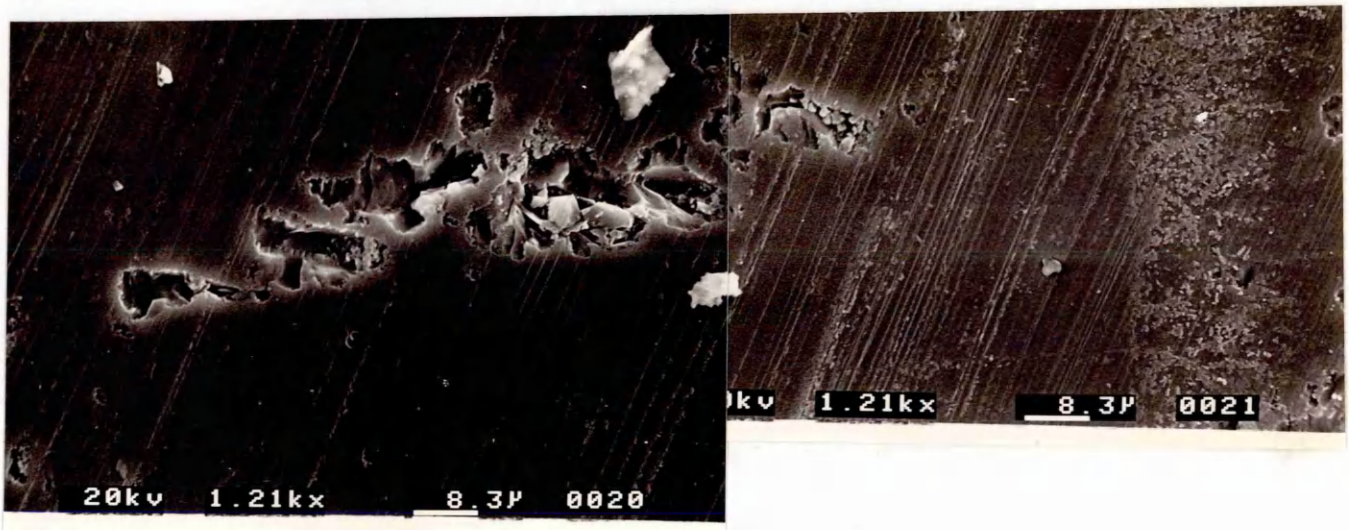

(b)

Fig. 5.21 Single crystal silicon wafer (111) sawn and etched surface (a) as received (b) after single pass of straight-edge (roof-corner) tool with cutting depth around 4.5 μm and cross-feed rate of 0.55 $\mu m/rev$.

used. Fig. 5.21(b) shows the surface generated by single pass of straight-edge (roof-corner) tool with cutting depth around 4.5 μm and cross-feed rate of 0.55 $\mu m/rev$. A few large "chips" were trapped inside the deep sawn marks remaining in the middle of this SEM micrograph. These chips, several micrometers in scale, were too large (larger than the cut) to be caused by plastic flow. A possible explanation is that these chips were caused by brittle chipping. However, the irregularity of the original rough surface caused the cracks to propagate upward and sideward instead of penetrating downward (and introducing large holes or deep cracks).

It was found in this work that the scattered large chips (from the damaged region or in the case of cutting rough silicon wafer the brittle chips) could sometimes be trapped between tool rake face and workpiece surface (worked as an extension of the tool). As a result, large hole and "partial" ring cracks (Fig. 5.23) (like the ones generated by sliding a blunt indenter across the surface as discussed in section 3.2.1) were obtained as the "cut depth" suddenly increased when the tool encountered and ran over the large debris.

Fig. 5.22 Large hole and "partial" ring cracks obtained as the "cut depth" suddenly increased when the tool encountered and ran over a large debris.

Chapter 6

Sub-Surface Damage

6.1 Introduction

One of the major problems in machining brittle materials is that almost all machining (shaping) methods will leave a layer of *sub-surface damage* (SSD). The plastic deformation and heat generated during machining causes the mechanical and physical properties of the base material near the machined surface to deteriorate.

As early as 1892 Lord Rayleigh noted that when a polished glass surface is etched with hydrofluoric acid a pattern of scratch marks is revealed (Rayleigh 1903). He proposed that the originally-invisible scratches were 'developed' by the etchant to become visible. Beilby (1921) reported that W. D. Haigh had made scratch marks on glass and quartz and, after removing them by polishing, had made them reappear by etching in hydrofluoric acid.

Polishing lenses, Rawstron (1958) found that, no matter how long the polishing continued, etching always showed scratch marks under the surface with marks following the polishing motion. Rawstron suggested that when a hard particle of polishing powder was moved across the lens, this penetrated the glass below the surface layer producing an abrasion, which was rapidly filled in by the viscous surface material (flowed into it by the drag of the polisher). The scratches lost their identity in the moving layer of glass, and were only revealed when the skin was fully penetrated by the etching fluid (the flowed material probably being different physically and chemically from the undisturbed glass). Preston (1921) found that ground glass was initially dissolved many times faster than polished glass by hydrofluoric acid, but after a few minutes the dissolution rate declined to the constant rate of a polished surface. He then suggested that the initially fast dissolution of a ground surface arose from its large surface area and the presence of surface cracks and stresses.

Understanding of the occurrence of *sub-surface damage* (SSD), in the form of micro-cracks or crazes, is likely to be vital in both structural ceramics and electro-optic materials. For structural ceramic materials, it could lead to failure under normally-acceptable stress/thermal environmental conditions. In the case of electro-optic materials, the unwanted increase of absorption and refraction in the sub-surface damage region could cause scattering and laser damage in optical systems. Also, electronic and magnetic properties, which are critical for semiconductor and disc-storage systems would be changed by sub-surface damage. For these reasons it is critical and important to understand the nature and extent of the sub-surface damage introduced in materials during the machining process if optimum workpiece quality is to be achieved.

Although the sub-surface damage has been noticed since almost a century ago and has in recent years been receiving increasing attention and great progress has been made, it is still far from fully understood. One reason for this is that the scale of the sub-surface damage generated by precision and ultra-precision machining is so small that it is extremely difficult to measure and quantify. To tackle this problem, there has been considerable effort and a wide range of methods have been employed, both destructive and non-destructive. Commonly-used destructive measuring techniques are etching and wedge polishing where the most popular non-destructive techniques include scanning acoustic microscopy (SAM), X-ray topography (diffraction), Rutherford back scattering and Raman spectroscopy. Within those mentioned techniques, micro-indentation, SAM, X-ray topography and Rutherford back scattering (RBS) have been used in this study and will be discussed in the following sections.

Due to the high cost of the precision measuring instruments (such as SAM, X-ray topography, and RBS) required, access tends to be obtained through collaborations. The SAM, X-ray topography, and RBS used in this study were located in Oxford University, (Dept for the Science of Materials), University of London (Royal Holloway and Bedford New College, Dept of Physics), and Surrey University (Department of Physics and of Electronic and Electrical Engineering) respectively. However, owing to the limited accessibility of these instruments, the results could only serve as a feasibility study.

6.2 Scanning Acoustic Microscope (SAM) Studies

An acoustic microscope, as revealed in its name, uses acoustic energy to interact with a specimen and the reflected acoustic radiation will carry the information of the specimen. The idea of using ultrasonic energy to generate an acoustic microscopic image was first proposed by a Sokolov (1949) and was accepted in the late 1960s. Unlike other forms of radiation, acoustic waves interact directly with the elastic properties of the materials through which it propagate.

[The following paragraph is taken from Scruby et al (1989) in which the present author co-authored] An acoustic lens is made from a crystal rod, e.g. sapphire, with a ground concave spherical surface in one end and polished optical flat in the other. At the flat end of the rod a thin film piezoelectric transducer, consisting of layer of zinc oxide sandwiched between two layers of gold, is bonded to the surface (as shown in Fig. 6.1). The transducer is pulsed and alternately acts as a transmitter and receiver. The front surface of the lens is coated with a quarter-wave layer of chalcogenide glass as an anti-reflection coating between the coupling fluid (water) and the sapphire. The input transducer converts an oscillatory electromagnetic field

Coupling Fluid

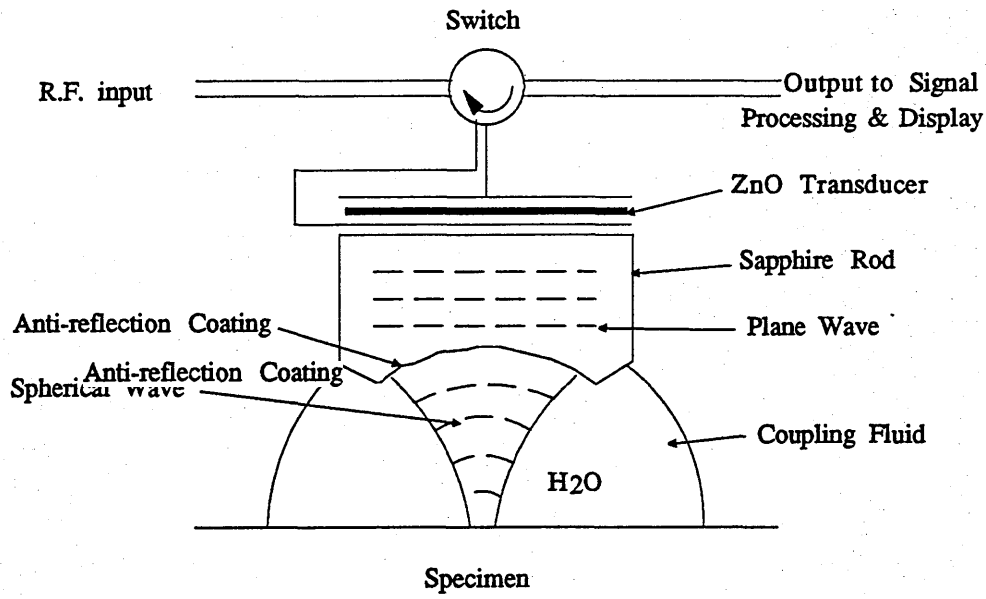

Fig. 6.1 A schematic layout of SAM lens. (After Quate, Atalar and Wickramasinghe 1979)

into a pulsed acoustic wave of the same frequency. In the crystal, the acoustic wave propagates as an approximately collimated beam until it is refracted at the lens surface. Part of the wave will propagate into the coupling fluid in the form of spherical wave which converge to a narrow waist at the focal plane. The specimen is positioned initially at the focal plane where it reflects much of this acoustic energy back through the lens into the sapphire where it is detected by the transducer. Pulsed radiation is used so that the signals of interest can be separated from the coupling liquid and other spurious reflections.

The contrast of the image produced by the acoustic microscope is dependent on the condition of interference between the Rayleigh waves (generated by the waves incident at the critical angle) and the waves incident normally.

Fig. 6.2 shows various focal conditions (Scruby et al 1989). The SAM has essentially two focal conditions:

(1) focused on the surface of the specimen (Fig. 6.2a), the reflected ray does not travel into and propagate alone the specimen surface so that the contrast in the image depends upon if there are cracks on the surface to scatter the incident wave. Since the focus point is on the surface, the critical angle ray does not penetrate into

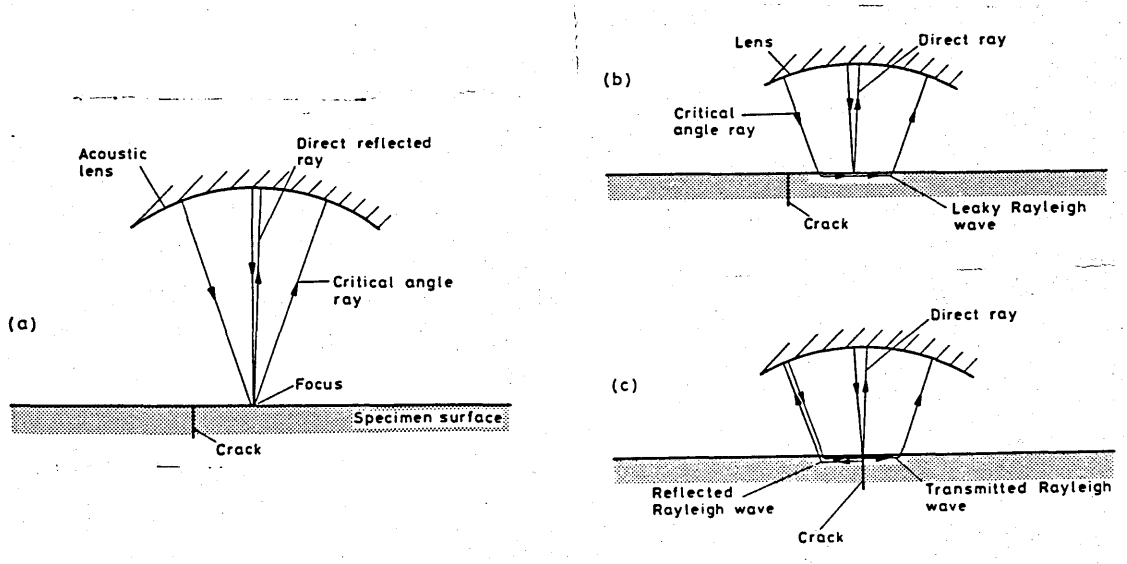

Fig. 6.2 (a) Showing two principal rays that interfere constructively when lens is forcused at surface. (b) When lens is moved towards specimen, ray at Rayleigh angle (approximately 15o in silicon nitride) converts to Rayleigh wave that leaks energy back into lens. (c) When crack is present there is additional interference between Rayleigh wave reflected from crack and the other two rays. (After Scruby et al 1989)

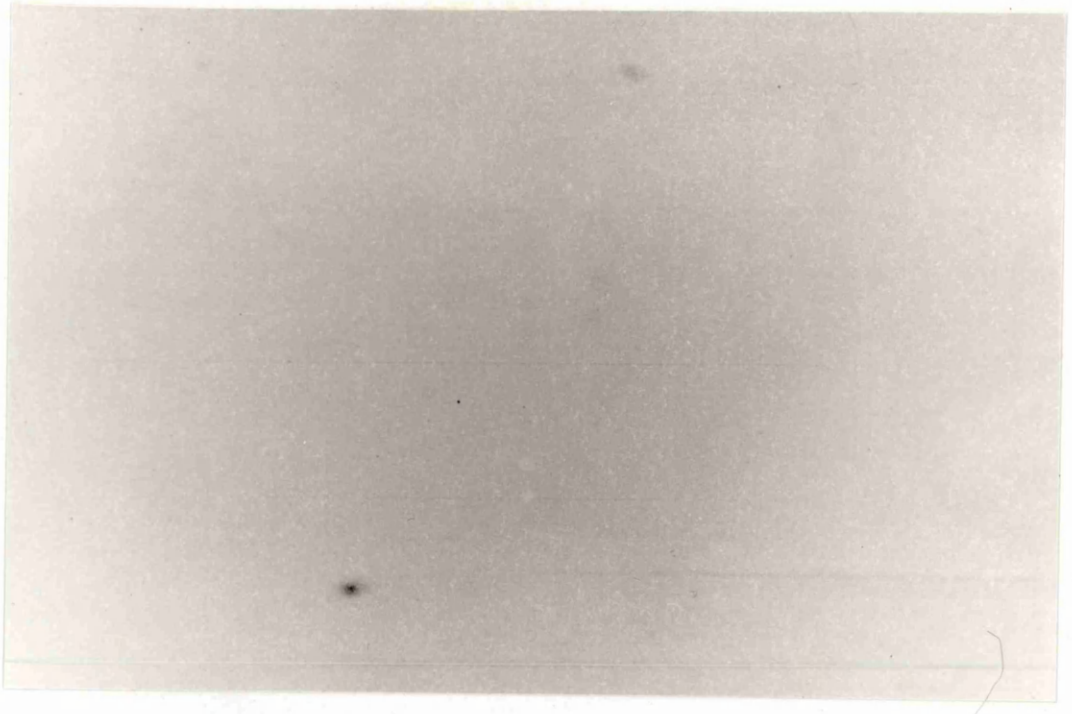

(a)

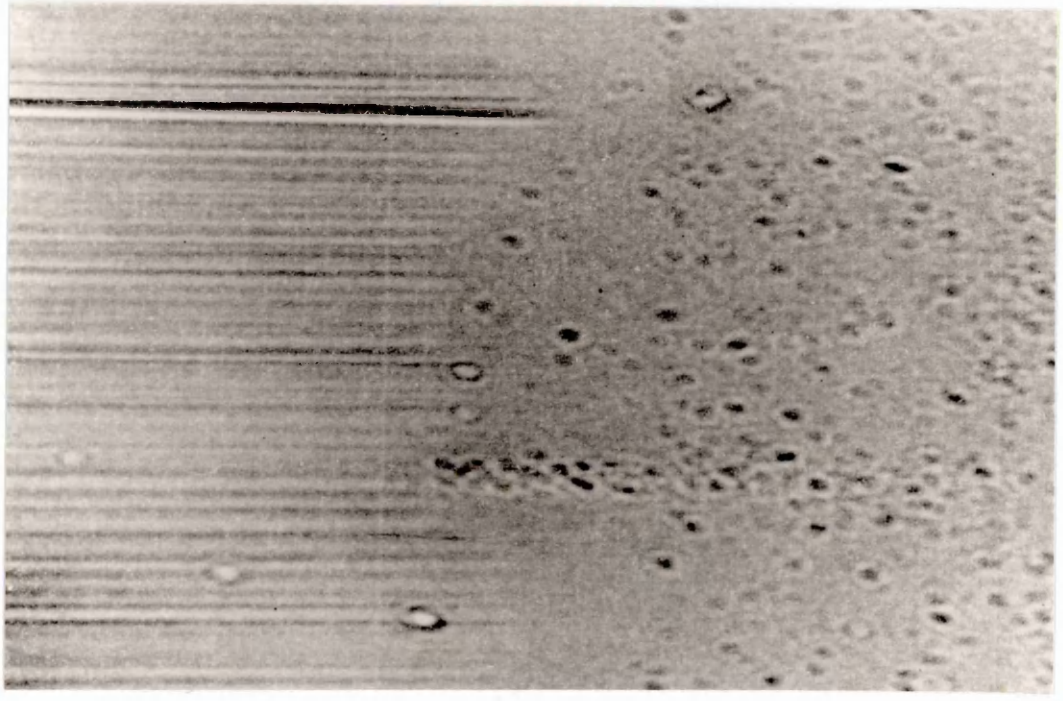

(b)

Fig. 6.3 Acoustic micrographs of zirconia specimen where left-hand side had been coarsely ground and whole surface was subsequently fine-ground until damage invisible optically. Sub-surface damage observed in (b) where z= -12 μm, although not visible in (a) where z= 0 (370 MHz operating frequency was used in both cases).

the specimen and the detected information is very superficial. Thus, a tightly closed crack might be very difficult to detect.

(2) negatively de-focused (moving the lens towards the specimen)(Fig. 6.2b,2c): the excited Rayleigh waves will penetrate some distance into the specimen and travel along (and beneath) the surface. These Rayleigh waves may be scattered and reflected by a crack and the reflected Rayleigh waves will interfere with the incident Rayleigh wave to produce fringes surrounding the crack.

The Rayleigh waves interaction described above makes SAM a very sensitive to material defects (e.g. cracks, inclusions, and porosity). An important application of this capability is to reveal a tightly closed surface crack or a sub-surface crack (sub-surface damage) which are very difficult to be detected by scanning electron microscope or optical microscope.

The SAM used in this study was located in the Department for the Science of Materials, Oxford University, with the experiments were assisted by Dr. C. B. Scruby, Dr. A. D. Briggs and Mr. C. W. Lawrence whose cooperation is gratefully acknowledged.

The SAM can be used over a wide range of frequencies (2 MHz to 8 GHz). Kino (1987) stated that, with an operating frequency of 3 GHz, the "definition" (spatial resolution) in water is better than 400 nm, and, operating in liquid helium with a frequency of 8 GHz, it is better than 30 nm. With the instrument available and operating frequency ranging from 200 MHz to 500 MHz in water, the possible resolution was in the range 3 μm to 5 μm. As outlined in Chapter 1, in this study, SAM was used to examine the damage caused by coarse-grinding. A higher operating frequency (ie above 3 GHz) is needed if the SAM is to be used to examine sub-micrometre sub-surface damage.

Shown in Fig. 6.3 is the acoustic image of a zirconia specimen which was coarsely ground in one corner at a shallow angle (wedged grinding) and was subsequently fine-ground until the machining marks were no longer visible in an optical microscope. When the SAM was focused on the surface of the specimen the acoustic image did not reveal evidence of SSD (FIG. 6.3a). However, when $z = -12\ \mu m$ (370 MHz frequency) the sub-surface damage caused by the machining appeared on the left of the acoustic image (Fig. 6.3b).

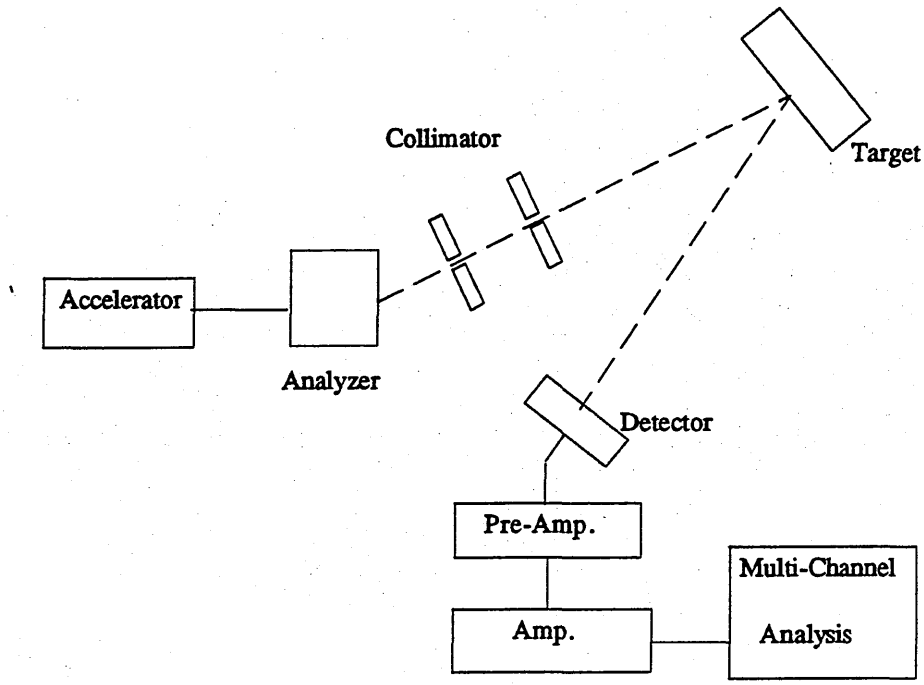

Fig. 6.4 Schematic layout of a ion back-scattering experiment.

6.3 Rutherford Back-Scattering

The basic concept of Rutherford back scattering (RBS) technique is to bombard the target material with a beam of ions and use the energy spectrum of back-scattering to analyze the material. As shown in Fig. 6.4, RBS consists of (1) a particle source which is a Van de Graaff accelerator (2) the beam line (under vacuum and containing the collimation system) (3) a goniometer and its associated equipment for aligning the target with respect to the beam (4) a charged particle detector, from which the back-scattered ion is detected, together with signal processing equipment which generate the energy spectrum signal.

When a source particle hits and penetrates a target, it loses energy through exchange of energy on collision with target particles. The energy lost per unit depth of penetration depends on the type and velocity of the source particle, together with the target material structure and composition. It is the changes of energy between input and back-scattered ions (energy loss) that carry the required information about the target material. By measuring this energy loss, the depth of a back-scattering event (from where it is back-scattered) in a target material can be calculated. The output signal from the detector is processed by a multi-channel analyzer which

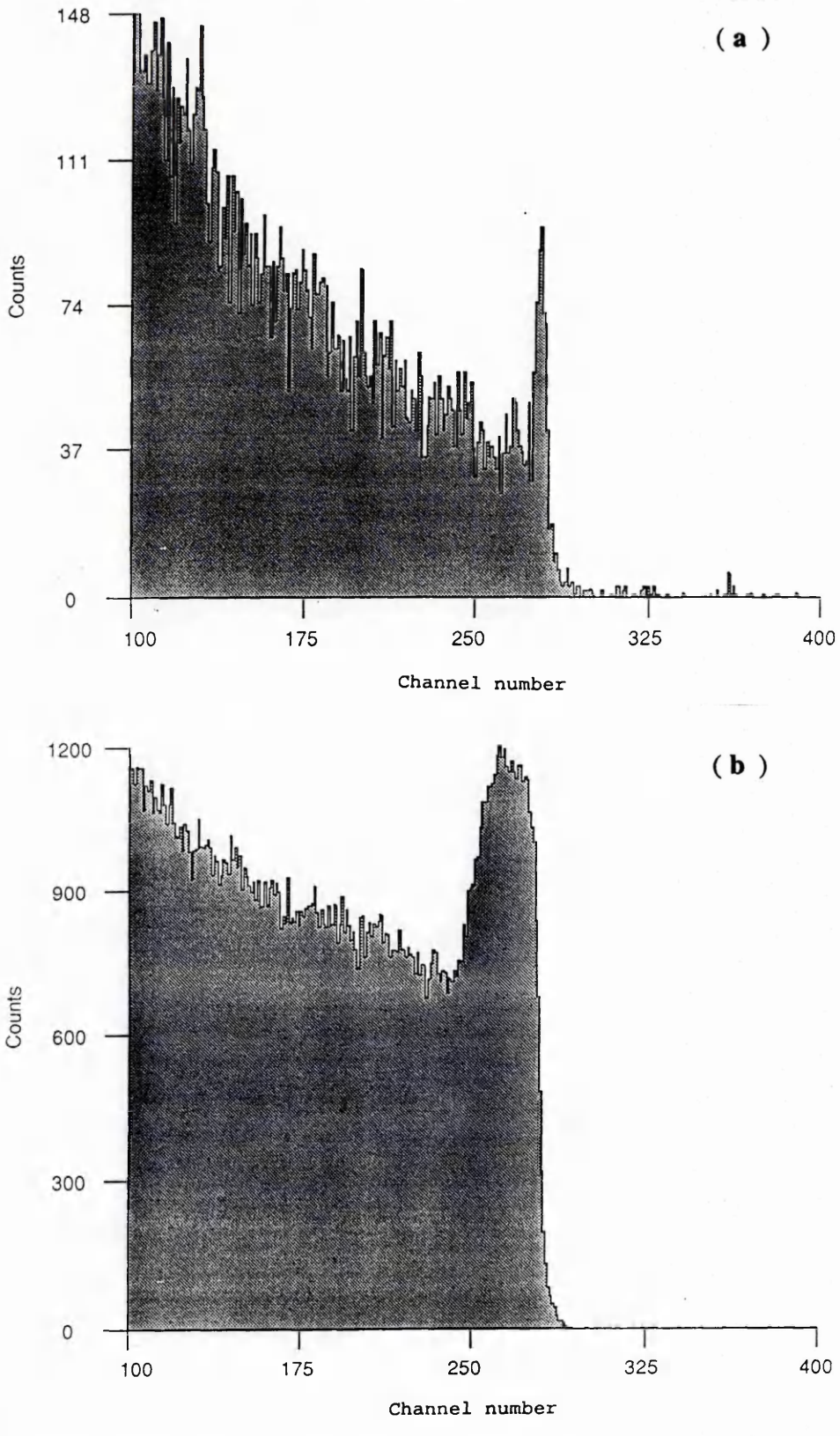

Fig. 6.5 Rutherford back-scattering spectrum (1.5 MeV He^+ ions) from (a) polished surface (b) single-point diamond turned, silicon disc.

produces the back-scattering energy spectrum as a series of counts (back-scattering yield) versus channel number which corresponds to energy and depth.

A standard sample is used to calibrate the energy per channel of a back scattering spectrum. From the measured energy per channel the energy scale was converted from channel numbers to depth scale.

The ion beam facility used in this research is located in Department of Electronic and Electrical Engineering, University of Surrey and the tests were arranged by Prof. K. Puttick, Mr. M. Rudman and Dr.C.Jeynes, whose cooperation is gratefully acknowledged.

In the present study, a beam of helium ions(He^+) at an energy of 1.5 MeV (beam current 3 nA to 15 nA) was used and the stability of the beam was better than ± 1.5 KeV. With 400 channels for 1.5 MeV this yields approximately 3.75 keV per channel.

Fig. 6.5a and Fig. 6.5b show the energy spectra recorded by the multi-channel analyzer from polished and diamond-turned surface of single crystal silicon. The (right hand) leading edge of the peak appearing at the right hand side of the figure represents the surface of the silicon specimen.

For a polished surface (Fig. 6.5a), the small peak is probably caused by the intrinsic surface scattering and oxide and/or other contaminated layer. The spectrum obtained from a turned specimen, however, has a relatively wide peak which can only be ascribed to subsurface damage. The peak width is 28 channels, and, since each channel represents 6 nm of depth, the damaged layer revealed by this method is 168 nm in depth.

6.4 X-ray Topography

X-ray topography is a non-destructive method which, using a diffracted beam of x-ray, can reveal imperfections, twinning, inclusions, dislocations and strains in crystals. The most commonly used x-ray topographic methods are the Berg-Barrett (reflection and transmission) method (Berg 1931, Barrett 1945), the Borrmann (1951) method, Schulz (1954) method, Lang (1957, 1959) (section and projection) method and the double-crystal method (Bond and Andrus 1952; Bonse and Kappler

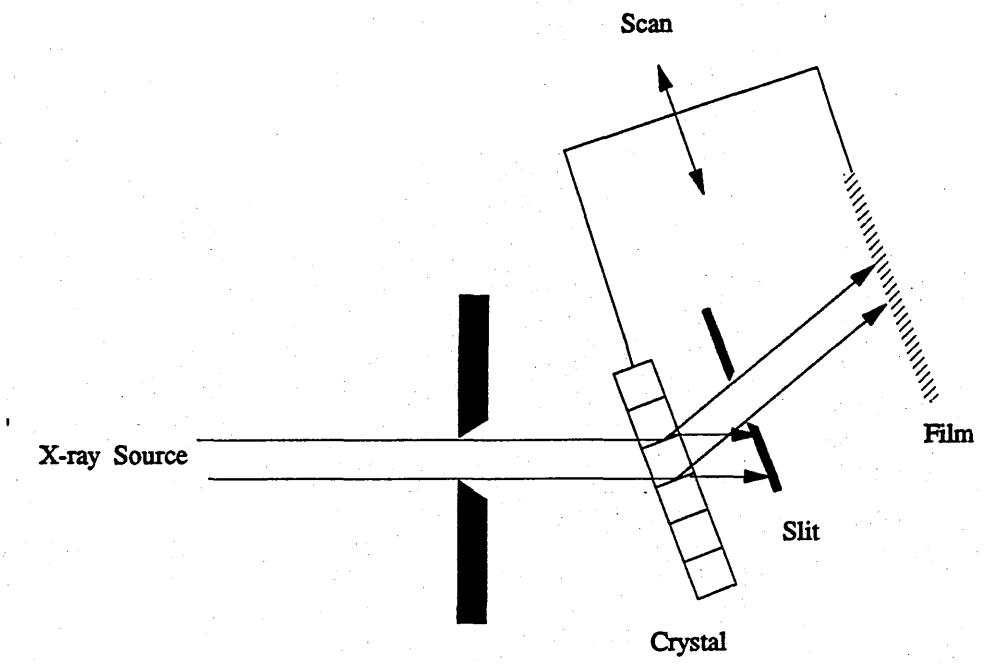

Fig. 6.6 Arrangement for the Lang's method. Section topographs correspond to the stationary situation. Specimen and film can be moved (scan) together across the beam to form projection topograph.

1958). [The details of these methods can also be found in Meieran (1969) and Tanner (1976)].

The method used in this study was Lang's method and its arrangement was shown in Fig. 6.6. This uses a slit-collimated beam of monochromatic x-ray (characteristic radiation) to pass through a crystal and the Bragg reflected beam of radiation ($K_{\alpha 1}$ and $K_{\alpha 2}$) was recorded by an emulsion plate held perpendicular to the Bragg reflected beam.

Lang's method can be used in a *section* or *projection* manner. The *section topography* is obtained when the film plate is held stationary so that the photograph produced is a thin section of the crystal. If the crystal and photographic plate are moved back and forth together across the Bragg reflected beam with a constant velocity, the obtained photograph is called a *projection topography*. A projection topography is actually a series of section topographies and can show the defects throughout the scanned volume of the tested crystal.

Fig. 6.7 Series of 2 $\bar{2}$ 0 section topographs of a coarsely machined single crystal silicon. Note that the local contrast is caused by ring of turning.

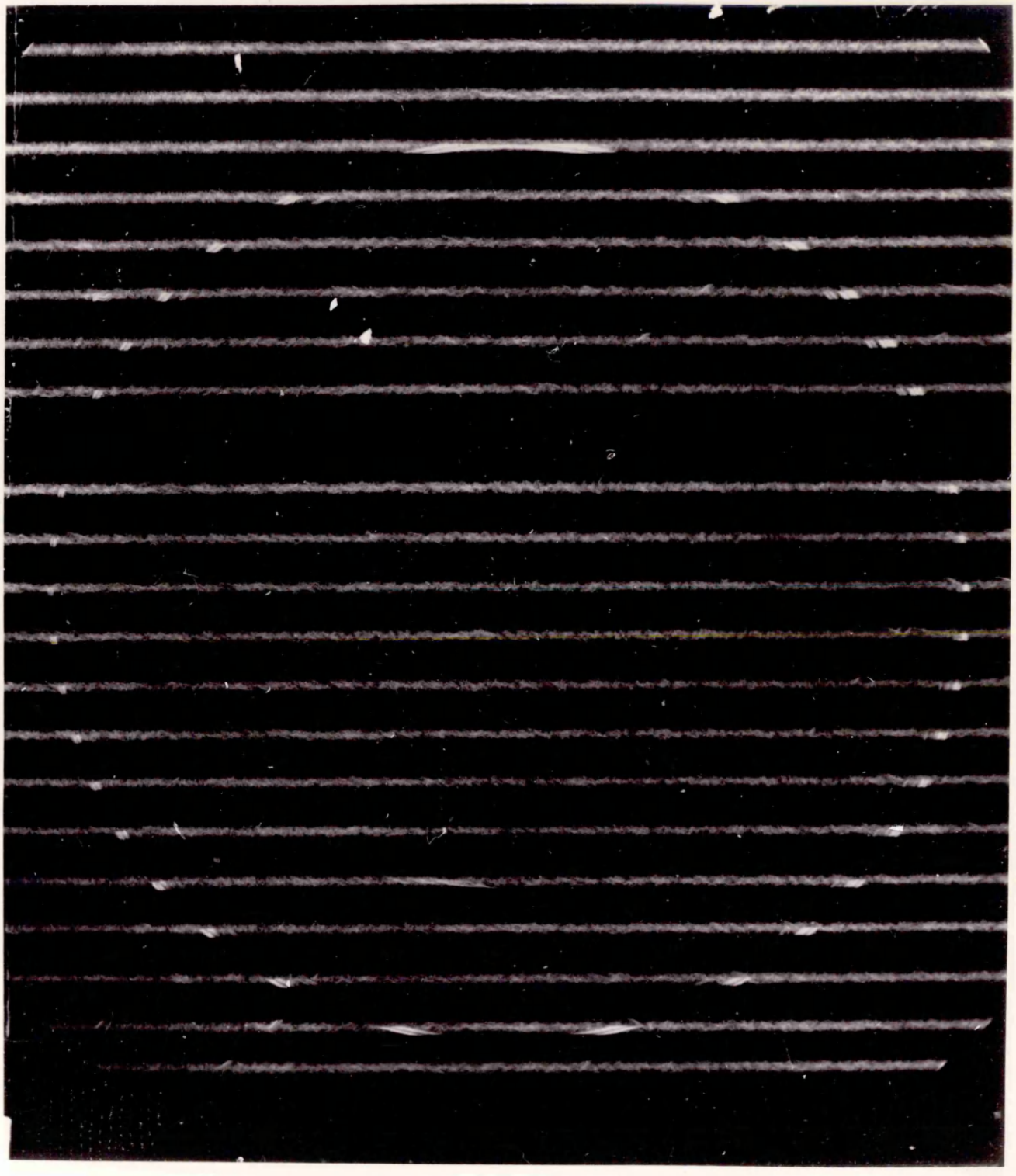

Fig. 6.7 Series of $2\bar{2}0$ section topographs of a coarsely machined single crystal silicon. Note that the local contrast is caused by ring of turning.

Fig. 6.8 $2\bar{2}0$ projection topograph of coarsely machined surface of silicon crystal.

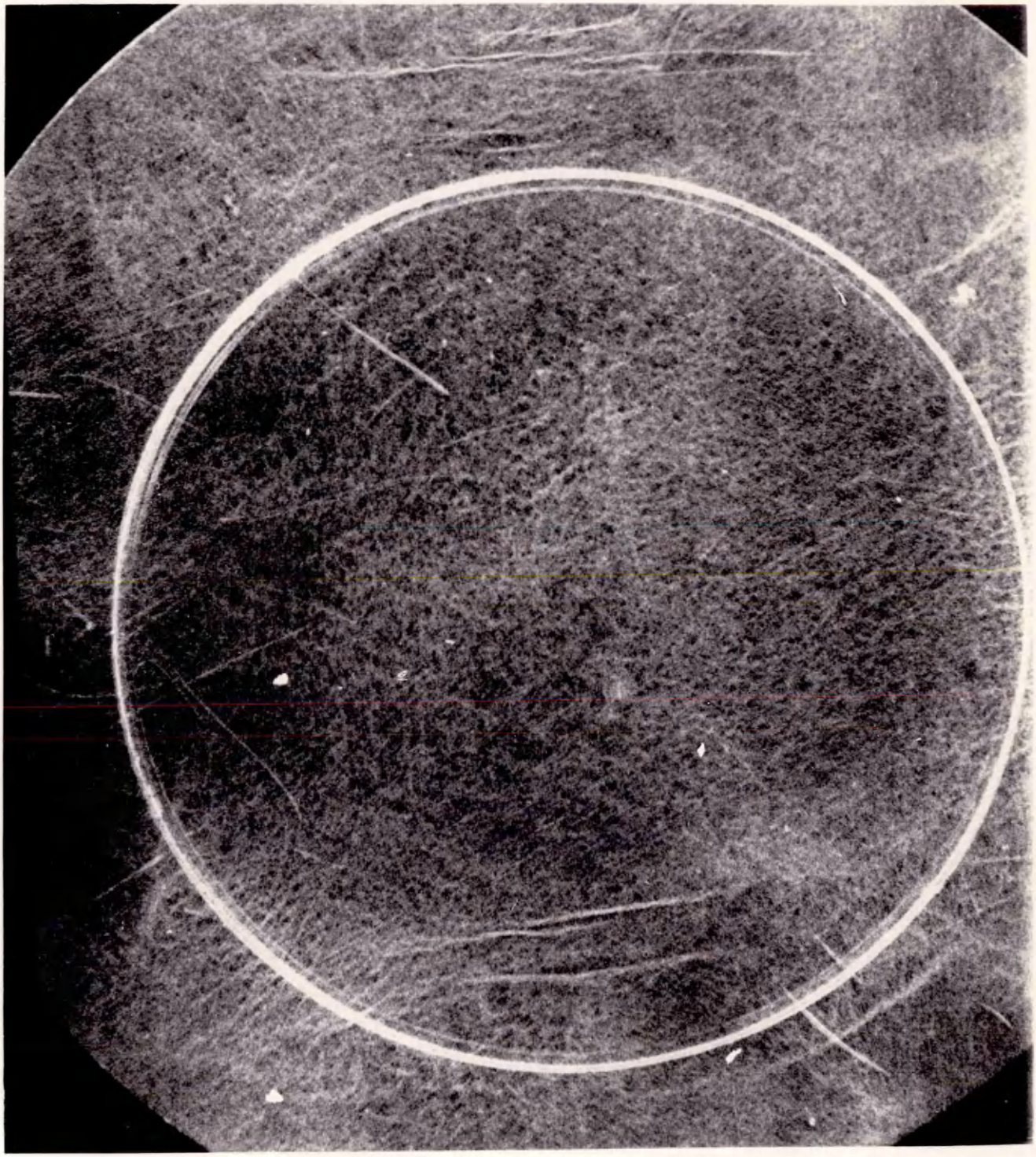

Fig. 6.8 $2\bar{2}0$ projection topograph of coarsely machined surface of silicon crystal.

The resolution of x-ray topography obtained by using Lang's method was decided by the characteristic lines ($K_{\alpha 2} - K_{\alpha 1}$ doublet) which is dependent on the x-ray target used. For copper, the difference between this two lines (wavelength) is 0.154433 - 0.154051 = 0.000382 nm and for molybdenum it is 0.071354 - 0.070926 = 0.000428 nm (Moore 1988).

The Lang camera used in the present study was located in University of London (Royal Holloway and Bedford New College) and the experiments were conducted with the help of Mr. R. Waggett and Dr. M. Moore of the Physics Department.

Fig. 6.7 and Fig. 6.8 show a series of *section topographs* and a *projection topographs* in 220 reflection of the same specimen which was coarse machined. The machined ring (or segments of ring) can be easily seen in both figures. The widths of the light contrast in Fig. 6.7 can be used to calculate the depth of damaged layer. Based on the measurements made on the original photographic plate, the damage layer thickness ranged from 160 μm to 300 μm.

Chapter 7

Conclusions

7.1 Review of the work

As discussed in chapter 1 and 2, brittle materials such as glass, ceramics and glass-ceramics, exhibit properties which are needed for present and future advanced technology applications. However, hardness and brittleness renders them very difficult to machine to required form and/or finish. Finish machining has hitherto required long tedious periods using traditional lapping and polishing processes. However, even that does not meet the demands of today's precision engineering which requires both fast production rates and surfaces of complex shape. In order to overcome these difficulties, the investigation of the feasibility of turning/grinding brittle materials in ductile-mode is important for the achievement of larger material removal rates.

Multi-point grinding is a complex process with multiple controlling variable associated with the rotating wheel (see section 1.3). The single-point process offers less variables and the possibility of modelling certain critical features of the multi-point process, and so the emphasis of this research was mainly on the single point process. Three types of single point processes have been investigated, namely indentation, ruling/scribing and lathe-facing.

The indentation technique was used to study the tool/specimen interaction on a micro-scale and quasi-static basis. The process of changing from plastic deformation to brittle fracture when materials are subjected to increasing load (and therefore penetration depth) was to certain degree similar to machining. Indentation was also used to evaluate the material properties (such as the yield stress and the stress intensity factor (see sections 2.2, 2.3) at microscopic scales).

Dead-load ruling and scribing experiments described in section 3.5 offered a simple way to study dynamic effects (by moving tool across the specimen surface) and material removal mechanisms involved (section 4.2).

On the experimental single point diamond turning machine described in sections 5.1 and 5.4, the effect of a number of variables was investigated, including cutting speed, cross-feed rate, and cutting depth.

Machined specimens were examined using the scanning electronic microscope (SEM) and the Talystep stylus instrument to study the quality of the surface, and by scanning acoustic microscopy (SAM) (section 6.2), X-ray topography (section 6.3), and Rutherford back-scattering (section 6.4) techniques to survey the sub-surface damage.

7.2 Conclusions and the Feasibility of Ductile Mode Machining

For the first time, continuous machining has been achieved by single-point diamond turning (facing) of highly brittle materials, resulting in surfaces with Ra values of the order of nanometres. Several brittle materials and tests have been used in this research and the principal conclusions are:

- Indentation (section 2.4) and scribing (section 3.4, 3.5) experiments have shown that when the load (which determines penetration depth) is below a certain critical value, in the cases of soda lime glass 50 grams, fused silica 10 grams, silicon 5 grams, and Zerodur 10 grams, the material is deformed by plastic flow instead of brittle fracture.

- Upon fracture the indentation crack pattern of

- (1) soda-lime glass shows radial cracks emanating from the corners of the residual impression and lateral cracks from the edge of the plastic zone (as shown in Fig. 2.1),

- (2) fused silica (and Zerodur) is a mixture of a series of concentric ring/cone cracks (surrounding the residual impression) and radial cracks (emanating from the corners of the Vickers indenter) (section 2.4.2),

- (3) single crystal silicon is strongly influenced by the crystallographic angle (section 2.4.3) at low loads (< 25 grams) but at high loads (>50 grams) the effect of indentation orientation becomes dominant.

- It has been shown in the indentation tests conducted in this study on diamond turned fused silica (section 2.4.2) that the presence of residual stress on the surface could suppress the initiation and propagation of radial cracks (with 500 grams load, radial cracks 20 μm long were observed on polished fused silica while no radial crack was initiated on a sample which was diamond turned). Generally, the diamond turned specimens showed lower hardness values than that of polished specimens.

- The role of various material removal mechanisms involved in machining brittle materials has been clarified in this study. These include *ploughing* (plastic flow) (section 4.2.2), *cutting mechanism* (section 4.2.3), *delamination* (centre-delamination, side-delamination) (section 4.2.4), and *brittle fracture* (section 4.2.5).

- With the *cutting mechanism*, material is removed by shearing (section 4.2.3) which is very similar to the mechanism commonly seen in traditional ductile metal cutting. Compared to *ploughing* and *delamination*, the *cutting mechanism* can provide larger material removal rates and better dimensional control (see section 4.2.2 and 4.2.4).

- In general, it has been found in this work that tool shapes are directly linked to the material removal mechanisms. Several different shaped diamond tools were used including canoe shaped (curve edged), straight edged (roof-edge), Vickers and scratching tool (see section 3.4.2) to identify the influence of tool shape. It is shown in sections 3.5 and 4.2 that the *cutting mechanism* is more favourable to tools with small rake angles while *delamination* and *ploughing* are more favourable for tools with large

negative rake angles. (The presence of a high negative rake angle may generate a highly compressed stress field in front of the tool which can delay the threshold of cracks. The high hydro-static pressure will also increase the yield stress.)

- Based on the results of indentation, ruling and scribing experiments on polished silicon single crystal (1 1 1) surface in this study, the cracks produced generally followed the < 1 1 0 > or < 1 1 2 > directions. This conformed with the previous work of Badrick et al (1977), Puttick and Shahid (1979) and Hosseini (1980). However, the *sense effect* with single crystal silicon experienced in scribing/ruling (section 3.5.2) becomes insignificant when the cut depth is smaller than the critical cut depth (section 5.4.2).

- It has also been showed in this study that when the cut depth is kept below the critical value a crack free ultra-fine machined surface can be obtained regardless of the crystallographic angle. This means that anisotropy may become insignificant if the cutting depth can be kept under the critical depth (0.6 to 0.8 μm).

- It is shown in this work that both fused silica and single crystal silicon can be diamond turned to a surface roughness (Ra) of the order of nanometres. These results (section 5.4.2) have demonstrated that, with a rigid machine, a stabilised environment (vibration and temperature), required measuring system and a cut depth smaller than the critical value, ductile-mode diamond turning is achievable. (The critical cut depth for soda lime glass, fused silica, and single crystal silicon, as obtained by "wedge-cut" experiments (section 5.6), are 0.8-1.2 μm, 0.7-0.9 μm, and 0.6-0.8 μm respectively. However, it should be borne in mind that critical cut depth is set as a limit for the "real" cutting depth which in practice is the combination of "programmed" cutting depth, spindle run-out, vibration induced depth variation and thermal expansion. As a consequence,

the increase of one of these terms means the reduction of tolerance of all the rest, and machine with, say, spindle axial run-out larger than the critical cutting depth can not produce ductile mode machining results.)

- Based on the experimental results of diamond turning a damaged specimen (section 5.6), the cut depth has to be kept very small (smaller than one quarter of the critical cutting depth) in order to prevent further propagating the existing cracks. This makes single point diamond turning an impractical process for machining a heavily damaged specimen, since it needs many passes to remove the damaged layer. (Creep-feed diamond grinding may be a possible answer for this kind of work. However, as discussed in chapter 6, a very good surface finish does not guarantee that deep-penetrating median cracks have been totally removed.)

- The diamond turning tests conducted on sawn and etched single crystal silicon (section 5.6) showed that it could be machined with cut depth up to five micrometres without producing large downward propagated cracks. However, the large chips produced in this deep cut process might sometime be trapped between tool rake face and specimen surface with consequent occasional high damage levels.

- The results of the *sub-surface damage* (SSD) study using the scanning acoustic microscope (SAM), Rutherford back-scattering (RBS) technique, and X-ray topography have shown (sections 6.2, 6.3, 6.4) that

  - (1) a good surface-finish does not always mean all the SSD, introduced by the coarse machining, has been removed
  - (2) when the cut depth is below the critical value (ductile machining) the SSD can be kept down to the 100 nm range
  - (3) frequencies higher than 3 GHz (resolution better than 400 nm) are required for measuring sub-micrometre SSD (200-500 MHz used on SAM in this study proved to be too low)

- (4) RBS and X-ray topography (especially the former) are possible nondestructive techniques to measure SSD.

Chapter 8

Suggestions for Continuing Research

As a result of the work the following recommendations for further study are offered:

(1) It would be appropriate to test a range of different materials and comment on their machinability and to what extent.

(2) Sub-surface damage needs further study so that it can be correlated with tool shape and machining condition such as cutting speed, depth, coolant. Accurate methods of measurement of sub-surface damage are required.

(3) In order to improve the existing experimental diamond turning machine, it would be worthwhile building and testing the tilt-stage and control algorithm proposed in section 5.2.

(4) Referring to section 3.5, 4.2 and 5.5, a study of a wider range of diamond tools is needed to obtain general rules about the influence of the tool shape and to study the tool wear.

(5) A thermal image system which can measure temperature with resolution of $0.1\ ^{o}C$ is required to ascertain the temperature of the tool tip and workpiece surface temperature and which may offer a technique to monitor first contact and tool and workpiece surface temperature.

(6) The effect of coolant needs to be studied.

Reference

Atkins, A.G. & Mai, Y.W.	1985	*Elastic and Plastic Fracture*, Ellis-Horwood, Chichester, UK
Atkins, A.G. & Mai, Y.W.	1986	*J. of Mat. Sci.*, Vol.21, p1093
Atkins, A.G. & Tabor, D.	1965	*J. Mech. Phys. Solids*, Vol. 13, p149
Arora, A. Marshall, D.B. & Lawn, B.R.	1979	*J. Non-Crystal. Solids*, Vol.31, p415
Auerbach, F.	1891	*Ann. Phys. Chem.*, Vol.43, p61
Badrick, A.S.T. Eldeghaidy, F. Puttick, K.E. & Shahid, M.A.	1977	*J. Phys. D: Appl. Phys.*, Vol.10, p195
Barrett, C.S.	1945	*Trans. AIME*, Vol. 161, p15
Beilby, G.T.	1907	*Trans. Opt. Soc.*, Vol.9, p22
Beilby, G.T.	1921	*Aggregation and Flow of Solids*, Macmillan London
Berg, W.F.	1931	*Naturwissenschaften*, Vol. 19, p391
Berman, R.	1979	*The Properties of Diamond*, ed. J.E. Field, Academic Press, London, p4
Bifano, T.G.	1989	PhD Thesis, North Carolina State University, Raleigh, USA

Bifano, T.G. Dow, T.A. & Scattergood, R.O. 1988 *Ductile-regime Grinding of Brittle Materials,* Proc. Conf. on Ultra-Precision in Manufacturing Engineering, Aachen, Germany

Bishop, R.F. Hill, R. & Mott, N.F. 1945 *Proc. Phys. Soc.*, Vol.57, p147

Blake, P.N. & Scattergood, R.O. 1988 *Ductile Regime Turning of Ge and Si,* Proc. 2nd Intersociety Sympos. of Ceramic Materials and Components, p249, ASME Winter Ann. Mtng., Chicago, Nov.30-Dec.2, 1988

Bond, W.L. & Andrus, J. 1952 *Am. Mineralogist*, Vol. 37, p622

Bonse, U. & Kappler, E. 1958 *Z. Naturforschung*, Vol. 13a, p348

Borrmann, G. 1951 *J. Appl. Phys.*, Vol. 22, p1139

Bowden, F.P. & Ridler, K.E.W. 1936 *Proc. Roy. Soc.* A.154, p640

Boyd, D.C. & Thompson, D.A. 1985 *Encyclopedia of Glass, Ceramics and Cement,* p462, John Wiley, New York

Boyer, H.E. 1987 *Hardness Testing*, ed. H.E. Boyer, ASM International, Metal Park, Ohio, USA, p67

Brinell, J.A. 1900 *Congr. Int. Methods d'Essai*, Paris, 1900

Broek, D. 1986 *Elementary Engineering Fracture Mechanics,* 4th ed., Martinus Nijhoff Publ.,Lancaster, UK

Broese van Groenou, A. & Veldkamp, J.D.B. 1978/79 *Philips Tech. Rev.*, Vol.38, p105

Bryan, J.B. & Carter, D.L.	1985	Lawrence Livermore Natl. Lab., Rep. No.: UCRL-92682, Berkeley, California
Busch, D.M.	1968	Dissertation, Technical University of Hanover
Carslaw, H.S. & Jaeger, J.C.	1959	*Conduction of Heat in Solids*, 2nd Ed., Clarendon Press, Oxford
Chao, C.L. & Gee, A.E.	1989	IPES5/ASPE Meeting, 18-22 Sept., Monterey, CA, Abstracts, p259
Cheng, W.L. & Finnie, I	1990	*J. Mat. Sci.*, Vol.25, p575
Chiang, S.S. Marshall, D.B. & Evans, A.G.	1982	*J. Appl. Phys.*, Vol.53, No.1, p298
Churchill, S.W. & Bernstein, M.	1977	*J. Heat Transfer*, Vol.99, p300
Dash, W.C.	1957	*Dislocations and Mechanical Properties of Materials*, Wiley, New York, p57
Dawihl, V.W. & Altmeyer, G.	1964	*Zeitschrift fur Metallhunde*, Vol.55, p231
Demichelis, M.F. Perucca, E.	1951	*Verres et Refractairies*, p1
Ditchburn, R.W. Thomson, J.J. & Custers, J.F.H.	1965	*Physical Properties of Diamond*, ed. R. Berman, Clarendon Press, Oxford, p1
Duduch, J. & Gee, A.E.	1990	Proc. ASPE Ann. Conf., p170, Sept. 23-28, 1990, Rochester, N.Y.

Ernst, H. & Merchant, M.E.	1941	*Chip Formation, Friction and High Quality Machined Surfaces* , in Surface Treatment of Metal, Vol.29, American Society of Metals, New York, p299
Evans, A.G.	1979	*Fracture Mechanics Applied to Brittle Materials*, (ASTM-STP678), p112, ASTM, Philadelphia
Evans, T.	1967	*Science and Technology of Industrial Diamonds*, Vol.1, ed. J. Burl, p105, Industrial Diamond Information Bureau, London
Evans, T. & Wild, R.K.	1965	*Phil. Mag.*, Vol.12, p479
Evans, A.G. & Wilshaw, T.R.	1977	*J. Mat. Sci.*, Vol.12, p97
Falter, P.J. & Dow, T.A.	1987	*Precision Engineering*, Vol. 9, p185
Farris, T.N. & Chandrasekar, S.	1990	*J. Mat. Sci.*, Vol.25, p4047
Frank, F.C. & Lawn, B.R.	1967	*Proc. Roy. Soc. Lond.* A229, p291
Frank, F.C. & Read, W.T.	1950	*Multiplication processes for slow-moving dislocations*, Pittsburgh Symposium, Office of Naval Research, p44
French, J.W.	1917	*Trans. Opt. Soc.*, Vol.18, p8
Gallagher, C.J.	1952	*Phys. Rev.*, Vol.88, p721
Geach, G.A. Irving, B.A. & Phillip, R	1957	*Research*, Vol.10, p411

Gee, A.E.	1974	Ph.D Thesis, University of Reading, England
Gee, A.E.	1990a	*Applied Optics Digest*, ed.: J.C. Dainty, p109, IOP, Bristol, UK
Gee, A.E.	1990b	*Nanotechnology Forum/ERATO Symposium*, Warwick, August 21-22
Gee, A.E. Green, D. & Pain, D.	1988	*Surface Topography*, Vol. 1, p183; also Proc. 4th Intl. Conf. on Metrology and Properties of Eng. Surfaces, Washington DC, Apr. 1988, p385, Kogan-page, London
Gee, A.E. McCandlish, S.G. & Puttick, K.E.	1988	SPIE 1015, p74, Proc. Conf.on *Micromachining Optical Components and Precision Eng.*, Hamburg, Sept. 1988
Gilman, J.J.	1959	*J. Appl. Phys.*, Vol.30 (No.10), p1584
Gilman, J.J. & Johnston, W.G.	1957	*Dislocations and Mechanical Properties of Materials*, Wiley, New York, p116
Griffith, A.A.	1921	*Phil. Trans. Roy. Soc. London*, A221, p163
Griffith, A.A.	1924	*Proc. 1st Int. Congr. Appl. Mech.*, p55
Gurney, C. & Hunt, J.	1967	*Proc. Roy. Soc. London*, A299, p508
Hagan, J.T.	1979a	*J. Mat. Sci.*, Vol.14, p462
Hagan, J.T.	1979b	*J. Mat. Sci.*, Vol.14, p2975
Hagan, J.T.	1980	*J. Mat. Sci.*, Vol.15, p1417

Hagan, J.T. & Swain, M.V.	1978	*J. Phys. D.*, Vol.11, p2091
Hagan, J.T.; Swain, M.V. & Field, J.E.	1979	*NBS Special Publ. 562*, Ed. by B.J. Hockey and R.W. Rice, p15, U.S. Government Print. Office, Washington D.C.
Hagan, J.T. & Van Der Zwaag, S.	1984	*J. Non-Crystal. Solids*, Vol.64, p249
Hamilton, G.M. & Goodman, L.E.	1966	*J. Applied Mechanics*, Trans. ASME, Vol.33, p371
Hertz, H.	1882	*Verhandlungen des Vereins zur Beforderung des Gewerbefleisses*, Leipzig, Nov. 1882 (English Translation: Miscellaneous Papers by H. Hertz, Eds. Jones and Schott, London: Macmillan, 1896)
Hill, R.	1950	*The Mathematical Theory of Plasticity*, Clarendon Press, Oxford
Hill, R. Tupper, S.J. & Lee, E.H.	1947	*Proc. Roy. Soc. A*, Vol.188, p273
Hirst, W. & Howse, M.G.J.W.	1969	*Proc. Roy. Soc. A*, Vol.311, p429
Horne, D.F.	1978	*Spectacle Lens Technology*, Adam Hilger, Bristol
Horsfield, W.R.	1965	*Appl. Opt.*, Vol.4, p189
Howse, M.G.J.W.	1968	Ph.D Thesis, University of Reading, England
Inglis, C.E.	1913	*Trans. Inst. Naval Architects*, Vol.55, p219

Irwin , G.R.	1958	*Fracture*, Handb. Phys., Vol.6, p551
Irwin, G.R. & Kies, J.A.	1952	*Welding J. Res. Suppl.*, Vol.17 (Feb.)
Ishida, Y. & Ogawa, G	1962	*J. Mechanical Lab. of Japan*, Vol.8, No.1, p15
Izumitani, T	1986	*Optical Glass*, American Inst. of Physics
Jaeger, J.C.	1943	*J. Proc. Roy. Soc. N.S.W.*,Vol.76, p203
Jenkins, F.A. & White, H.E.	1981	*Fundamentals of Optics*, 4th ed., McGraw-Hill, London
Johnson, K.	1970	*J. Mech. Phys. Solids*, Vol.18, p115
Johnson, K.	1985	*Contact Mechanics*, Cambridge University Press, Cambridge
Johnson, W. & Mellor, P.B.	1983	*Engineering Plasticity*, Ellis Horwood, Chichester, UK
Joos, P.	1957	*Z. Angew. Phys.*, Vol. 9, p556
Karman, T. von	1921	*Z. Angew. Math. Mech.*, Vol.1, p233
King, A.G. & Wilks, J.	1976	*Int. J. Mach. Tool Design Res.*, Vol.16, p95
Kingery, W.D. Bowen, H.K. & Uhlmann, D.R.	1975	*Introduction to Ceramics*, 2nd ed., John Wiley, New York
Kino, G.S.	1987	Acoustic Waves, Prentice-Hall, Inc, Englewood Cliffs, New Jersey, USA

Kirchner, H.P.	1979	*NBS Special Publ. 562*, Ed. by Gruver, R.M. & B.J. Hockey and R.W. Rice, Richard, D.M. p23, U.S. Government Print Office, Washington D.C., USA
Klemm, W. Smekal, H.	1941	*Naturwissenschaften*, Vol. 29, p688
Lang, A.R.	1957	*Acta Met.*, Vol. 5, p359
Lang, A.R.	1959	*Acta. Cryst.*, Vol. 12, p249
Lankford, J.	1981	*J. Mat. Sci.*, Vol.16, p1177
Lankford, J. & Davidson, D.L.	1979	*J. Mat. Sci.*, Vol.14, p1662
Lawn, B.R.	1967	*Proc. Roy. Soc. A*, Vol.299, p307
Lawn, B.R.	1980	*J. Amer. Ceram. Soc.*, Vol.63 (No.9-10), p574
Lawn, B.R. & Evans, A.G.	1977	*J. Mat. Sci.*, Vol.12, p2195
Lawn, B.R. & Fuller, E.R.	1975	*J. Mat. Sci.*, Vol.10, p113
Lawn, B.R. & Marshall, D.B.	1978	*Fracture Mechanics of Ceramics 3*, Plenum Press, New York, p205
Lawn, B.R. Marshall, D.B. & Chantikul, P.	1981	*J. Mat. Sci.*, Vol.16, p1769
Lawn, B.R. & Swain, M.V.	1975	*J. Mat. Sci.*, Vol.10, p113

Lawn, B.R. & Wilshaw, T.R.	1975a	*J. Mat. Sci.*, Vol.10, p1049
Lawn, B.R. & Wilshaw, T.R.	1975b	*Fracture of Brittle Solids*, Cambridge University Press, Cambridge, UK
Leu, H.J. & Scattergood, R.O.	1988	*J. Mat. Sci.*, Vol.23, p3006
Mai, Y.W.	1977	*Int. J. Mech. Sci.*, Vol.19, p325
Marsh, D.M.	1964	*Proc. Roy. Soc. A*, Vol.279, p420
Marshall, D.B. & Lawn, B.R.	1979	*J. Mat. Sci.*, Vol.14, p2001
Marshall, D.B. & Lawn, B.R.	1986	*ASTM Special Tech. Publ. 889*, Ed. by P.J. Blau and B.R. Lawn, p26, Philadelphia, USA
McKeown, P.	1986	*Proc. Instn. Mech. Engrs.*, Vol.200, p1
McSkimin, H.J. & Andreatch, P.	1972	*J. Appl. Phys.*, Vol.43, p2944
Merchant, M.E.	1945	*J. Appli. Phys.*, Vol.16, No.5, p267
Meyer, E.	1908	*Z. Ver. drsch. Ing.*, Vol. 52, p645
Mindlin, R.D.	1936	*Physics*, Vol.7, p85
Minomura, S. & Drickamer, H.G.	1962	*Phys. Chem. Solids*, Vol.23, p451
Misra, A. & Finnie, I	1979	*J. Mat. Sci.*, Vol.14, p2567
Moore, M.	1988	*Industrial Diamond Review*, No.2, p59
Morrell, R.	1985	*Handbook of Properties of Technical &*

Engineering Ceramics (Part I), NPL publ., London

Motonishi, S. Hara, Y. & Yoshida, K. 1990 *Kobe Steel Eng. Rep.*, Vol.40, No.2, p77

Mulheam, T.O. 1959 *J. Mechanics and Physics of Solids*, Vol.7, p85

Mykolajewycz, R. Kalnajs, R. & Smakula 1964 *J. Appl. Phys.*, Vol.35, p1773

Orowan, E. 1955 *Welding J. Res. Suppl.*, Vol.20, p157

Owen, J.M. & Rogers, R.H. 1989 *Flow and Heat Transfer in Rotating-Disc Systems*, Research Studies Press Ltd., Somerset, England

Palmer, E.W. Hutley, M.C. Franks, A. Verrill, J.F. & Gale, B. 1975 *Rep. Prog. Phys.*, Vol.38, p975, IOP, London

Palmqvist, S. 1962 *Archiv Eisenhuettenwesen*,Vol.33, p629

Palmqvist, S. 1963 *Jernkontorets Annalen*, Vol.167, p208

Perrot, C.M. 1977 *Wear*, Vol.45, p293

Peter, K.W. 1970 *J. Non. Cryst. Solids*, Vol.5, p103

Piispanen, R. 1969 *Ann. C.I.R.P.*, Vol.XVII, p561

Preston, F.W. 1922 *Trans. Opt. Soc.*, Vol.23, p141

Puttick, K.E.	1973	*J. Phys. E: Sci. Instrum.*, Vol.6, p116
Puttick, K.E.	1980	*J. Phys. D: Appl. Phys.*, Vol.13, p2249
Puttick, K.E. & Hosseini, M.M.	1980	*J. Phys. D: Appl. Phys.*, Vol.13, p875
Puttick, K.E. Rudman, M.R. Smith, K. Franks, A. & Lindsey, K.	1989	*Proc. Roy Soc. A.* 426, p19
Puttick, K.E. & Shahid, M.A.	1977	*Industrial Diamond Review*, July, p228
Puttick, K.E. Shahid, M.A. & Hosseini, M.M.	1979	*J. Phys. D: Appl. Phys.*, Vol.12, p195
Puttick, K.E. Smith, L.S.A. & Miller, L.E.	1977	*J. Phys. D: Appl. Phys.*, Vol.10, p617
Quate, C.F.	1985	*Physics Today*, Aug. , p34
Quate, C.F. Atalar, A & Wickramasinghe, H.K.	1979	*Acoustic Microscopy with Mechanical Scanning - a Review*, Proc. IEEE, Vol. 67
Rawstron, G.O.	1958	*J. Soc. Glass Tech.*, Vol.42, pp253T-260T
Rayleigh, J.W.S.	1903	*Scientific Papers (1892-1901)*, Vol.4, p.54, 74, Cambridge University Press, Cambridge

Reed-Hill, R.E.	1973	*Physical Metallurgy Principles*, 2nd ed.,
Roesler, F.C.	1956	*Proc. Phys. Soc.*, Vol.B69, p53
Samuels, L.E. & Mulhearn, T.O.	1957	*J. Mechanics and Physics of Solids*, Vol.5, p125
Schinker, M.G. & Doll, W.	1985	*Strength of Inorganic Glass* (ed. C.R. Kurkijan), Plenum Publishing, New York
Schinker, M.G. & Doll, W.	1987	*Proc. SPIE*, Vol. 802, p70
Schulz, L.G.	1954	*Trans. AIME*, Vol. 200, p1082
Scruby, C.B. Lawrence, C.W. Fatkin, D.G.P. Briggs, G.A.D. Dunhill, A., Gee, A.E. & Chao, C.L.	1989	*Br. Ceram. Trans. J.*, Vol.88, p127
Seal, M.	1958	*Proc. Roy. Soc.*, A248, p379
Sedricks, A.J. & Mulhearn, T.O.	1964	*Wear*, Vol.7, p451
Shahid, M.A.	1977	PhD Thesis, University of Surrey, England
Shaw, M.C.	1984	*Metal Cutting Principles*, Oxford University Press, London
Sih, G.C.	1973	*Handbook of Stress Intensity factors*, Lehigh University Press, Bethlehem

Smith, R. & Sandland, G.	1925	*J.I.S.I.*, Vol.111, p285
Sneddon, I.N.	1965	*Int. J. Eng. Sci.*, Vol.3, p47
Sokolov, S.Y.	1949	*Dokl. Akad. Nauk. SSSR*,Vol. 64, p333
Stewart, D.R.	1985	*Encyclopedia of Glass, Ceramics and Cement*, pp538-549, John Wiley & Sons, Inc., New York
Stroh, A.N.	1957	*Adv. Phys.*, Vol.6, p418
Stroke, G.W.	1967	*Diffraction Gratings*, Handbuch der Physik, ed. S. Flugge, vol 29 p426, Springer-Verlag, Berlin
Studman, C.J. Moore, M.A. & Jones, S.E.	1977	*J. Phys. D: Appl. Phys.*, Vol.10, p949
Sutherland, G.B. Blackwell, D.E. & Simeral, W.G.	1954	*Nature*, Vol.174, p901
Swain, M.V.	1979	*J. Amer. Ceram. Soc.*, Vol.62, No.5-6, p318
Swain, M.V. & Hagan, J.T.	1976	*J. Phys. D: Appl. Phys.*, Vol.9, p2201
Tabor, D.	1951	*Hardness of Metals*, Clarendon Press, Oxford
Tanner, B.K.	1976	*X-ray Diffraction Topography*, Pergamon Press, Oxford
Taylor, E.W.	1949	*J. Sci. Inst.*, Vol.26, p314

Taylor, E.W.	1950	*J. Soc. Glass Tech.*, Vol. 34, p69
Thomas, M.H.	1985	*Encyclopedia of Glass, Ceramics and Cement*, p265, John Wiley & Sons, New York
Tolkowsky, M.	1920	D.Sc. Thesis, University of London
Toulkian, V.S.	1970	*Thermalphysical Properties of Matter*, Vol.1-13, Plenum Publ., New York
Truss, R.W. Duckett, R.A. & Ward, I.M.	1981	*J. Mat Sci.*, Vol.16, p1689
Twyman, F.	1952	*Prism and Lens Making*, 2nd Ed.,Hilger and Watts, London
Veldkamp, J.D.B. Hattu, N. & Snijders, V.A.C.	1978	*Fracture Mechanics of Ceramics*,Vol.3, ed. R.C. Bradt, D.P.H. Hasselman and ,F.F. Lange, Plenum Press, New York, p273
Veldkamp, J.D.B. & Klein-Wassink, R.J.	1976	*Philips Res. Rep.*, Vol.31, p153
Wickramasinghe, K.H.	1989	*Scientific American*, Oct., p74
Wiederhorn, S.M. & Lawn, B.R.	1977	*J. Am. Ceram. Soc.*, Vol.60, p451
Wilks, J.	1980	*PrecisionEngineering*, Vol.2, No.2, p57
Wilks, E.M. & Wilks, J.	1959	*Phil. Mag.*, Vol.4, p158

Wilks, E.M. & Wilks, J.	1965	*Physical Properties of Diamond*, ed. by R. Berman, Ch.8, Oxford University Press, London
Wilks, J. & Wilks, E.M.	1979	*The Properties of Diamond*, ed. J.E. Field, p351, Academic Press, London
Wortman, J.J. & Evans, R.A.	1965	*J. Appl. Phys.*, Vol.36(1), p153

Appendix 1.1: Vickers Hardness Numbers of Silicon (111)

Load / Test No.	10 g	25 g	50 g	100 g	200 g	300 g
1	1405	1078	962	983	948	907
2	1380	1007	971	952	898	911
3	1481	1021	948	1064	910	928
4	1383	1052	1025	898	925	929
5	1352	1108	972	894	902	933
6	1506	997	963	1015	945	917
7	1402	1089	1021	903	906	904
8	1489	1056	1015	915	914	920
9	1339	1031	961	955	950	906
10	1392	1078	971	905	952	902
11	1382	1022	965	915	931	931
12	1354	1123	1071	927	914	928
13	1366	1140	982	998	940	924
14	1432	1051	958	943	920	911
15	1341	1025	966	967	948	915
16	1491	1031	985			
17	1410	998	965			
18	1381	1038	1012			
19	1442	1036	958			
20	1473	1058	950			
High	1506	1140	1071	1064	952	933
Ave.	1410	1052	981	949	924	918
Low	1339	997	948	894	898	902

Appendix 1.2: Vickers Hardness Numbers of Fused Silica

Load / Test No.	10 g	25 g	50 g	100 g	200 g	300 g	500 g
1	1402	1072	949	941	942	928	903
2	1380	995	969	954	950	926	884
3	1071	1094	985	911	927	893	897
4	1483	1007	979	902	932	924	907
5	1471	1104	915	983	937	915	891
6	1506	1037	995	1059	931	934	881
7	1453	1152	1011	908	940	907	894
8	1320	1083	972	894	914	898	871
9	1091	1064	945	906	921	919	895
10	1173	1019	989	902	945	906	871
11	1245	1033	997	897	917	934	910
12	1491	951	941	914	938	913	891
13	1412	1123	918	927	910	932	880
14	1350	1013	971	931	898	917	901
15	1256	1056	921	921	913	928	904
16	1380	1038	974				
17	1440	1129	963				
18	1312	1141	1004				
19	1483	1095	934				
20	1341	1074	928				
High	1506	1152	1011	1059	950	934	910
Ave.	1353	1064	963	930	927	918	892
Low	1071	951	915	894	898	893	871

Appendix 1.3: Vickers Hardness Numbers of Zerodur

Load / Test No.	10 g	25 g	50 g	100 g	200 g	300 g	500 g
1	1282	950	1125	877	831	784	639
2	1021	1206	1246	798	757	693	650
3	1371	1229	1271	890	761	736	671
4	1532	964	988	868	672	651	670
5	996	1088	1011	876	816	759	723
6	1228	1184	1039	896	697	771	629
7	1283	878	978	785	776	693	696
8	995	1046	946	794	754	685	624
9	984	942	982	884	683	767	688
10	1491	1307	1085	843	632	810	706
11	1388	1158	865	774	785	724	675
12	1422	1059	995	804	721	766	649
13	925	1341	1282	788	736	839	661
14	1401	1063	1008	876	709	705	682
15	1282	954	944	846	801	798	654
16	1486	1292	1098				
17	1056	1313	967				
18	996	899	993				
19	967	1285	894				
20	1043	1064	977				
High	1532	1341	1282	896	831	839	723
Ave.	1208	1111	1035	840	742	745	668
Low	925	878	865	774	632	651	624

Appendex 1.4: Vickers Hardness Numbers of Soda lime Glass

Load / Test No.	10 g	25 g	50 g	100 g	200 g	300 g	500 g
1	653	640	592	539	489	488	478
2	763	611	589	574	512	510	492
3	701	568	572	508	495	480	462
4	693	597	632	568	457	483	466
5	783	553	604	519	522	500	451
6	692	662	579	524	519	515	434
7	751	704	634	573	461	476	433
8	730	682	665	529	531	482	490
9	653	619	626	586	520	511	454
10	639	632	588	566	518	470	478
11	621	681	604	524	520	498	448
12	654	668	619	497	488	462	438
13	639	589	622	531	503	506	457
14	721	672	604	582	526	490	489
15	681	634	628	564	501	511	490
High	783	704	665	586	531	515	492
Ave.	692	635	611	546	504	492	464
Low	621	553	572	497	457	462	433